Residual Stress Measurement on Different Length Scales Using Neutron and Synchrotron X-ray Diffraction

Thesis

The Open University

Faculty of Technology

Department of Materials Engineering

Residual Stress Measurement on Different Length Scales Using Neutron and Synchrotron X-ray Diffraction

Sumit Pratihar

August 2006

A thesis submitted to the Department of Materials Engineering of The Open University for the Degree of Doctor of Philosophy

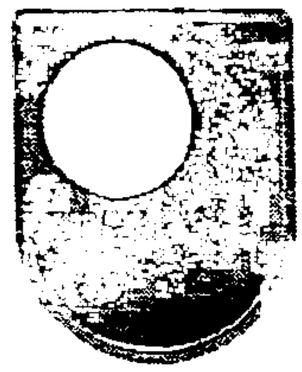

EX12

RESEARCH SCHOOL

Library Authorisation Form

Please return this form to the Research School with the two bound copies of your thesis to be deposited with the University Library. All candidates should complete parts one and two of the form. Part three only applies to PhD candidates.

Part One: Candidates Details

Name: SUMIT PRATIHAR PI: W2458642

Degree: PhD

Thesis title: Residual Stress Measurement on Different Length Scales Using Neutron and Synchrotron X-ray Diffraction.

Part Two: Open University Library Authorisation

I confirm that I am willing for my thesis to be made available to readers by The Open University Library, and that it may be photocopied, subject to the discretion of the Librarian.

Signed: Sumit Pratihar. Date: 09/03/2007

Part Three: British Library Authorisation [PhD candidates only]

If you want a copy of your PhD thesis to be available on loan to the British Library Thesis Service as and when it is requested, you must sign a British Library Doctoral Thesis Agreement Form. Please return it to the Research School with this form. The British Library will publicise the details of your thesis and may request a copy on loan from the University Library. Information on the presentation of the thesis is given in the Agreement Form.

Please note the British Library have requested that theses should be printed on one side only to enable them to produce a clear microfilm. The Open University Library sends the fully bound copy of theses to the British Library.

The University has agreed that your participation in the British Library Thesis Service should be voluntary. Please tick either (a) or (b) to indicate your intentions.

(a) [✓] I am willing for The Open University to loan the British Library a copy of my thesis. A signed Agreement Form is attached

(b) [ ] I do not wish The Open University to loan the British Library a copy of my thesis.

Signed: Sumit Pratihar. Date: 09/03/2007

ABSTRACT

This thesis presents the analysis of micro and macro residual stress distribution in different materials exploiting the synchrotron X-ray and neutron diffraction technique. This work can be broadly classified into two parts; the first part investigates the feasibility of using synchrotron X-ray diffraction for high resolution crack tip strain and stress mapping around a fatigue crack inside a bulk material under in-situ loading and the second part presents the investigation of macro residual stress distribution on several welded specimens of different alloys using neutron diffraction.

Synchrotron X-ray diffraction was used to capture the strain and stress distribution around a fatigue crack under different loading conditions. The investigation was employed in two fine-grained Al-5091 compact tension (CT) specimens, with both the samples having a fatigue crack of 10mm where one of them was subjected to a 100 % overload after the fatigue crack was grown. The results show the presence of significant triaxial tensile stresses in front of the fatigue crack in the as-fatigued sample and the overloaded sample, with maximum stresses of 250 MPa and 550 MPa observed respectively in the longitudinal direction. The crack tip stress value reduces to zero in the as-fatigued sample when unloaded, whilst in the overloaded sample, a compressive stress region is observed in front of the crack tip in the unloaded condition. A constant magnitude of compressive stress is observed along the crack wake just behind the crack tip in both samples under loaded and unloaded conditions; however the extent of this compressive zone was found to be greater in the overloaded sample.

The macro-stress distribution in different welded samples has been investigated using the neutron diffraction technique in the second part of work. This study can be sub-divided into three parts. The first part discusses the 3D residual stress distribution in a 316L austenitic stainless steel bead-on-plate welded specimen using neutron diffraction and the results are compared to the results obtained from the contour method. In the second part, an investigation was carried out to study whether the condition of similitude exists in a laboratory size welded component when extracted from the original structure. To study this phenomenon residual stress analysis was carried out in metal inert gas (MIG) welded Al-2024 and Al-7150 alloy compact tension specimens. A substantial amount of stress relaxation is observed in the compact tension specimen when the results are compared with the original welded specimens from where the CT specimens were extracted, which clearly shows that similitude does not apply in the case of welded specimens and care must be taken in using the results from laboratory size fracture and fatigue specimens extracted from real structures. Finally, the third part discusses the residual stress redistribution phenomenon due to the presence of a fatigue crack. To study this redistribution phenomenon an investigation has been carried out in a variable polarity plasma arc-(VPPA)-welded Al-2024 sample with different crack lengths. Stresses in these samples were analysed using neutron diffraction at HMI facility, Berlin. The result shows significant redistribution of residual stress in both samples.

ACKNOWLEDGEMENTS

I would like to express my sincere gratitude to my supervisors Prof Lyndon Edwards and Dr. Mike Fitzpatrick for their continuous encouragement, guidance and valuable advice throughout this project. I also thank The Open University for providing financial support throughout the project.

I would like to acknowledge British Energy and Cranfield University for providing the welded specimens.

I must thank all the instrument scientists especially Dr. Mark Daymond and Dr. Ed. Oliver of ISIS (Oxford), Dr. Jon James of The Open University, Dr Rainer Schneider of HMI (Berlin) and Dr. U. Stuhr of PSI (Switzerland) for their support during the diffraction experiments.

Special thanks are due to Dr. Javier Santisteban for his valuable suggestions, help and advice during this period of my work. My sincere thanks to Peter Ledgard, Tim Gough, Gordon Imlach and Stan Hiller for providing excellent technical support in specimen preparation, metallography and texture analysis. I am thankful to Rehana Malik and Debby Derbyshire for helping me in several other respects. Particular thanks are due to Dr. Mark Turski and Jeffrey Tan for their help in using various software packages, useful discussions and most importantly friendly advice. Thanks are due to Mushiur Rahman, Dr. Supriyo Ganguly for their encouragement and useful discussions. I would like to acknowledge all other fellow students and members of the Structural Integrity Group at The Open University for their friendly advice and continuous encouragements through all the years of my PhD study.

Finally, my deepest thanks and regards to my parents and sister for their continuous encouragement, support and good wishes over the years, without whom this work would not have been finished. I am thankful to all my family members, all friends in India and UK for their encouragement and good wishes. Special thanks to Debalay Chakroborty (friend of mine) for his continuous encouragement and friendly advice during these years. I would leave my final word of thanks to my wife for being supportive, helpful, loving and most importantly, patient in the final year of my work, which at stages seemed never ending.

PREFACE

This thesis is submitted for the degree of Doctor of Philosophy of The Open University. The work described in this thesis is carried out in the Department of Materials Engineering of The Open University, between January 2003 and August 2006 under the co-supervision of Prof Lyndon Edwards and Dr. Mike Fitzpatrick. The work reported is the original work of the author except where reference is made to others. None of this work has been submitted for a degree or other qualification at this or any other university.

Certain part of this work has been published (or accepted for publication) in academic journals or presented at the conference and is listed as following:

Journal

1. S. Pratihar, V. Stelmukh, M. T. Hutchings, M. E. Fitzpatrick, U. Stuwe and L. Edwards, "Measurement of the Triaxial Stress Field in Welded Aluminium Alloy Compact Tension Specimens Using the POLDI Neutron Diffractometer", Materials Science and Engineering: A; In Press, Accepted 15 April, 2006
2. Y. Zhang, S. Pratihar, M. E. Fitzpatrick and L. Edwards, "Residual Stress Mapping in Welds Using the Contour Method", Material Science Forum, No 490/491: P 294-299, 2005.

3. A. Steuwer, L. Edwards, S. Pratihar, S. Ganguly, M. Peel, M. E. Fitzpatrick, J. Marrow, P. J. Withers, I. Sinclair, K. D. Sing, N. Gao, T. Buslaps, J-Y. Buffiere, "In-situ Analysis of Cracks in Structural Materials Using Synchrotron X-ray Tomography and Diffraction ", Nuclear Instruments and Methods in Physics Research, 2006. B 246: p. 217-225.
4. S. Pratihar, S. Ganguly, J. A. James, M. E. Fitzpatrick and L. Edwards, "Non-destructive Determination of the 3D Residual Stress in a AA 7050 Upper Wing Skin Stringer Panel Using Neutron Diffraction", Submitted to Journal of Neutron Diffraction in 2005.
5. Jeffrey. M. L. Tan, S. Pratihar, M. E. Fitzpatrick, L. Edwards, "Residual Stress Redistribution at Fatigue-Aged Stress Wave Cold-worked Holes", Submitted to Journal of Neutron Diffraction in 2005.

Conference

1. P. J. Bouchard, J. Santisteban, L. Edwards. M. Turski, J. James, S. Pratihar, P. J. Withers, "Residual Stress Measurements Revealing Weld Bead Start and Stop Effects in Single and Multi-Pass Weld-Runs", Proceedings of PVP2005, Denver, Colorado, 2005.

NOMENCLATURE

σ	General symbol of stress; units of MPa
σ_{max}	Maximum principal stress
σ_{min}	Minimum principal stress
β	Angle measured clockwise from the x-axis to the maximum principal stress direction
$\bar{A}, \bar{B}$	Hole-drilling calibration constants for finite area strains
CMM	Co-ordinate measurement machine
EDM	Electro discharge machining
λ	Wavelength of photon, X-ray, neutron
d	Interplaner spacings; units of length
θ	Bragg scattering angle; units of degree
h	Plank's constant
c	Speed of light in vacuum
E	Energy of the photon
m_n	Mass of neutron
v	Velocity of neutron
L	Distance from moderator to the detector
t	Time of flight of neutrons (μs)
d_0	Interplaner spacing of unstressed material
Δd_{hkl}	Uncertainty in the measured d_{hkl}
ψ	The angle of inclination which is the angle between the plane normal and the measured direction in surface stress measurement using X-ray diffraction

ε	General symbol of strain, with subscripts for principal strain
E	Young modulus
υ	Poissons ratio
δ	Kronecker's delta
T	Temperature of the moderator
K_B	Boltzmann constant
θ^M	Scattering angle at the monochromator
D_L	Long diagonal in a gauge volume
I_o	Intensity of incident beam
μ	Linear absorption co-efficient
ρ	Density of the material
$\left(\frac{\mu}{\rho}\right)$	Mass absorption co-efficient
N	Number of applied fatigue cycle
K_{max} , K_{min}	Maximum and minimum stress intensity factor at the crack tip
R	Ratio of K_{min} to K_{max} during fatigue cycle
K_I , K_{II} , K_{III}	Stress intensity factor in mode-I, mode-II and mode-III loading
a	Crack length
$\beta(a/W)$	Function of specimen and crack geometry.
$\sigma_{xx}, \sigma_{yy}, \sigma_{zz}$	Stress in x, y and z direction respectively
σ_{YS}	Yield stress
r_p	Plastic zone size

TABLE OF CONTENTS

Chapter 1

Introduction

Stresses, which are locked inside a material without any application of external force are termed residual stresses. By nature, residual stresses remain in a stationary body in equilibrium with its surroundings. In practice, it is impossible to fabricate any component entirely free of residual stress. Residual stresses can be detrimental or beneficial to the performance of a structure or component depending on the magnitude and nature of the stress. Tensile surface stress can aid the initiation and growth of fatigue cracks from surface defects, which eventually affect load carrying capacity and resistance to fracture. On the other hand, compressive residual stress has been proved to be beneficial, as it can suppress crack initiation and crack growth. Thus, residual stresses can be used to increase the life span of a component if compressive residual stresses can be introduced deliberately. It is important to understand that residual stress and applied stress are separate entities. While the magnitude and the effect of applied stresses are well understood, it is difficult to evaluate and predict the magnitude and the effect of residual stress as it is superimposed on service stresses and can cause a premature failure of a component. On the other hand, overestimation of the magnitude of the residual stress values in design can greatly increase production costs. That is why, for engineers, it is very important to have reliable techniques by means of which residual stress can be measured accurately, so that its effect can be taken into account for design calculations and fatigue life predictions.

To have a better understanding about residual stress, it is worth knowing more about the sources, different types and different techniques to measure these stresses, which will be discussed later in this chapter. Although many techniques (destructive and non-destructive) have been around for many years, the recent development of neutron and synchrotron diffraction technique has provided engineers and researchers with the opportunity to investigate these stresses deep inside the material non-destructively together with sufficient accuracy. The combination of these new tools can be used to investigate in-situ residual stresses with very high spatial resolution and very fast counting time.

In this current work, synchrotron and neutron diffraction have been used in two different sets of applications, demonstrating the broad range of investigation which can be carried out using these two techniques. The outline of this work is briefly presented below:

In chapter 1, the basic concepts of residual stress are discussed along with a brief description of the different techniques used to measure residual stresses.

In chapter 2, the details of the diffraction technique in measuring residual stress are presented with special emphasis on the neutron and synchrotron diffraction techniques.

Chapter 3 reviews two aspects of residual stress; the first part discusses the effect of residual stress on fatigue crack growth and the second part discusses the issues related to development of weld residual stress and reviews the different aspect of weld residual stress on different alloys.

Chapter 4 presents results from the first part of this work which investigates the feasibility of use of synchrotron diffraction for high resolution strain and stress field

mapping around a fatigue crack inside a bulk metallic component under various in-situ loading conditions.

Chapter 5 discusses the investigation of macro residual stress in different welded components using the neutron diffraction technique along with detailed discussions of different issues related to weld stress measurement.

Chapter 6 describes the conclusions of the work carried out in this project along with some suggestions for future work.

1.1 Theoretical review of residual stress

1.1.1 Nature and origin of residual stress

Residual stresses can develop in almost every step of a given manufacturing process, from grinding to heat-treatment. These stresses are mainly produced by inhomogeneous plastic deformation, which causes misfits between different phases or different regions within the material [1.1]. Figure 1.1 shows different process that can generate residual stresses in a component. Heat-treatment, such as welding, and inhomogeneous plastic deformation during any kind of forming processes, for example grinding, rolling, hot-working etc. causes misfits between different phases or different regions within the material resulting in residual stress. Methods like shot-peening [1.2-1.4] and cold expansion of holes [1.5] are widely practised in industry to deliberately introduce compressive residual stress in the component (figure 1.1), so that fatigue crack growth is retarded resulting in increased service life of the

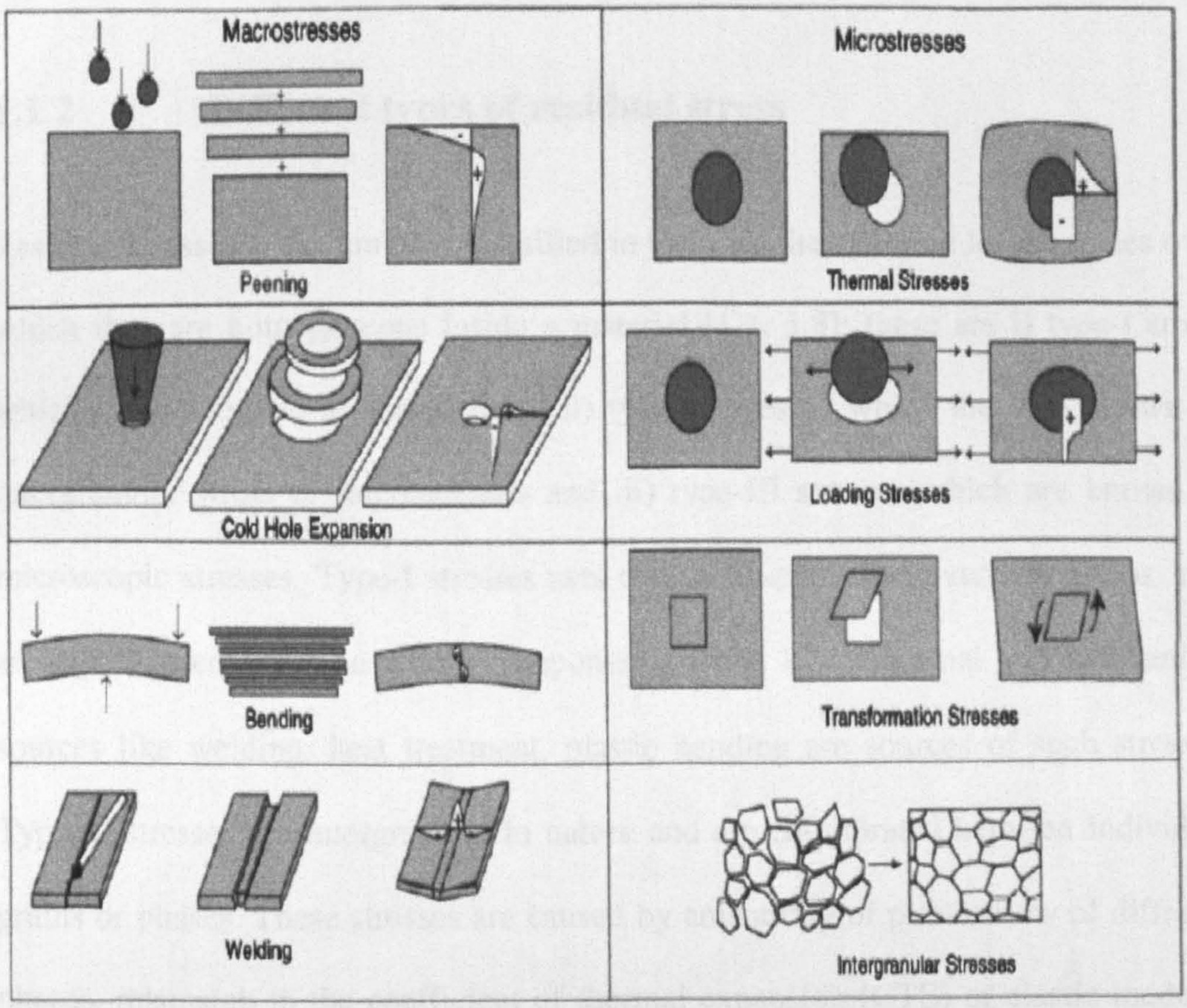

Figure1.1: Different types of macro and micro residual stress are shown [1.1].

component. In this current work, weld residual stresses in stainless steel and aluminium alloys have been analysed and discussed. Residual stress generation in weld material mainly occurs due to the contraction of heated weld metal after solidification during cooling [1.6, 1.7]. This contraction is resisted by the surrounding material which is cooler than the welded region. As a result tensile residual stress is generated in the weld counter-balanced by the compressive stress in surrounding region. Weld residual stress generation is discussed more details in chapter 3.

1.1.2 Different types of residual stress

Residual stresses are commonly classified in terms of the different length scales over which they are homogeneous inside a material [1.1, 1.8]: these are i) type-I stress which is also known as macrostress, ii) type-II stresses which are also known as intergranular stress or microstresses and iii) type-III stresses which are known as microscopic stresses. Type-I stresses acts over a macro scale, over few grains, and are equilibrated over the whole component (figure 1.2). Thermal and mechanical sources like welding, heat treatment, plastic bending are sources of such stresses. Type–II stresses are intergranular in nature and are equilibrated between individual grains or phases. These stresses are caused by anisotropy of plastic flow of different phases, mismatch in the coefficient of thermal expansion (CTE) or elastic modulus between different phases. Type-III stresses are inhomogeneous across microscopic distances, perhaps several atomic distances, within a single grain. Type-II and type-III stresses are also termed as micro-stresses. Lattice imperfections such as dislocations and inclusions are mainly responsible for these kinds of stresses. These micro-stresses are also called "pseudo–micro stress" [1.9] as they can only be detected by diffraction techniques but not by any other destructive technique (for example hole drilling), as these stresses are equilibrated or sum to zero over very small volume of the material. However, it is worth mentioning that type-II stresses can be quantified using diffraction technique while type-III stresses can be detected but are difficult to quantify. A typical variation of different kind of residual stress

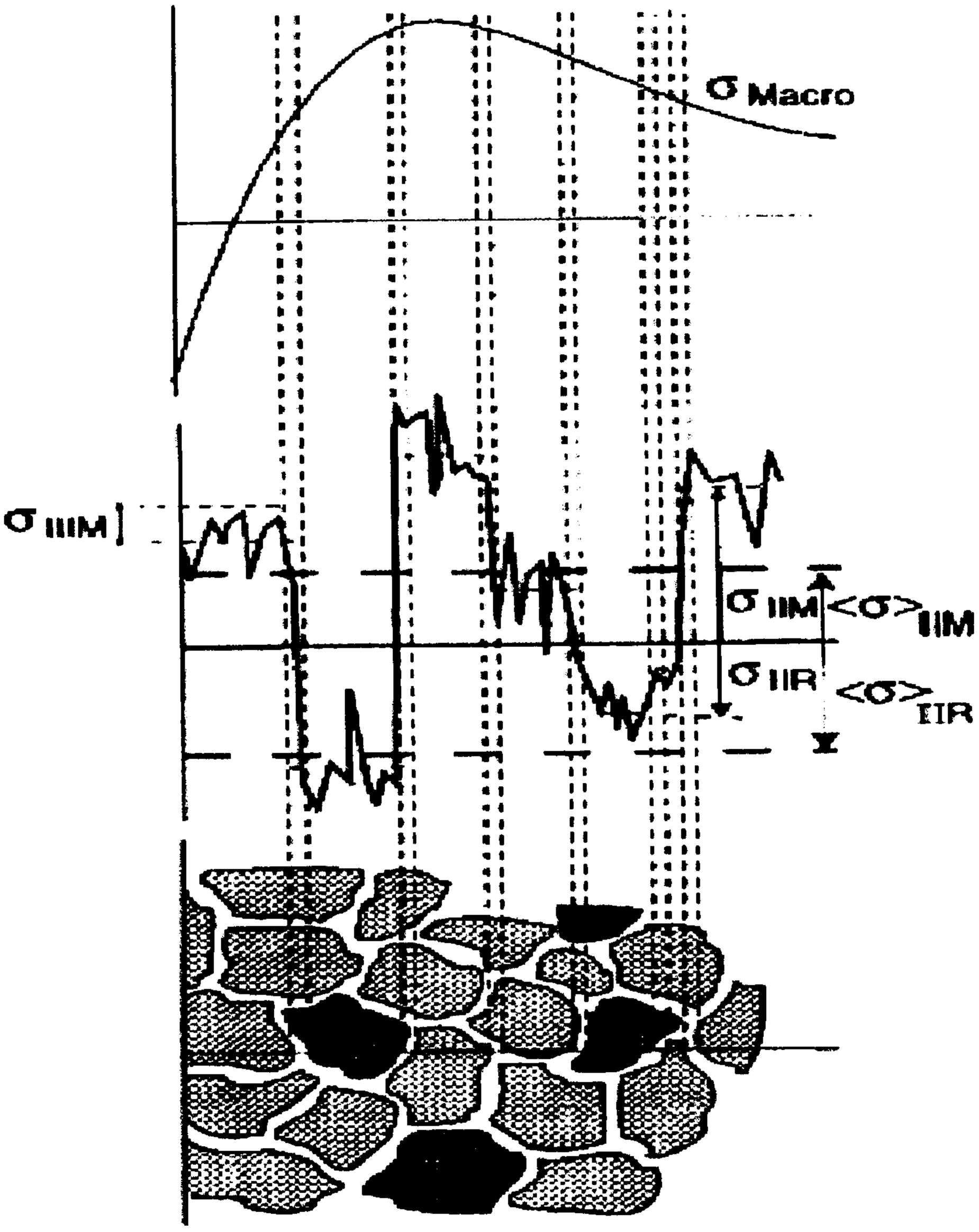

Figure 1.2: Variation of residual stress distribution over different length scale [1.1].

distribution is shown in figure 1.2. Although engineers are more concerned about the macrostress as it gives broader idea of the performance of the material, investigation of microstress is also important because measurement of residual stresses by diffraction technique gives the superposition of both stress components. So it is important to have a better understanding of the microstress in order to have a better

knowledge of macrostresses. In this current work, although most effort was given in the calculation of macro-stress, an attempt has been made to minimize the presence of micro-stresses in the macro-stress calculation.

1.2 Different techniques to measure residual stresses

Over the last few decades, many qualitative and quantitative techniques have been developed to evaluate residual stress. However, in recent years with the advancement of computer technology, much development of the previous techniques and the emergence of new techniques have become possible, which has opened up the opportunity for engineers to measure residual stresses in a wide range of materials with improved accuracy. Residual stress measurement techniques can be divided into two broad categories- I) Destructive techniques, II) Non–destructive techniques.

Examples of destructive techniques are hole drilling [1.10, 1.11] the ring core technique [1.12], the Sachs boring method [1.13], the compliance method [1.14] and the recently developed contour method [1.15, 1.16]. Details of these techniques will be discussed in the following section. The principle of destructive techniques lies in strain relaxation, which takes place when some portion of material is taken out; and as a result of the relaxation a change of material shape takes place which can be measured with a strain gauge and hence stresses are determined using back calculation [1.17]. On the other hand, non-destructive techniques use physical and crystallographic properties of the material, which change with change in strain, as a tool to measure the residual stresses. Both destructive and non-destructive techniques have their advantages and disadvantages. Destructive techniques are very useful in case of quick measurements in industry, but the disadvantages of these techniques is

that once the measurement is carried out the sample cannot be remeasured or used for further investigation. These techniques are also unable to give any information about type–II and type–III stresses.

Among the non-destructive techniques the most important and widely used techniques are X-ray diffraction [1.18] and neutron diffraction [1.19]. Besides these, there are a few other techniques, like the magnetic method [1.20] and the ultrasonic method [1.21]. Non-destructive techniques are very popular simply because the sample can be used for further studies after the measurement is completed. Neutron diffraction can determine residual stresses deep inside the material non-destructively, while other non-destructive techniques are limited to near surface only. Diffraction techniques are also sensitive to the microstresses (type-II and type-III stresses). The drawbacks of these techniques are that they are expensive and very sensitive towards the crystallographic orientation (texture) of the material. So, it is crucial to understand the microstructure of the material and be sure about the nature of the stresses (for example macro or micro) to be measured before deciding which techniques to opt for.

1.2.1 Destructive techniques

In destructive methods, some portion of material is removed from the component, as a result of which stress relaxation takes place in the remaining material [1.17]. The consequence of this stress relaxation is observed in the form of a strain change or shape change. Measurement of this relieved strain is achieved typically by means of strain gauges. The relative stress is then calculated from the strain using analytical solutions. However, special care must be taken during material removal as it can introduce some external stress, which will effectively increase the level of

uncertainty. Although with the advancement of machining technology, nowadays precision tools and instruments (for example, electro discharge machining) are available which ensures surface removal without introducing any new stresses.

1.2.1.1 Hole-drilling and ring-core method

Among all destructive techniques the hole-drilling and ring-core methods are the two most common methods used to measure residual stresses. These two techniques are very similar in nature and both involve localized removal of stressed material. In the case of hole drilling, a small hole, with diameter typically from 1-4 mm, is drilled on the material surface to a depth approximately equal to the diameter of the hole [1.10]. A specially designed rosette [1.11, 1.22] of strain gauges (as shown in figure1.2) are placed around the hole which measures the relieved strain in the surrounding region of the hole. Stress can then be calculated using equation 1.1.

$$\sigma = (\sigma_{max} + \sigma_{min})\bar{A} + (\sigma_{max} - \sigma_{min})\bar{B}\cos 2\beta \qquad (1.1)$$

Where $\bar{A}$ and $\bar{B}$ are hole drilling constants whose values depend on measurement condition such as material property, rosette geometry, hole diameter etc. Their values can be calculated numerically or by FE calculations [1.1, 1.23], σ_{max} and σ_{min} are the principal stresses, β is the angle from the x axis to the direction of maximum principal stress (figure 1.3).

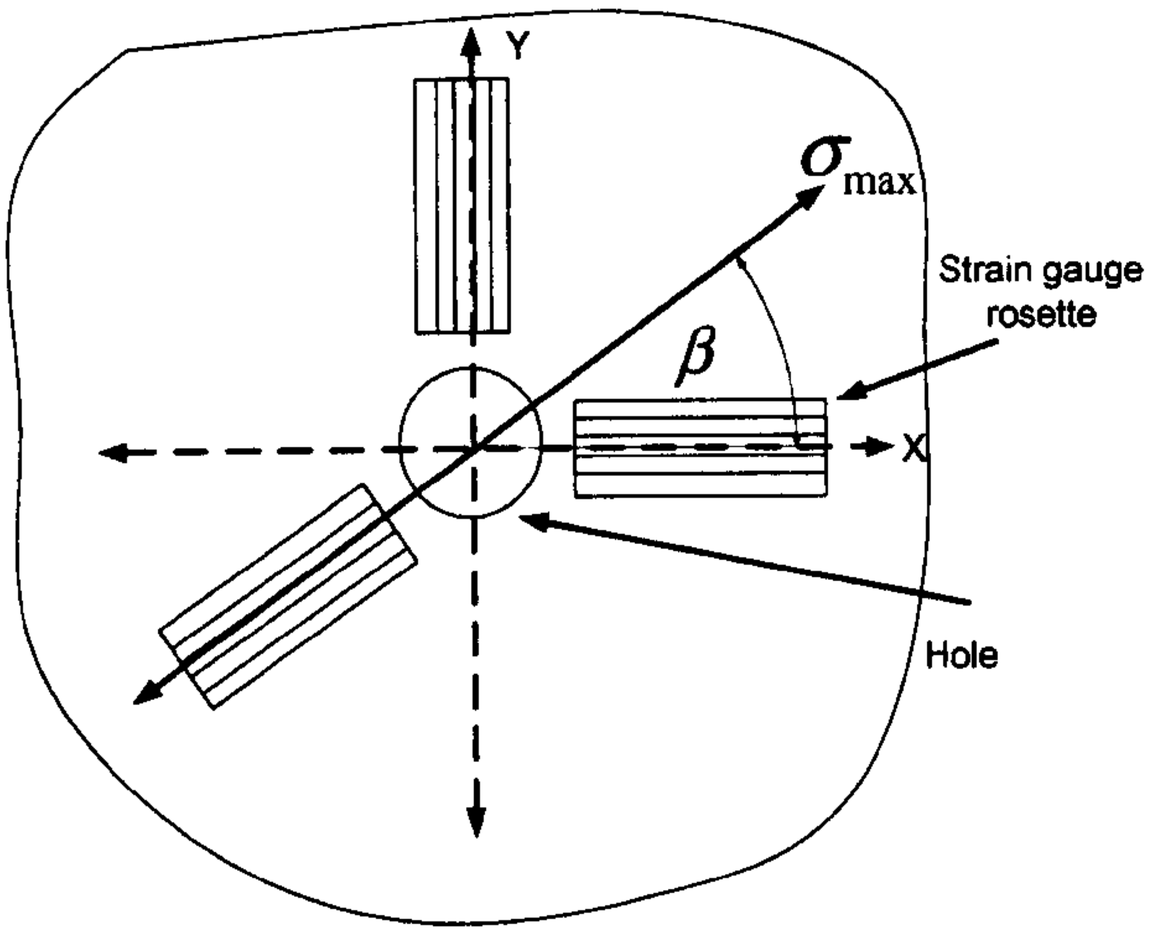

Figure 1.3: Hole drilling method.

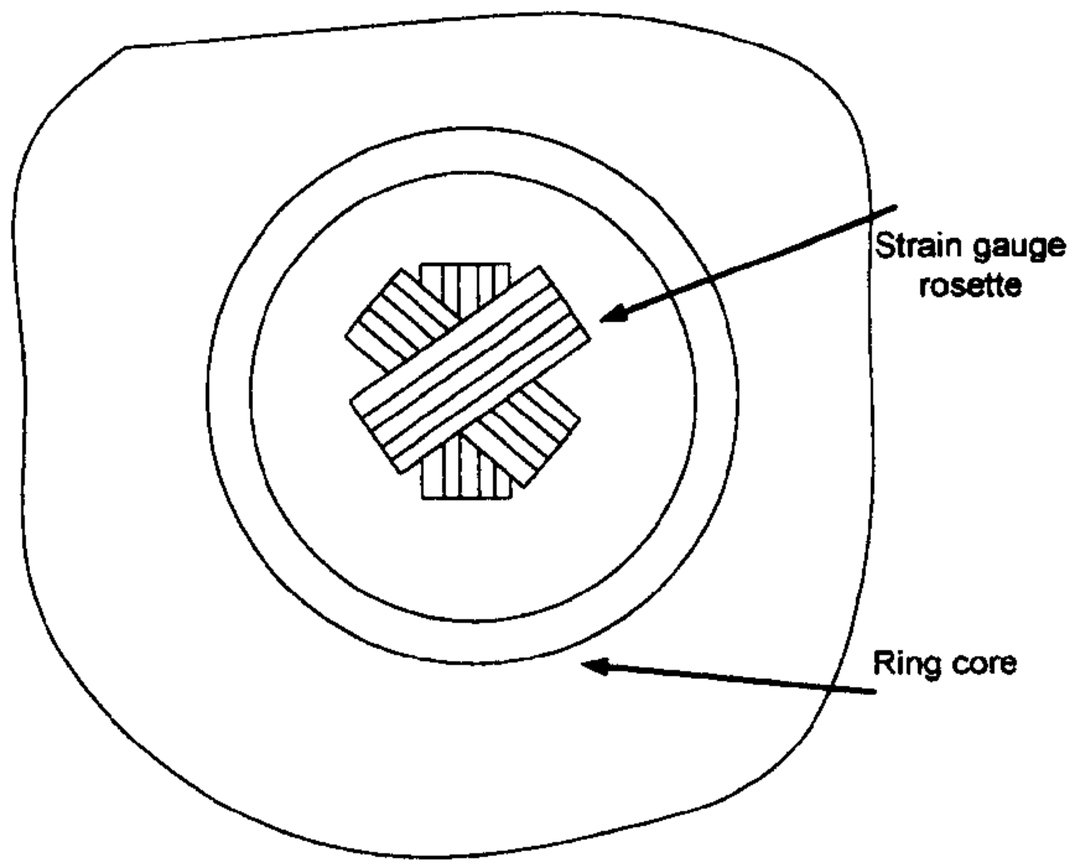

Figure 1.4: Ring core method.

On the other hand, in the **ring-core** method [1.12] an annular slot (internal diameter of around 15-150 mm) is cut, instead of drilling a hole, from the surface of the material. A strain gauge rosette is placed inside the ring as shown in figure 1.3, which measure the relieved strain in the material inside the ring. The ring core method is mostly used in case of large samples.

The limitations with these two techniques are: a) they can only measure stresses up to a certain depth of around 8 mm [1.24], b) also the hole drilling technique cannot be used for those cases where very steep stress gradients exist in the component, as this technique assumes constant stress across the hole or the diameter of the core.

In spite of these limitations, the hole drilling technique, which is well established theoretically and experimentally, is the most widely used non-destructive method mainly due to its simplicity and its ability to measure quickly.

1.2.1.2 The deep hole drilling method

Unlike the hole drilling or ring core method, the deep hole drilling technique [1.25, 1.26] allows residual stress measurement very deep inside the component (almost up to a depth of 500 mm in steel). In this technique, a reference block is attached to the component, which ensures proper alignment for drilling, followed by drilling of a reference hole through the component. The drilling is mainly done by gun-drilling method as it ensures good surface finish and makes the hole fairly straight. The diameter of this hole is then measured very accurately by using an air probe. This was followed by drilling another higher diameter hole containing the reference hole as its axis. Thus the residual stress present in the core get relaxed which can be calculated by re-measuring the diameter of the deformed reference hole and then transforming this into the corresponding stress using an elastic analysis approach [1.26]. This analysis assumes that there will be no plastic deformation during the stress relaxation. This technique is very useful in measuring residual stresses in very thick sections and is being practised widely in engineering application.

1.2.1.3 The Sachs boring method

The Sachs method [1.13] is also based on the same principle of measuring the relaxed strain when a concentric layer of material is removed from the surface of the material. This technique is restricted only to cylindrical components where hoop stresses vary mostly with radius and the axial stresses are negligible. In this technique, a thin annular layer is removed from the inside of the cylinder and the strain is calculated from strain changes measured by attaching a pair of strain gauges on the outer surface of the cylinder.

1.2.1.4 Compliance method

This method involves cutting of a small slots and monitoring the strain relaxation in front of the crack using strain gauges attached on the surface [1.27]. The normal stress can also be resolved with this technique by slowly increasing the depth of the slot. The slots can be introduced into the component without putting much stress inside the material by using electro discharge machining technique.

1.2.1.5 Contour method

This is the most recently developed method to measure residual stress. It can be used for all metallic materials and is particularly useful for those cases where conventional methods cannot be applied. This method was originally developed by Michael B. Prime [1.15, 1.16] of Los Alamos National Laboratory, USA. The basic principle of this method relies on Bueckner's elastic superposition principle [1.28]. Like the other destructive techniques this method uses the stress relaxation of the material when it is cut, but unlike the other methods it does not need layer by layer removal. In this technique the material is cut into two pieces by using Electro Discharge Machining, which ensures that significant stress does not get introduced during the cutting. As a result of this cut the residual stress present in the material will be relaxed and the cut surface will no longer be flat. The contour of the cut surface is then measured using

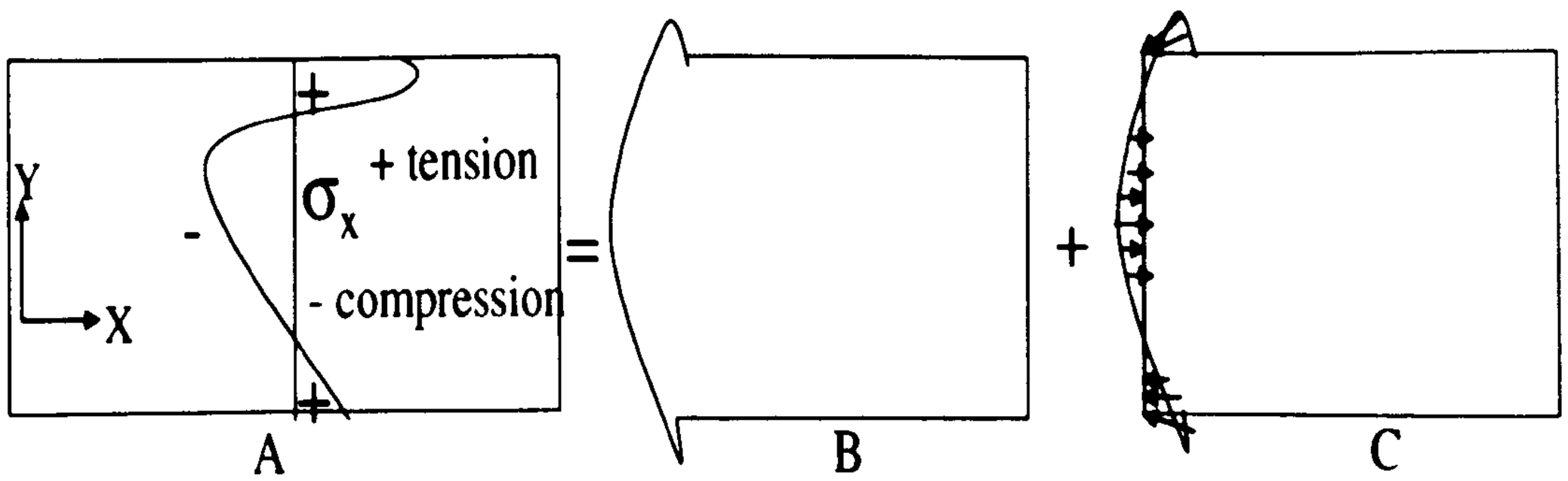

Figure 1.5: Steps involved in the contour method.

the co-ordinate measurement machine (CMM) and the measured surface is then forced back in to the flat original surface using finite element model. Thus, by back calculation of the change of shape, stress is then calculated. The steps of this process are shown schematically in figure 1.5.

It should be noted that the direction of the measured stress will always be normal to the cut surface. The advantage of this technique is that a full field stress map of a very thick sample can be obtained in relatively short period of time, when compared to diffraction technique. This technique is also not affected by texture or micro structural effects in the material. Disadvantages of this technique are that it can not measure stresses in three directions, and the accuracy of this technique is largely dependent on the quality of the EDM cut. This technique is becoming very popular among the engineering and research community; although, much development is still going on in order to understand the measurement uncertainties [1.29, 1.30].

1.2.2 Non-destructive techniques

The principle of non-destructive techniques is based on the measurement of the lattice parameter or other physical property of the material. Some of the important and widely used non-destructive techniques will be discussed in the following sections.

1.2.2.1 Diffraction techniques

Among the non-destructive techniques, diffraction techniques are the most popular and reliable. Laboratory X-ray diffraction, neutron diffraction and synchrotron X-ray diffraction are the three most frequently used and reliable non-destructive techniques. A detailed discussion on these three techniques will be presented in the next chapter. Besides these three diffraction techniques, the electron diffraction technique is also used for stress measurement which enables very high spatial resolution to be achieved, as small as 10 nm [1.31]. This technique is able to determine type-II stresses and also can give some information about type-III stress. The electron diffraction technique is restricted to measure very thin sample because of its low penetrability.

1.2.2.2 Magnetic methods

This method exploits the interaction between the magnetization and elastic strain of ferromagnetic materials. There are mainly two different kinds of magnetic methods available to determine residual stresses. These methods are: **Barkhausen noise** method and **magnetostriction** method. The Barkhausen method relies on analysis of magnetic domain wall motions, which is affected by the application of stress on the

material [1.32]. The movement of magnetic domains was first observed by Barkhausen [1.33]. An electric pulse is generated when domain wall movement takes place, and if these pulses are added for several domain wall, a noise-like signal is generated, which is termed Barkhausen noise. This noise gets damped as a function of distance as it goes inside the material and as a result of this phenomenon, this technique is restricted to surface stress measurement [1.34]. The intensity of the Barkhausen noise is also dependent on the material properties, for example texture and microstructure.

On the other hand the **magnetostriction** method relies on the measurement of permeability and magnetic induction, which are also affected due to the presence of residual stress [1.32].

These two methods can be used to measure stress in the bulk material as well as on the surface. The magnetic methods provide a relatively cheap, portable and quick way to measure stresses non-destructively.

1.2.2.3 Ultrasonic techniques

When an ultrasonic wave is passed through a stressed material, a change in velocity of the wave is observed relative to the unstressed material [1.35]. By measuring the change in velocity, the stress is then calculated by using the following equation.

$$v = v_o + k\sigma . \tag{1.1}$$

Where v is the velocity of the wave in the stressed material, v_o is the velocity of the wave in unstressed material, σ is the stress and k is the acoustoelastic constant. The

value of k depends on material property and is usually obtained by calibration [1.36]. The waves are launched by a transmitting transducer and detected by a receiving transducer after being passed through the region of interest in the material. This technique can be used to determine the surface stress as well as the stresses inside the component. The disadvantages of this technique are that the acoustoelastic constant values change with the material property for example, with texture and microstructural changes. In addition, this technique also requires very precise determination of path length and time of flight of wave as the shift in velocity is very small. For example to measure a stress change of 10% Yield Strength (Y.S) corresponds to a shift in velocity of only about 0.1% [1.37], which means very small error in determining change in velocity can lead to significant stress error. The spatial resolution obtained in this technique is very low as macrostress is determined over the relatively large volume of material through which the wave propagates. However, this technique is widely used in routine inspection of large components, due to the fact that it is convenient to use, quick to set up and also relatively cheap.

1.3 Summary

A detailed review of different aspect of residual stress is presented in this chapter. It describes the different sources of residual stress generation along with a brief description of different measurement techniques available to measure residual stresses and their respective advantages.

1.4 References

1.1. P. J. Withers and H. K. D. H. Bhadeshia, *Residual stress, Part1-Measurement Technique.* Materials Science & Technology, 2001. **17**: p. 355-365.

1.2. A. Ezeilo, *Shot Peening*, in *Analysis of Residual Stress by Diffraction using Neutron and Synchrotron Radiatio*, Fitzpatrick, M. E. and Lodini, A., Editors. 2003, Taylor and Francis: London. p. 251-262.

1.3. P. D. Townsend and V. Zaretsky, *Effect of Shot Peening on the Surface Fatigue Life of Carburized and Hardened AISI 9310 Spur Gears*, in *Nasa Technical Paper 2047*. 1982.

1.4. A. Tange and K. Ando. *Study on Shot Peening Processes of Coil Springs*. in *6th International Conference on Residual Stresses*. 2000. Oxford, UK.

1.5. L. Edwards and A. T. Ozdemir. *Residual Stresses at Cold Expanded Fastner Holes*. in *Proceedings of the NATO Advanced Research Workshop on Measurement of Residual and Applied Stress Using Neutron Diffraction*. 1991. Oxford, UK: Kluwer Academic Publishers.

1.6. C. Weismen, *Welding Handbook, Fundamentals of Welding, 7th ed, American Welding Society, 1981.*

1.7. D. Radaj. *Heat Effect of Welding*. 1992. Heideberg: Springer-Verlag-Berlin.

1.8. L. Pintschovius. *Macrostresses, Microstresses and Stress Tensor*. in *Proceedings of the NATO Advanced Research Workshop on Measurement of Residual and Applied Stress Using Neutron Diffraction*. 1991. Oxford, UK: Kluwer Academic Publishers.

1.9. B. D. Cullity, *Some Problems in X-ray Stress Measurements.* Adv. in X-ray Anal, 1977. **20**: p. 259-271.

1.10. A. Nikulari, J. Lu, and J. F. Flavenot, *Measurement of Residual Stress Distribution by the Incremental Hole Drilling Method.* J. of Mech. Working Tech, 1985. **11**(2): p. 167-188.

1.11. K. Sasaki, M. Kishida, and T. Itoh, *The Accuracy of Residual Stress Measurement by the Hole-Drilling Method.* Exp. Mech, 1997. **37**: p. 250-257.

1.12. H. Wolf and W. Bohm, Arch. Eisenhuttenwes, 1971. **42**: p. 175.

1.13. V. G. Sachs, *Zeitschrift fur Metalkunde.* 1927. **19**: p. 352.

1.14. Y. Y. Wang and F. P. Chiang, *Experimental Study of Three-dimensional Residual Stresses in Rails by Moire Interferometry and Dissecting Methods.* Opt. Lasers Eng, 1997. **27**: p. 89-100.

1.15. M. B. Prime and A. R. GONZALES. *The Contour Method:Simple 2-D Mapping of Residual Stresses*. in *6th International Conference on Residual Stress*. 2000. Oxford, UK.

1.16. M. B. Prime, *Cross-Sectional Mapping of Residual Stresses by Measuring the Surface Contour After a Cut.* Journal of Engineering Materials and Technology, 2001. **123**: p. 162-168.

1.17. J. F. Flavenot, *Handbook of Measurement of Residual Stresses*, Lu, J., Editor. 1996, Lilburn, GA, Society for Experimental Mechanics. p. 35-48.

1.18. I. C. Noyan and J. B. Cohen, *Residual Stress-Measurement by Diffraction and Interpretation*, in *A very Complete Treatment of Stress and Stress Tensors and How Stresses are Measured in Polycrystalline Samples.*, Ilschner, B. and Grant, N. J., Editors. 1987, Springer-Verlag: New York.

1.19. P. J. Withers and P. J. Webster, *Neutron and Synchrotron X-ray Strain Scanning*. Strain 2001, 2001. **37**(1): p. 19-33.

1.20. S. Abuku, Jpn J. Appl. Phys, 1977. **16**: p. 1161-1170.

1.21. R. E. Green. *in Treatise on Materials Science and Technology*. 1973: New York, Academic Press.

1.22. G. S. Schajer and M. Tootoonian, *A New Rosette Design for More Reliable Hole-drilling Residual Stress Measurements*. Exp. Mech, 1997. **37**(3): p. 299-306.

1.23. G. S. Schajer, M. T. Flaman and G. Roy, *Hole Drilling & Ring Core Methods*, in *Handbook of Measurement of Residual Stresses*, J.Lu, Editor. 1996, Fairmont Press: Lilburn. p. 5-34.

1.24. V. Hauk, A. Troost and D. Ley. *Lattice Strain Mesurements and Evaluation of Residual Stresses on Polymetric Materials*. in *Proceeding of Residual Stresses*. 1986. Garmisch Partenkirchen: DGM Informationsgesellschaft.

1.25. R. H. Leggatt, D. J. Smith, S. D. Smith and F. Faure, *Development and Experimental Validation of the Deep Hole Method for Residual Stress measurement*. J. Strain. Anal, 1996. **31**: p. 177-186.

1.26. D. George and D. J. Smith, *Through Thickness Measurement of Residual Stresses in a Stainless Steel Cylinder Containing Shallow and Deep Weld Repairs*. Int Journal of Pressure Vessels and Piping, 2005. **82**: p. 279-287.

1.27. S. Vaidyanathan and I. Finnie, *Determination of Residual Stress from Stress Intensity Factor Measurement*. Journal of Basic Engineering, 1971. **93**: p. 242-246.

1.28. H. F. Buckner, *The Propagation of Cracks and the Energy of Elastic Deformation.* Transactions of the American Soceity of Mechanical Engineers, 1958. **80**: p. 1225-1230.

1.29. Y. Zhang, S. Ganguly, L. Edwards and M. E. Fitzpatrick, *Cross-Sectional Mapping of Residual Stresses in a VPPA Weld Using the Contour Method.* Acta Materialia, 2004. **52**: p. 5225-5232.

1.30. M. B. Prime, R. J. Sebring, J. M. Edwards, D. J. Hughs and P. J. Webster, *Laser Surface-Contouring and Spline Data Smoothing for Residual Stress Measurement.* Exp. Mech, 2004. **44**: p. 176-184.

1.31. C. J. Humphreys and E. G. Bithhell. *Electron Diffraction Techniques*. 1992. Oxford: Oxford University Press.

1.32. S. Tiitto, *Magnetic Methods*, in *Handbook of Measurement of Residual Stresses*, Lu, J., Editor. 1996, Fairmont Press: Lilburn. p. 179-223.

1.33. J. Iwayanagi, *Fundemental Study of the Residual Stress Measurement of Carbon Steel by the Magnetostriction Effect*, in *Ship Research Institute Report (in Japanese)*. 1975. p. 67-132.

1.34. B. A. Auld, *Acoustic Fields and Waves in Solids*. 1973, New York: Wiley Interscience.

1.35. R. B. Thompson, W.-Y.Lu, and A.V.Clark, *Ultrasonic Methods*, in *Handbook of Measurement of Residual Stresses*, Lu, J., Editor. 1996, Fairmont Press: Lilburn. p. 149-177.

1.36. G. S. Schajer, *Residual Stresses: Measurement by Destructive Testing*, in *Encyclopedia of Materials : Science and Technology*, al, K. H. J. B. e., Editor. 2001.

1.37. R. B. Thompson. *An Overview of Ultrasonic Measurement Techniques*. in *Proc. of the Fourth International Conference on Residual Stress (ICRS 4)*. 1994. Baltimore.

Chapter 2

Residual stress analysis using diffraction

This chapter describes the basics of the diffraction technique used for the analysis of residual stress. It also describes the neutron and synchrotron X-ray diffraction techniques in detail, describing the use of the techniques in the field of residual stress analysis and their respective advantages and disadvantages.

2.1 Basic principle of diffraction

When a wave interacts with a material, which has atoms arranged in a periodic manner, scattering in all directions takes place. Diffraction occurs when scattered waves mutually reinforce one another, or in other words constructive interference takes place. This phenomenon can be better explained mathematically. If we assume a parallel, monochromatic and coherent X-ray beam, having a wavelength of λ, incident on two parallel planes of atoms C$\acute{\text{C}}$ and B$\acute{\text{B}}$ (figure 2.1) at an angle of θ, separated by interplanar spacing d, then constructive interference will occur when

$$n\lambda = 2d\sin\theta \qquad (2.1)$$

Equation 2.1 is called Bragg's law [2.1] (where, n is the order of reflection which could be any integer value (1, 2, 3-----) providing $\sin\theta \leq 1$.

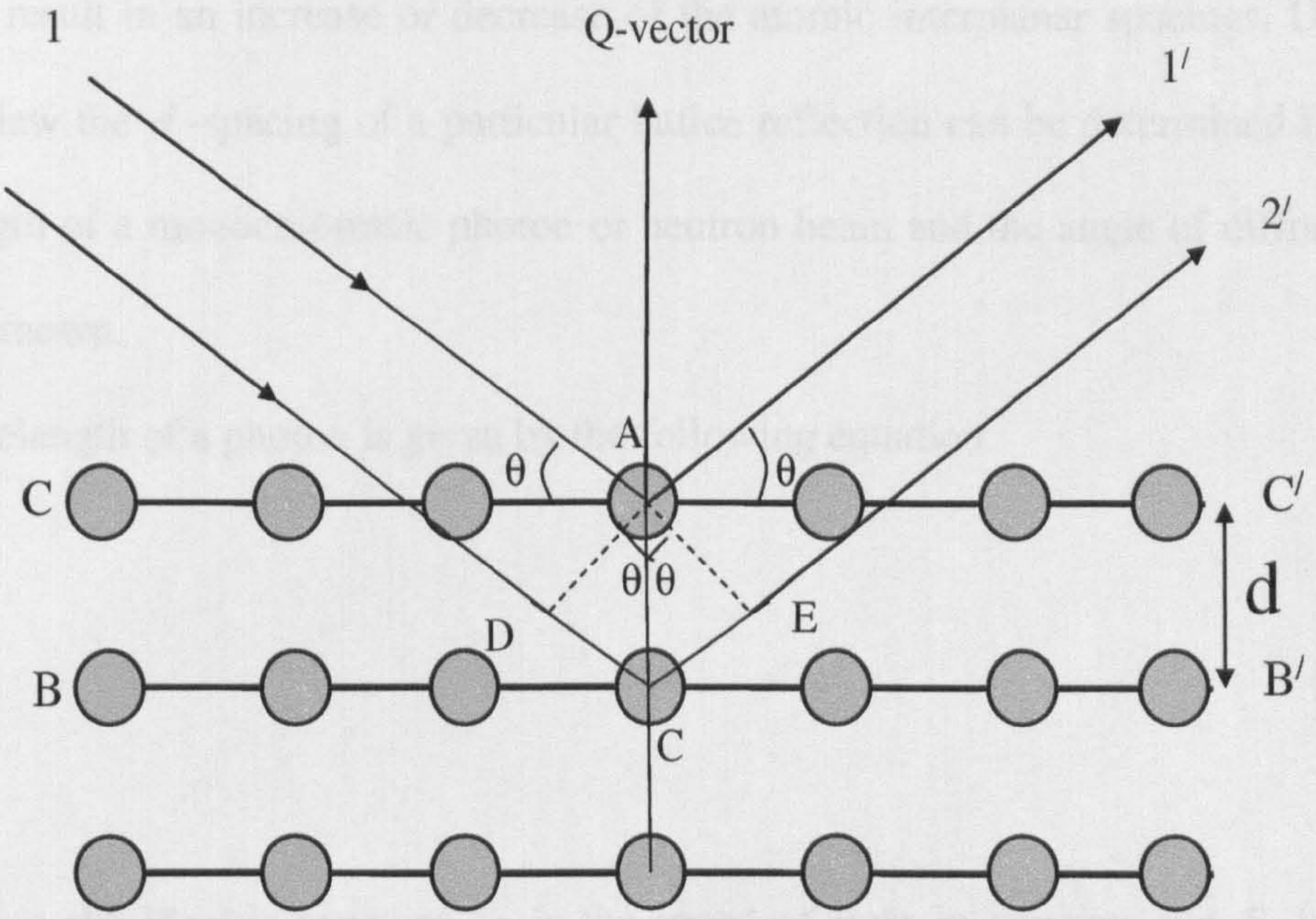

Figure 2.1: X-ray diffraction by plane of atoms.

In summary, diffraction will only take place if the following basic conditions are satisfied:

- Generally the wavelength of the incident beam should have the same order of magnitude as the interplanar spacings of the sample or diffracting material.
- The scattered beam should satisfy Bragg's law.

Diffraction has become an important technique to analyse residual stress non-destructively and accurately. X-rays and neutrons both can be used to study residual stress as they have wavelengths of the order of the interplanar spacings of most common engineering materials. Laboratory-generated X-rays are limited to measure only surface stresses (depth of few hundreds nm) due to the strong absorption of this radiation, while neutrons, having higher penetrability, are capable of analysing stresses deep inside the material. When a material is under tension or compression,

this will result in an increase or decrease of the atomic interplanar spacings. Using Bragg's law the d -spacing of a particular lattice reflection can be determined if the wavelength of a monochromatic photon or neutron beam and the angle of diffracted beam is known.

The wavelength of a photon is given by the following equation:

$$\lambda = \frac{hc}{\mathrm{E}} \tag{2.2}$$

Where h is the Plank's constant, c is the speed of light in vacuum and E is the energy of the photon. Substituting equation 2.2 in equation 2.1 yields:

$$\frac{hc}{\mathrm{E}} = 2d\sin\theta \tag{2.3}$$

Thus, for a known fixed diffraction angle the interplanar spacing d can be determined by measuring the energy of the photon from equation 2.3.

The wavelength of the thermal neutron can be related to its velocity by the following equation:

$$\lambda = \frac{h}{m_n v} \tag{2.4}$$

Where m_n is the mass of neutron and v is the velocity of the neutron. If, to travel a distance of L, time-of-flight of neutron is t, then the velocity of neutrons can be deduced from the following equation:

$$v = \frac{L}{t} \tag{2.5}$$

Hence from equation 2.4 and equation 2.5 we get:

$$\lambda = \frac{ht}{m_n L} \tag{2.6}$$

Now, substituting equation in Bragg's equation (2.1) the following equation can be obtained:

$$\frac{ht}{m_n L} = 2d \sin\theta \tag{2.7}$$

Therefore, for a fixed diffraction angle, the interplanar spacing d can be determined by measuring the time-of-flight of neutron t to travel the distance L.

Thus, strain can be calculated using:

$$\varepsilon = \frac{d - d_0}{d_0} = \frac{\Delta d}{d_0} \tag{2.8}$$

Where d_0 is the interplanar spacing of unstressed material and d is the interplanar spacing of stressed material.

Differentiating Bragg's equation (2.1) assuming constant wavelength and substituting in equation 2.8, strain can be determined as:

$$\varepsilon = \frac{\Delta d}{d_0} = -\cot\theta \Delta\theta \tag{2.9}$$

Strain can also be obtained by differentiation of equation 2.3 and is given by:

$$\varepsilon = \frac{\Delta d}{d_0} = \frac{-\Delta \mathrm{E}}{\mathrm{E}} \tag{2.10}$$

Similarly, strain can also be calculated by differentiating equation 2.7 and can be expressed by the following equation:

$$\varepsilon = \frac{\Delta d}{d} = \frac{\Delta t}{t} \tag{2.11}$$

Therefore, using diffraction technique strain can be calculated in three different ways:

- By keeping the wavelength fixed and determining the peak shift in terms of Bragg angle.
- By determining the peak shift in the energy spectrum at a fixed Bragg angle.
- By measuring the peak shift in the time-of-flight spectrum at a fixed diffraction angle.

2.2 Calculation of stress from the strain values

For isotropic solids the strain tensor can be related to the stress according to Hooke's law [2.2].

$$\varepsilon_{ij} = \frac{1+\upsilon}{E}\sigma_{ij} - \delta_{ij}\frac{\upsilon}{E}\sigma_{kk}. \qquad (2.12)$$

Where k is a dummy suffix that sums over all k (i.e. $\sigma_{kk} = \sigma_{11} + \sigma_{22} + \sigma_{33}$),

E is the Youngs modulus, υ is the Poissons ratio and δ is Kronecker's delta function, which is defined as:

$\delta_{ij} = 1$ when, $i = j$,

$\delta_{ij} = 0$, when, $i \neq j$.

Stress tensor can be obtained by inverting equation 2.12 and is given by:

$$\sigma_{ij} = \frac{E}{1+\upsilon}\varepsilon_{ij} + \frac{\upsilon E}{(1+\upsilon)(1-2\upsilon)}\delta_{ij}\varepsilon_{kk} \qquad (2.13)$$

If the three principal stress directions in the component are known, strain can be calculated in these directions using equation 2.12, and the principal stresses can then be calculated using equation 2.13.

2.3 Residual stress measurement using laboratory X-ray diffraction

This is one of the oldest methods to measure residual stresses, dating back to 1920, with most of the pioneering work carried out in Germany [2.3]. Laboratory X-ray diffraction is widely used to measure stresses non-destructively. However due to the X-rays' relatively low energy and high absorption in materials, measurements cannot be made deep inside the material [2.4]. The typical penetration depth in engineering material is in the range of tens of microns. Since the measurement is restricted to the near surface, the stress measurement can be carried out with the assumption of having zero stress in the normal direction; that means the plane stress condition can be assumed [2.4]. The in-plane stresses on the surface can be measured by measuring the out of plane strain at different ψ angles using the measurement geometry in reflection. Figure 2.2 shows the schematic diagram of the co-ordinate system of the laboratory X-ray stress measurement. Stress in any chosen direction can be calculated using the following equation [2.1]:

$$\frac{d_{\phi\varphi} - d_0}{d_0} = \frac{1+\upsilon}{E}\sigma_\phi \sin^2\psi - \frac{\upsilon}{E}(\sigma_{11} + \sigma_{22}) \qquad (2.14)$$

Where E is the modulus of elasticity, ψ is the angle of inclination which is the angle between the plane normal and the measured direction, $d_{\phi\psi}$ is the lattice parameter at angle ψ and d_0 is the stress free lattice parameter. Now, if $d_{\phi\psi}$ can be measured for several different ψ values and the measured values are plotted as a

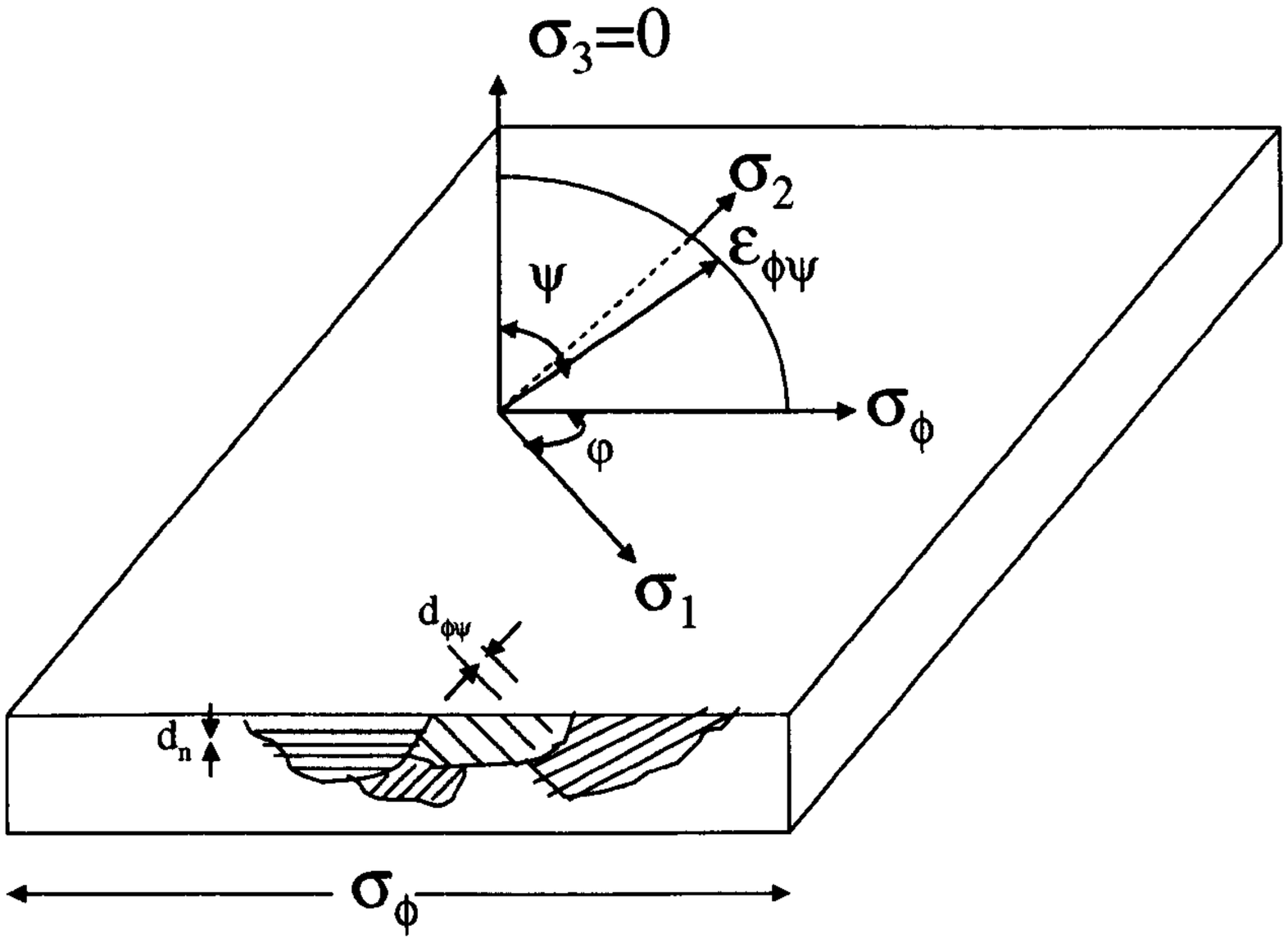

Figure 2.2: A schematic diagram of conventional X-ray diffraction using the $\sin^2\psi$ technique.

function of $\sin^2\psi$, the value of $\sigma_{\phi\psi}$ can be calculated from the slope of the plot and equation 2.5, provided that the values of E, υ and d_0 are known. Normally, the d value measured at $\psi = 0$ is used as d_0. This assumption is reasonable as it has been found not to introduce significant error (error < 0.1%) [2.1, 2.2]. In practice, three different types of d vs $\sin^2\psi$ plots are observed depending upon the nature of the stresses present in the material (figure 2.3). Plots show linear variation when biaxial or uniaxial stress is present in the material (figure 2.3-a), while ψ splitting is observed where there are shear stresses present in the component. Oscillatory behaviour (figure 2.3-c) in the d vs $\sin^2\psi$ plot indicates the presence of a inhomogeneous stress state in the material, which is mainly caused by the presence

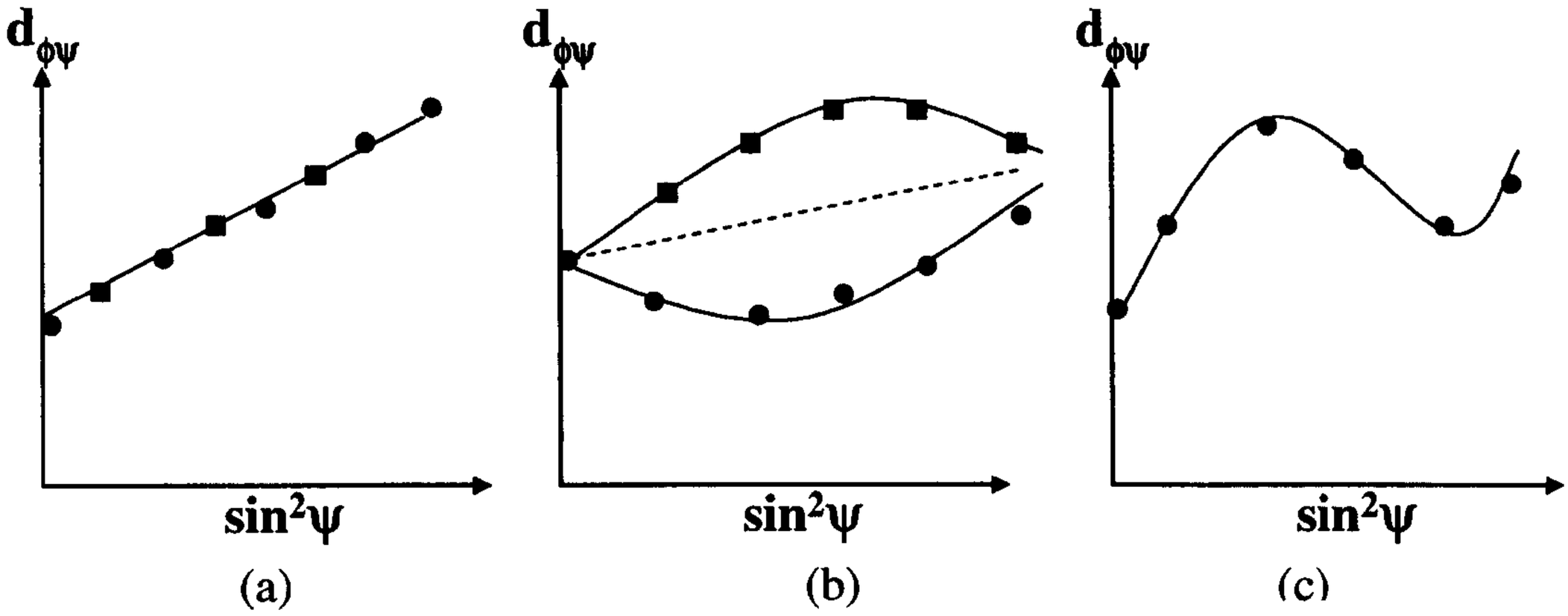

Figure 2.3: Different types of d vs $\sin^2\psi$ plots.

of texture in the material [2.2]. Although the laboratory X-ray diffraction method is mainly used for surface stress measurement, it can also be used to determine subsurface information by removing the surface layers by chemical or mechanical means, providing no additional stresses are generated by the process.

2.4 Stress measurement using neutron diffraction

For a long time, engineers and researchers around the world have been looking for a technique which would enable them to measure the residual stress–state deep inside materials non-destructively. Although the neutron was discovered by Chadwick in 1932, residual stress analysis using neutron diffraction did not materialise until the early 1980s, when the experimental set up for the measurement was first developed at Harwell, Oxfordshire [2.5]. Also, within the same period parallel work was carried out in other places [2.6, 2.7]. Since then, in the last two decades a lot of development has been undertaken on this technique, which has now become the most established

and reliable method to measure residual stress deep inside polycrystalline materials. In recent years engineering industry has accepted this technique as a potential tool for stress measurement, which is clearly evident by the increasing number of industrial users [2.8]. In addition, a draft ISO standard (CEN ISO/TS 21432 :2005) has recently been published for this technique. This is a reflection of the fact that the neutron diffraction technique has become popular among engineers and researchers. The following is a list of advantages of this method over other techniques.

- This is the only technique available which has enabled engineers to measure the three dimensional residual stress deep inside a material non-destructively, which can be used to validate FE analysis.
- Neutron penetration is of the order of centimetres in most engineering materials.
- Phase specific information can be obtained; this means individual phase response in a multiphase material can be observed, in addition to information on intergranular stresses it is especially useful for new metal matrix composites.
- Neutron diffraction can be used for in-situ residual stress measurement of components as neutrons can penetrate furnaces and other environmental enclosures.

2.4.1 Neutron sources

Neutrons are difficult and expensive to produce. At present there are mainly two different types of neutron source available, which can produce sufficient fluxes for diffraction experiments, namely, 1) fission reactor sources [2.9] and 2) spallation

sources [2.10]. Neutrons produced from both these sources have very high energy, too high to be used in a diffraction experiment. To reduce this high energy, the neutrons are passed through a moderator [2.10, 2.11], which typically consists of light atoms such as heavy water or liquid methane, to obtain energy and wavelength of the required order of magnitude which can be used for most polycrystalline engineering material. The role of a moderator is to slow down the high energy neutrons, which reaches equilibrium with the moderator temperature after numerous collisions with the atoms of the moderator.

From the wave particle nature of neutrons the following relationship can be written

$$\lambda = \frac{h}{mv} \tag{2.15}$$

Where λ = wavelength of neutron, m = mass of neutron, h is Planck's constant and v is the velocity of the neutron.

Also, $\mathrm{E} = \frac{1}{2}mv^2$ (2.16)

Where E is the energy of neutron.

From equation 2.15 and equation 2.16 we get

$$\lambda = \frac{h}{\sqrt{2m\mathrm{E}}} \tag{2.17}$$

Now, if the temperature of the moderator is T, then

$$E = K_B T \tag{2.18}$$

Where K_B = Boltzmann constant.

From equation 2.17 and equation 2.18 we get:

$$\lambda = \frac{h}{\sqrt{2mK_B T}} \tag{2.19}$$

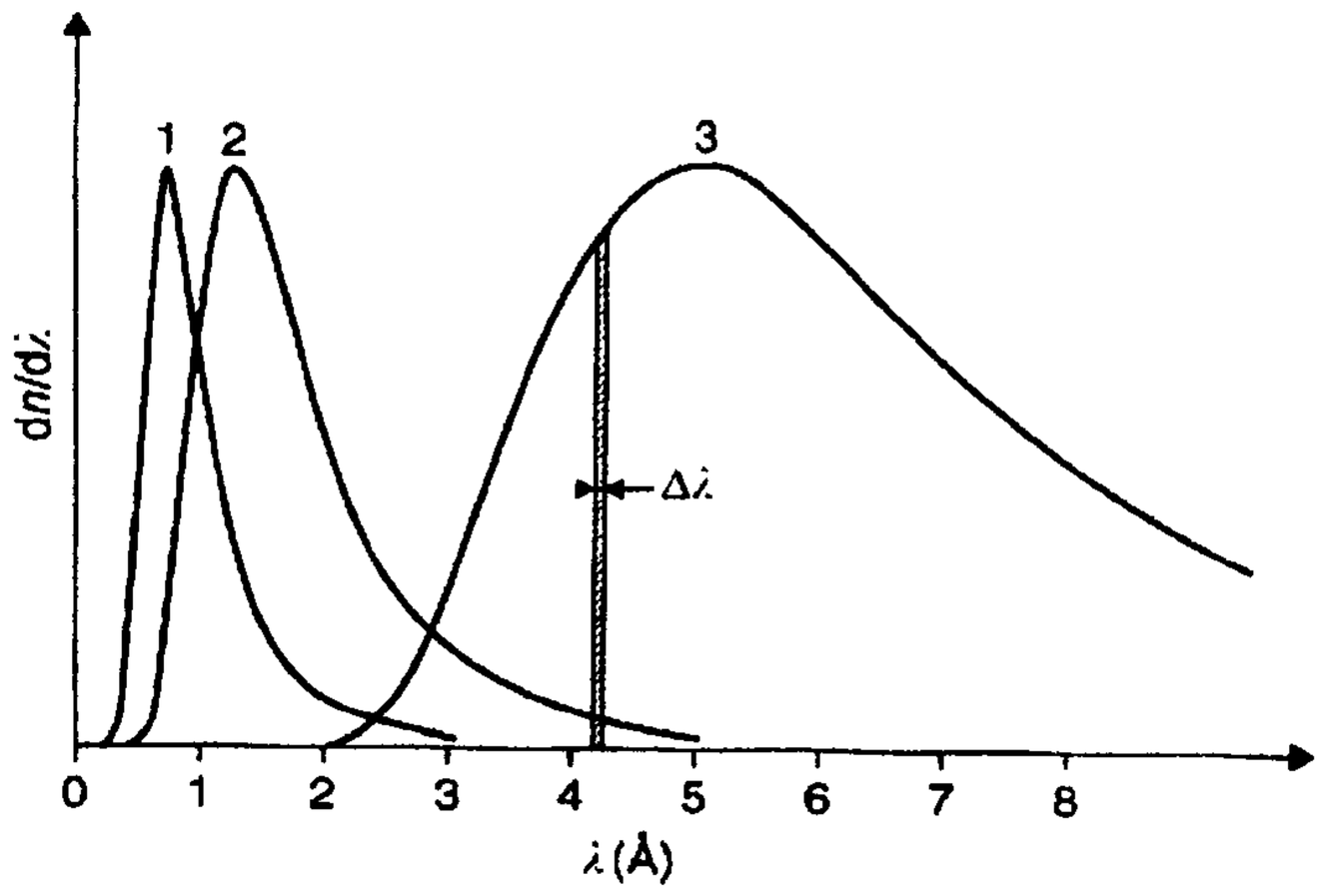

Figure 2.4: Wavelength distribution of thermal neutrons for several thermalization temperatures T: (1) T = 1000K ("hot" neutrons), (2) T = 300K ("thermal" neutrons), (3) T = 20K ("cold" neutrons) [2.10].

The energy of neutrons follow the Maxwellian distribution when they achieve to equilibrium with the moderator temperature [2.8, 2.9] and by varying this temperature, a specific wavelength distribution can be selected for various types of neutron spectrometers, which may require different energies for different applications (figure 2.4). For a reactor source, a continuous monochromatic beam of fixed wavelength is obtained by Bragg reflection of a polychromatic beam using a

single crystal monochromator [2.8, 2.12]. In this case information from a single peak is recorded. On the other hand, a spallation source produces short pulses of neutrons where each pulse contains a wide range of wavelengths allowing information from several peaks to be recorded at the same time [2.10]. This will be further discussed in the following sections.

2.4.1.1 Reactor neutron source

In reactor sources, continuous beams of very high energy neutrons are produced by fission of Uranium (U^{235}) [2.11, 2.13]. These high energy neutrons are then passed through the moderator to bring down the energy level. The neutron beam obtained from the moderator is polychromatic in nature, having a wide distribution of wavelength. This polychromatic radiation (white beam) is converted to a monochromatic beam by Bragg scattering via a monochromator [2.12], which is placed at a specific angle with respect to the beam in the neutron guide. Usually, a single crystal such as graphite or germanium is used as a monochromator and according to the requirement of the experiment, suitable wavelengths can be selected by positioning the monochromator crystal at different angles [2.8]. Neutron guide tubes are made of coated borated glass and are sometimes curved so that fast neutrons, X-rays and γ rays are filtered from the beam before reaching the sample. Reactor sources produce the most intense beams in terms of total integrated flux [2.8].

2.4.1.2 Diffractometers at reactor sources

The schematic diagram of a typical neutron diffractometer used for strain measurements is shown in figure 2.5. The polychromatic beam that comes out from the moderator is monochromated to a single wavelength using a single crystal monochromator, using the principle of Bragg's Law.

$$n\lambda = 2d_{hkl} \sin\theta^{M} \tag{2.20}$$

Where d_{hkl} = lattice spacing of the monochromator, θ^{M} is the scattering angle at the monochromator and λ is the neutron wavelength. In most instruments the monochromator take off angle $2\theta^{M}$ is variable in order to have the flexibility of selecting suitable wavelengths for different experiments. The beam divergence can be controlled by placing Soller collimators (figure 2.5) before and after the monochromator. The neutron flux of the beam incident on the sample can be monitored by placing a monitor counter after the monochromator. The sample table is positioned in such a way that the incident beam passes through the centre of

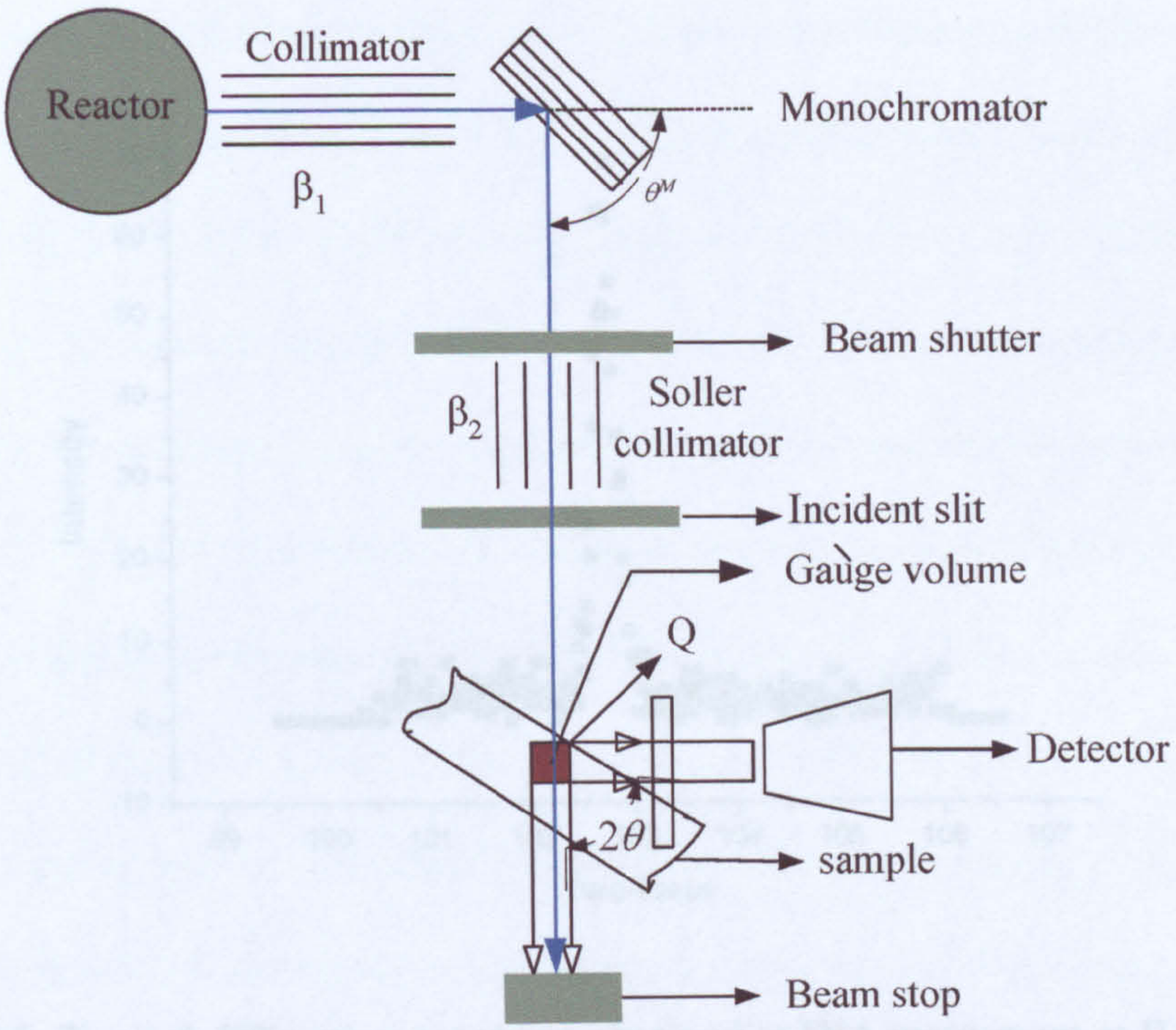

Figure 2.5: Schematic diagram for strain measurement on a reactor neutron source.

rotation of the sample table. The diffracted intensity is recorded by a detector that moves around the centre of rotation of the sample table. The gauge volume is defined by the intersection of the incident and diffracted beams and is fixed by slits placed in front of the sample and in front of the detector. The diffracted intensity is obtained by scanning the diffracted beam using the detector. The detector counts the distribution of neutrons as a function of 2θ for a given reflection. A typical spectrum of a diffracted beam obtained in reactor source diffractometer is shown in figure 2.6. A fitting routine is used to accurately determine the peak centre

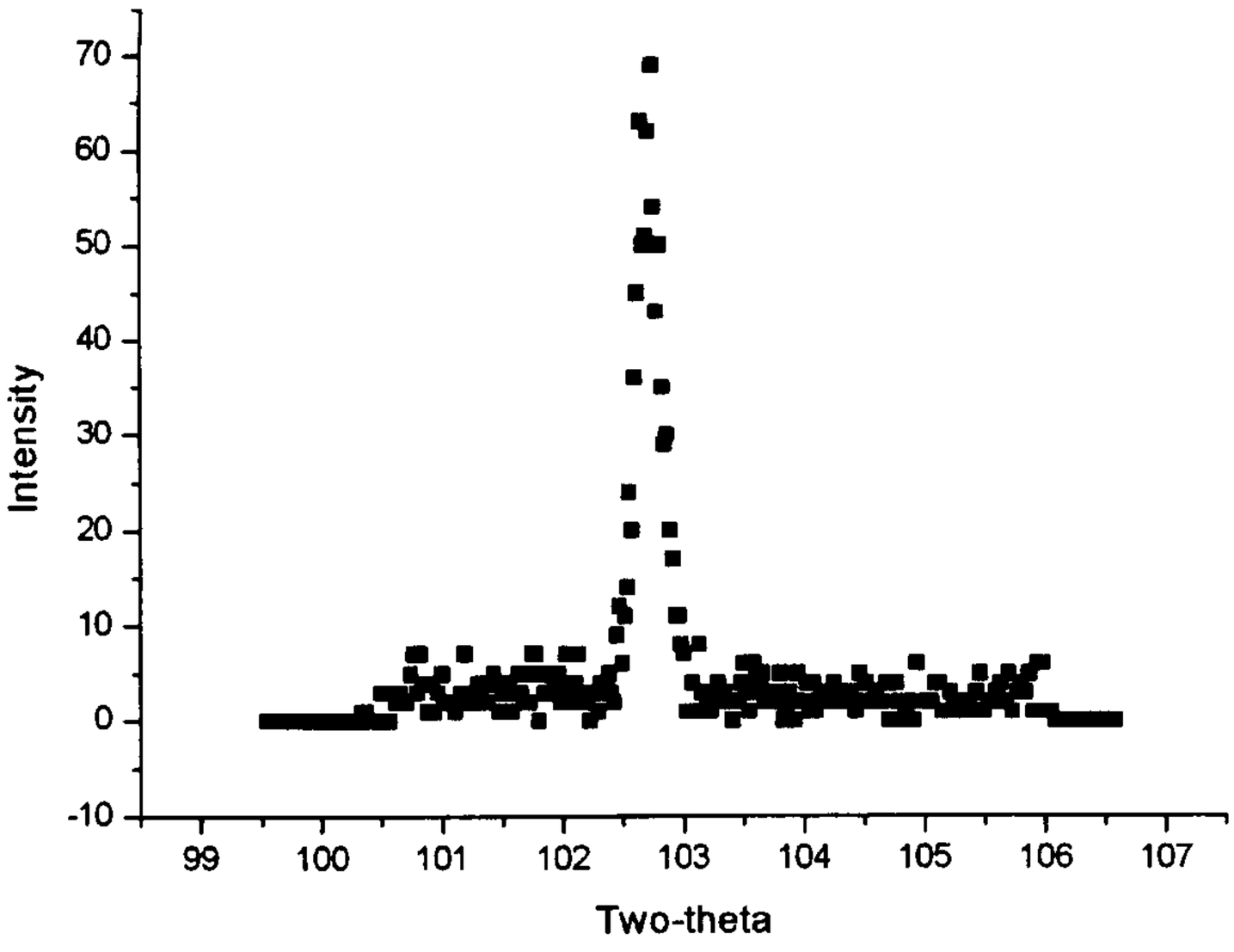

Figure 2.6: Typical diffraction spectrum obtained at DIA instrument at ILL reactor neutron source [2.14].

depending upon the shape of the peak [2.8] and will be discussed later. Strain is then calculated for a particular set of crystallographic lattice spacings; i.e. (111) or (311).

2.4.2 Pulsed neutron source

In pulsed neutron sources, sharp pulses of high energy protons are generated in a synchrotron by accelerating in bursts to 800 MeV. These protons are then directed to a heavy metal target material (Pb, W, Ta, U). Protons interact with the target nuclei and a spallation reaction takes place, exciting the nuclei and as a result of this, neutrons are evaporated [2.9]. The main advantage of a spallation source over a reactor source is that much lower heat is generated in spallation source. Thus, fast neutrons produced from spallation reactions are thermalised using a moderator made of hydrogenous material (see section 2.2.1) [2.15]. Most of the instruments at pulsed sources use polychromatic radiation enabling full diffraction spectra to be obtained.

The intensity of each neutron pulse is very high and comparable to the intensity of neutron beams in reactor source [2.8]. In recent years pulsed sources such as ISIS (UK) [2.10], IPNS (USA) [2.16], LANSCE (Los Alamos, USA) [2.17] have become popular due to their advantages over reactor sources, and processes are ongoing to make them more intense. At the moment the most intense spallation source in the world is at ISIS, at Oxfordshire, UK. Neutron generation in this facility is described in detail in many publications [2.10, 2.18]. In this facility H^- are accelerated to 665 keV by a five stage Cockcroft-Walton multiplier and then to 70 MeV by four linear r.f. accelerating cavities. On injection both the electrons are stripped off as they are passed through 0.25 μm thick aluminium oxide stripping foil. Remaining protons are then accelerated to 800 MeV in a 50 Hz synchrotron by repeatedly passing through six r.f. accelerating cavities. Pulses of protons are produced by this process and are directed to water cooled depleted uranium target where a spallation reaction takes place producing a pulse of neutrons. Approximately 15 neutrons are produced for each incident proton. These neutrons are high energy neutrons (1 to 800 MeV) and need to be moderated by passing through a hydrogenous moderator (CH_4, H_20) which reduces the energy level to 1-100 meV, making them suitable for use in diffraction experiments.

2.4.2.1 Basic principles of strain measurement using a pulsed neutron source

In a pulsed neutron source, short pulses of neutrons are directed to a polycrystalline sample, the diffracted neutrons are then measured by a detector, which is placed at a fixed scattering angle (normally of $2\theta = 90^0$). As each pulse of neutrons contains a

continuous range of velocities and therefore wavelengths, separation of each wavelength is achieved by measuring the time-of-flight of each neutron. This is due to the fact that the energy and therefore the velocity of each neutron are inversely proportional to the wavelength. The detected neutrons are recorded in separate time channels, each corresponding to a certain velocity or wavelength. Therefore, if the distance between the moderator and sample is known, then the time of flight can be calculated from the following equations:

From Bragg's law,

$$\lambda = 2d \sin\theta \tag{2.21}$$

The velocity (v) of a neutron is related to the wavelength λ by,

$$\lambda = h/mv = 3956/v \tag{2.22}$$

Where h is Planck's constant and m is the mass of the neutron. The time of flight (t) of detected neutrons can be calculated by,

$$t = 505.5L[m]d\ [\text{Å}] \tag{2.23}$$

Where L is the total flight path of neutrons from the moderator to the detector (figure 2.7). If the detected neutron counts are plotted as a function of time, a

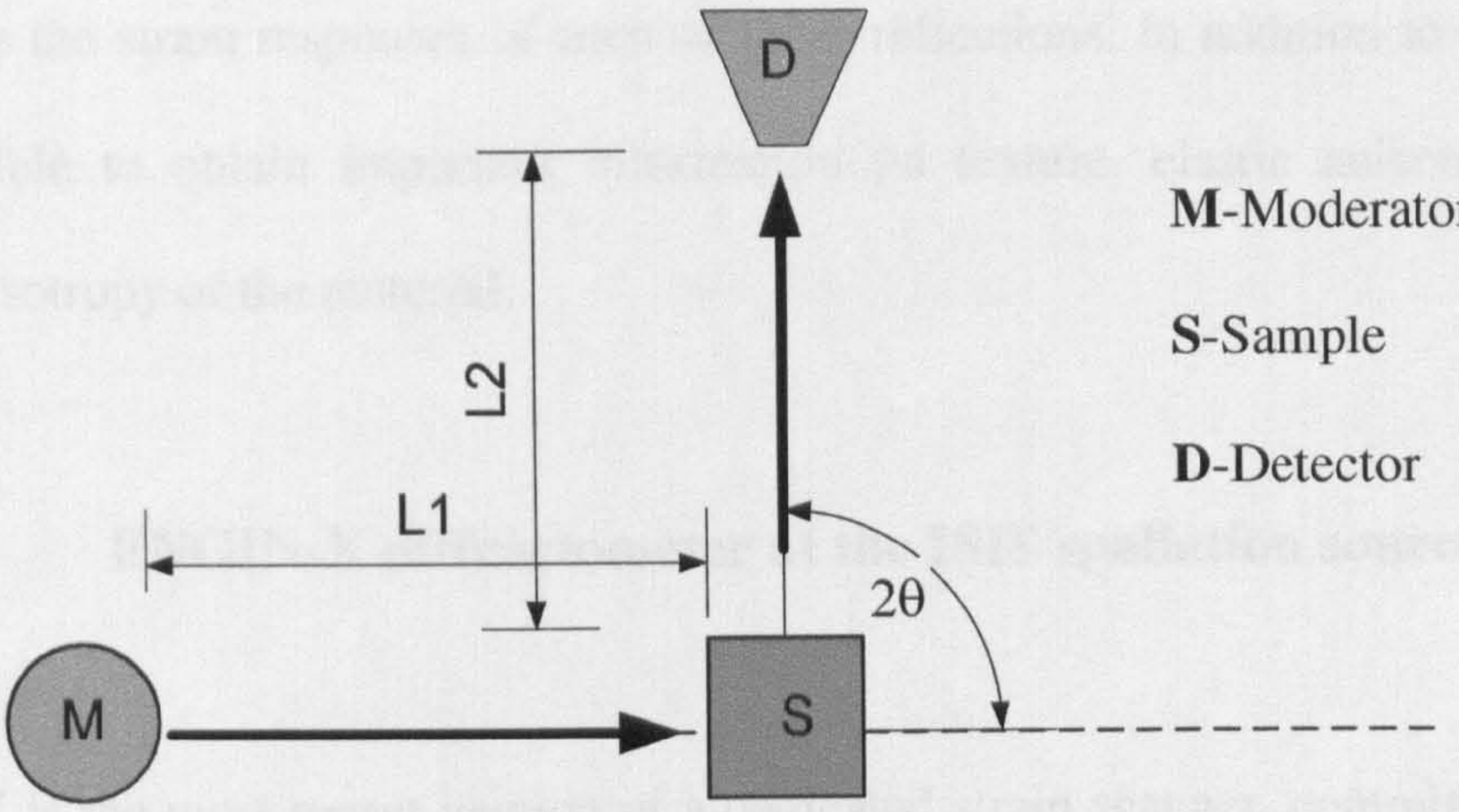

Figure 2.7: The basic component of a time of flight diffractometer.

diffraction spectrum (figure 2.8) will be obtained which will have several peaks corresponding to the different interplanar spacings within the polycrystalline material. The advantage of this method is that information corresponding to many

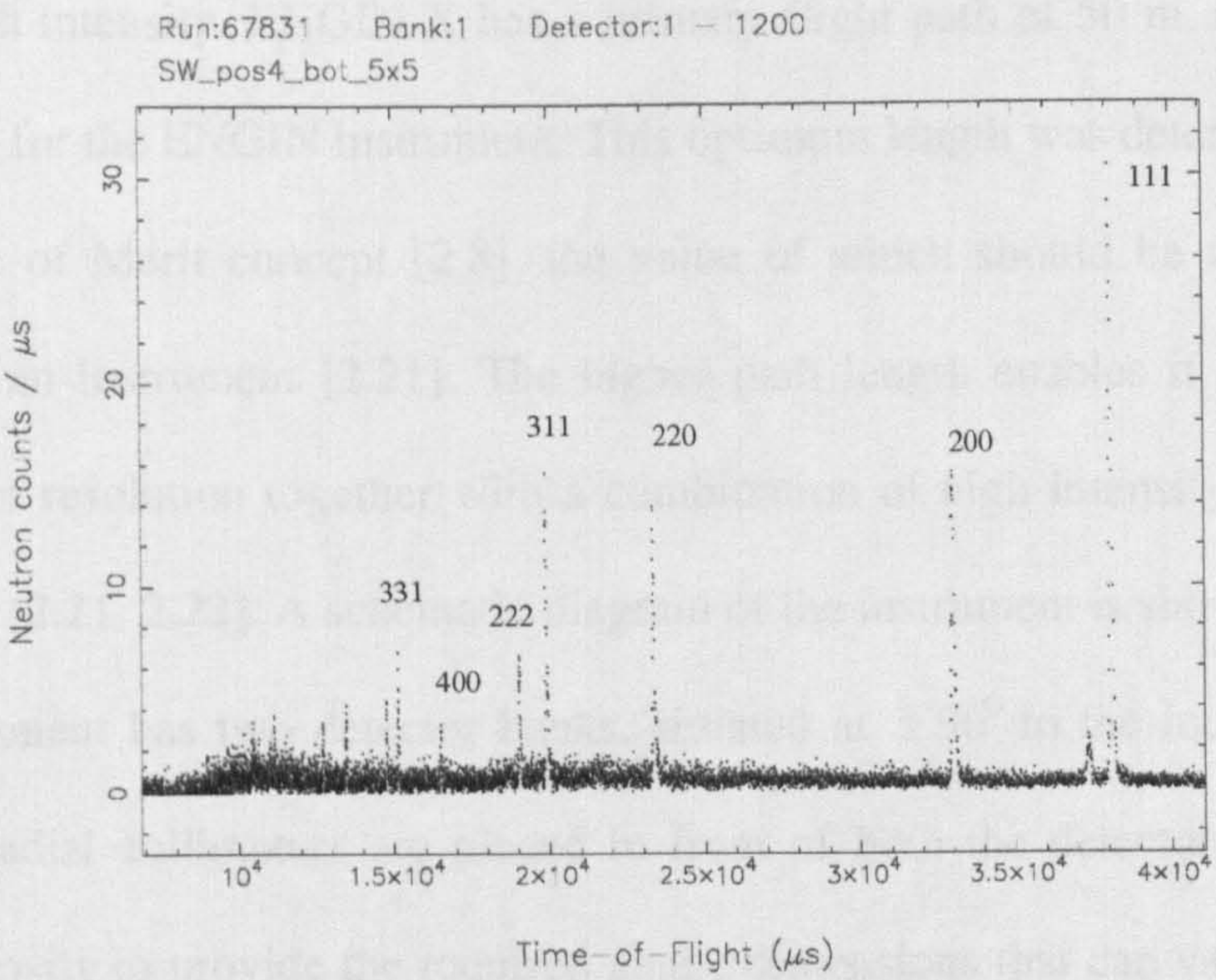

Figure 2.8: A typical time-of-flight diffraction pattern from stainless steel obtained in ENGIN-X.

crystallographic reflections can be obtained simultaneously giving the opportunity to investigate the strain responses of each of these reflections. In addition to this, it is also possible to obtain important information on texture, elastic anisotropy and plastic anisotropy of the material.

2.4.2.2 ENGIN-X diffractometer at the ISIS spallation source

ENGIN-X is the most recent version of a dedicated strain scanner, commissioned in 2003, and is the successor of ENGIN [2.19], which was built at ISIS in 1994. The purpose of the development of this instrument was to meet the increasing requirements of the engineering community. ENGIN-X provides considerable improved performance over the ENGIN instrument [2.20]. One of the major problems with spallation instruments is in obtaining very good resolution together with a high intensity. ENGIN-X has a primary flight path of 50 m, unlike the 15 m flight path for the ENGIN instrument. This optimum length was determined based on the Figure of Merit concept [2.8], the value of which should be maximum when designing an instrument [2.21]. The higher path length enables it to provide very good strain resolution together with a combination of high intensity and good time resolution [2.21, 2.22]. A schematic diagram of the instrument is shown in figure 2.9. The instrument has two detector banks, situated at $\pm 90^0$ to the incident beam. An array of radial collimators are placed in front of both the detectors, which can be changed easily to provide the required gauge dimensions that can vary from 0.5 to 4 mm. Both sides of the collimators are covered with boron carbide shielding to reduce the effect of background radiation. The incident beam is defined by motorized boron carbide slits (0.2-10 mm horizontal, and 0.2-30 mm vertical). The sample table is

capable of handling a maximum of 500 kg; it can be moved to ± 250 mm in the X and Y directions and up to 600 mm in the Z direction, with a maximum rotation of 370^0. A wide range of wavelengths can be used in ENGIN-X, from 0.5 to 10 Å [2.23]. Further, it has a stress rig and radiant furnace to facilitate measurements under applied loads and realistic (high temperature) environments. Furthermore, the very recent development of SSCANS software [2.24], has allowed measurements to

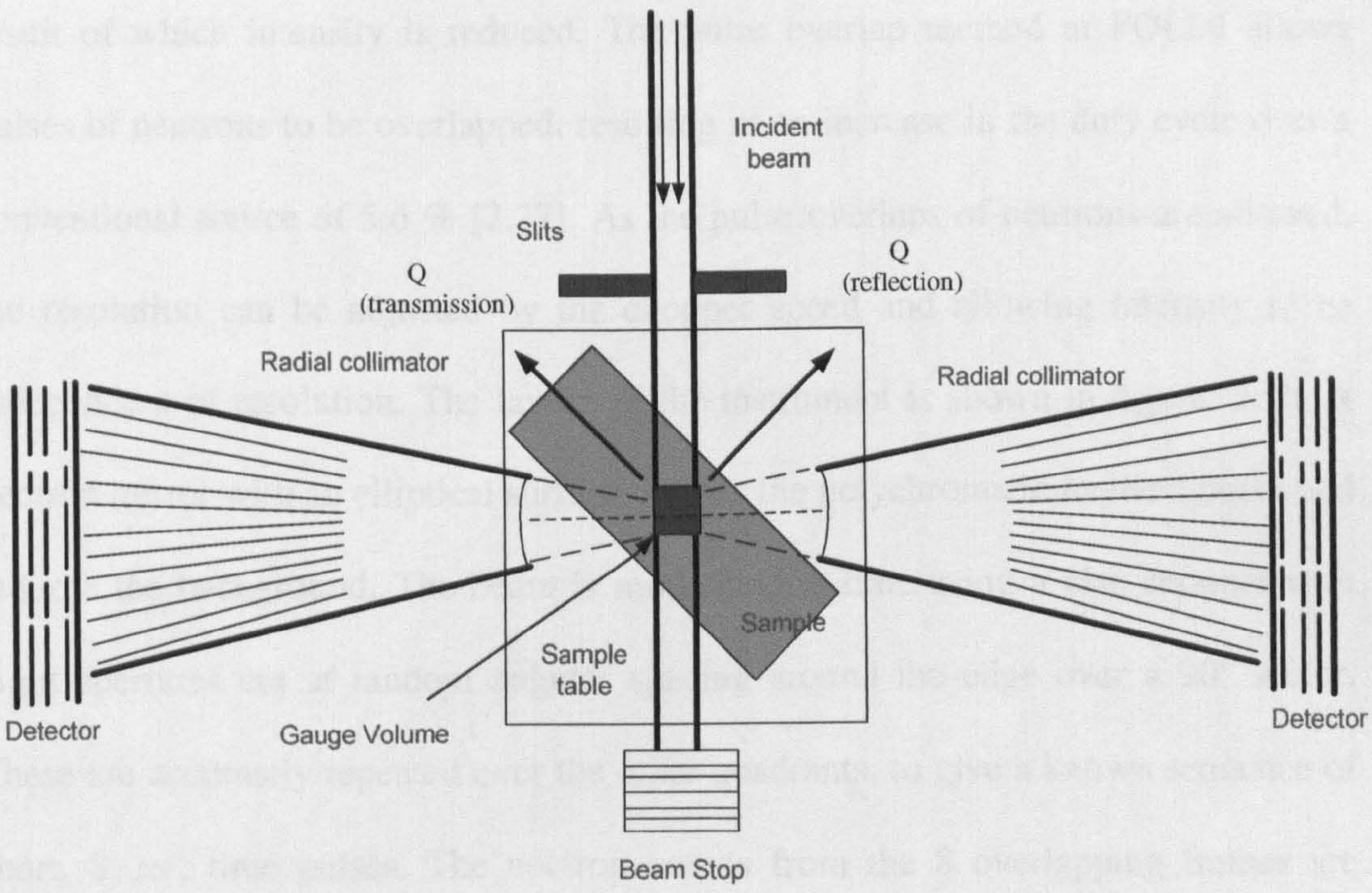

Figure 2.9: Schematic diagram of ENGIN-X diffractometer.

be carried out in very complex samples and together with the in-house data analysis software, Open Genie [2.25], has made this instrument one of the most advanced in the world.

2.4.2.3 POLDI pulse overlap–diffractometer

A new diffractometer has been installed at the continuous spallation source at PSI, POLDI, which works on the time-of-flight principle allowing a multiple pulse overlap method, resulting in measurements with good resolution together with high intensity [2.26]. In a conventional time of flight diffractometer, good resolution is achieved by shortening of the pulse which eventually reduces the duty cycle and as a result of which intensity is reduced. The pulse overlap method at POLDI allows pulses of neutrons to be overlapped, resulting in an increase in the duty cycle over a conventional source of 5.6 % [2.27]. As the pulse overlaps of neutrons are allowed, the resolution can be adjusted by the chopper speed and allowing intensity to be independent of resolution. The layout of the instrument is shown in figure. 2.10. A neutron mirror with an elliptical surface defines the polychromatic incident beam and reduces the background. The beam is modulated in time using a disc chopper with eight apertures cut at random angular spacing around the edge over a 90° sector. These are accurately repeated over the other quadrants, to give a known sequence of short, 8 μs, time pulses. The neutron counts from the 8 overlapping frames are collected from a time-focused helium (He_3) PSD detector at about 2 m distance from the sample over a 30° range of scattering angle. The total flight path is nearly 14 m. The overlapping TOF diffraction patterns are deconvolved by identifying their time

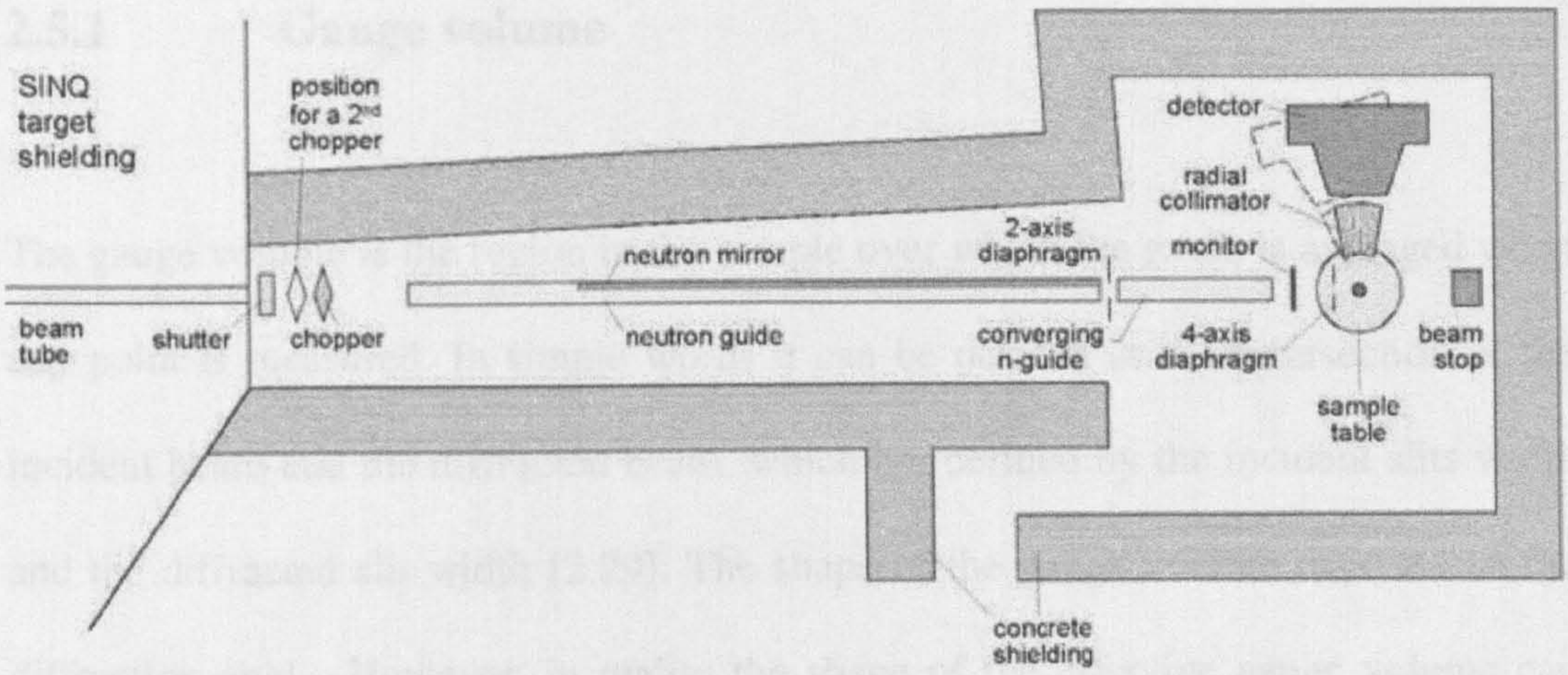

Figure 2.10: Schematic diagram of the POLDI instrument [2.28].

origin from their time intervals, and from the slope of peak intensity contours in a plot of intensity vs time of arrival, t, and scattering angle, ϕ^s. The instrument also suppresses the neutrons below a well-defined cut-off wavelength (1.1Å) by using neutron optics to define the incident beam. A resolution of $\Delta d/d \sim 2x10^{-3}$ FWHM can be attained.

2.5 Important aspects of neutron strain measurement

There are several parameters, for example instrument alignment, gauge volume, instrumental resolution, peak fitting, etc, which are important when making precise and accurate strain measurements [2.8]. Before performing an experiment, it is important to know the effect of these parameters as each parameter could introduce significant error in the final results. A few of the important parameters are discussed in the following sections.

2.5.1 Gauge volume

The gauge volume is the region in the sample over which the strain is averaged when any point is measured. In simple words it can be defined as the intersection of the incident beam and the diffracted beam, which are defined by the incident slits width and the diffracted slit width [2.29]. The shape of the gauge volume depends on the diffraction angle. However, in reality the shape of the effective gauge volume can vary depending on instrumental uncertainties. The gauge volume can be defined

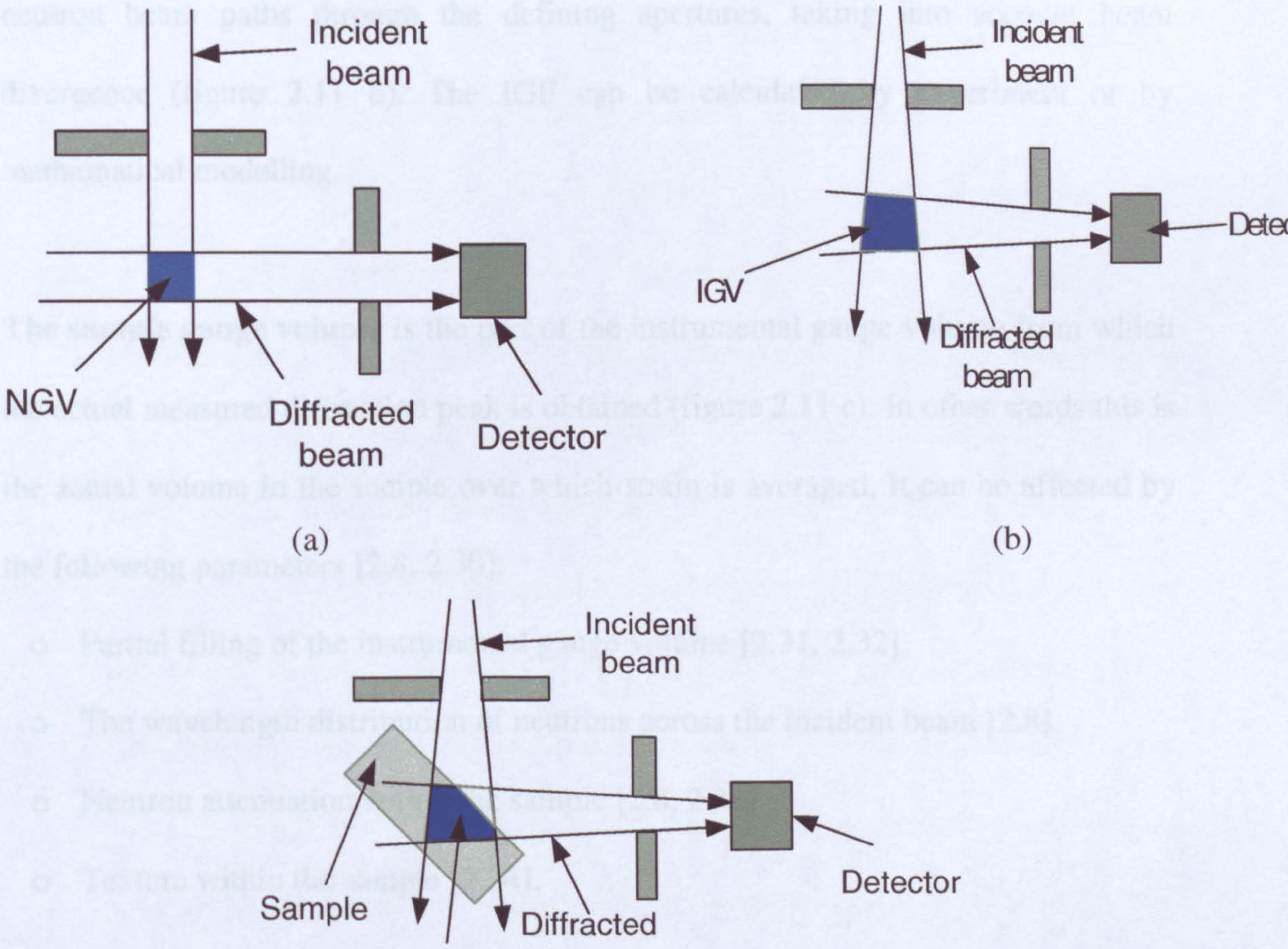

Figure 2.11: Schematic diagram of (a) nominal gauge volume (NGV), (b) instrumental gauge volume (IGV) and (c) sample gauge volume (SGV) in neutron diffraction where $2\theta = 90^0$.

in three categories [2.30], a) nominal gauge volume (NGV), b) the instrumental gauge volume (IGV) and c) the sampled gauge volume.

The nominal gauge volume is defined by the intersection of a perfectly parallel incident neutron beam and the diffracted neutron beam (figure 2.11 a). This volume can simply be calculated by knowing the aperture width of the incident and diffracted slits [2.8].

The instrumental gauge volume is the area defined by the intersection of the actual neutron beam paths through the defining apertures, taking into account beam divergence (figure 2.11 b). The IGF can be calculated by experiment or by mathematical modelling.

The sample gauge volume is the part of the instrumental gauge volume from which the actual measured diffraction peak is obtained (figure 2.11 c). In other words this is the actual volume in the sample over which strain is averaged. It can be affected by the following parameters [2.8, 2.30]:

- Partial filling of the instrumental gauge volume [2.31, 2.32].
- The wavelength distribution of neutrons across the incident beam [2.8].
- Neutron attenuation within the sample [2.8, 2.33].
- Texture within the sample [2.34].

If the IGV is completely submerged in a non-absorbing and non-textured material, then the IGV is the same as SGV. It is very important to know the SGV properly, as this is the actual volume over which the strain within the sample is averaged. Before

performing an experiment, care has to be taken in selecting the appropriate gauge volume. Selection of a larger gauge volume ensures shorter counting times, but with a loss in spatial resolution. In many cases it is very important to have a high spatial resolution if large stress gradients exist in the component being investigated.

2.5.2 Measurement of stress free reference sample

Measurement of stress using diffraction techniques is based on comparative measurement of lattice spacing (d_{hkl}) and strain free lattice parameter (d_0) in the sample (equation 2.2). An error of 0.1% in the estimation of d_0 can lead to significant error in the final stress analysis [2.35]. Thus, accurate measurement of strain and the corresponding stress is dependent on the accuracy of the measured d_0 value. The following are a range of methods available to measure d_0 [2.8]:

a) **Measurement of far-field d_0 value:** This is the most convenient and common way of measuring a stress free reference value, where a measurement is carried out far from the affected region of the material. This approach is based on the assumption that for many components stresses fade away from the main stress affected zone and so the component will have a minimum of residual stress at distances far away from the main affected zone. This approach is widely used except for the cases where compositional changes or phase transformation can take place and due to that the stress free reference value changes point to point.

b) **Measurement of a powder:** In many occasions a powder sample of the same material is used to measure d_0 value. The concept behind the use of powder is that fine particles are unable hold any significant stress. However, one has to

be very careful in using powder as some external stresses might be introduced during the mechanical processing of the powder particle. Powders are measured by filling a vanadium or quartzite tube and placing it in the neutron beam.

c) **Use of machined cube or a 'Comb' sample:** This approach is used in those cases where the component under investigation is expected to have compositional variation and local stress free parameter varies from point to point [2.36]. This mainly occurs in the heat treated alloy due to the precipitation of a second phase. In this method, many small cubes are taken out from part of the original specimen or an identical specimen using the EDM technique, which ensures no extra stresses are introduced during cutting. Cubes are cut as small as possible, providing that a sufficient number of grains are available for diffraction to take place. Furthermore, as this approach allows point to point variation, the effects of intergranular stress or type II stress can be minimised. In this project, this method was used in measuring stress in a welded specimen and will be discussed later in the next chapter.

2.5.3 Fitting of diffraction peaks

To obtain an accurate lattice parameter and consequently strain and stress, it is crucial to be able to locate the diffraction peak centre accurately. The diffraction peak profile obtained from steady-state source can be described by symmetric functions. Typically a Gaussian-shaped function [2.37] is most commonly used to fit

these symmetric profiles. In some occasions, in the elastic region the peak profile can be well described by the Gaussian function, but in the plastic region the peak profile is best described by Lorentzian function [2.8]. The combination of these two profiles is represented by 'Voigt' function or the 'Pearson type VII' function [2.37, 2.38]. Both these functions can fit a peak profile where gradual transition from Gaussian to Lorentzian takes place.

Unlike the symmetric profile in steady-state sources, peak profile obtained in the pulse-neutron source is asymmetric in nature, which is generated mainly due to the moderation process involve in this technique [2.10]. A typical asymmetric peak profile obtained from pulse-neutron source recorded on the ENGIN beamline at ISIS is shown in figure 2.12. This sort of asymmetric peak profile, which consist of a

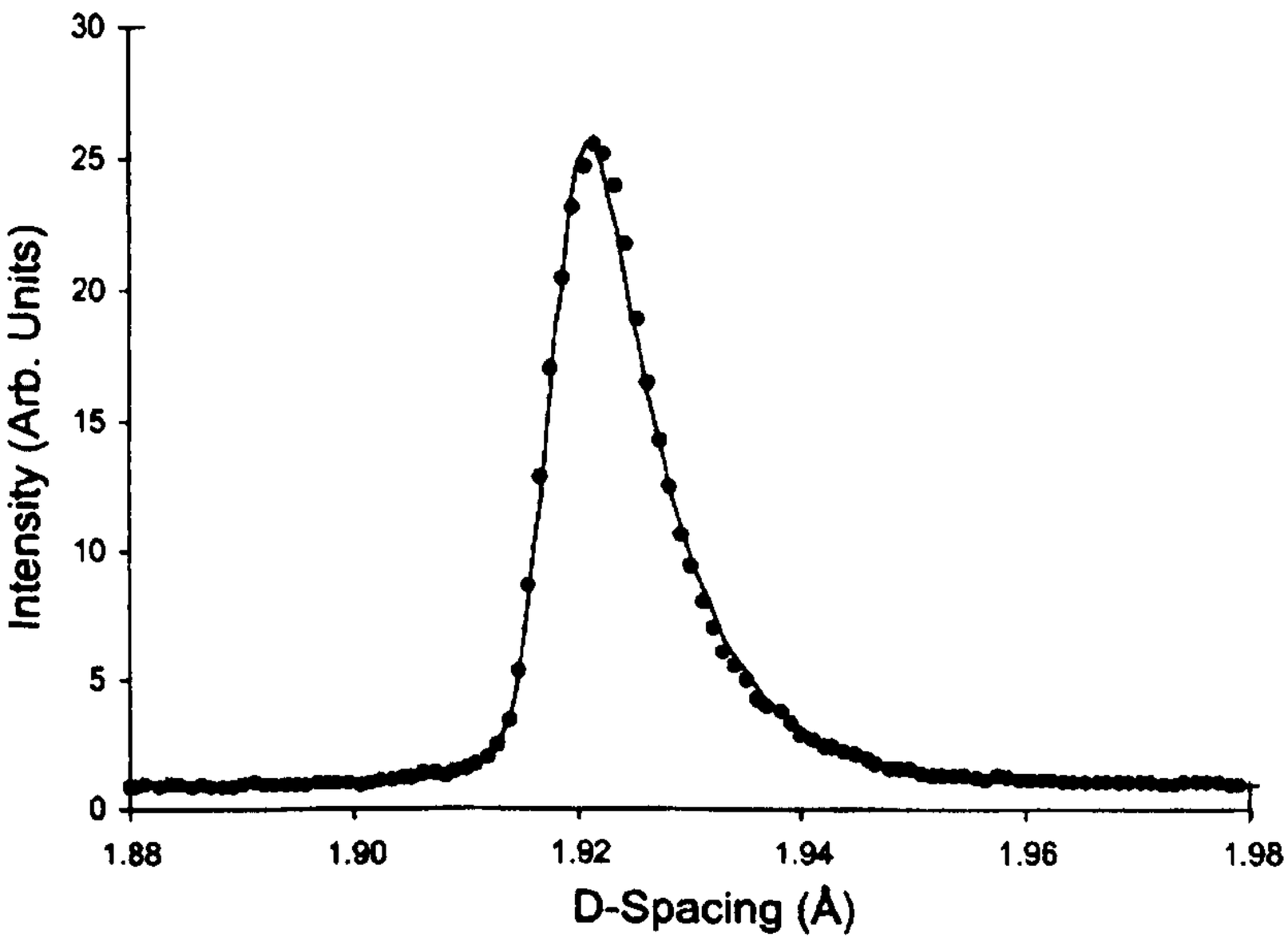

Figure 2.12: A Si 220 Bragg peak recorded on the ENGIN beamline at the ISIS time-of-flight source [2.8]. The fitting of the profile is done by Carpenter et al [2.39].

leading and trailing exponentials, is usually described using Voigt function. However a better fit to the data can be achieved by a function developed by Carpenter et al [2.39], which is currently used to fit the data in ENGIN-X, ISIS instrument.

The whole diffraction spectrum obtained in the pulse-source is fitted using the Reitvelt [2.40] or Pawley [2.41] refinement approach to obtain an average lattice parameter of the unit cell. These refinements can be performed using freely available software or computer codes such as Generalized Structure Analysis System (GSAS) by Larson and Von Dreele [2.42]. Use of Reitvelt or Pawley approach has become very popular among researchers and engineers, particularly for strain and stress measurement, due to its ability to provide a weighted average of the strain from all reflections in the diffraction peak and thus enabling to obtain a strain value close to macroscopic strain response in a particular direction [2.43]. The basic concept behind the Reitvelt and Pawley fitting routine is to fit the observed diffraction profile with a theoretical intensity profile of the whole diffraction spectrum, which include peak profile, unit cell parameters, structures, multiplicity factors, absorption and background. Although a texture factor can also be included in both these technique to allow for any preferential orientations in the grains the Pawley technique is more suitable in case of textured material as it does not put any constraint on the calculated intensities of the peaks and instead allows intensity of each reflection to vary independently.

2.5.4 Selection of suitable crystallographic planes

Selection of the most appropriate diffraction peaks is crucial in determining macroscopic strain and corresponding stress for reactor source. It is generally recommended to select a peak which will represent large number of grains that essentially means the peak with high structure factor and multiplicity [2.8]. However, in reality, selection of a suitable plane is often found to be complicated as most engineering materials are affected with texture, elastic anisotropy and plastic anisotropy.

Elastic anisotropy arises due to the fact that the elastic response of individual grains in a polycrystalline material are anisotropic to applied stress, as a result of which different lattice planes shows different response to macroscopic stress [2.44, 2.45]. However, it has been found that in the elastic region the strain response for individual reflections are linear (figure 2.13). Therefore, in this region any lattice reflection can be selected to determine the macroscopic strain provided the accurate diffraction elastic constant for that particular plane in the polycrystalline sample is known. The elastic constants can be calculated either by in-situ experiments using neutron diffraction technique or by using Reuss [2.46], Voigt [2.47] or Kroner [2.48] models.

Plastic anisotropy arises due to the heterogeneous plastic flow of different grains during deformation [2.8, 2.49]. As a result, in the plastic regime an individual reflection does not follow linear behaviour with the application of external loading. When a polycrystalline material is loaded into the plastic regime, some grains are oriented in such way that the shear stress reaches critical value and deformations in these grains occur before the other grains. Once deformation occurs in these grains,

some load is then transferred to the other grains and deformation takes place. Thus, anisotropy effects in the plastic region are complicated and, till now there is

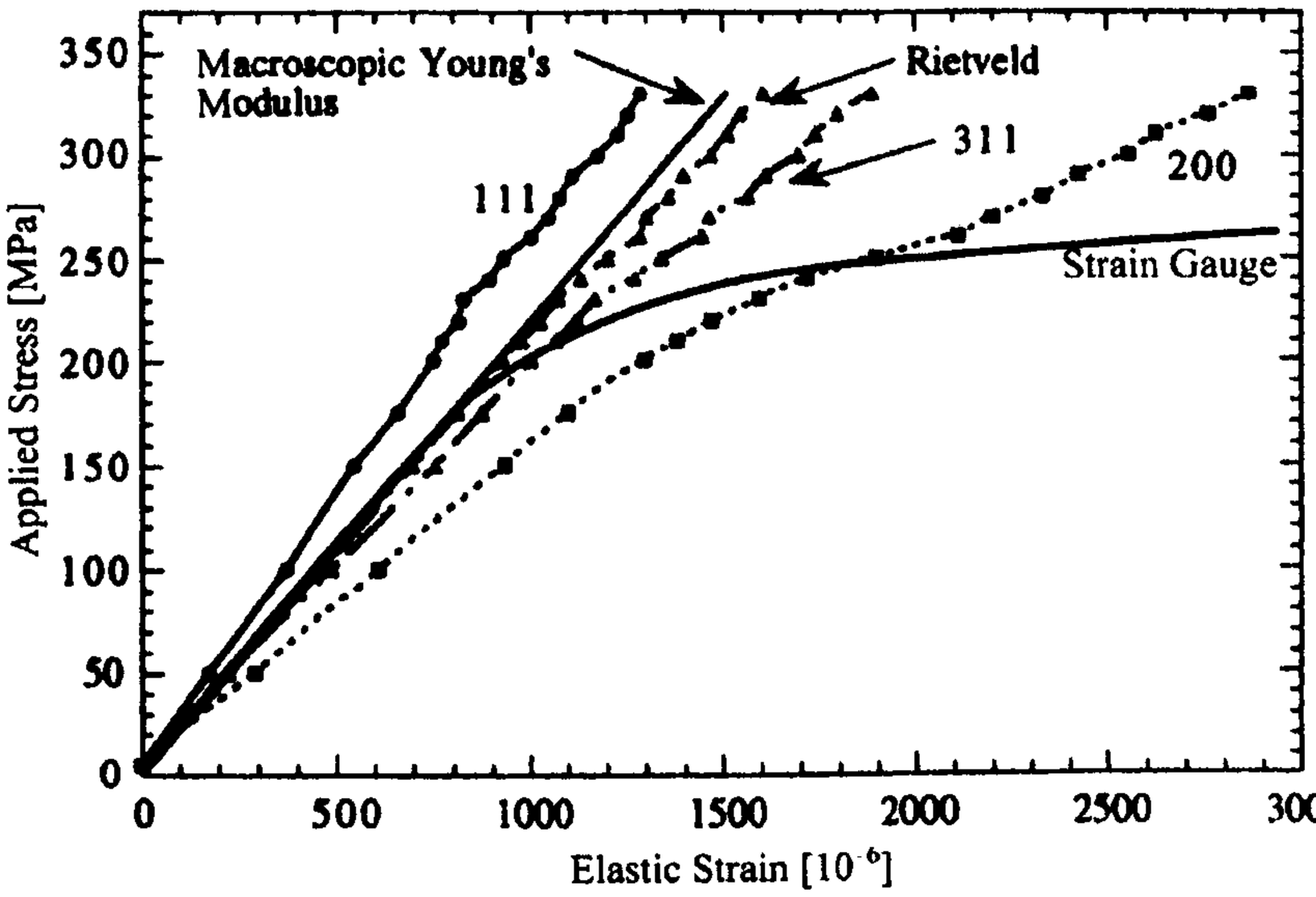

Figure 2.13: The elastic lattice strain response for austenitic stainless steel parallel to uniaxial loading as determined from individual peak analysis and by Rietveld analysis of the whole diffraction profile [2.8, 2.43].

a lack of complete understanding in many issues in the plastic region. To predict the mechanism of polycrystalline deformation in the plastic regime elastoplastic self-consistent (EPSC) approach has been used extensively which are all based on formalism given by Hill [2.50, 2.51], later a significant work on this is done by Hutchingson [2.52] and more recently by Clausean and Lorentz [2.53, 2.54]. However, due to the non-linear behaviour of the individual reflections in the plastic region it is difficult to quantify plastic anisotropy. To determine the macro-stresses in the plastic regime, it is recommended to use those reflections that are less sensitive to plastic deformation or in other words which shows linear response in both elastic and plastic regime. Lattice planes which is known to show good linearity and is affected

less by intergranular strains is given in the draft VAMAS standard [2.30] and is presented in table 1.1. Alternatively, the Reitvelt or Pawley analysis (discussed in the previous section), widely used to fit the diffraction spectrum obtained in the pulse-neutron source, has been reported to be insensitive to the intergranular affects even in the plastic region up-to several percent plastic strain [2.43]. Use of Reitvelt or Pawley analysis has been found to show linear response as a function of stress in the elastic and plastic region (figure 2.13). This effectively means that use of this multiple-peak fitting approach can be used as a tool to deal with these elastic and plastic anisotropy problems.

Table 1.1: Lattice planes weakly and strongly affected by intergranular strains [2.8].

Material	**Recommended Planes (Weakly affected by intergranular strains)**	**Problematic planes (strongly affected by intergranular strains)**
fcc (Ni , Fe, Cu)	(111), (311), (422)	(200)
fcc (Al)	(311), (422), (220)	(200)
bcc (Fe)	(110), (211)	(200)
hcp (Ti)	Pyramidal (1012), (1013)	Basal (0002) and prism (1010), (1210)
hcp	Second -order pyramidal (2021), (1122)	Basal, Prism, and first-order pyramidal (1012), (1013)

2.6 Synchrotron X-ray radiation

Laboratory X-ray diffraction is the most popular conventional diffraction method for investigating surface stress; on the other hand, development of the neutron diffraction technique has given scientists the opportunity to measure residual stress deep inside the material non-destructively. These two techniques are used widely as complementary techniques to map the strain and stress in a sample. But, both these techniques have their limitations, for example, neutrons have low intensity which gives slow counting rates and also with neutrons it is difficult to achieve very high spatial resolution (not less than 1mm), whereas X-ray can only measure surface stress. With the advancement of technology and to meet the new challenges of complex research activities, scientists and engineers around the world have been looking for something which would enable them to achieve both in one go, that is - good resolution as well as fast counting time. The development of 3rd generation synchrotron source [2.55] such as ESRF (in Grenoble, France) has given scientists many new opportunities, where measurements can be made in seconds rather than minutes together with a very high spatial resolution (down to 1 μm). Synchrotron X-ray intensities are millions of times greater than that of conventional X-rays. The combination of high spatial resolution along with fast counting time, has opened up the opportunity to the scientific community to explore many areas which were earlier thought to be impossible to investigate.

2.6.1 Production of synchrotron X- ray

High energy synchrotron X-rays are produced by accelerating bunches of electrons circulating at a very high velocity, close to the speed of light [2.56-2.58]. Synchrotron X-ray radiation at the ESRF is generated in a polygon shaped electronic storage ring (figure 2.14). The electrons path is controlled by passing them through dipole magnets or through a number of periodically arranged magnets, called insertion devices. Dipole magnets give angular motion to the electron, enabling the acceleration of the electron from one straight section to another. The loss of energy of the electron beam in the storage ring is compensated by RF (radio frequency) cavities. Bending magnets produces a white beam (a wide range of wavelength) of

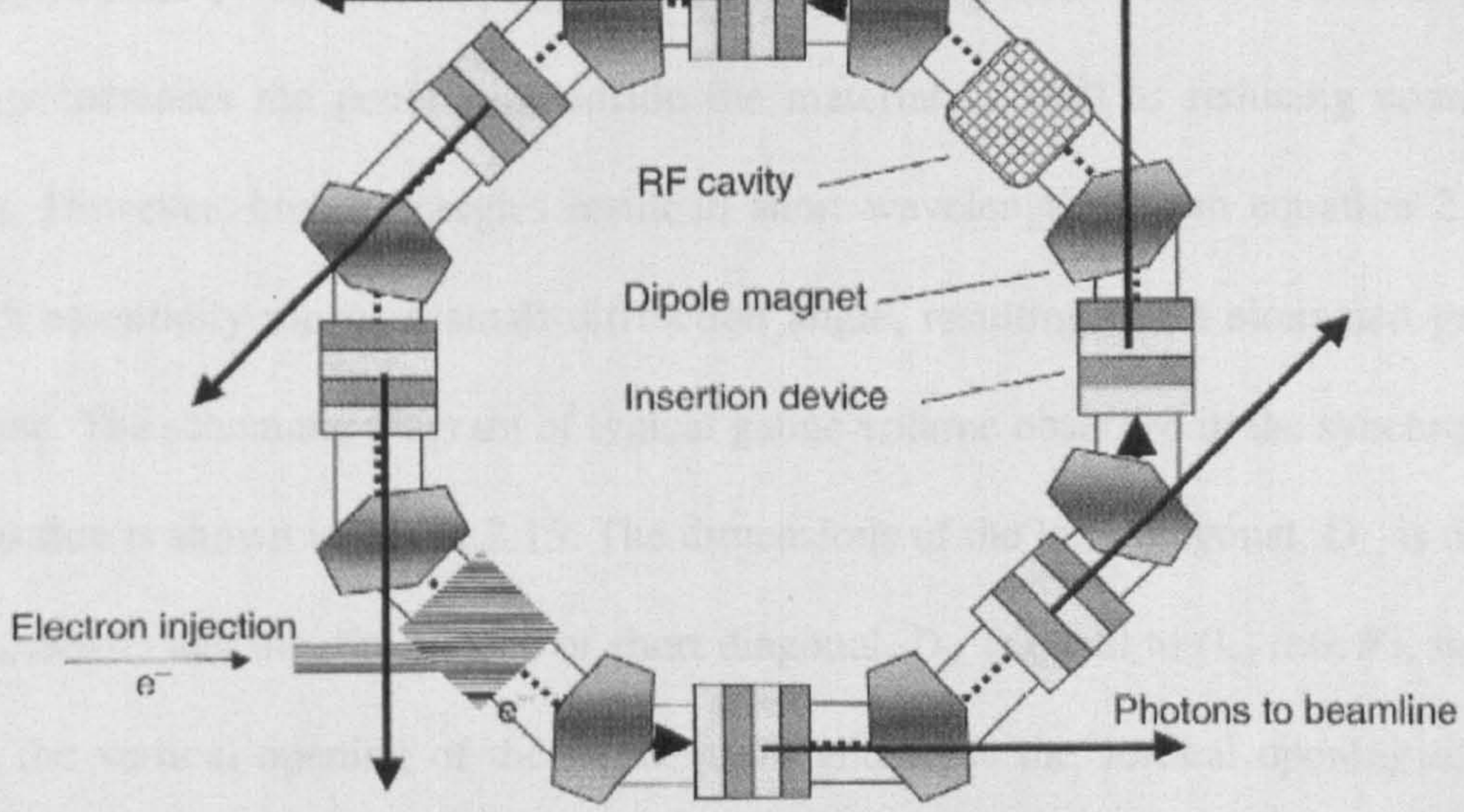

Figure 2.14: Schematic diagram of synchrotron radiation storage ring [2.56].

X-rays in the medium energy range (<40 keV), whereas insertion devices produce high energy (>80 keV) X-rays of fixed wavelength depending on the geometry of the undulator [2.56].

2.6.2 Basic principle of synchrotron X-ray diffraction

Like the other diffraction techniques, synchrotron X-ray diffraction also exploits Bragg's law to determine the interplanar lattice spacing. From the relationship between X-ray energy and wavelength we know that,

$$E = hc / \lambda \tag{2.24}$$

Where h is Planck's constant and c is the speed of light. This leads to:

$$\lambda \approx 12.4 / E \tag{2.25}$$

Where the units of E and λ are in keV and Å respectively. At the ESRF, maximum energy (E) can be obtained as high as 300 keV, starting from 40 keV. Use of higher energy increases the penetration inside the material as well as reducing counting times. However, higher energies result in short wavelengths (from equation 2.25), which essentially means a small diffraction angle, resulting in an elongated gauge volume. The schematic diagram of typical gauge volume observed in the synchrotron diffraction is shown in figure 2.15. The dimensions of the long diagonal, D_L, is equal to $(L_i / \sin\theta)$ and the dimensions of short diagonal, D_S, is equal to $(L_d / \cos\theta)$, where L_i is the vertical opening of the incident slit and L_d is the vertical opening of the diffracted slit (figure 2.15). It is also reported in the literature that in case of aluminium, using higher energies of 80 keV ($\theta = 2^0$) elongates the gauge length to about 14 times the aperture width, while the use of relatively low energy of 15 keV

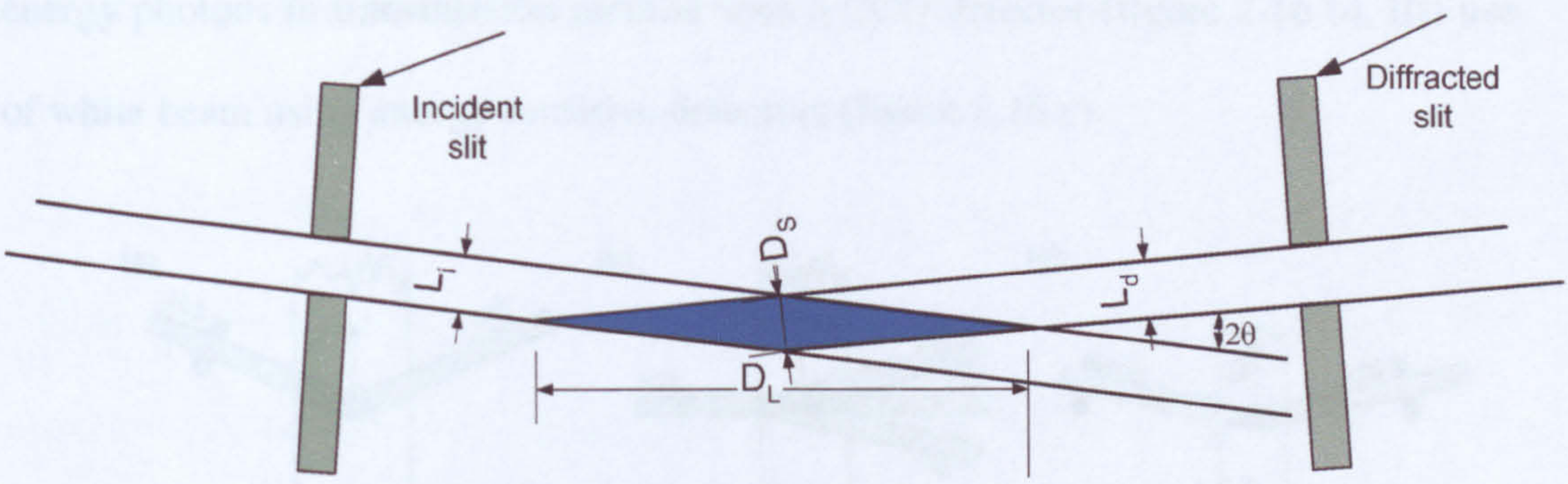

Figure 2.15: Typical gauge dimensions observed in synchrotron X-ray diffraction.

($\theta = 10^0$) elongates the gauge length only 3 times the aperture width [2.59]. Due to these characteristics of the synchrotron source, it is possible to measure in-plane stresses in relatively thick specimens using transmission geometry, while it is almost impossible to measure strain in the normal direction due to greatly increased path lengths at low diffraction angles. High penetration can be obtained in the transmission geometry as the path length as the diffraction path length inside the material remains the same for all points through the thickness. However, in the reflection geometry (normal direction measurement), the path length (2× depth/sin θ) starts to increase rapidly with the increase in depth of measurement.

2.6.3 Stress measurement using synchrotron X-ray diffraction

At present there are three different methods available to measure stress using the synchrotron X-ray diffraction method [2.60]. These methods are: I) Traditional θ /2θ scanning in reflection or transmission geometry (figure 2.16 a), II) use of high-

energy photons in transmission method with a CCD detector (figure 2.16 b), III) use of white beam using energy sensitive detectors (figure 2.16 c).

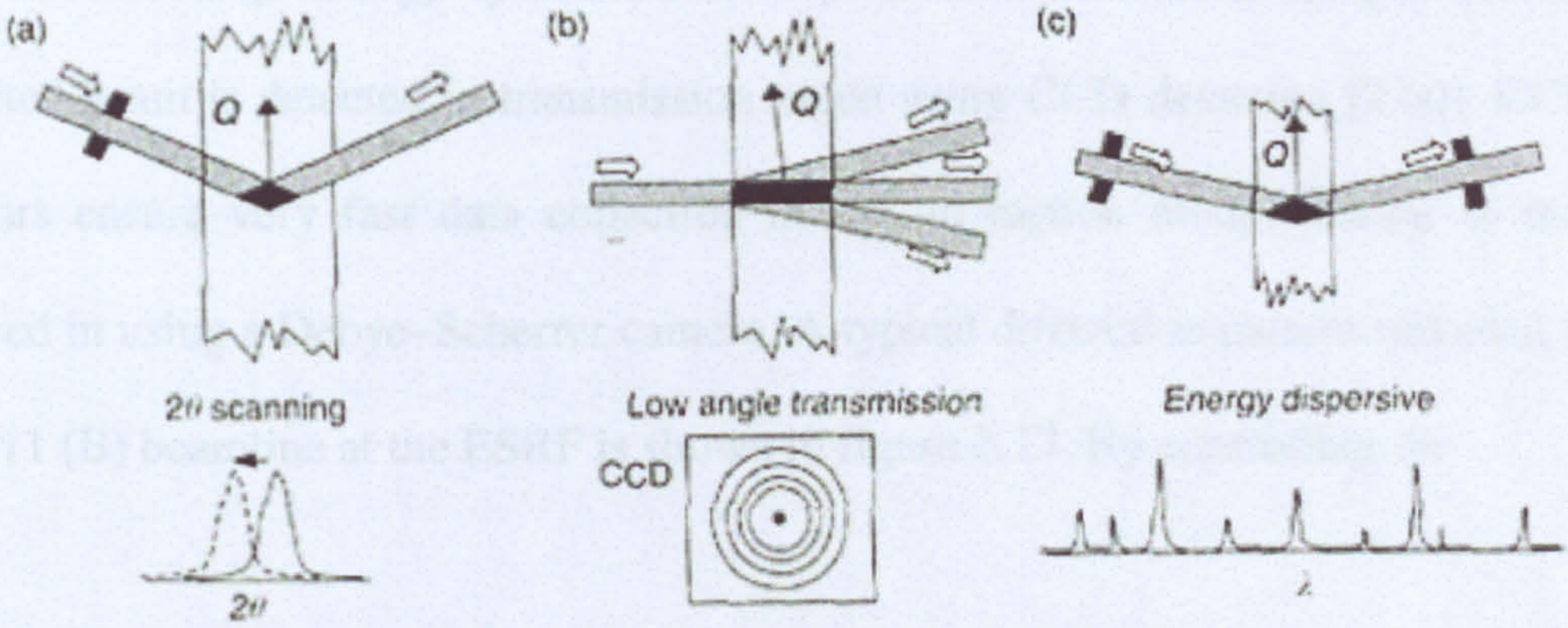

Figure 2.16: Schematic diagram of three different strain measurement geometries and the diffraction spectrum obtained from theses measurements [2.60].

2.6.3.1 Traditional θ /2θ scanning

This technique uses the same principles as conventional X-ray diffraction. The only difference is that, in the case of synchrotron X-ray diffraction very small scattering angles are used due to the high X-ray energies. As already stated in the previous section, high penetration can be obtained in transmission geometry while it is difficult to make measurements inside the material in the reflection geometry. Thus, reflection geometry is restricted to measurement of surface stress only. It is worth mentioning that surface measurement can also be influenced by a pseudo–strain effect due the problem of partial filling of the gauge volume which is a known problem in neutron diffraction [2.61]. However, it has been reported that the use of an analyser crystal in front of the detector has been proved to be very effective in solving the pseudo-strain problem [2.60].

2.6.3.2 Transmission method using 2-D detector

In this method, high-energy synchrotron X-rays are focused on the sample and the diffracted beam is detected in transmission mode using CCD detectors [2.60]. CCD detectors ensure very fast data collection in 2D diffraction mode, similar to that observed in using a Debye–Scherrer camera. A typical diffraction pattern recorded at the ID11 (B) beamline at the ESRF is shown in figure 2.17. By controlling the

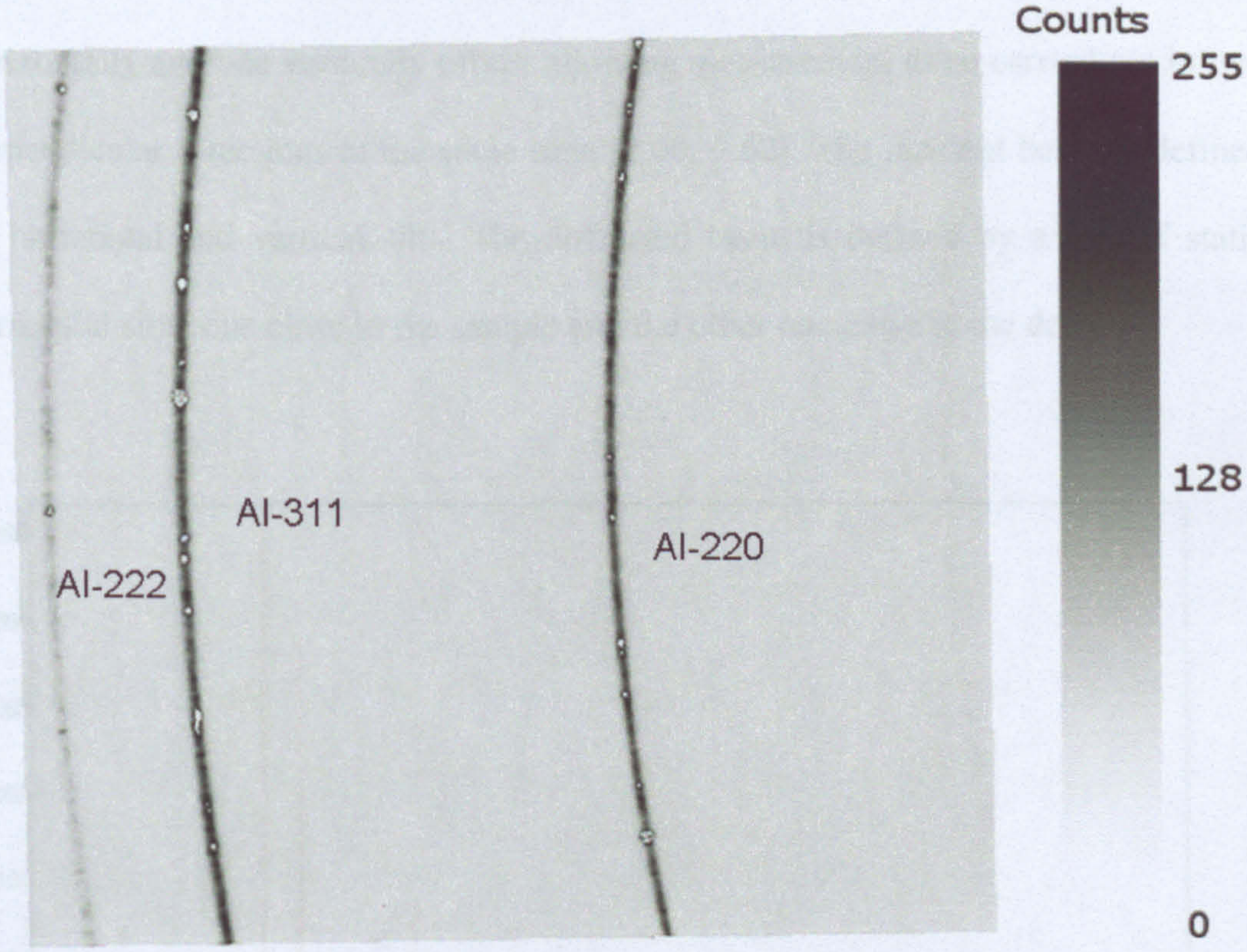

Figure 2.17: A typical diffraction image of Al-5091 in CCD detector at ID11(B) beamline at the ESRF facility.

incident apertures it is possible to achieve very high lateral resolution, as low as 10 x 10 μm^2. It has to be ensured that the distance between the diffraction volume and CCD detectors remains the same throughout the experiment, as a slight change in

this distance will lead to an apparent strain. This instrument is very useful for stress mapping of very fine-grained samples due to the high spatial resolution that can be achieved from this instrument.

2.6.3.3 Use of white beam using energy sensitive detectors

In this technique, a high energy (ranging from 40 to 300 keV) white beam is incident on the sample and the transmitted beam is detected in two photoconductive solid state X-ray detectors placed at small diffraction angle ($2\theta = 5^0$ to 8^0), one horizontally and one vertically offset, allowing measurement to be carried out in two perpendicular directions at the same time [2.60, 2.62]. The incident beam is defined by horizontal and vertical slits. The diffracted beam is defined by a pair of static horizontal slits, one close to the sample and the other one close to the detector.

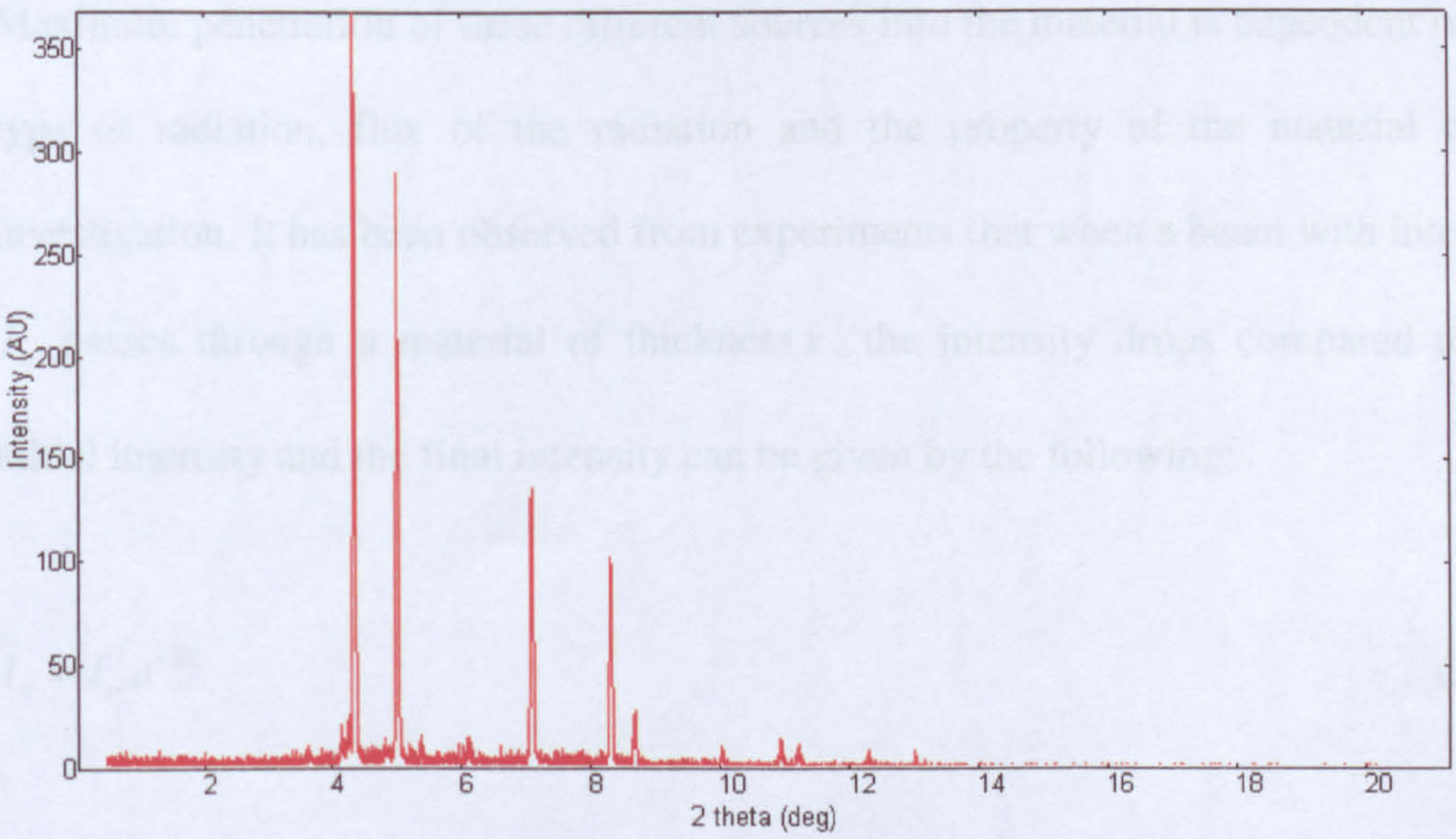

Figure 2.18: Typical diffraction spectrum obtained in the ID15 (A) beamline at the ESRF facility.

Unlike the angular dispersive mode, in this case diffraction spectrum of intensity is obtained as a function of photon energy. Using this technique very high spatial resolution (as low as 20 x 20 μm^2) can be obtained. This technique is very useful for the study of multiphase materials as well as materials with very small grain size. A typical diffraction spectrum recorded at ID15 (A) beamline at the ESRF facility is shown in figure 2.18. As it is evident from the figure that the diffraction profile consist of several peak, the profile can be fitted using Pawley type fitting routine typically used to fit the diffraction spectrum from pulsed neutron source as discussed in the previous section [2.62].

2.7 Comparative study of depth capabilities of different source

Maximum penetration of these different sources into the material is dependent on the type of radiation, flux of the radiation and the property of the material under investigation. It has been observed from experiments that when a beam with intensity I_o passes through a material of thickness x, the intensity drops compared to the initial intensity and the final intensity can be given by the following:

$$I_x = I_o.e^{-\mu x} \tag{2.26}$$

Where μ is the linear attenuation co-efficient of the material. Equation 2.26 can be modified by incorporating density of the material and is given by:

$$I_x = I_o.e^{-\left(\frac{\mu}{\rho}\right)\rho x} \tag{2.27}$$

Where $\left(\frac{\mu}{\rho}\right)$ is termed mass absorption coefficient and ρ is the density of the material. The value of mass absorption co-efficient for different material for a given radiation can be found from the literature [2.63].

The penetrability of different radiation can also be expressed in an alternative ways, which is by using the concept of attenuation length (I_μ). The attenuation length can be defined as the length in a material that will attenuate 63% of the incident beam. Attenuation lengths for 63% attenuation for different radiation sources in different material are presented in table 2.2 [2.64]. It is evident from the table that commonly used laboratory X-rays cannot penetrate far inside the material and, thus, are restricted to surface only. Synchrotron radiation can measure 39 mm deep inside the aluminium using 150 keV energy in ID 15 (A) beamline, whereas neutron has the highest penetrating power inside the bulk material (almost 100 mm inside the Al) allowing measurement to be carried out in very large samples with complex geometries. This is mainly due to the fact that the neutron particles are neutral or charge less and interact with the material very weakly, allowing much more penetration than synchrotron X-ray. However, synchrotron X-ray sources can generate much higher flux than the neutron sources that gives synchrotron the advantage of being able to measure faster than the neutron. Besides these factors

Table 2.2: Table of attenuation lengths (mm) to 63% attenuation for neutrons, and synchrotron X-ray and laboratory X-rays [2.64].

			Approximate attenuation length (I_μ) (mm)		
	Energy (keV)	Wavelength (Å)	Al	Ti	Fe
Thermal neutrons	2.5×10^{-5}	1.80	96	18	8
ID 15 (ESRF)	150	0.08	39	14	7
ID 31 (ESRF)	60	0.21	13	3	1.1
ID 11 (ESRF)	49	0.25	10	2	0.7
BM16 (ESRF)	38	0.32	6.5	1	0.4
16.3 SRS	31	0.40	3.3	0.5	0.16
Laboratory –X ray (Cu $K\alpha$)	8.05	1.54	0.076	0.011	0.004

measurement depth inside a material is also influenced by the background level [2.8, 2.33]. However, it is worth mentioning that if measurement is important then it is possible to investigate more than 63% attenuation length by increasing the energy level or the measurement time. For example, measurements of 25 mm thick (4 times more than 63% attenuation length as mentioned in table 2.2) stainless steel sample have been reported [2.62] at the ID15 (A) beamline with the increase of higher energy (300 keV). More recently, through the thickness of 35 mm stainless steel (5 times more than the 63% attenuation length) has been successfully measured at the ESRF facility by The Open University Structural Integrity Research Group [2.65]. A detailed study regarding the depth capabilities of neuron and synchrotron sources in different material and the interrelated issues has been carried out by Withers [2.33], where he also discussed about the economically feasible path length for different sources in different material. Therefore, before applying for beamtime in different facilities it is crucial to have proper understanding of the sample property and the maximum depth needed to be measured.

2.8 Summary

Detailed discussions have been done on the use of X-ray, neutron and synchrotron X-ray diffraction technique in residual stress measurement. Furthermore, the problems associated with these measurement techniques and the various other aspects related to these techniques along with their advantages and disadvantages has been reviewed in this chapter.

2.9 References

2.1. B. D. Cullity, *Elements of X-ray Diffraction*. 1967, Reading, Massachusetts: Addison- Wesley Publishing Co.

2.2. I. C. Noyan and J. B. Cohen, *Residual Stress-Measurement by Diffraction and Interpretation*, in *A very Complete Treatment of Stress and Stress Tensors and How Stresses are Measured in Polycrystalline Samples.*, Ilschner, B. and Grant, N. J., Editors. 1987, Springer -Verlag: New York.

2.3. A. E. v. Arkel, *Uber die Verformung des Kristallgitters Von Metallen Durch Mechanische Bearbeitung*. Physica B, 1925. **5**: p. 208-212.

2.4. M. E. Fitzpatrick, A. T. Fry, P. Holdway, F. A. Kandil, J. Shackleton and L. Suominen, *Determinatin of Residual Stresses by X- Ray Diffraction-A Good Practice Guide, National Physical Laboratory, London.* 2002.

2.5. A. J. Allen, C. Andreani, M. T. Hutchings and C. G. Windsor, *Measurement of Internal Stress Within Bulk Materials Using Neutron Diffraction.* NDT Int, 1981. **15**: p. 249-254.

2.6. M. J. Schmank and A. D. Krawitz, *Measurement of Stress Gradient Through the Bulk of an Aluminium Alloys Using Neutrons.* Met Trans A, 1982. **13**: p. 1069-1075.

2.7. A. D. Krawitz, J. E. Brune, M. J. Schmank, E. Kula and V. Weiss. *Measurement of Stresses in the Interior of Solids with Neutrons in Residual Stress and Stress Relaxation.* in *Proceedings of the 28th Army Materials Research Conference.* 1981. New York: Plenum Press.

2.8. M. T. Hutchings, P. J. Withers, T. M. Holden and T. Lorentzen, *Diffraction Technique and Instrument Design*, in *Introduction to the Characterization of Residual Stress by Neutron Diffraction.* 2005, Taylor and Francis: New York.

2.9. C. H. D. Novion, *The use of Neutrons for Materials Characterization*, in *Analysis of Residual Stress by Diffraction by Using Neutron and Synchrotron Radiation*, Fitzpatrick, M. E. and Lodini, A., Editors. 2003. p. 1-27.

2.10. M. W. Johnson and M. R. Daymond, *Neutron Pulsed Source Instrumentation*, in *Analysis of Residual Stress by Diffraction using Neutron and Synchrotron Radiation*, Fitzpatrick, M. E. and Lodini, A., Editors. 2003, Taylor and Francis: London. p. 146-169.

2.11. J. M. Carpenter and W. B. Yelon. *Neutron Sources, in Methods of Experimental Physics, Vol 23A, Neutron Scattering, K. Skold, D. L. Price, Eds., Academic Press, New York, 1986, 99-186.* 1986: Academic Press , New York.

2.12. L. Pintschovius, *Neutron Diffraction using Constant Wavelength*, in *Analysis of Residual Stress by Diffraction by Using Neutron and Synchrotron Radiation*, Fitzpatrick, M. E. and Lodini, A., Editors. 2003, Taylor and Francis: London. p. 133-145.

2.13. P. Ageron, *Neutrons in the Investigation of Matter: Neutron Beam Reactors.* Neutron News, 1998. **9**: p. 14-16.

2.14. S. Ganguly, *Non-Destructive Measurement of Residual Stresses in Welded Aluminium 2024 Airframe Alloy, Ph.D Thesis*, in *Materials Engineering Dept.* 2004, The Open University: Milton Keynes. p. 255.

2.15. C. G. Windsor, *Pulsed Neutron Scattering. London, Taylor and Francis Ltd.* 1981.

2.16. K. Crawford, *The Intense Pulsed Neutron Source.* Neutron News, 1990. **1**: p. 9-15.

2.17. J. A. Roberts, *The Los Alamos Neutron Science Centre (LANSCE).* Neutron News, 1999. **10**: p. 11-14.

2.18. C. C. Wilson, *A Guided Tour of ISIS-the UK Spallation Neutron Source.* Neutron News, 1995. **6**: p. 27-34.

2.19. M. W. Johnson, L. Edwards and P. J. Withers, *ENGIN-a New Instrument for Engineers.* Physica B, 1997. **234**: p. 1141-1143.

2.20. J. A. Dann, M. R. Daymond, L. Edwards, J. A. James and J. R. Santisteban, *A Comparison between Engin and Engin-X,a New Diffractometer Optimized for Stress Measurement.* Physica B: Condensed Matter, 2004. **350**(1-3): p. E511-E514.

2.21. M. W. Johnson and M. R. Daymond, *An Optimum Design for a Neutron Diffractometer for Measuring Engineering Stresses.* J.Appl.Crystallography, 2002. **35**: p. 49-57.

2.22. M. R. Daymond and M. W. Johnson. *Optimisation of the Design of a Neutron Diffractometer for Strain Measurement.* in *Proceedings of International Colloquium on Advanced Neutron Sources XV.* 2000. Tsukuba, Japan.

2.23. *Available at: http://www.isis.rl.ac.uk/engineering/, accessed on 31st July.2006.*

2.24. J. James, J. R. Santisteban, L. Edwards and M. R. Daymond, *A Virtual Laboratory for Neutron and Synchrotron Strain Scanning.* Physica B : Condensed Matter 350, 2004. **350**(1-3): p. E743-E746.

2.25. *Available at : www.isis.rl.ac.uk/opengenie/, accessed on 31st July. 2006.*

2.26. P. Allenspach, *The Continious Spallation Neutron Source SINQ*, in *Neutron News*. 2000. p. 15-18.

2.27. U. Stuhr. *Concept and Performance of POLDI- the New TOF-Strain Scanner at PSI*. in *Proceedings ICANS-XVI*. May 12-15, 2003. Dusseldof-Neuss, Germany.

2.28. U. Stuhr, *The New Time of Flight Diffractometer at PSI for Strain Field Measurement*. Journal of Neutron Research, 2001. **9**: p. 423.

2.29. P. J. Withers, M. W. Johnson and J. S. Wright, *Neutron Strain Scanning Using a Radially Collimated Diffracted Beam*. Physica B, 2000. **292**: p. 273-285.

2.30. G. A. Webster, *Polycrystalline Materials -Determinations of Residual Stresses by Neutron Diffraction, ISO/TTA3 Technology Trends Assesment, Geneva, 2001*.

2.31. L. Edwards, *Near-Surface Strain Measurement Using Neutron Diffraction*, in *Analysis of Residual Stress by Diffraction by Using Neutron and Synchrotron Radiation*, Fitzpatrick, M. E. and Lodini, A., Editors. 2003, Taylor and Francis: London.

2.32. D. Q. Wang, L. Edwards, I. B. Harris and P. J. Withers. *Near Surface Stress Measurement Using Neutron Diffraction*. in *ECRS 4*. 1996. France.

2.33. P. J. Withers, *Depth Capabilities of Neutron and Synchrotron Diffraction Strain Measurement Instruments.II.Practical Implications*. Applied Crystallography, 2004. **37**: p. 607-612.

2.34. T. M. Holden, *The Effect of Texture on Residual Stress Measurement and Interpretation*, in *Analysis of Residual Stress by Diffraction by Using Neutron and Synchrotron Radiation*, Fitzpatrick, M. E. and Lodin, A., Editors. 2003, Taylor and Francis: London.

2.35. M. Rogante, *The Stress-free Reference Sample: the Problem of the Determination of the Interplanar Distance d_o*. Physica B, 2000. **B 276- 278**: p. 202-203.

2.36. A. D. Krawitz and R. A. Winholtz, *Use of Position -Dependent Stress-Free Standards for Diffraction Stress Measurements*. Mat.Sci.Eng.A, 1994. **185**: p. 123-130.

2.37. T. J. Devine, *Comparison of Full-Profile Peak Finding Methods for use in X-Ray Residual Stress Analysis, M. S. Thesis*, in *Northwestern University*. 1985.

2.38. M. M. Hall, V. G. Veeraaghavan, H. Rubin and P. G. Winchell, Journal of Applied Crystallography, 1977: p. 10-66.

2.39. J. M. Carpenter, R. A. Robinson, A. D. Taylor and D. J. Picton, *Measurement and Fitting of Spectrum and Pulse Shapes of a Liquid Methane Moderator at IPNS.* Nucl. Ins. Methods Phys. Res, 1985. **A234**: p. 542-551.

2.40. H. M. Reitvelt, J. Appl.Cryst, 1969. **2**: p. 65.

2.41. G. S. Pawley, *Unit-Cell Refinement From Powder Diffraction Scan.* J.Appl.Crystallography, 1981. **14**: p. 357-361.

2.42. A. C. Larson and R. B. V. Dreele, *GSAS: Generalized Structure Analysis System, Los Alamos national Laboratory, Los Alamos, NM.* 1985.

2.43. M. R. Daymond, M. A. M. Bourke, R. B. V. Dreele, B. Clausen and T. Lorentzen, *Use of Reitvelt Refinement for Elastic Macrostrain Determination and for Evaluation of Plastic Strain History from different Spectra.* J. Appl. Phys, 1997. **82**: p. 1554-1562.

2.44. C. G. Windsor and T. Izuyama, *The Effects of Crystalline anisotropy on the Elastic Response of Materials*, in *Measurement of Residual and Applied stress Using Neutron Diffraction*, Hutchings, M. T. and Krawitz, A. D., Editors. 1992, Kluwer Academic Publishers.

2.45. M.T. Hutchings. *Neutron Diffraction Measurement of Residual Stress Fields: Overview and Points for Discussions.* in *Proceedings of the NATO Advanced Research Workshop on Measurement of Residual and Applied Stress Using Neutron Diffraction.* 1991. Oxford, Uk: Kluwer Academic Publishers.

2.46. A. Reuss, *Calculation of Flow Limits of Mixed Crystals on Basis of Plasticity of Single Crystal.* Z. Angew. Math. Mech, 1929. **9**: p. 49-58.

2.47. W. Voigt, *Lehrbuch der Kristall Physik, Teubner, Leipzig.* 1928.

2.48. E. Kroner, *Berechnung der Elastischen Konstanten des Vilkristalls aus Den konstanten des Einkrystalls.* Z. Phys, 1958. **151**: p. 504-518.

2.49. T. Leffers and T. Lorentzen. *The Plastic Regime, Including Anisotropy Effects.* in *Proceedings of the NATO Advanced Research Workshop on Measurement of Residual and Applied Stress Using Neutron Diffraction.* 1991. Oxford, UK: Kluwer Academic Publishers.

2.50. R. Hill, *Continum Micromechancs of Elastoplastic Polycrystals.* J. Mech. Phys. Solids, 1965. **13**: p. 89-101.

2.51. R. Hill, *A Self-Consistent Mechanics of Composite Materials.* J. Mech. Phys. Solids, 1965. **13**: p. 213-222.

2.52. J. W. Hutchingson, *Elastic-Plastic Behaviourof Polycrystalline Metals and Composites.* Proc. R. Soc, 1970. **A 319**: p. 247-272.

2.53. B. Clausen and T. Lorentzen, *A Self-Consistent Model for Polycrystal Deformation: Description and Implementation, Riso National Laboratory, Report R-970(EN), Roskilde, Denmark, 1997.*

2.54. B. Clausen, *Charecterisation of Polycrystal Deformation by Numerical Modelling and Neutron Diffraction Measurements*, in *Technical University of Denmark, Riso national Laboratory*. 1997.

2.55. *European Synchrotron Radiation Facility*: Grenoble, France,Highlights 95-96,2000, available at : www.esrf.fr , accessed on 9th Sept.2004.

2.56. C. Rickel, *The Use of Synchrotron Radiation for Materials Research*, in *Analysis of Residual Stress by Diffraction by Using Neutron and Synchrotron Radiation*, Fitzpatrick, M. E. and Lodini, A., Editors. 2003, Taylor and Francis: London. p. 29-44.

2.57. C. Kunz. *Properties of Synchrotron Radiation-Techniques and Applications.* in *Synchrotron Radiation-Techniques and Applications*. 1979: Springer Verlag: Berlin.

2.58. H. Winick. *Properties of Synchrotron radiation.* in *Synchrotron Radiation Research*. 1980: Plenum Press : New York.

2.59. P. J. Withers and P. J. Webster, *Neutron and Synchrotron X-Ray Strain Scanning*. Strain, 2001. **37**(1): p. 9-33.

2.60. P. J. Withers, *Use of Synchrotron X-ray Radiation for Stress Measurement*, in *Analysis of Residual Stress by Diffraction by Using Neutron and Synchrotron Radiation*, Fitzpatrick, M. E. and Lodini, A., Editors. 2003, Taylor and Francis: London. p. 170-188

2.61. P. J. Webster, G. Mills, X. D. Wang, W. P. Kang and T. M. Holden, *Impediments to Efficient Through -Surface strain Scanning*. J. Neutron Research, 1996(3): p. 223-240.

2.62. A. Steuwer, J. R. Santisteban, M. Turski, P. J. Withers, and T. Buslaps, *High-resolution Strain Mapping in Bulk Samples Using Full-profile Analysis of Energy-dispersive Synchrotron X-ray Diffraction.* Journal of Applied Crystallography, 2004. **37**: p. 883-889.

2.63. C. W. C. Kaye and T. H. Laby, *Tables of Physical and Chemical Constants, 16th ed, Longman Scientific and Technical, Essex, 1995.*

2.64. P. J. Withers, Depth Capabilities of Neutron and Synchrotron Diffraction Strain Measurement Instruments .I. The Maximum Feasible Path Length, Applied Crystallography, 2004, **37**: p.596-606

2.65. M. Turski, *Private Communication*. 2006: The Open University, Milton keynes.

Chapter 3

The effect of residual stress on the material performance

This chapter consists of two parts; the first part reviews the fundamental concept of fatigue crack growth, crack closure mechanisms and the effect of residual stress on fatigue crack growth; and the second part discusses the different aspects of the development of welding residual stress which is followed by a review of residual stress distribution in different alloys joined with different welding techniques.

3.1 Effect of residual stress on fatigue crack growth

3.1.1 Fatigue crack growth phenomenon

Fatigue crack growth can be defined as the propagation of a crack under the condition of dynamic or fluctuating loading. The fatigue life of a component can be divided into three different stages: (a) crack initiation stage, when a crack is initiated from a defect or a region of high stress concentration; (b) crack growth stage, where the crack grows in incremental steps with each stress cycle; and finally (c) fracture or final failure occurs very rapidly when the crack reaches a critical value. In practice, the fatigue life of a component, which is often referred to as the number of cycles to failure (N_f), is estimated by the summation of the number of cycles for crack initiation (N_i) and the number of cycles for the crack propagation (N_p); that is:

$$N_f = N_i + N_p \tag{3.1}$$

The contribution of final failure is normally ignored in the above relation as it occurs very fast. In the case of high cycle fatigue (low stress), a large portion of fatigue life is consumed during the crack initiation stage. In the case of low cycle fatigue (high stress), crack initiation takes place relatively quickly and the fatigue crack propagation consumes most of the fatigue life [3.1].

In practice, crack growth rate is controlled by a parameter called the stress intensity factor range, ΔK , which can be described by [3.1] :

$$\Delta K = K_{max} - K_{min} \tag{3.2}$$

Where K_{max} and K_{min} are maximum and minimum stress intensity factor at the crack tip in a constant amplitude fatigue cycle and will be defined in next section.

3.1.2 Stresses at the crack tip

Once a crack is initiated, the fatigue crack growth events will be governed by the local crack tip stresses. Thus, it is important to understand the relation between the remotely applied stress and the local crack tip stress and the events that are taking place at the crack tip. The crack tip stress field is described by a parameter termed the stress intensity factor (K). The stress intensity factor describes the local stress distribution in front of a crack tip and relates the local crack tip stresses as a function of applied stress. Depending upon the mode of deformation (mode-I, mode-II and mode-III) (figure 3.1), stress intensity factor values are referred to K_I , K_{II} and K_{III} . The current discussion will be concentrated on crack tip stress events under mode I

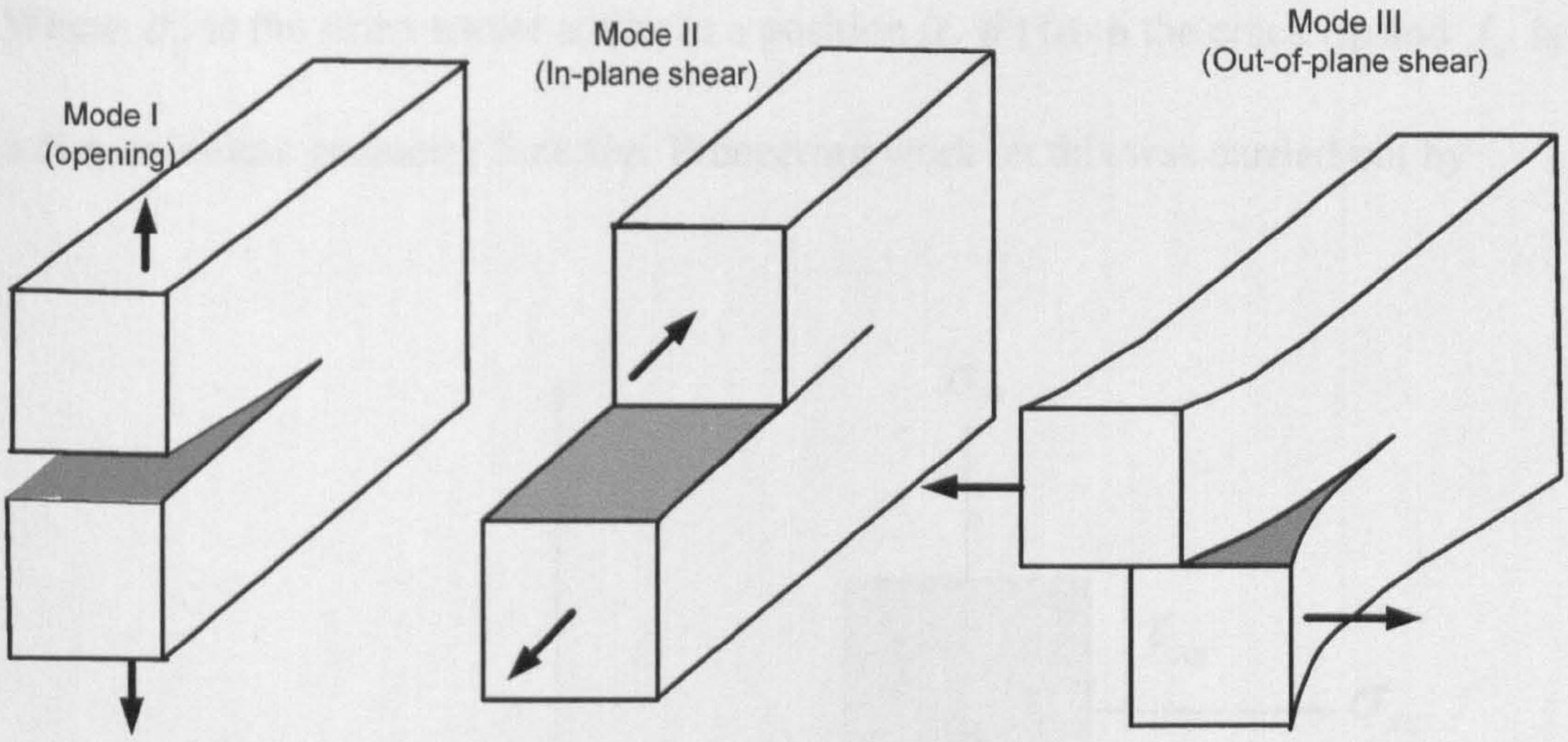

Figure 3.1: Three basic modes of loading that can be applied to a crack.

loading, where load is applied to the direction perpendicular to the crack surface, as majority of the crack occurs under mode-I loading. According to the LEFM (linear elastic fracture mechanics) approach, the stress intensity factor in front of a crack tip in mode-I loading is defined by the following equation:

$$K_I = \beta(a/W)\sigma\sqrt{\pi a} \tag{3.3}$$

Where σ is the applied stress, a is the crack length, W is the width of the specimen and $\beta(a/W)$ is function of specimen and crack geometry. The crack tip stresses can be calculated using the following equation:

$$\sigma_{ij}(r,\theta) = \frac{K_I}{\sqrt{2\pi r}} f_{ij}(\theta) - - - + - - - + - - - + - - - + - - - \tag{3.4}$$

Where σ_{ij} is the stress tensor acting at a position (r, θ) from the crack tip and f_{ij} is a dimensionless geometry function. Pioneering work on this was carried out by

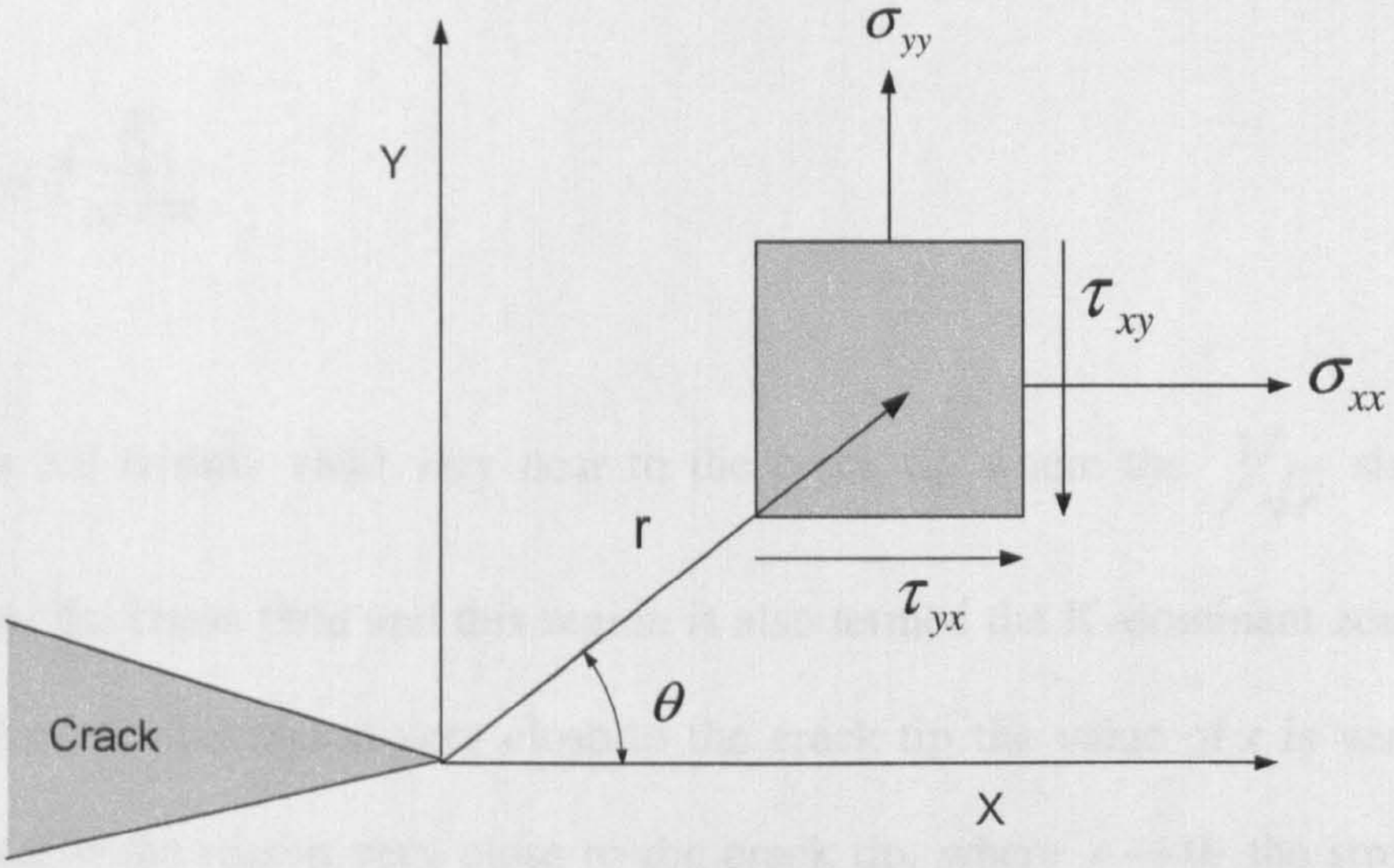

Figure 3.2: Definition of co-ordinate axis of crack tip stress in an infinite body. The z axis is perpendicular to the plane of the diagram.

Westergaard [3.2], Irwin [3.3], Sneddon [3.4] and Williams [3.5] and many closed form solutions have since been derived. The complete form of stress in front of a crack tip at a distance (r, θ) under mode-I loading is given by the following equations:

$$\sigma_{xx} = \frac{K_I}{\sqrt{2\pi r}} \cos\left(\frac{\theta}{2}\right)\left[1 - \sin\left(\frac{\theta}{2}\right)\sin\left(\frac{3\theta}{2}\right)\right] \tag{3.5}$$

$$\sigma_{yy} = \frac{K_I}{\sqrt{2\pi r}} \cos\left(\frac{\theta}{2}\right)\left[1 + \sin\left(\frac{\theta}{2}\right)\sin\left(\frac{3\theta}{2}\right)\right] \tag{3.6}$$

$$\sigma_{zz} = \begin{cases} 0 & \text{plane stress} \\ \nu(\sigma_{xx} + \sigma_{yy}), & \text{plane strain} \end{cases} \tag{3.7}$$

$$\tau_{xy} = \frac{K_I}{\sqrt{2\pi r}} \cos\left(\frac{\theta}{2}\right)\sin\left(\frac{\theta}{2}\right)\cos\left(\frac{3\theta}{2}\right) \tag{3.8}$$

For the case of, $\theta = 0$ (at the crack plane), the shear stress, τ_{xy}, is zero. At the crack plane ($\theta = 0$), the stress value can be calculated to be:

$$\sigma_{xx} = \sigma_{yy} = \frac{K_I}{\sqrt{2\pi r}} \tag{3.9}$$

Equation 3.9 is only valid very near to the crack tip where the $1/\sqrt{r}$ singularity dominates the stress field and this region is also termed the K–dominant zone or 'K-field'. Now, in the region very close to the crack tip the value of r is very small. Therefore, in the region very close to the crack tip, where $r \to 0$, the stress value becomes infinity (from equation 3.9). But, practically, this is unrealistic, as when the stress goes beyond the yield stress, the material yields and plastic deformation takes place in a small region very near to the crack tip, which is known as the plastic zone. The thickness of this plastic zone can be estimated using a plane stress and plane strain assumption, with the condition that all the material subjected to stress more than the yield stress (σ_{YS}) will be plastically deformed, under the consideration of linear elastic fracture mechanics. In case of plane stress condition ($\sigma_{zz} = 0$) material will yield when $\sigma_{yy} = \sigma_{YS}$ of the material, as according to Tresca criteria, yielding begins when the difference between the maximum and minimum principal stresses is equal to the yield stress. The plane stress plastic zone size, r_p, can be calculated using the following equation:

$$r_p = \frac{1}{2\pi}\left(\frac{K_I}{\sigma_{YS}}\right)^2 \tag{3.10}$$

However, in reality the plastic zone size is found to be twice the value calculated using the equation 3.10. The reason behind this is the redistribution of that portion of the stress field that exceeds σ_{ys}, which effectively enlarges the size of the

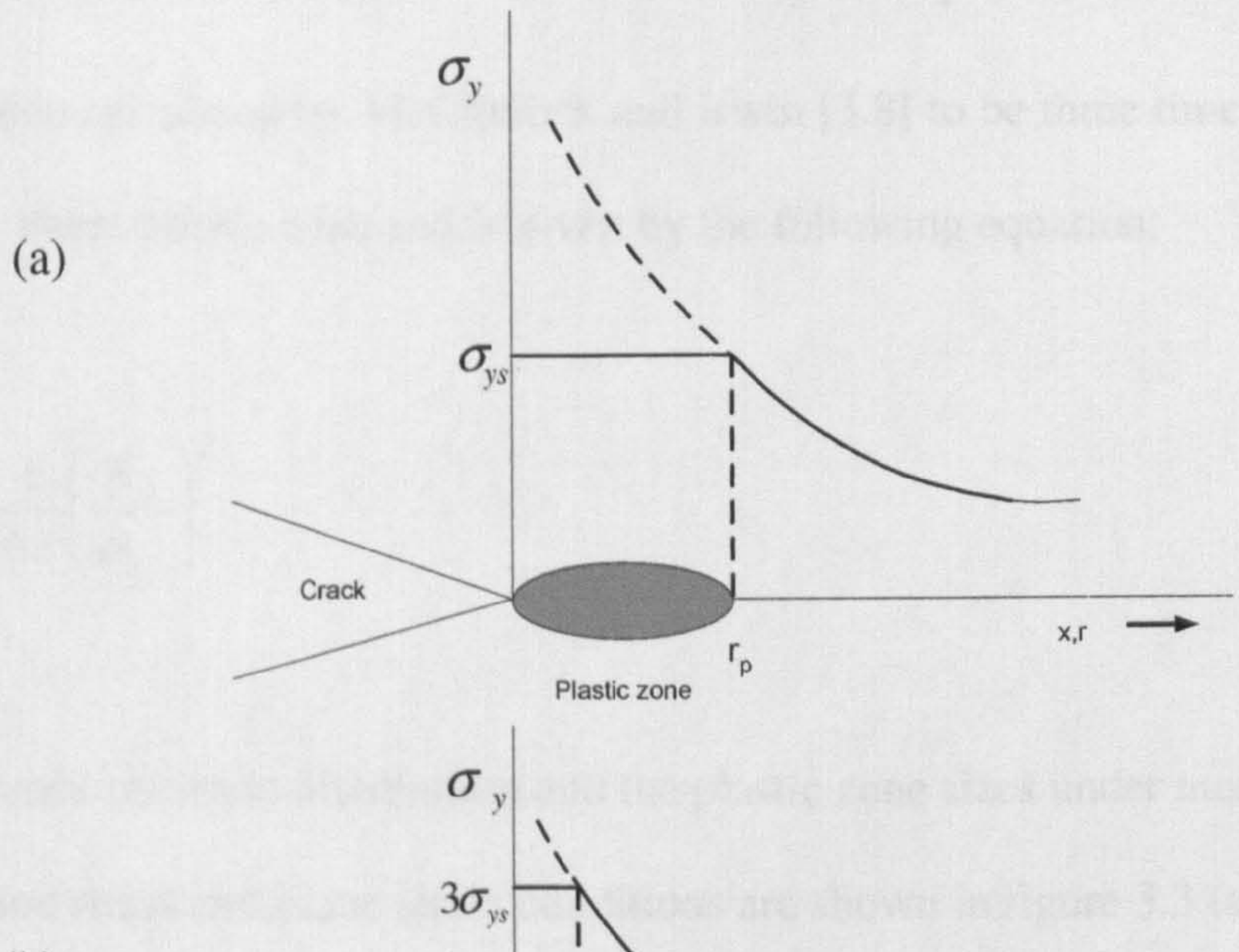

Figure 3.3: Crack tip stress distribution in (a) plane strain and (b) plane stress condition.

plastic zone [3.6]. Taking this stress redistribution into account, the plastic zone size has been modified by Irwin [3.7] using a force balance equilibrium condition and was calculated to be :

$$r_p = 2\left(\frac{1}{2\pi}\left(\frac{K_I}{\sigma_{YS}}\right)^2\right) = \frac{1}{\pi}\left(\frac{K_I}{\sigma_{YS}}\right)^2 \tag{3.11}$$

In the case of plane strain, $\sigma_{zz} \neq 0$, the contraction in the thickness direction is restricted by the thicker material in the normal direction. Subsequently, using the Tresca yield criterion, it is estimated that in the plane strain condition plastic deformation will take place when $\sigma_{yy} = 3\sigma_{YS}$. The plastic zone size in plane strain has been calculated by McClintock and Irwin [3.8] to be three times smaller than the plane stress plastic zone and is given by the following equation:

$$r_p = \frac{1}{6\pi}\left(\frac{K_I}{\sigma_{YS}}\right)^2 \tag{3.12}$$

The crack tip stress distribution and the plastic zone sizes under monotonic loading in plane stress and plane strain conditions are shown in figure 3.3 (a and b).

3.1.3 General fatigue crack growth behaviour of metallic material

The rate of fatigue crack growth in a material is described by increase in crack length per load cycle, da/dN, and the fatigue crack growth behaviour in a metal is typically represented as a log da/dN versus $\log \Delta K$ plot, which is represented schematically in figure 3.4. The sigmoidal curve is usually subdivided into three distinct regions, with a linear portion in the middle (region II) while the beginning (region I) and end

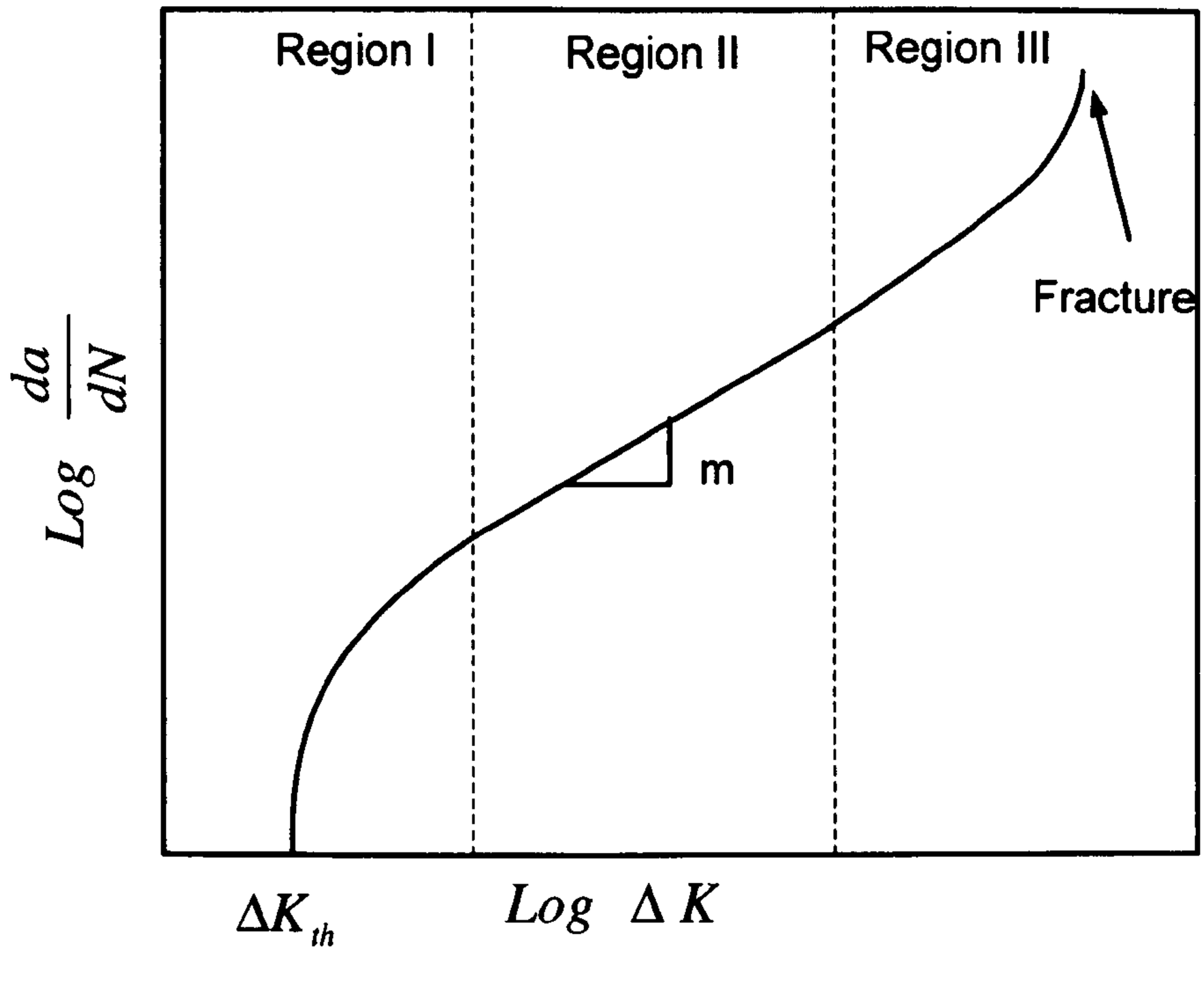

Figure 3.4: Stages of fatigue crack growth (by Ritchie [3.9]).

portion (region III) of the curve deviates from the linear trend. The first portion of the curve demonstrates very slow crack growth and there is no growth below a certain threshold ΔK (ΔK_{th}) value. The crack growth in this region is influenced by microstructure and environmental effects [3.10]. When plastic zone size in front of the crack tip is smaller than the grain size, the crack growth proceeds by a (stage I) single shear decohesion mechanism associated with mode I and mode II displacements [3.11].

The transition from region I to region II takes place when the plastic zone size in front of crack tip becomes larger than the grain size [3.12, 313]. The crack growth in this region is not a strong function of microstructure, which is mainly due to the fact that in this region fatigue growth is controlled by cyclic flow properties rather than monotonic tensile properties. Further, crack growth in region II proceeds by successive increments by each loading cycle producing striations on the fracture

surface and follows a straight path, indicating a constant and steady crack growth rate [3.13]. Considerable research has been conducted to predict the crack growth in region II. Paris and Erdogan [3.14] were first to propose a law, widely known as the Paris law, describing region II crack growth, which can be described by the following power law:

$$\frac{da}{dN} = C\Delta K^{m} \tag{3.13}$$

Taking logarithms of the above equation gives,

$$\log\left(\frac{da}{dN}\right) = \log C + m\log\Delta K \tag{3.14}$$

C and m are material constants which can be calculated experimentally. Plotting the experimental values of $\log\left(\frac{da}{dN}\right)$ vs $\log\Delta K$, results in a similar diagram as shown in figure 3.4. For most engineering materials the value of m, often referred as Paris slope, lies between 2 to 4. Although, the Paris Law (equation 3.13) can describe the crack growth relationship in region II, it is unable to describe the crack growth behaviour in region I and region III. Further, this law does not take account of the effect of R ratio (ratio of minimum and maximum stress intensity factor). Later on, Forman [3.15] proposed a relationship which can describe region II and region III crack growth behaviour, which also takes the effect of R ratio into account. This relation can be described by the following equation:

$$\frac{da}{dN} = \frac{C\Delta K^m}{(1-R)K_c - \Delta K} \tag{3.15}$$

Where K_c is the fracture toughness of the material.

In region III, a non linear and accelerated fatigue crack growth is observed which eventually leads to failure of the component when K_{max} reaches the fracture toughness (K_c) of the material.

3.1.4 Effect of crack closure on fatigue crack growth

Crack closure is a mechanism by which both the crack faces come into contact as a result of which fatigue crack growth rate reduces as the effective stress intensity range (ΔK) is reduced. This effect was first discovered by Elber [3.15], when he found that crack faces can still be closed whilst under a low level of applied tensile load. According to Elber, when a cyclic load is applied to a specimen, the crack faces only open when the value of stress intensity factor reaches a value K_{op} , which is the

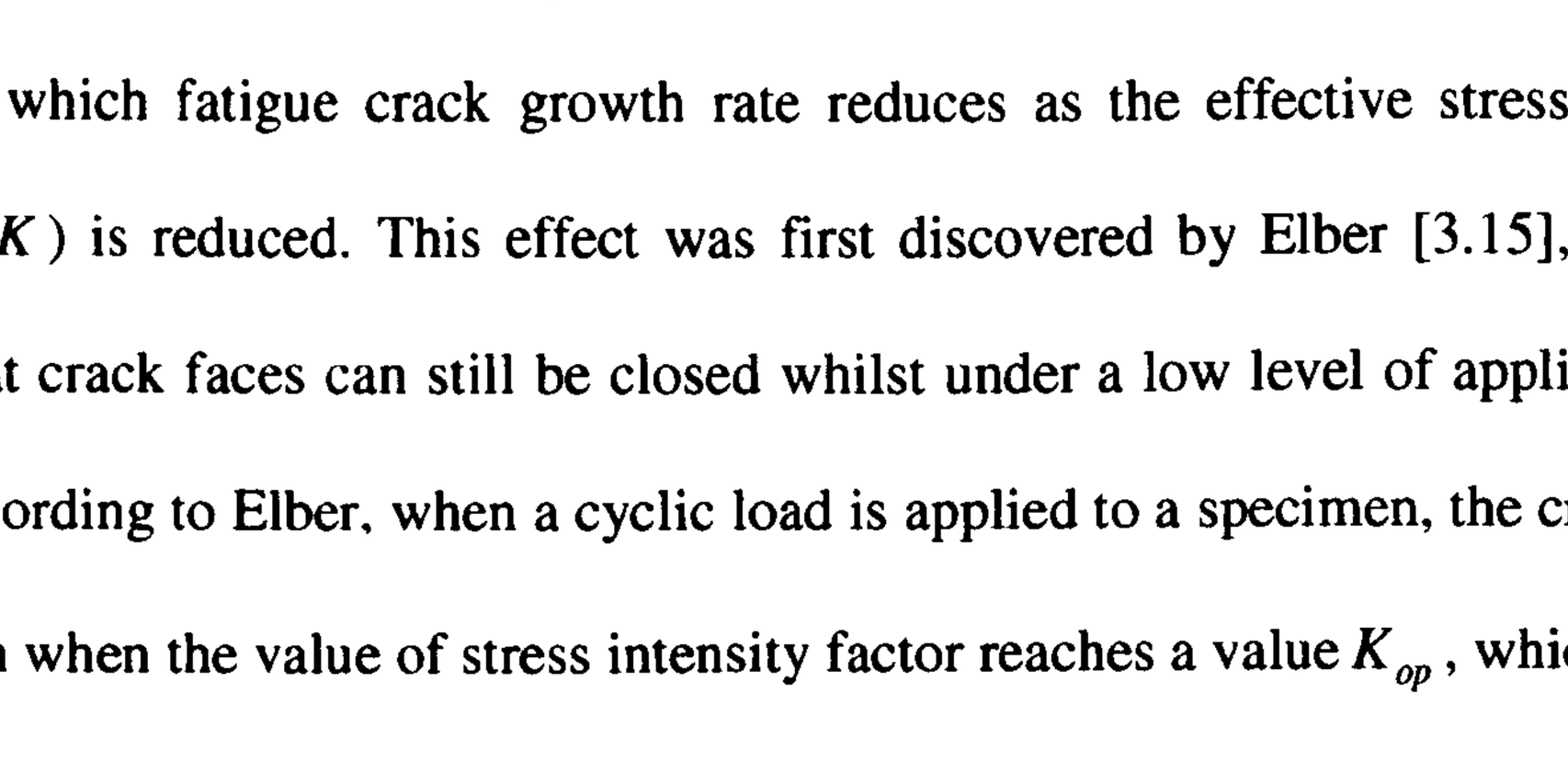

Figure 3.5: Definition of effective stress intensity range.

stress intensity factor at which the crack opens (figure 3.5). Elber assumed that the portion of the load cycle below K_{op} does not contribute to the fatigue crack growth. He also redefined the Paris law by the following equation:

$$\frac{da}{dN} = C\Delta K_{eff}^{m} \tag{3.16}$$

Where $\Delta K_{eff} = K_{\max} - K_{op}$

Since Elber's study, much research has been carried out to study the crack closure effect in different materials and the underlying mechanism associated with it [3.17-3.19]. It is now an established fact that crack closure plays a significant part in fatigue crack growth, however, a lot of research is still undergoing to understand the mechanism of crack closure. The important crack closure mechanisms are reviewed in the following paragraphs.

Plasticity induced closure develops due to the development of compressive residual stresses in the plastic wake [3.16]. During the propagation of the fatigue crack, the monotonic plastic zone created in front of a crack tip when it is loaded. As a result there will be a band of material adjacent to the crack flanks left behind and as a result a region of stretched material is created all along the crack and behind the

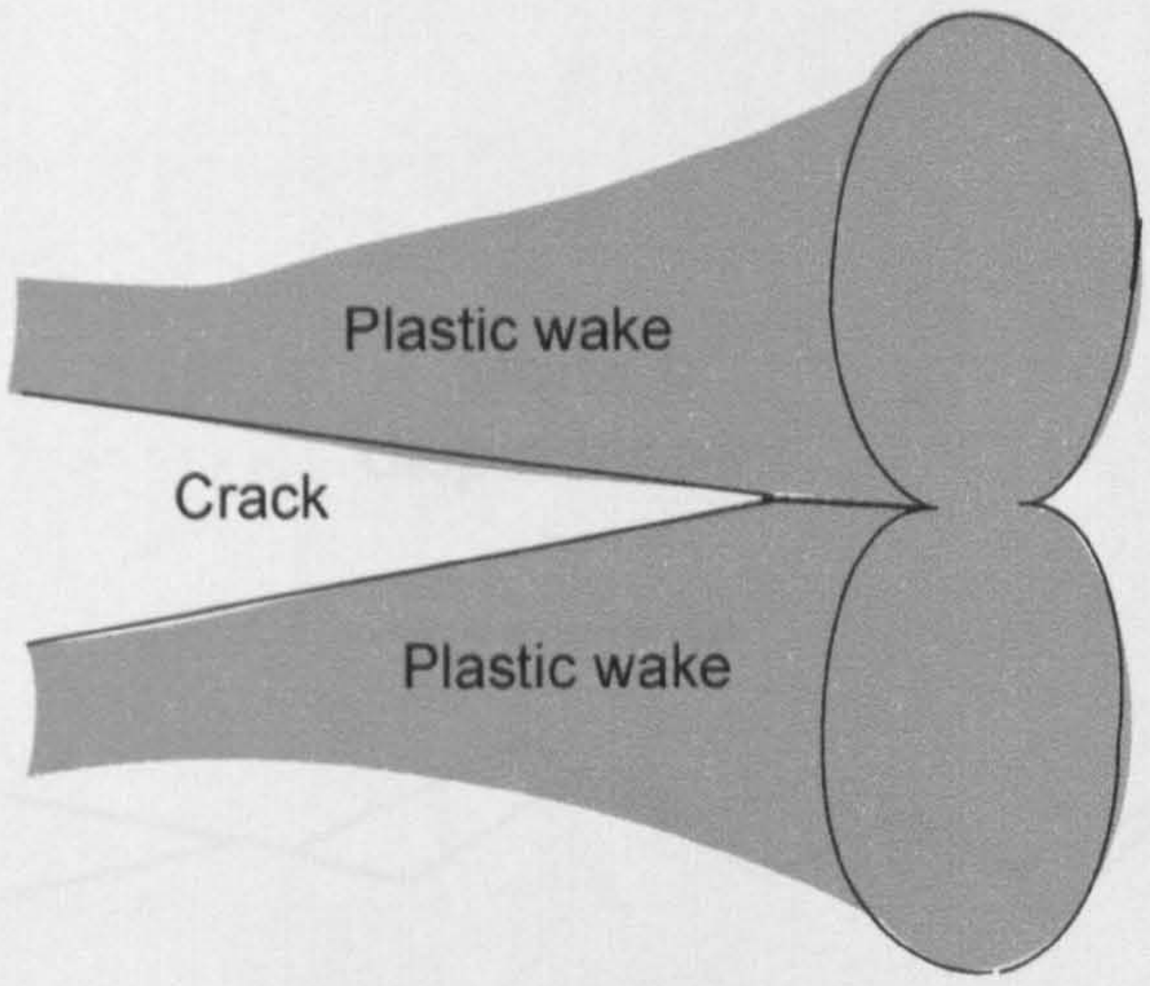

Figure 3.6: Mechanism of plasticity induced crack closure.

crack tip, which is known as a plastic wake. The plastic wake region experiences a compressive force (figure 3.6), which closes the two faces of the crack, by the surrounding elastic material when the component is unloaded or at a lower level of load. Elber's original work on crack closure was attributed to plasticity induced closure. Later, Budiansky and Hutchinson [3.20-3.22] demonstrated the effect of plasticity on crack closure. In recent years much research has been carried out to study the plasticity induced crack closure using finite element analysis [3.23-3.26].

Roughness induced closure is a phenomenon mainly influenced by the microstrutural properties of material [3.27]. A crack growing under mode I loading condition, often deviates from the mode I plane and follows a mode II or mode III path (figure 3.7) due to the deflection of the crack, which occurs due to microstructural heterogeneity [3.28]. As a result of this, a mismatch occurs between the two faces of the crack leading to crack closure. It has been observed that a coarse grained material is likely to produce a higher degree of crack closure which is caused

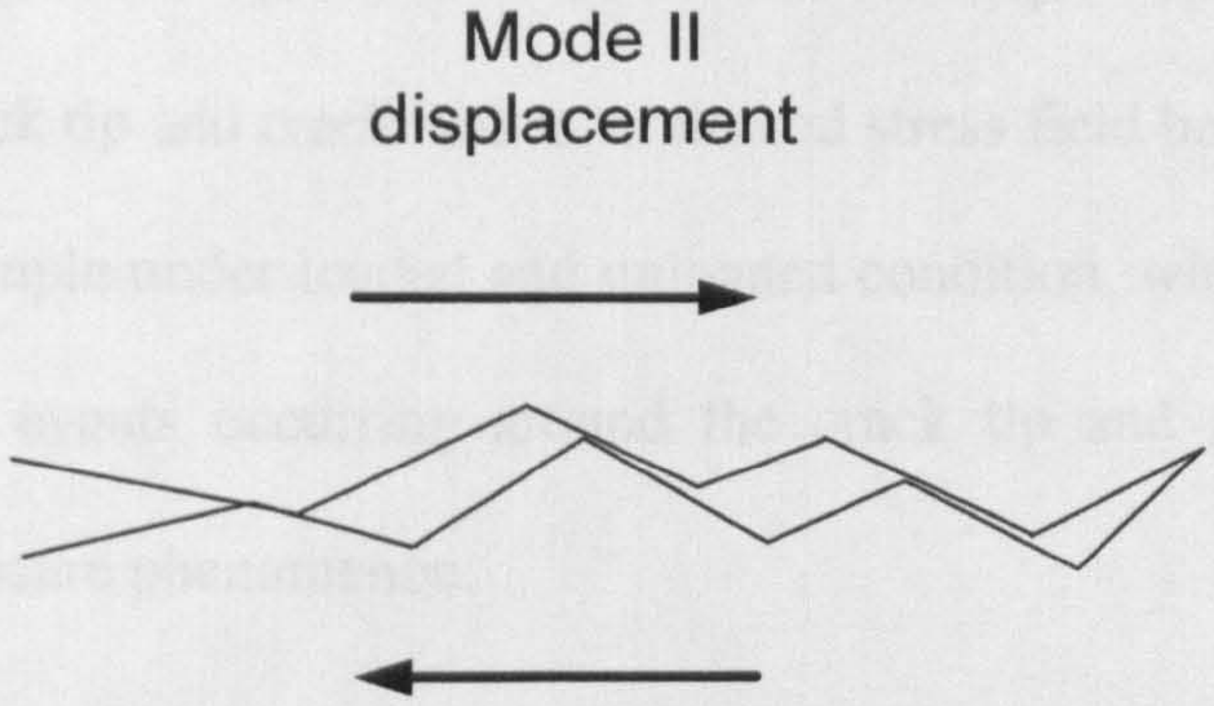

Figure 3.7: Roughness induced crack closure.

by a higher surface roughness [3.27]. One of the important characteristics of roughness induced closure is that unlike the plasticity induced closure the compressive stresses behind the crack occurs at discrete locations [3.29].

Oxide–induced crack closure occurs due to the formation of an oxide layer on the crack surface, particularly when the material is exposed to a corrosive environment. These layers also enhance the effect of already present roughness induced crack closure. This mechanism was first postulated by Ritchie [3.30] and

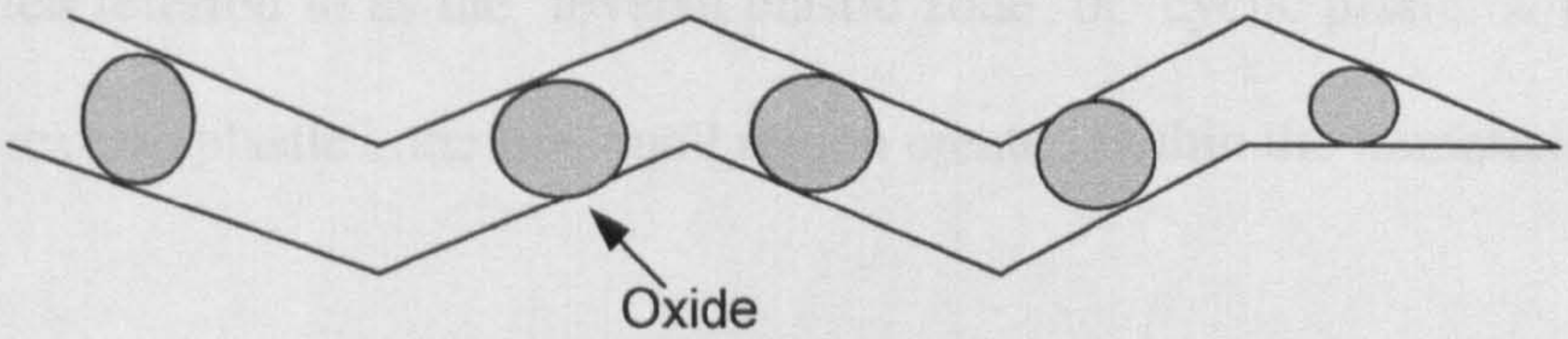

Figure 3.8: Oxide-induced crack-closure.

later further work was carried out by Suresh [3.31, 3.32] on the crack growth rate behaviour in different environments.

In this project, the synchrotron diffraction technique has been employed to understand the crack tip and crack wakes strain and stress field behaviour in fatigued and overloaded sample under loaded and unloaded condition, which would allow us to understand the events occurring around the crack tip and give us some idea regarding crack closure phenomenon.

3.1.5 Crack tip stress field under fatigue loading

When constant amplitude fatigue loading is applied, the monotonic plastic zone created on loading in front of a crack tip experiences a compressive force by the surrounding elastic material when the material is unloaded. This produces a compressive residual stress within the plastic zone at the crack tip, which will eventually yield in compression when the yield stress is reached. Thus, under constant amplitude fatigue loading a small plastic zone is created in front of a crack tip, due to the repeated yielding in tension and compression. This region of plastic zone is often referred to as the 'reverse plastic zone' or 'cyclic plastic zone' (figure 3.9). This reverse plastic zone is a small region created within the monotonic plastic

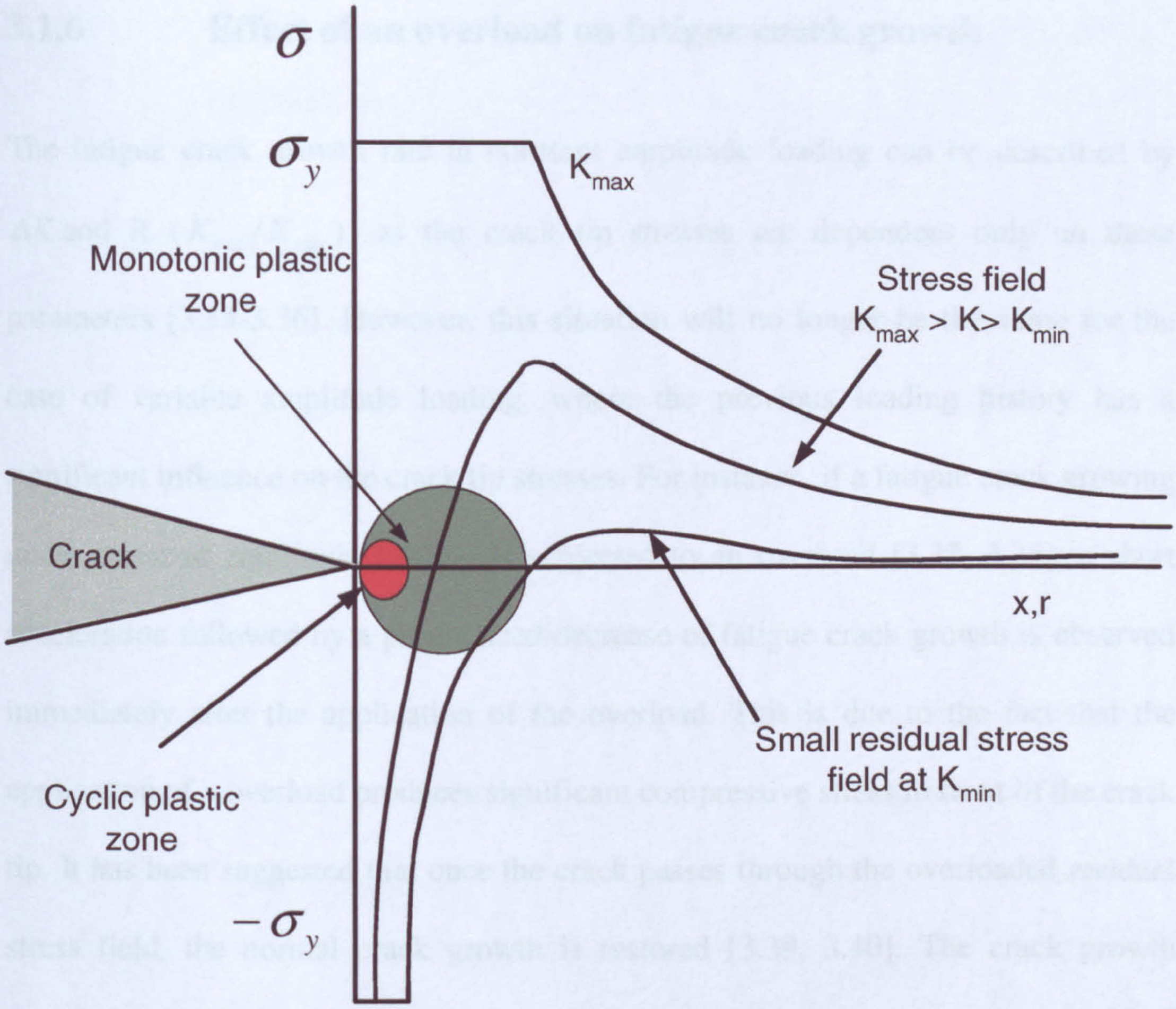

Figure 3.9: Crack tip stress field under fatigue loading condition.

zone and the radius of it has been calculated by Rice [3.33] and is given by the following equation:

$$r_c = \frac{1}{\pi}\left(\frac{\Delta K_I}{2\sigma_{YS}}\right)^2 \tag{3.17}$$

For $K_{\min} = 0$, the cyclic plastic zone is predicted to be four times smaller ($r_c = \frac{r_p}{4}$) than the monotonic plastic zone.

3.1.6 Effect of an overload on fatigue crack growth

The fatigue crack growth rate in constant amplitude loading can be described by ΔK and R (K_{min}/K_{max}), as the crack tip stresses are dependent only on these parameters [3.34-3.36]. However, this situation will no longer be the same for the case of variable amplitude loading, where the previous loading history has a significant influence on the crack tip stresses. For instance, if a fatigue crack growing under constant amplitude loading is subjected to an overload [3.37, 3.38], a short acceleration followed by a pronounced decrease of fatigue crack growth is observed immediately after the application of the overload. This is due to the fact that the application of a overload produces significant compressive stress in front of the crack tip. It has been suggested that once the crack passes through the overloaded residual stress field, the normal crack growth is restored [3.39, 3.40]. The crack growth retardation following an overload is a complex phenomenon, and a lot of research has been carried out to understand the underlying mechanism, however, no consensus has yet been achieved in this regard. A considerable number of models have been constructed using numerical and mathematical approaches to predict the retardation phenomenon [3.41-3.43]. Some models assume that the crack closure is mainly responsible for the retardation phenomenon. On the other hand, other models have been constructed assuming that the crack tip plastic zone size is increased due to the overload, which in turn increases the compressive residual stress when the material is unloaded [3.44]. In this current work an attempt has been made to study the crack tip strain and stress field behaviour in an overloaded sample under the loaded and unloaded condition with the use of synchrotron X-ray diffraction technique (chapter 4).

3.1.7 Measurement of crack tip stress fields using diffraction techniques

Many empirical models have been established to predict the behaviour of crack tip strain and stress fields and fatigue crack growth behaviour under constant amplitude loading. However, in practice, most components or structures experience variable amplitude fatigue loading during most of their fatigue life. The crack tip strain and stress field and the fatigue crack growth phenomenon under variable amplitude loading are complicated and difficult to model without having reliable experimental data. To study this complicated phenomenon, it is important to understand the crack tip strain and stress field under in-situ loading conditions with knowledge of the loading history (prior plastic deformation). Thus, to construct a reliable fatigue life prediction model it is important to be able to measure the local crack- tip strain and stress field under different loading conditions.

The X-ray and neutron diffraction techniques have been widely used to measure strain and stress fields non-destructively and can be used to measure local crack tip strain and stress field in polycrystalline samples. Although neutron diffraction has become very popular due to its excellent penetrability inside materials, use of this technique is limited in this sort of application where very high spatial resolution is required due to the very high strain gradient near the crack tip. In many occasions, the conventional laboratory X-ray diffraction technique has been employed to study crack tip strain and stress fields [3.45-3.47]. But the limitation with this technique is its inability to measure stresses below the surface, which means stresses can only be calculated in a plane stress condition. Therefore, measuring the local crack tip strain and stress field inside a bulk material has always been a challenge for researchers. The recent development of 3rd generation

synchrotron X-ray sources, which provide high penetration together with very good spatial resolution (details of which have been discussed in chapter 2), has opened up the possibility of measuring the crack tip strain and stress field inside the bulk of a polycrystalline sample. In this current project, the synchrotron X-ray diffraction technique has been successfully used to map the strain and stress field ahead of a fatigue crack under in-situ loading condition inside a bulk material which will be discussed in details in chapter 4. Some of the previous work related to this project is reviewed in the following paragraphs.

Allison [3.45] studied the crack tip strain and stress profile under the application of different overloads and applied loads in a compact tension 1045 steel specimen using conventional X-ray diffraction. Measurements were made along the crack plane on the surface of the sample. Allison observed the presence of residual compressive stress in front of the crack tip. He also reported the increase of the extent of this compressive zone with the application of applied overloading.

Wang et al [3.47] carried out FE analysis and X-ray diffraction on the surface of a low-alloy high–strength structural steel to study the residual stress effect on fatigue crack growth under constant amplitude fatigue in mode-I loading condition. They have reported that the compressive stress or the crack closure effect at the surface do not have any influence on the residual stress distribution ahead of the crack tip and thus on the fatigue crack growth.

Ramos et al [3.46] studied the crack tip stress field to investigate the effect of single and multiple overloading. The measurement was carried out on the surface of a low carbon steel CT specimen using the X-ray diffraction technique. The experiment was performed along the crack plane using the beam size of $1mm^2$ area and a surface sampling depth of $10\,\mu m$. The result showed that the compressive

stresses in the vicinity of the crack tip increases with the increase of overload, which slows down the fatigue crack growth resulting in increase of the fatigue life of the component.

James et al [3.48] have studied the crack tip strain and stress field in a fatigue cracked CT-geometry aluminium alloy specimen using synchrotron X-ray diffraction.

More recently, Croft et al [3.49] has studied the strain profile around fatigue cracks in 4140 steel specimen using energy dispersive X-ray diffraction technique. He observed a compressive strain region along the crack wake which was independent of loading condition. Thus, he ruled out the effect of crack face contact interaction in generating the compressive strain and instead suggested that the anisotropic strain in the plastic wake is responsible for this. Further, he studied the crack tip strain field in fatigued, fatigued-overloaded and fatigued-overloaded fatigued condition of the sample. A significant compressive strain at the crack tip of the overloaded sample has also been reported in his work.

3.1.8 Effect of residual stress on fatigue crack growth behaviour

It is a well established fact that the fatigue resistance of a material can be altered due to the presence of residual stress. A lot of research work has been carried out in this regard and plenty of literature are available covering the effect of different kind of residual stresses on the fatigue life in different material systems [3.50-3.52]. Before predicting the fatigue crack growth it is important to know whether the component under consideration is uncracked; in that case the maximum portion of the fatigue life will be taken up by the crack initiation; or cracked, in which case the fatigue life

will be controlled by crack propagation. Thus, delaying crack initiation by deliberate introduction of compressive stress has become common practice and a wide range of work has been carried out by many researchers on the beneficial effects of these compressive stresses [3.53-3.55]. However, as most engineering components contain small cracks or defects, the current discussions will be mostly concentrated on the effect of residual stress on a growing crack.

Generally residual stresses, generated during a manufacturing process or any other heat treatment process, are simply superimposed as a mean stress (σ_m) with the dynamic stresses or static loading.

The effect of residual stress on the fatigue life can be studied using two different approaches; a) applying the principle of superposition of the respective stress intensity factor for the applied stress and the residual stress and b) using a simplified crack closure model.

The superposition principle in the presence of residual stress can be expressed by the following equation:

$$K_{eff} = K_{\max} + K_{res} \tag{3.18}$$

Where K_{res} is the residual stress intensity factor. To understand the effect of residual stress on the fatigue crack growth, the effect of K_{res} on ΔK has to be investigated.

Depending on the nature of the residual stress, ΔK_{eff} can be calculated using the following equations:

$$\left.\begin{aligned} \Delta K_{eff} &= K_{\max} + K_{res} \\ R_{eff} &= 0 \end{aligned}\right\} K_{\min} + K_{res} \le 0 \qquad (3.19)$$

$$\left.\begin{aligned} \Delta K_{eff} &= K_{\max} - K_{\min} = \Delta K \\ R_{eff} &= \frac{K_{\min} + K_{res}}{K_{\max} + K_{res}} \end{aligned}\right\} K_{\min} + K_{res} > 0 \qquad (3.20)$$

Figure 3.10 (a and b) shows the effect of tensile and compressive residual stress on ΔK. It is clearly evident that ΔK_{eff} does not get affected and is equal to ΔK_{app}, when the residual stress is tensile. However, in this case the value of R_{eff} is changed. The fatigue crack growth in this situation is predicted by Forman's equation (equation 3.7).

On the other hand, if the residual stress is compressive enough ($R = 0$) so that $K_{\min} + K_{res} \le 0$, the crack remains closed for some part of the fatigue cycle and the fatigue crack growth rate is reduced. In this case, fatigue crack growth can be predicted by the Paris Law, which does not account for the R effect. Furthermore, if the compressive stress is high enough so that, $\Delta K_{eff} \le \Delta K_{th}$, the fatigue crack growth is completely retarded.

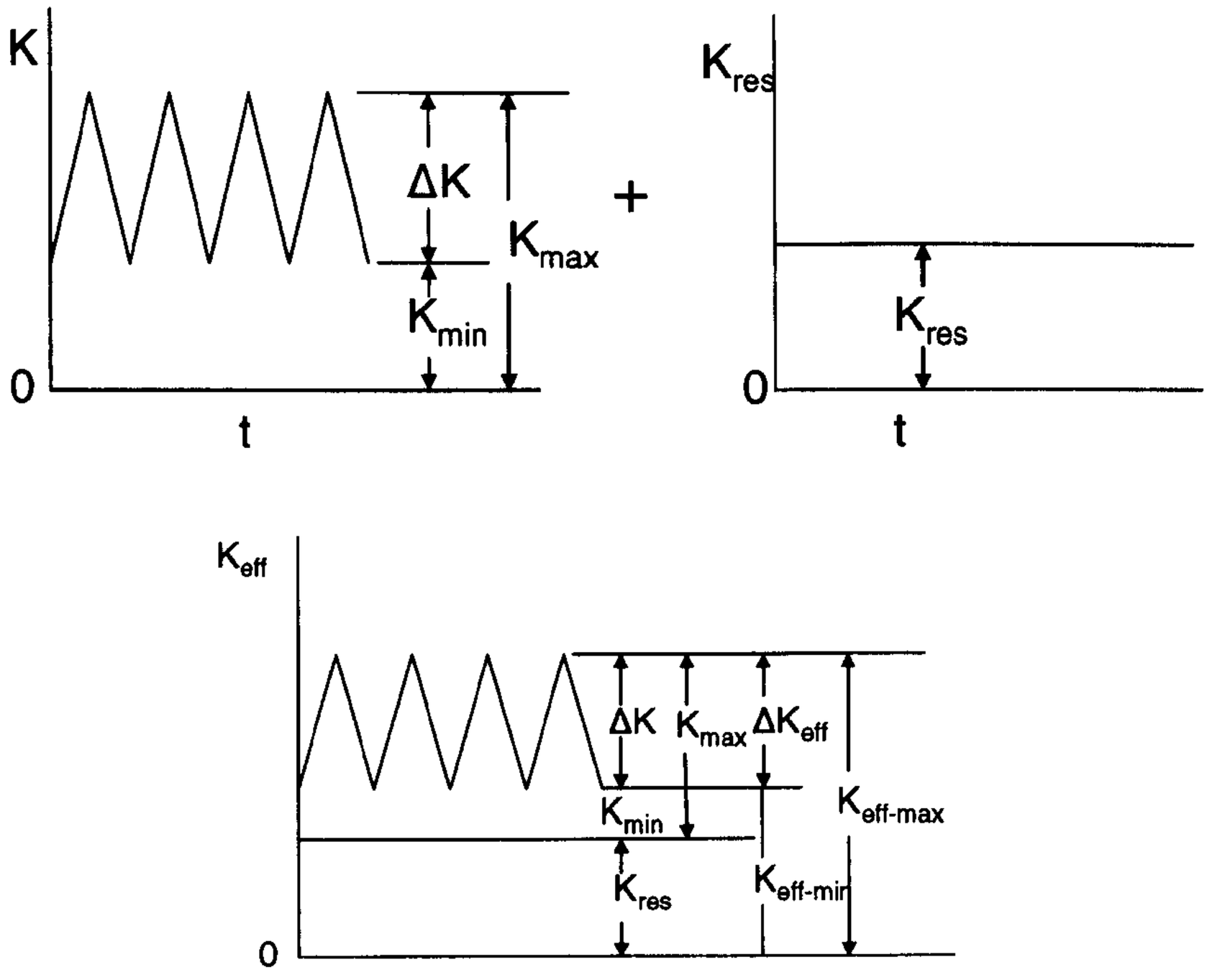

(a) Tensile K_{res}

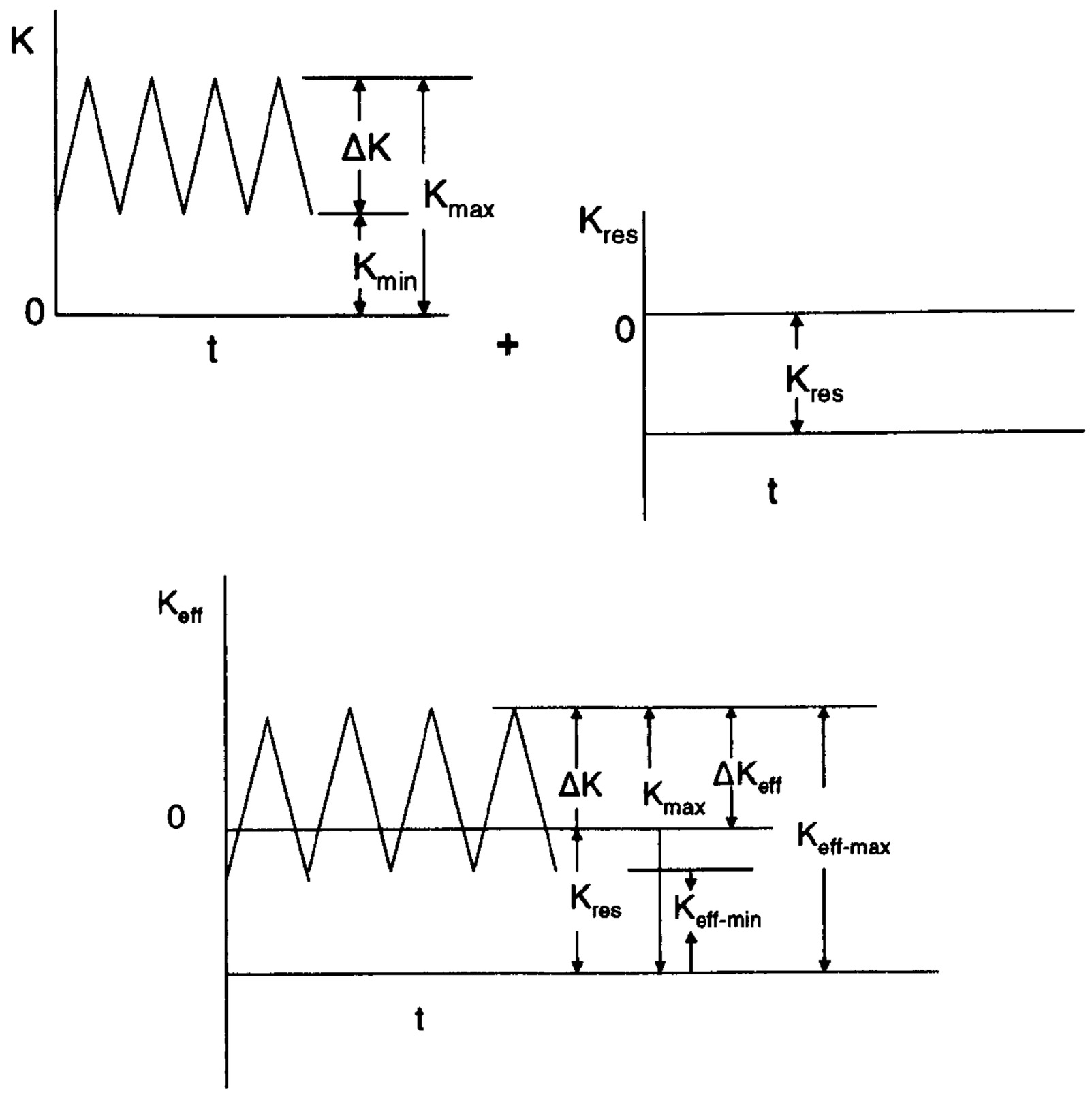

(b) Compressive K_{res}

Figure 3.10: Effective stress intensity factor for applied loading in case of (a) tensile K_{res} and (b) compressive K_{res}.

Thus, to be able to predict the accurate fatigue life, it is imperative to be able to calculate K_{res} values properly. However, the success of these methods depends on the accuracy of the determination of the exact residual stress field accompanying crack growth. It has been observed that a crack growing through compressive stress shows an expected retardation in growth rate, but it does not show the expected crack growth acceleration when it reaches the area of material where tensile residual stress is present [3.52]. This phenomenon can only be attributed to the relaxation and redistribution of residual stresses due to the fatigue crack growth, some of which is associated with crack tip plasticity. Therefore, in a case where a fatigue crack has already begun to grow, an analysis based on the elastic residual stress distribution present in the component prior to the fatigue crack growth will almost certainly lead to a non-conservative life approach [3.56]. Further, the relaxation of micro and macro residual stress field has been reported in stress controlled fatigue specimen [3.57], which indicates about the high possibility of residual stress redistribution in a long cracked specimen due to the relaxation of stress in front of crack tip. In this current work, investigation has been carried out to study the residual stress redistribution phenomenon due to the growth of a fatigue crack in a welded Al-alloy specimen.

3.2 Weld residual stresses

3.2.1 Generation of welding residual stress

Residual stresses in a weld mainly arise due to the inhomogeneous temperature field between the heated zone and the colder zone of the material [3.58]. During the welding process, the area close to the weld is heated up rapidly which in turn causes

a volume expansion of the heated material. This volume expansion is restricted by the surrounding colder material giving rise to an elastic thermal stress. Consequently, the thermal stresses may reach the plastic limit and the material yields locally. Subsequently, contraction of the heated weld metal takes place during solidification, which is hindered by the surrounding colder material. This results in a tensile residual stress near the weld region and a counterbalancing compressive stress in the surrounding region. However, the welding residual stress pattern does not remain the same in those cases where during cooling phase transformation for example, transformation of austenite into martensite, bainite or pearlite takes place [3.59, 3.60]. These phase transformations are associated with a volume expansion which in turn is hindered by the surrounding materials, producing a compressive residual stress. Thus, during phase transformation the compressive stress generated during hindered volume expansion are superimposed on the tensile stresses developed as a result of hindered shrinkage. A lot of work has been carried out on the phase transformation compressive stresses associated with austenite to bainite or martensitic transformation and can be found in the literature [3.61, 3.62]. Typical welding residual stress distribution pattern in different alloys is presented in figure 3.11. It is evident from the figure 3.11, that mild steel and low alloy steel follows the general trends with tensile stress in the weld centre which is balanced by compressive stresses on both sides of the weld.

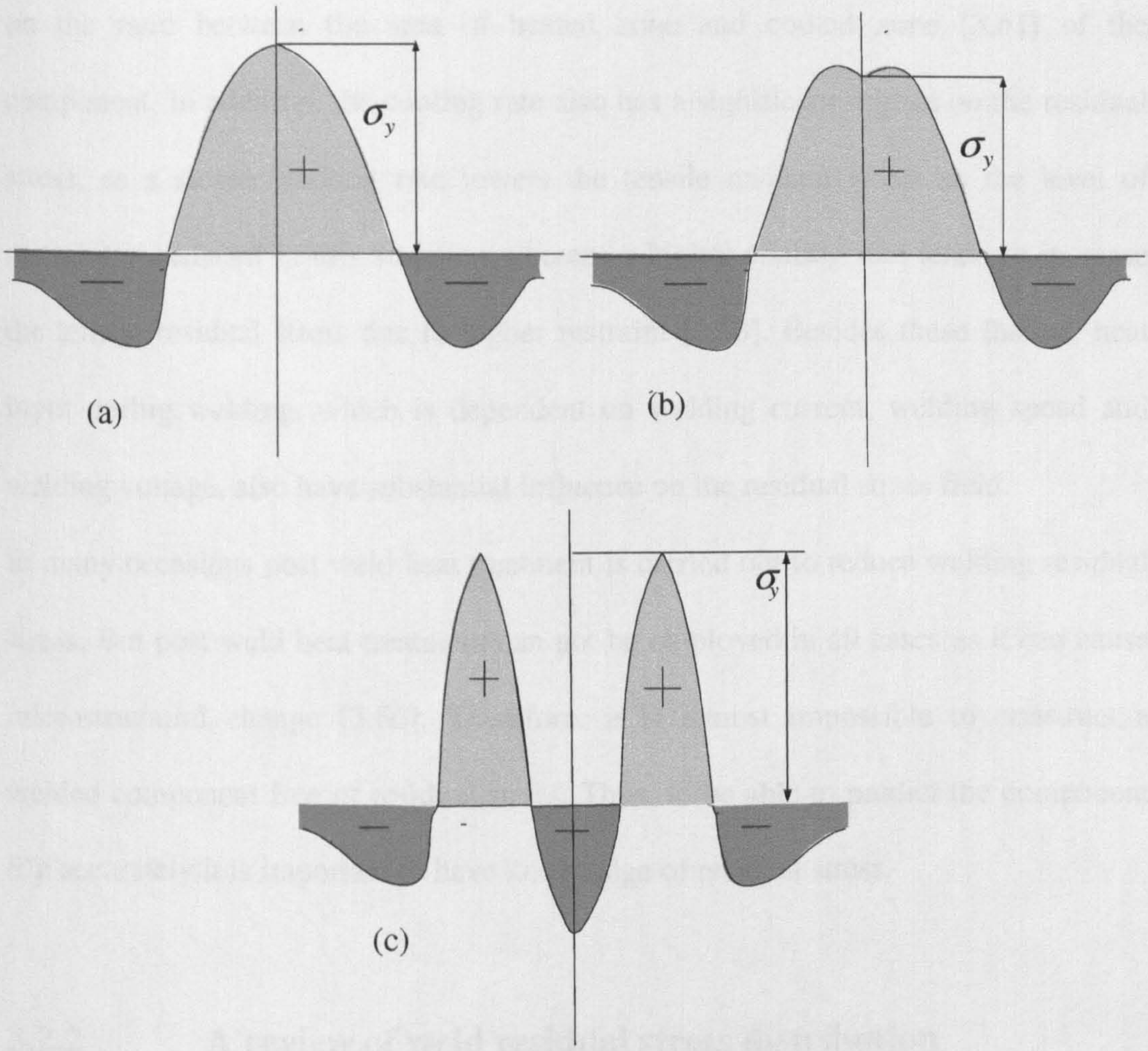

Figure 3.11: Typical weld-longitudinal residual stress profile in (a) mild steel, (b) aluminium alloys and (c) high alloy structural steel with ferritic filler metal.

Aluminium alloys show almost the similar kind of distribution except the fact that a narrow depression region is observed in the weld centre [3.63, 3.64]. In the case of high alloy steel a compressive region is observed in the weld centre, which is effectively the effect of phase transformation stress.

The nature and magnitude of the residual stress is mainly dependent on the level of restraint [3.65] of the weld metal together with the transformation temperature [3.58]. Initially, it was reported that the level of the restraint was dependent on the size of the weld pool but later on further investigation has proved the previous assumption wrong and suggested that the grade of restraint is dependent

on the ratio between the area of heated zone and cooled zone [3.61] of the component. In addition, the cooling rate also has a significant impact on the residual stress, as a slower cooling rate lowers the tensile residual stress as the level of restraint is reduced in this situation whereas a higher cooling rate tends to increase the tensile residual stress due to higher restraint [3.58]. Besides these factors, heat input during welding, which is dependent on welding current, welding speed and welding voltage, also have substantial influence on the residual stress field.

In many occasions post weld heat treatment is carried out to reduce welding residual stress. But post weld heat treatment can not be employed in all cases as it can cause microstructural change [3.66]. Therefore, it is almost impossible to construct a welded component free of residual stress. Thus, to be able to predict the component life accurately it is important to have knowledge of residual stress.

3.2.2 A review of weld residual stress distribution

It is a well-established fact that residual stress generated during welding can increase the stress corrosion cracking, brittle fracture and cold cracking of a component [3.61]. It has a detrimental effect on the fatigue strength of a material as well as on the fracture toughness of welded steels. Numerous researches have been carried out in previous years and many investigations are in progress to study the weld residual stress distribution in different alloys and the effect of theses stresses on the fatigue life of the component. Some of the previous work is reviewed in the following paragraph.

Acceleration of fatigue crack growth due to the presence of tensile residual stress in a 316H austenitic stainless steel has been reported by Spindler and Cotton

[3.67]. Work by Itatani et al [3.68] has demonstrated that the crack growth rate in the HAZ of a 304 stainless steel is reduced due to the presence of compressive residual stress. In small diameter socket welded pipe joints, the compressive stress is reported near the toe while tensile stress is observed near the root, prompting the crack initiation from the root [3.69]. In many applications, post weld heat treatment is carried out to reduce the residual stresses. Complete removal of residual stresses by heat treatment has been reported in a work by Takashasi et al [3.70].

To quantify the effect of these weld residual stresses on the resistance to failure of components, it is important to know the residual stress distribution and their magnitude accurately. Although many techniques, such as hole drilling, slicing, X-ray diffraction, have been available for a long time to measure these stresses, in the last two decades the neutron diffraction technique has become most popular to investigate weld residual stress due to its ability to measure stresses non-destructively inside the bulk material. Numerous investigations have been carried out using neutron diffraction to measure the weld stresses in pipes [3.71-3.73], rails [3.74] and welded blocks [3.75-3.78]. Measurement has also been carried out in welded component of wide range of materials, such as aluminium alloys [3.79, 3.80], austenitic [3.75, 3.76] steel, ferritic steel [3.81] and nickel base super alloys [3.82, 3.83].

The general trend of welding residual stress distribution has long been known. Generally the stresses in the longitudinal direction, that is the stress parallel to the weld direction, are found to be strongly tensile near the weld and HAZ region while counterbalancing compressive stresses are observed away from the HAZ and is reported in many literature [3.75-3.77, 3.81]. The strain in the transverse direction, which is the direction perpendicular to the weld, follows the same trend with smaller

amplitude while the normal direction strains are low in magnitude with the reverse profile. In the case of multi-pass welds, the stress distribution changes with each pass. A significant increase of longitudinal tensile stress after the second weld pass in a ferritic steel weld has been reported by Prask et al [3.84]. Further, difference in residual stress distribution with varying thickness has been reported by Spooner et al [3.75, 3.85], where they observed relatively higher tensile stresses in the top and the bottom than that in the mid-thickness of a single V butt welded stainless steel plate.

3.2.3 Residual stresses in repair welds

In recent years, a lot of effort is given to study the residual stress distribution in repair welds and its effect on the service life of the component. Repair welds are generally introduced into a structure to rectify any damage or defects found in the component [3.86] following welding. There can be various kind of repair weld ranging from small localized welding to welding of significant portion of the structure. These repair welds are associated with a triaxial residual stress field which if not accounted for can lead to premature failure of the component. In a recent survey, carried out by EPRI [3.87], it has been revealed that 40 % of all repairs related to steam chests, piping and headers results in subsequent cracking and more interestingly among these 70% of the repairs were not subjected to any post weld heat treatment. This investigation clearly suggests that the residual stress generated during repair welding plays a significant role in many of these failures. Repair welding is practiced quite often in the pipes of nuclear power plant. A lot of effort is being given to understand and quantify the effect of these repair weld stresses on the

component service-life. The detrimental effect of residual stress in the case of steam leak in a repair weld has been reviewed by Dunn et al [3.88].

The Finite Element analysis method is being increasingly employed to model the residual stress field in wide range of weld materials. A substantial work has been carried out to simulate the residual stress in multi-pass weld plates [3.89, 3.90] and pipes [3.91]. It has been reported that except for a few discrepancies in most cases 2D analysis shows very good agreement with the experimental results, although in order to get good results in large structures it is necessary to use 3D analysis [3.92]. In recent years many projects have been undertaken to simulate the weld stresses in repair welds used in power plants. To validate these results, conventional destructive and non-destructive techniques are being used to measure the stresses experimentally. In this current work analysis of residual stress distribution in a 316L austenitic stainless steel bead on plate specimen will be discussed, which was carried out as a part of work of NET project [3.93], the final aim of which was to be able to simulate the residual stress field in repair weld used in nuclear power plant pipes.

3.2.4 Weld residual stresses in aluminium alloys

Aluminium alloys are widely used in aerospace applications, automotive industry, marine and power plants. One of the main features, which have made them very popular in key structural applications, is their favourable strength-to-weight ratio. Furthermore, it has excellent atmospheric corrosion resistance and can be formed to any desired shape very easily. AA-2000 and AA-7000 series alloys are the two most commonly used aluminium alloys in aircraft applications. Joining of these alloys is a key issue as it plays an important role in determining the component life span. In

many applications joining of two components is carried out by mechanical fastening, riveting or bolting. But these processes are expensive and time consuming and most importantly elimination of fasteners can provide considerable weight reduction, which is highly desirable in aircraft applications. In recent years, welding technique has been identified as an important joining technique, which has the potential to replace the mechanical fastening. Use of this technique can reduce the cost substantially giving a lighter and less complicated structure [3.94]. In addition, welded joints provide easy transfer of loads between different parts and are also less time consuming. However, the welding process is also associated with its own problems, which include hot cracking during welding, poor weld microstructure in the fusion and heat affected zone (HAZ) giving rise to loss of strength and toughness and the creation of local and global residual stress field [3.95, 3.96]. Among these problems residual stress has the most significant influence on the fatigue life of a component. Plenty of research has been carried out to investigate the residual stress profile of aluminium alloys using different welding techniques. Welding of aluminium alloys is associated with the following difficulties [3.97, 3.98]:

a) These alloys are highly susceptible to liquation cracking in the heat affected zone, which mainly occurs if the gap between the liquidus and solidus lines increases [3.95].

b) Al-alloys have very high thermal conductivity (four times more than steel), which results in very fast heat loss. This essentially implies that higher heat input is needed in welding of aluminium alloys.

c) It has a high co-efficient of thermal expansion, which together with the high thermal conductivity can lead to distortion if proper care is not taken.

However, this problem can be minimized by controlling the heat input and welding speed.

d) Al-alloys are susceptible to porosity problems due to hydrogen contamination. Hydrogen gas can be entrapped as gas bubbles when the liquid metal is solidified as solubility of hydrogen reduces in the solid phase [3.97].

Heat treatable alloys are found to be the most difficult to weld by fusion welding processes as the weld metal and the HAZ region loses a considerable amount of strength [3.97, 3.99]. This is due to the reason that during the welding the fusion zone is melted completely and partial melting in the HAZ region takes place, resulting in dissolution of all the precipitate in the melt which later forms a low melting eutectic and segregates at the grain boundaries [3.95].

In recent years considerable development in welding techniques has been achieved and a lot of research is being undertaken to develop new welding techniques and improve the quality of existing techniques [3.100-3.102]. Many welding techniques can be used to weld aluminium alloys for example, oxy-acetylene, submerged arc welding, Metal inert gas (MIG) welding, tungsten inert gas (TIG) welding, variable polarity plasma arc welding (VPPA), electron beam welding and laser beam welding. Submerged arc welding and oxy-acetylene welding is not popular in aircraft industry, because it uses flux which increases the risk of corrosion if cleaning is not done properly and further these processes are difficult in automation. Some welding techniques have attracted considerable attention in the aircraft industry, which include tungsten inert gas (TIG) welding, metal inert gas welding (MIG), variable polarity plasma arc welding (VPPA) and friction stir

welding. Among these friction stir welding is a relatively new method with the potential to be used in the aircraft industry. Friction stir welding (FSW), a solid state welding process developed at TWI in 1991 [3.103], has drawn considerable attention in the aircraft industry particularly due to its solid state nature [3.104]. Friction stir welding is carried out by moving one component relative to the other along a common interface with the application of a compressive force across the joints. As it is a solid-state process, the temperature experienced near the weld will be lower than the other fusion welding process. It is also expected that FSW will result in lower residual stress in compared to the other fusion welding techniques [3.105]. Due to the exciting properties of this new generation welding technique, a considerable amount of research is being carried out to study the feasibility of this welding technique and inter-related issues in high strength Al-2xxx and Al-7xxx alloy [3.102, 3.106]. However, more investigation is required on this technique before it is implemented in aircraft applications.

TIG welding has received considerable attention, particularly, in the case of Al-2xxx alloys. The effect of welding parameters on the microstructure has been studied in detail by Norman et al [3.95]. The grain structure effect of the Al alloy TIG weld has been studied by many researchers [3.107, 3.108]. Owen et al [3.109] has investigated residual stress profile characteristics of TIG welded aluminium 2024 alloy.

Significant progress has already been achieved in developing good quality and research is also being carried out to study the issues related to residual stress, microstructure and their effect on the fatigue life of the component [3.110]. MIG

welding is a form of fusion welding where a consumable electrode is used and the arc is formed between the consumable electrode and the work piece.

The VPPA welding technique was mainly designed for space application and was used firstly by NASA for the welding of external fuel tank of a space shuttle [3.111]. A detail study of residual stress distribution and the related micro structural changes in MIG and VPPA welded Al-2024 alloy and Al-7150 alloy has been carried out by Ganguly [3.63, 3.98] and Stelmukh [3.64, 3.112]. Further, the effect of these stress on the fatigue crack growth behaviour has been studied by Lin et al [3.113]. This current work describes the study of residual stress distribution in the MIG and VPPA welded Al-2024 alloy CT specimen, which has been investigated as a part of an integrated project.

3.3 Summary

A brief review on fatigue crack growth phenomenon and interrelated issues has been presented in this chapter. The effect of residual stress on fatigue crack growth has also been discussed in detail. In addition, development of weld residual stress in different alloys has been discussed along with a brief review of weld residual stress measurement using neutron diffraction technique.

3.4 References

3.1. M. F. Ashby and D. R. H. Jones. *Engineering Materials: An Introduction to Their Properties and Applications, Pergamon, Oxford, 1980.*

3.2. H. M. Westergaard, *Bearing Pressures and Cracks.* Journal of Applied Mechanics, 1939. **6**: p. 49-53.

3.3. G. R. Irwin, *Analysis of Stress and Strains Near the End of a Crack Traversing a Plate.* Journal of Applied Mechanics, 1957. **24**: p. 361-364.

3.4. I. N. Sneddon. *The Distribution of Stress in the Neighbourhood of a crack in an Elastic Solid.* 1946. Royal Society of London.

3.5. M. L. Williams, *On the Stress Distribution at the Base of a Stationary Crack.* Journal of Applied Mechanics, 1957. **24**: p. 109-114.

3.6. D. Broek, *Elementary Engineering Fracture Mechanics, 4th Edition, Nijhoff.* 1985.

3.7. G. R. Irwin. *Plastic Zone Near a Crack and Fracture Toughness.* in *Sagamore Research Conference Proceedings.* 1961.

3.8. F. A. McClintock and G. R. Irwin, *Plasticity Aspects of Fracture Mechanics.* Fracture Toughness Testing and its Applications ASTM STP 381, ASTM: Baltimore, MA,1964. p. 84-113.

3.9. R. O. Ritchie, *Near-Threshold Fatigue-Crack Propagation in Steels.* Int. Met. Rev, 1979. **24**: p. 205-230.

3.10. R. J. Cooke and C. J. Beevers, *Slow Fatigue Crack Propagation in Pearlitic Steels.* Mat. Sci. Eng, 1974. **13**: p. 201-210.

3.11. R. O. Ritchie and S. Suresh , *Some Considerations on Fatigue Crack Closure at Near-Threshold Stress Intensities Due to Fracture Surface Morpholog. Metall. Trans A, 1982,* **13A***: 937-940.*

3.12. J. E. King, *Effects of Grain Size and Microstructure on Thresold Values and Near Thresold Crack Growth in Powder-Formed Ni-base Superalloy.* Metal Sci., 1982. **16**: p. 344-355.

3.13. J. Albrecht and G. Lutjering, *Structure of Crack -Tip Plastic Zone in High-Strength aluminium Alloys as Function of Microstructure.* Metal. Sci., 1981. **15**: p. 323-329.

3.14. P. C. Paris and F. Erdogan, *A Critical Analysis of Crack Propagation Laws.* Journal of Basic Engineering, 1960. **85**: p. 528-534.

3.15. R. G. Foreman, V. E. Keary and R. M. Engle, *Numerical Analysis of Crack Propagation in Cyclic-Loaded Structures.* Journal of Basic Engineering, 1967. **89**: p. 459-464.

3.16. W. Elber, *Fatigue Crack Closure Under Cyclic Tension.* Engineering Fracture Mechanics, 1970. **2**: p. 37-45.

3.17. S. Suresh and R. O. Ritchie, *A Geometric Model for Fatigue Crack Closure Induced by Fracture Surface Morphology.* Metallurgical Transactions, 1982. **13A** : p. 1627-1631.

3.18. S. Banerjee, *AFWAL-TR-84-4031. A Review of Crack Closure. Materials Laboratory, Air Force Systems Command, Wright-Patterson Air Force Base, Ohio.* 1984.

3.19. R. O. Ritchie, *Mechanism of Fatigue Crack Propagation in Metals, Ceramics and Composites: Role of Crack Tip Shielding.* Mat. Sci. Eng, 1988. **A103**: p. 15-28.

3.20. B. Budiansky and J. W. Hutchinson, *Analysis of Closure in Fatigue Crcak Growth.* Journal of Applied Mechanics, 1978. **45**: p. 267-276.

3.21. J. C. Newman, *A Finite Element Analysis of Fatigue Crack Closure.* ASTM STP 590, American Society for Testing and Materials, Philadelphia, 1976: p. 281-301.

3.22. R. C. McClung and S. T. Raveendra, *On the Finite Element Analysis of Fatigue Crack closure-1. Basic Modelling Issues.* Engineering Fracture Mechanics, 1989. **33**: p. 237-252.

3.23. N. A. Fleck, *Finite Element Analysis of Plasticity-Induced Crack Closure Under Plane Strain Conditions.* Engineering Fracture Mechanics, 1986. **25**(4): p. 441-449.

3.24. H.-J. Lee and J.-H. Song, *Finite-Element Analysis of Fatigue Crack Closure Under plane Strain Conditions; Stabilization Behaviour and Mesh Size Effect.* Fatigue Fract ENGNG Mater Struct, 2005. **28**: p. 333-342.

3.25. Y. Jiang, M. Feng and F. Ding, *A Reexamination of Plasticity-Induced Crack Closure in Fatigue Crack Propagation.* International Journal of Plasticity, 2005. **21**: p. 1720-1740.

3.26. K. Solanki, S. R. Daniewicz and J. C. Newman, *Finite Element Analysis of Plasticity-Induced Fatigue Crack Closure: An Overview.* Engineering Fracture Mechanics, 2004. **71**: p. 149-171.

3.27. G. T. Gray, J. C. Williams and A. W. Thompson, *Roughness Induced Crack Closure: An Explanation for Microstructurally Senssitive Fatigue Crack Growth.* Metallurgical Transactions, 1983. **14A**: p. 421-433.

3.28. N. Walker and C. J. Beevers, *A Fatigue Crack Closure Mechanism in Titanium.* Fatigue Engng. Mater. Struct, 1979. **1**: p. 135-148.

3.29. I. Wallhead, *Crack Closure Measurement by the Optical Method of Caustics*, in *Materials Engineering Department*. 1994, The Open University: Milton Keynes.

3.30. R. O. Ritchie, S. Suresh and C. M. Moss, Journal of Engineering Materials Technology, Transactions ASME, Series H,102, 1980: p. 293-299.

3.31. S. Suresh, G. F. Zamiski and R. O. Ritchie, *Oxide-Induced Crack Closure: An Explanation for Near- Threshold Corrosion Fatigue Crack Growth Behaviour.* Metallurgical Transactions, 1981. **12A**(8): p. 1435-1443.

3.32. S. Suresh, D. M. Parks and R. O. Ritchie. *Crack Tip Oxide Formation and its Influence on Fatigue Thresholds*. in *Fatigue Thresholds,First International Conference Proceedings*. 1982. Stockholm: EMAS Ltd., Warley, U.K.

3.33. J. R. Rice, *Mechanics of Crack Tip Deformation and Extension by Fatigue.* Fatigue Crack Propagation, ASTM STP 415, ASTM: Baltimore, MD, 1967: p. 247-309.

3.34. A. K. Vasudevan, K. Sadananda and N. Louat, *Two Critical Stress Intensities for Threshold Fatigue Crack Propagation.* Scripta Metall Mater, 1993. **28**: p. 65.

3.35. K. Sadananda and A. K. Vasudevan, *Analysis of Fatigue Crack Closure and Thresholds.* ASTM Fracture Mechanics, ASTM STP, 1995. **1220**: p. 484.

3.36. A. K. Vasudevan and K. Sadananda, *Analysis of Fatigue Crack Growth Under Compression-Compression loading.* Int J Fatigue, 2001. **23**: p. s365-374.

3.37. K. Sadananda, A. K. Vasudevan, R. L. Holtz and E. U. Lee, *Analysis of Overload Effects and Related Phenomena.* Int J Fatigue, 1999. **21**: p. s233-246.

3.38. B. Verma and P. K. Ray, *Fatigue Crack Growth Retardation in Spot Heated Mild Steel Sheet.* Bull Mater Sci, 2002. **25**: p. 301-308.

3.39. D. Broek, *The Practical Use of Fracture Mechanics*. 1989: Kluwer Academic Publishers. 540.

3.40. T. L. Anderson, *Fracture Mechanics Fundementals and Applications*. Second ed. 1995: CRC Press. 688.

3.41. P. D. Bell and A. Wolfman, *Mathematical Modelling of Crack Growth Interaction Effects.* ASTM STP 595, 1976: p. 157-171.

3.42. H. Fuhring and T. Seeger, *Structural Memory of Cracked Components Under Irregular Loading.* ASTM STP 667, 1979: p. 144-167.

3.43. D. Broek, *A Similitude Criterion for Fatigue Crack Growth Modelling.* ASTM STP 868, 1985: p. 347-360.

3.44. O. E. Wheeler, *Spectrum Loading and Crack Growth.* Journal of Basic Engineering, 1972. **94**: p. 181-186.

3.45. J. E. Allison, *Fracture Mechanics, ASTM STP 677, (C.W. Smith, Ed).* American Society for Testing and Materials, 1979: p. 550-562.

3.46. M. S. Ramos, M. V. Pereira, F. A. Darwish, S. H. Motta and M. A. Carneiro, *Effect of Single and Multiple Overloading on the Residual Fatigue Life of a Structural Steel.* Fatigue Fract Engng Mater Struct, 2003. **26**: p. 115-121.

3.47. H. Wang, F.-G. Buchholz, H. A. Richard, S. Jagg and B. Scholtes, *Numerical and Experimental Analysis of Residual Stresses for Fatigue Crack Growth.* Computational Materials Science, 1999. **16**: p. 104-112.

3.48. M. N. James, D. G. Hattingh, D. J. Hughes, L.-W. WEI, E. A. Patterson and J. Q. D. Fonseca, *Synchrotron Diffraction Investigation of the Distribution and Influence of Residual Stresses in Fatigue.* Fatigue Fract Engng Mater Struct, 2004. **27**: p. 609-622.

3.49. M. Croft, Z. Zhong, N. Jisrawi, I. Zakharchenko, R. L. Holtz, J. Skarikta, T. Fast, K. Sadananda, M. Lakshmipathy and T. Tsakalakos, *Strain Profiling of Fatigue Crack Overload Effects Using Energy Dispersive X-Ray Diffraction.* International Journal of Fatigue, 2005. **27**: p. 1408-1419.

3.50. P. Holdway, R. Cook and A. W. Bowen, *Residual Stress Distribution and Fatigue Properties of Aluminium-Lithium 8090 5mm Plate Containing Plain and Cold-Expanded Fastener Holes. ibid. Society for Experimental Mechanics.* 1994.

3.51. A. J. Fletcher, W. Geary and J. E. King. *Fatigue Crack Propagation and Residual Stress in a Quenched and Tempered C-Mn-B Steel.* in *Analytical and Experimental Methods for Residual Stress effects in Fatigue, ASTM STP 1004, eds. R. L. Champoux, J. H. Underwood and J. A. Kapp. ASTM: Philadelphia, 1988 :p. 82-96.*

3.52. J. H. Underwood, L. P. Pook and J. K. Sharples, *Fatigue-Crack Propagation Through a Measured Residual Stress Field in Alloy Steel,.* Flaw Growth and Fracture, ASTM STP 631,:1977. : p. 402-415.

3.53. L. Jinkui, S. Peige, W. Shengping and Y. Mei, *An Understanding of the Effect of Residual Stress Induced by Shot Peening on Fatigue Strength. ibid, : p. 1002-1007.*

3.54. B. Jaensson and M. Ahmad, *Influence of Shot Peening on the Fatigue Life and Subsurface Deformation Phenomena of Torsionally Loaded Aluminium Alloy Specimens. ibid,: p. 1031-1037.*

3.55. K. Xu, N. Hu and H. Zhou, *Prediction of Notch Fatigue Limits in a Compressive Residual Stress Field. ibid, : p. 1038-1045.*

3.56. Y. C. Lam and K. S. Lian, *The Effect of Residual-Stress and its Redistribution on Fatigue.* Theoret. Appl. Fract. Mech, 1989. **12**(1): p. 59-66.

3.57. R. A. Winholtz and J. B. Cohen, *Changes in Macrostresses and Microstresses in Steel with Fatigue.* Mat. Sci. Eng, 1992. **A154**: p. 155-163.

3.58. T. Nitschke-Pagel and H. Wohlfahrt. *Residual Stresses in Welded Joints-Sources and Consequences.* in *6th European Conference on Residual Stresses.* 2002. Coimbra, Portugal, July-2002: Trans Tech Publications Ltd.

3.59. T. Nitschke-Pagel and H. Wohlfahrt. *Residual Stresses-Measurement, Calculation and Evaluation.* in *DGM-Verlag.* 1991.

3.60. T. Nitschke-Pagel and H. Wohlfahr. *Mechanical Effects of Welding.* in *Proc. of the IUTAM Symposium,10.* 1992. Lulea, Swdean: Springer Verlag.

3.61. T. Nitschke-Pagel and H. Wohlfahrt, *Residual Stresses in Welded Joints-Sources and Consequences.* Materials Science Forum, 2002. **404-407**: p. 215-226.

3.62. J. Heeschen, T. Nitschke and H. Wohlfahrt. *Residual stresses in Science and Technology.* in *DGM-Verlag.* 1987.

3.63. S. Ganguly, M. E. Fitzpatrick and L. Edwards, *Comparative Neutron and Synchrotron X-Ray Diffraction Studies to Determine Residual Stress on an As-Welded AA2024 Plate.* Material Science Forum, 2005. **490-491**: p. 223-228.

3.64. V. Stelmukh, L. Edwards and S. Ganguly, *Full Stress Tensor Determination in a Textured Aerospace Aluminium Alloy Plate Using Synchrotron X-Ray Diffraction.* Textures and Microstructures, 2003. **35**(3-4): p. 175.

3.65. D. Radaj. *Heat Effect of Welding.* 1992. Heideberg: Springer-Verlag-Berlin.

3.66. L. Bertini, V. Fontanari and G. Straffelini, *Influence of Post Weld Treatments on the Fatigue Behaviour of Al-alloy Welded Joints.* Int J Fatigue, 1998. **20**(10): p. 749-755.

3.67. M. W. Spindler and C. C. Cotton, *Creep-Fatigue Crack Growth in Type 316H Stainless Steel Through a Zone of Tensile Residual Stress.* Mater. at High Temp, 1998. **15**(2): p. 117-121.

3.68. M. Itatani, J. Fukakura, M. Asano, M. Kikuchi and N. Chujo, *Fatigue Crack Growth Behaviour of Weld Heat-Affected Zone of Type-304 Stainless Steel in High Temperature Water.* Nuclear Engng. Design, 1994. **153**(1): p. 27-34.

3.69. T. Yamashita, T. Hattori, K. Iida, T. Nomoto and M. Sato, *Effects of Residual Stress on Fatigue Strength of Small- Diameter Welded Pipe Joint.* Trans. ASME- J. Press. Vessel Tech., 1997. **119**(4): p. 428-434.

3.70. I. Takahasi, T. Yoshit, H. Iidaka, E. Fujii and K. Matasuoka, *Fatigue Strength of Non-Load-Carrying Fillet Welded Joints-Effects of Weld Residual Stresses and Stress Concentration.* Fatigue Fract. Engng. Mater Struct, 1993. **16**(1): p. 37-51.

3.71. M. Nasstrom, P. J. Webster and J. Wang. *Residual Stresses and Deformations Due to Longitudinal Welding of Pipes.* in *Proc International Trends in Welding Science and Technology.* 1993: ASM International, Materials Park, OH.

3.72. R. A. Winholtz and A. D. Krawitz, *The Relaxation of Residual-Stresses with Postweld Heat-Treatment in a High Performance Weld Measured with Neutron Diffraction.* Metall. Mater. Trans.-A, 1995. **26**(5): p. 1287-1295.

3.73. J. H. Root, C. E. Coleman, J. W. Bowden and M. Hayashi, *Residual Stresses in Steel and Zirconium Weldments.* Trans. ASME- J. Press. Vessel Tech., 1997. **119**(2): p. 137-141.

3.74. P. J. Webster, G. Mills, X. D. Wang, W. P. Kang and T. M. Holden, *Residual Stresses in Alumino-Thermic Welded Rails.* J. Strain Anal. Engng. Design, 1997. **32**(6): p. 389-400.

3.75. S. Spooner, J. A. F. Baca, S. A. David, C. R. Hubbard, T. M. Holden and J. H. Root. *Investigation of Residual Stresses In a Multipass Weld In 1" Stainless Steel Plate.* in *Proc of the Fourth International Conference on Residual Stress (ICRS 4).* 1994. Baltimore, MA: Society for Experimental Mechanics.

3.76. P. J. Webster, G. Mills, X. D. Wang, W. P. Kang and T. M. Holden, *Neutron Strain Scanning of a Small Welded Austenitic Stainless Steel Plate.* J. Strain Anal. Engng. Design, 1995. **30**(1): p. 35-43.

3.77. G. Albertini, F. M. Cernuschi, G. Cicognani, S. Ghia, T. Lorentzen and F. Rustichelli. *Residual Strain Measurements in Welded Steel Fe510D.* in *Proc of the Fourth International Conference on Residual Stresses (ICRS 4).* 1994. Baltimore, MA: Society for Experimental Mechanics.

3.78. T. Lorentzen and J. B. Ibso, *Neutron Diffraction Measurements of Residual Strains in Offshore Welds.* Mat. Sci. Engng.-A, 1995. **197**: p. 209-214.

3.79. G. Albertini, G. Bruno, B. D. Dunn, F. Fiori, W. Reimers and J. S. Wright, *Comparative Neutron and X-ray Residual Stress Measurements on Al-2219 Welded Plate.* Mater. Sci. Engng.-A, 1997. **224**: p. 157-165.

3.80. D. J. Smith, R. H. Leggatt, G. A. Webster, H. J. MacGillivary, P. J. Webster and G. Mills, *Neutron Diffraction Measurements of Residual-Stress and Plastic-Deformation in an Aluminium -Alloy Weld.* J. Strain Anal. Engng. Design, 1988. **23**(4): p. 201-211.

3.81. J. H. Root, T. M. Holden, J. Schroder, C. R. Hubbard, S. Spooner, T. A. Dodson and S. A. David, *Residual Stress Mapping in Multipass Ferritic Steel Weld.* Mater. Sci. Tech, 1993. **9**(9): p. 754-759.

3.82. H. J. Stone, P. J. Withers, T. M. Holden, S. M. Roberts and R. C. Reed, *Comparison of Three Different Technique for Measuring the Residual stress in an Electron Beam Welded Plate of WASPALOY, Metall. Mater. Trans.-A.* Metall. Mater. Trans.-A, 1999. **30**(7): p. 1797-1808.

3.83. M. Preuss, J. W. L. Pang, P. J. Withers and G. J. Baxter, *Inertia Welding Nickel-Based Superalloy: Part II. Residual Stress Characterization.* Met Trans A, 2002. **33**(10): p. 3227-3295.

3.84. H. J. Prask, R. J. Fields, P. C. Brand and J. M. Blackburn, *Evolution of Residual Stresses Around a V-Notch Weldment,ibid, :p.1198-1204.*

3.85. M. Dutta, *Residual Stress Measurement in Engineering Materials and Structures using Neutron Diffraction, Ph.D Thesis*, in *Materials Engineering*. 1999, The Open University: Milton Keynes.

3.86. P. J. Bouchard, D. George, J. R. Santisteban, G. Bruno, M. Dutta, L. Edwards, E. Kingston and D. J. Smith, *Measurement of the Residual Stresses in a Stainless Steel Pipe Girth Weld Containing Long and Short Repairs.* International Journal of Pressure Vessels and Piping, 2005. **82**: p. 299-310.

3.87. D. W. Gandy, S. J. Findland and R. Viswanathan, *Weld Repair Steam Turbine Casings and Piping and Industry Survey.* Trans. ASME- J. Press. Vessel Tech., 2001. **123**: p. 157-160.

3.88. J. Dunn, J. MacGuigan, R. McLean, L. Miles and R. A. Stevens. *Investigation and Repair of a Leak at a High Temperature Stainless Steel Butt Weld.* in *Proceedings of International Conference on Integrity of High Temperature Welds*. 1998. London: PEP Ltd.

3.89. E. F. Rybicki, J. R. Shadley, A. S. Sandhu and R. S. Stonesifer, *Experimental and Computational Residual-Stress Evaluation of a Weld Clad Plate and Machined Test Specimens.* Trans. ASME- J. Engng. Mater. Tech., 1988. **110**(4): p. 297-304.

3.90. S. Brown and H. Song, *Finite- Element Simulations of Welding of Large Structures.* Trans. ASME- J. Engng. for Industry, 1992. **114**(4).: p.441-451.

3.91. Y. Dong, J. K. Hong, C. L. Tsai and P. Dong, *Finite Element Modelling of Residual Stresses in Austenitic Stainless Steel Pipe Girth Welds.* Welding J, 1997. **76**(10): p. S442-S449.

3.92. J. M. J. McDill, A. S. Oddy and J. A. Goldak. *Comparing 2-D Plane Strain and 3-D Analysis of Residual Stresses in welds.* in *Proc International Trends in Welding Science and Technology.* 1993. Materials Park, OH: ASM International.

3.93. P. J. Bouchard, J. R. Santisteban, L. Edwards, M. Turski, J. James and S. Pratihar. *Residual stress Measurements Revealing Weld Bead Start and Stop Effects in Single and Multi-Pass Weld Runs.* in *ASME Pressure Vessels and Piping Division Conference.* 2005. Denver, Colorado.

3.94. A. Heinz, A. Haszler, C. Keidel, S. Moldenaur, R. Benedictus and W. S. Miller, *Recent Development in Aluminium Alloys for Aerospace Applications.* Mat. Sci. Eng A, 2000. **280**: p. 102-107.

3.95. A. F. Norman, V. Drazhner and P. B. Prangnell, *Effect of Welding Parameters on the Solidification Microstructure of Autogeneous TIG welds in an Al-Cu-Mg-Mn.* Mat. Sci. Eng, 1999. **A259**: p. 53-64.

3.96. D. E. Schillinger, I. G. Betz, F. W. Hussey and H. Markus, Welding J, 1963. **42**: p. s269.

3.97. J. R. Davis, *ASM Speciality Handbook: Aluminium and Aluminium Alloys, ASM International, Metal Park, OH,1993, p. 376.*

3.98. S. Ganguly, *Non-Destructive Measurement of Residual Stresses in Welded Aluminium 2024 Airframe Alloy, Ph.D Thesis*, in *Materials Engineering Dept.* 2004, The Open University: Milton Keynes. p. 255.

3.99. R. Onjukka, *Welding vs. Riveting: Which Has the Fatigue Life for Airplanes?* Welding J, 1996. **75**: p. 29-34.

3.100. N. J. Woodward, I. M. Richardson and A. Thomas, *Variable Polarity Plasma arc Welding of 6.35 mm Aluminium Alloys: Parameter Development and Preliminary Analysis.* Sci Technol Welding Joining, 2000. **5**(1): p. 21-25.

3.101. N. J. Woodward and I. M. Richardson. *Process Enhancement for the Automated GTA and Plasma Welding of Aluminium Alloys. 7th International Conference: Joints in Aluminium: INALCO 98, Cambridge (UK); 1998.*

3.102. W. M. Thomas. *Friction Stir Welding and Related Friction Process Charecteristics.* in *7th International Conference: Joints in Aluminium. IALCO 98.* 1998. Cambridge (UK).

3.103. W. M. Thomas, E. D. Nicholas, J. C. Needham, M. G. Church, P. Templemith and C. J. Dawes, *International Paten Application No. PCT/GB92/02203 and GB Patent Application No. 9125978.8; 1991.*

3.104. M. A. Sutton, A. P. Reynolds, D.-Q. Wang and C. R. Hubbard, *A Study of Residual Stress and Microstructure in 2024-T3 Aluminium Friction Stir Butt Welds.* Journal of Engineering Materials Technology, 2002. **124**: p. 215.

3.105. M. James, M. Mahoney and D. Waldron. *Residual Stress Measurements in Friction Stir Welding*. in *Proceedings of the 1st International Symposium on Friction Stir Welding*. 1999. Thousand Oaks, CA.

3.106. C. J. Dawes and W. M. Thomas, *Friction Stir Process Welds Aluminium Alloys.* The Welding Journal, 1996. **3**(75): p. 41-46.

3.107. T. Ganaha, B. P. Pearce and H. W. Kerr, Metall. Trans, 1980. **A 11**: p. 1351.

3.108. S. Kou and Y. Le, Welding J, 1986. **65**: p. 305S.

3.109. R. A. Owen, R. V. Preston, P. J. Withers, H. R. Shercliff and P. J. Webster, *Neutron and Synchrotron Measurements of Residual Strain in TIG Welded Aluminium Alloy 2024.* Mat. Sci. Eng, 2002. **A346**: p. 159-167.

3.110. A. W. Thomas, *Parameter Development for the MIG Welding of High Strength Aerospace Aluminium Alloys, Ph.D Thesis*, in *School of Industrial and Manufacturing Science*. 2000, Cranfield University.

3.111. A. C. Nuflez and E. O. Bayless, *Variable Polarity Plasma Arc Welding of the Space Shuttle External Tank.* Welding J, 1984. **63**(9): p. 27-35.

3.112. V. Stelmukh, *Neutron and Synchrotron X-ray Residual Stress Mapping of 7XXX Aluminium, Ph.D Thesis*, in *Materials Engineering Deparetment*. 2003, The Open University: Milton Keynes.

3.113. J. Lin, S. Ganguly, L. Edwards and P. E. Irving, *The Effects of Residual Stress and HAZ on Fatigue Crack Growth in MIG Welded 2024 and 7150 Aluminium.* Engineering Integrity Society; Fatigue 2003 Fatigue and Durability Assessment of Materials, Components and Structures, 2003: p. 65-72.

Chapter 4

Mapping of strain and stress around a fatigue crack within bulk material using the synchrotron diffraction technique

This chapter describes an investigation to assess the feasibility of non-destructive measurement of the elastic strain and stress distribution in the immediate vicinity of a fatigue crack inside a metallic component during in-situ loading using a high energy synchrotron X-ray source. The measurement was carried out using a high energy X-ray diffraction at the ESRF. The very high spatial resolution achieved with this technique allowed measurements to be carried out using 25 x 25 μm^2 incident slit sizes, enabling measurement within the plastic zone and crack wake field surrounding the crack tip.

4.1 Background

A lot of research has been carried out over the last 30 years regarding the fundamental mechanism of fatigue crack growth and the overload/underload interaction under variable amplitude loading. Despite this no consensus has yet been achieved on the mechanism of these phenomena. Understanding of fatigue crack growth phenomena requires detailed knowledge of the crack tip strain/stress field, as the events in the vicinity of the crack tip play a major role in crack growth and final fracture. Thus, to construct accurate fatigue life prediction models, it is essential to have experimental data describing the crack tip strain/stress field accompanying

fatigue crack growth. But, until recently no techniques had been available to map the residual stress field in front of crack tip at a sufficiently high spatial resolution within bulk material. As a result of this most of the available fatigue life prediction models are phenomenological rather than physically based.

The development of third generation synchrotron sources such as the ESRF has opened up the opportunity to map the local strain and stress fields in front of fatigue cracks inside the bulk material. Energy dispersive synchrotron X-ray techniques allow exploration of the very minute details of a fatigue crack tip stress field variation, which is likely to decay within a few hundred microns distance, and is beyond the spatial resolution of neutron diffraction.

In this work an attempt has been made to map the entire plastic zone and the accompanying crack tip field including the crack wake region inside a 12 mm thick Al-5091 compact tension specimen, using high resolution and energy dispersive (EDXRD) synchrotron X-ray diffraction at the ESRF on the ID15 (A) beam line.

4.2 Material description

The material used for this experiment was ultra–fine–grained Al-5091 [4.1], which is an Al-Li-Mg-C–O alloy. It has a very fine equiaxed grain structure, with a dispersion of very fine precipitates, i.e, Al_2O_3, Al_4C_3 and MgO. The grain size of the material is less than 1 μm. This material has yield strength of 559 MPa and an ultimate tensile strength of 596 MPa. This fine grained alloy was produced by mechanical alloying method using conventional powder metallurgy route [4.2] by Inco Alloy International. Although, by nature, the alloy is precipitation hardenable, it gets most of its strength due to the combined effect of the dispersion strengthening mechanism

and presence of very fine grains (Hall-Petch strengthening). The major advantage of using this alloy in the present investigation is that it shows linear crack path length compared to the ingot metallurgy aluminium alloys. This alloy is known to exhibit very low level of crack closure due to the presence of microscopically straight crack [4.3]. In addition, another important advantage of having such a fine-grained material in such a high resolution experiment is that it ensures that an adequate number of grains are available to diffraction within the gauge volume.

4.3 Specimen geometry

Two nominally identical 12 mm thick compact tension (CT) specimens were manufactured as specified in the fatigue crack standard ASTM E647. A schematic diagram of the sample is shown in figure 4.1. Both specimens had a 50 mm width (W) with a 15.2 mm slot machined into the CT notch root. Finally, the slot was fatigued sharpened to a total crack length of 25 mm (a/W = 0.4) in both specimens. Fatigue sharpening was carried out under the condition of constant $\Delta K = 6MPa\sqrt{m}$ (where $K_{max} = 6.6MPa\sqrt{m}$ and $K_{min} = 0.6MPa\sqrt{m}$) and R = 0.09 in an MTS servo-hydraulic testing machine. In both cases crack lengths were monitored using a travelling microscope. In addition, a back face strain gauge was

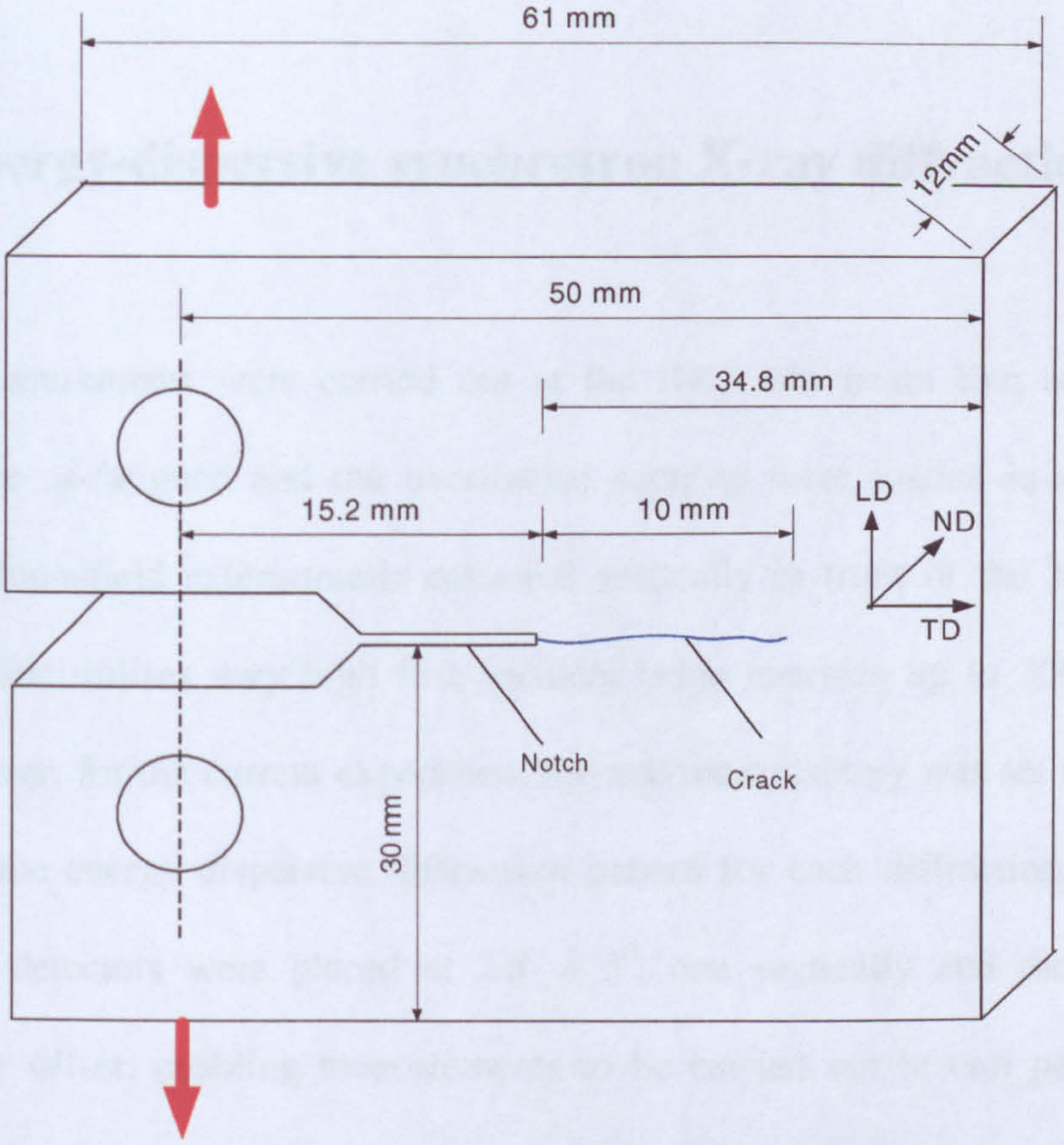

Figure 4.1: Schematic diagram of the CT specimen under investigation.

attached on both the samples to record the compliance of the specimens. The relationship between the load and back face strain was recorded, in order to infer the load in the specimens during the in-situ experiment from the back face strain (as no load cell was available on the in situ straining rig used). Once the fatigue crack was grown, one of the samples was subjected to a 100 % overload ($\Delta K = 13.2 MPa\sqrt{m}$). The thickness (B) of the as-fatigued and overloaded samples were measured to be 12.25 mm and 12.35 mm respectively.

4.4 Energy-dispersive synchrotron X-ray diffraction

All the measurements were carried out at the ID15 (A) beam line at the ESRF facility. The as-fatigued and the overloaded samples were loaded in-situ using a modified Hounsfield extensometer mounted vertically in front of the X-ray beam. This beamline utilises very high flux incident beam energies up to 300 keV [4.4, 4.5]. However, for the current experiment the maximum energy was set to 250 keV. To record the energy dispersive diffraction pattern for each diffraction beam, two solid state detectors were placed at $2\theta = 5^0$, one vertically and the other one horizontally offset, enabling measurements to be carried out in two perpendicular directions simultaneously (figure 4.2 (a and b)). Each detector comprised a liquid nitrogen cooled germanium crystal, which was attached to a multichannel analyser (MCA) [4.4]. The incident beam size was defined by the horizontal and vertical slits, positioned in front of the sample. The incident slit dimensions were kept to 25 μm in both horizontal and vertical directions. The diffracted beam was defined by two pairs of receiving slits, one placed near to the sample and the other one close to the detector. Both the receiving slits in the horizontal directions were fixed to 40 μm.

(a)

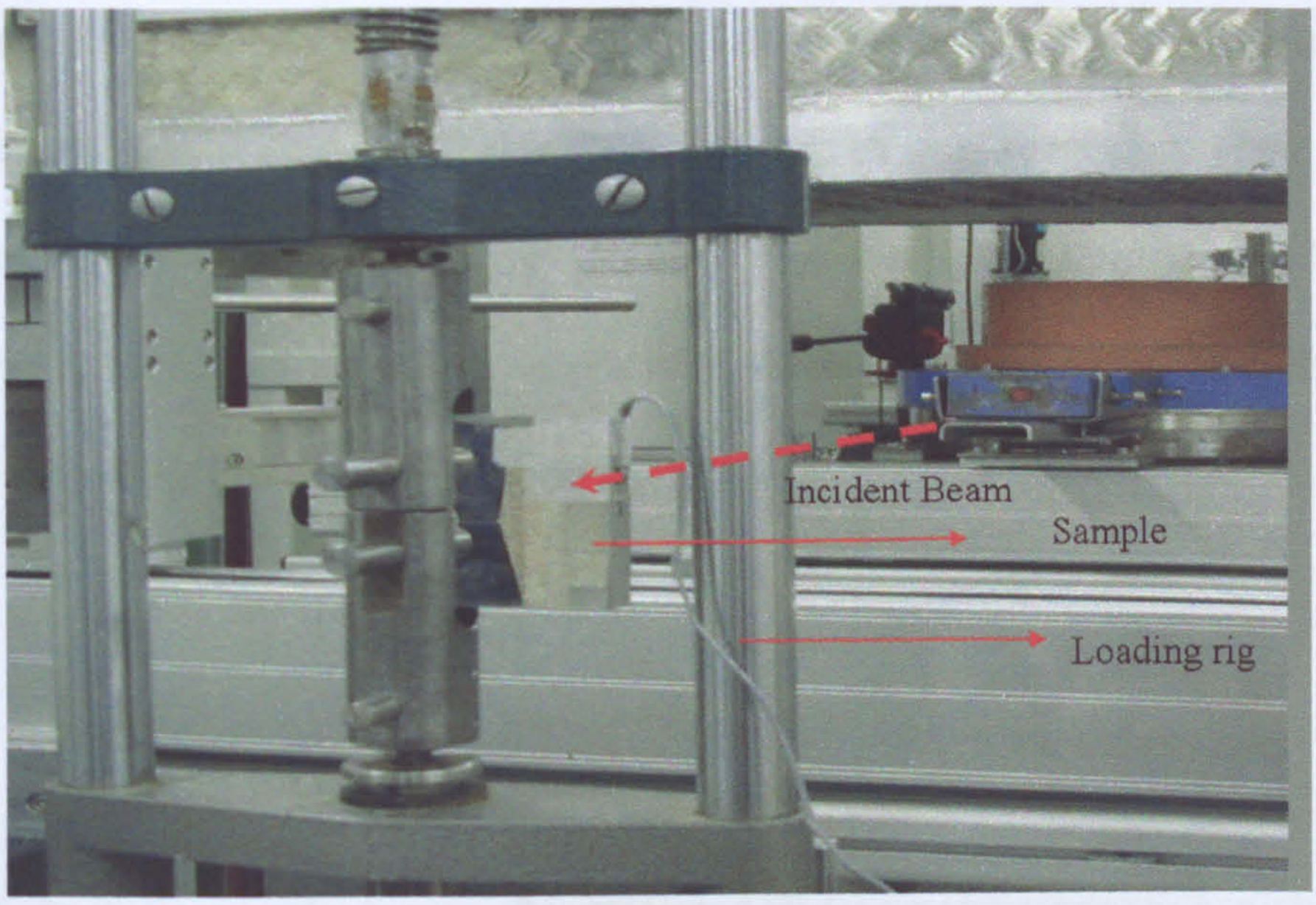

(b)

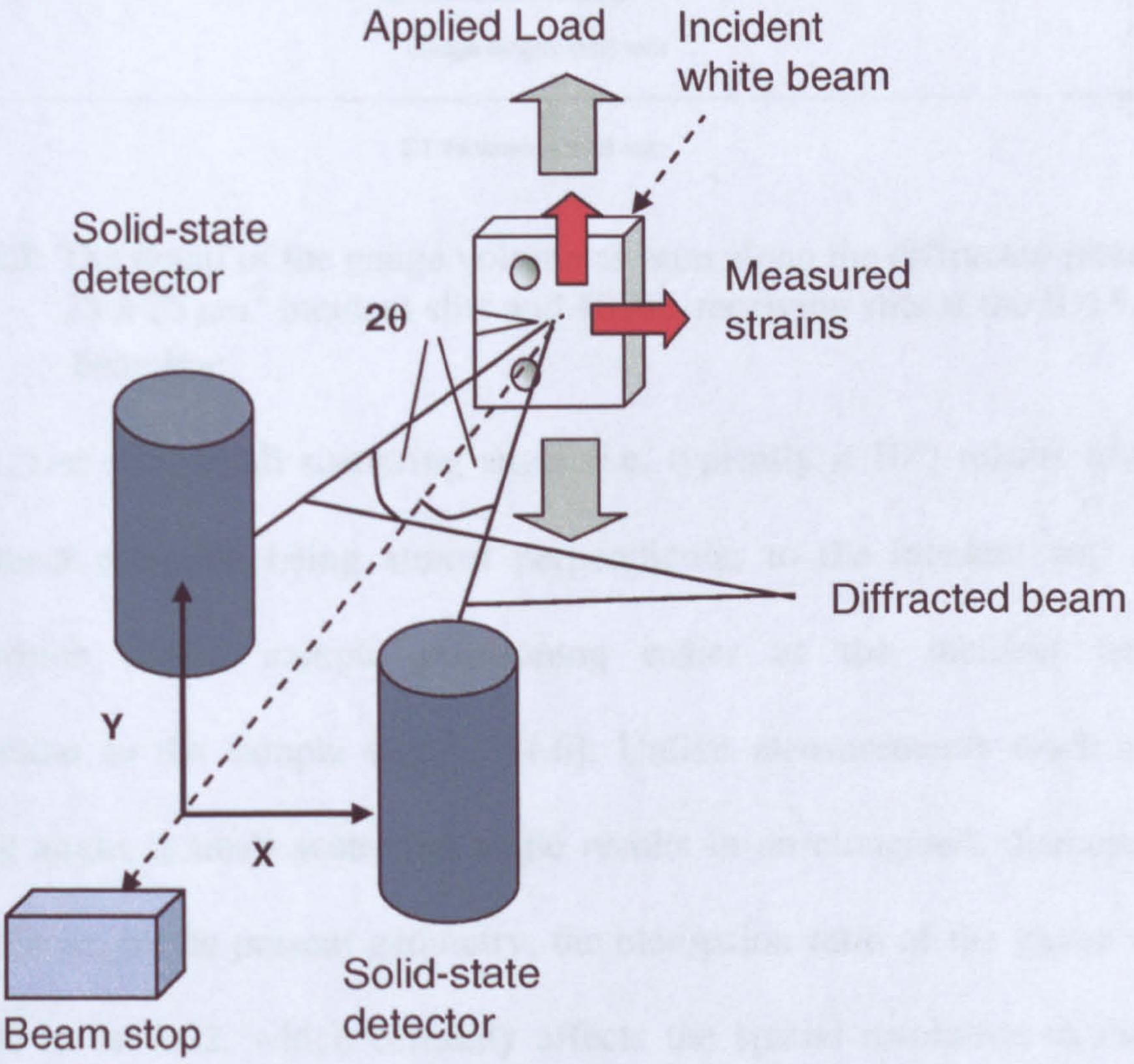

Figure 4.2: (a) the photograph of the original experimental setup and (b) a schematic diagram of the experimental set up.

The vertical beam geometry of the diffracted beam was defined by the vertical gap of the incident slits as no vertical slit was used in the receiving slits. Such a configuration is possible due to the inherent very low divergence of the beam. A copper tube, with lead shielding, is placed between the two receiving slits, which helps to define the diffracted beam and shield the detector from background

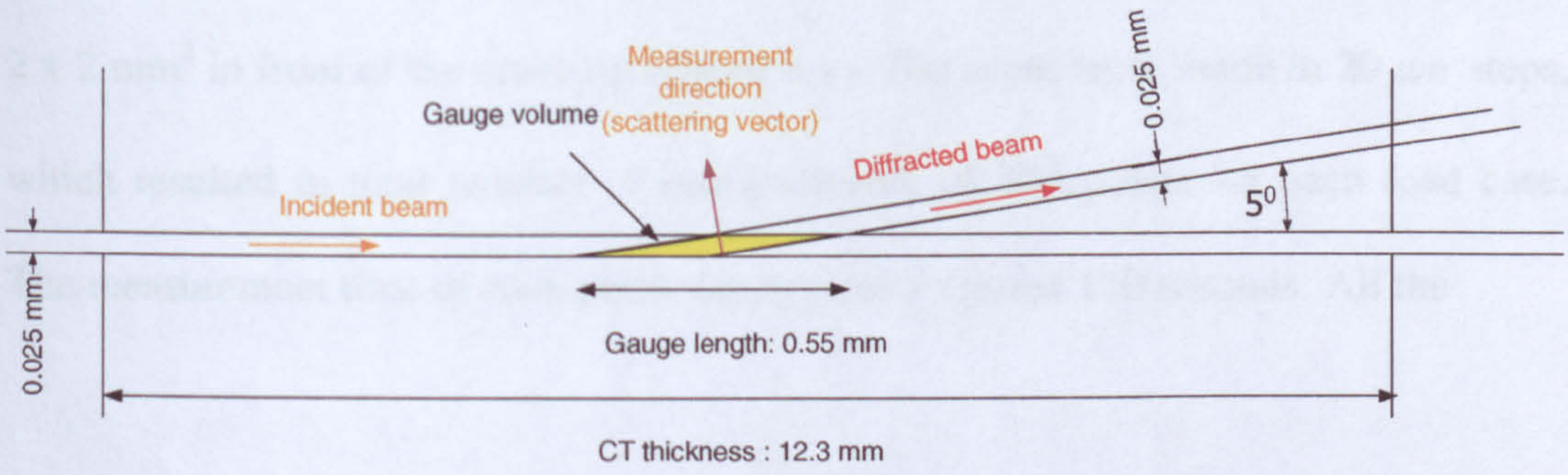

Figure 4.3: The detail of the gauge volume as seen along the diffracted plane using 25 x 25 μm^2 incident slits and 40 μm receiving slits at the ID15 (A) beamline.

radiation. Use of a small scattering angle (i.e. typically < 10°) results in the strain measurement direction being almost perpendicular to the incident and diffracted beam, which makes sample positioning easier as the incident beam falls perpendicular to the sample surface [4.6]. Unlike measurements made at a large scattering angle, a small scattering angle results in an elongated, diamond shaped, gauge volume. In the present geometry, the elongation ratio of the gauge volume is calculated to be 1:22, which certainly affects the spatial resolution in the through thickness direction. However, in practice most of the signal received by the detector comes from the middle portion of the gauge volume. Finding the location of the crack tip proved to be a challenging task and was accomplished by scanning a steel pin (0.5 mm in diameter) using the synchrotron X-ray beam. The pin was inserted into the surface of the sample and its position with respect to the crack tip was

precisely determined using an optical microscope. Finally, the location of the crack tip was confirmed by a fine scan using the synchrotron X-ray beam.

4.4.1 Measurement plan

The measurement was carried out using a beam size of 25 x 25 μm^2 in a total area of 2 x 2 mm^2 in front of the crack tip (figure 4.4). The scans were made in 20 μm steps, which resulted in total number of measurements of 400 points for each load case. The measurement time of each point was typically around 120 seconds. All the

Figure 4.4: The schematic diagram of the area of the measurement in front of the crack tip of the CT specimen.

measurements were carried out in two mutually perpendicular directions. The loading direction (perpendicular to the crack length) is termed as the longitudinal direction (LD) and the direction perpendicular to it is called the transverse direction (TD). Both the samples (As-fatigued and overloaded) were measured under different level of in-situ loading. As-fatigued samples were measured with

$K_{max} = 6.6MPa\sqrt{m}$ and $K_{min} = 0.6MPa\sqrt{m}$ and the 100 % overloaded sample was measured at $K_{max} = 13.2MPa\sqrt{m}$ and $K_{min} = 0.6MPa\sqrt{m}$.

4.4.2 Data analysis

For each measurement, the diffracted spectra of all the peaks were recorded in two solid-state detectors since a white beam was used. A typical diffraction spectrum obtained in energy dispersive mode and its Pawley fit is shown in figure 4.5. It is clear from the spectrum that the level of background adjacent to the peak is very low and also no significant texture is apparent. The experimental data obtained in energy–dispersive mode was transformed to an artificial angular dispersive mode

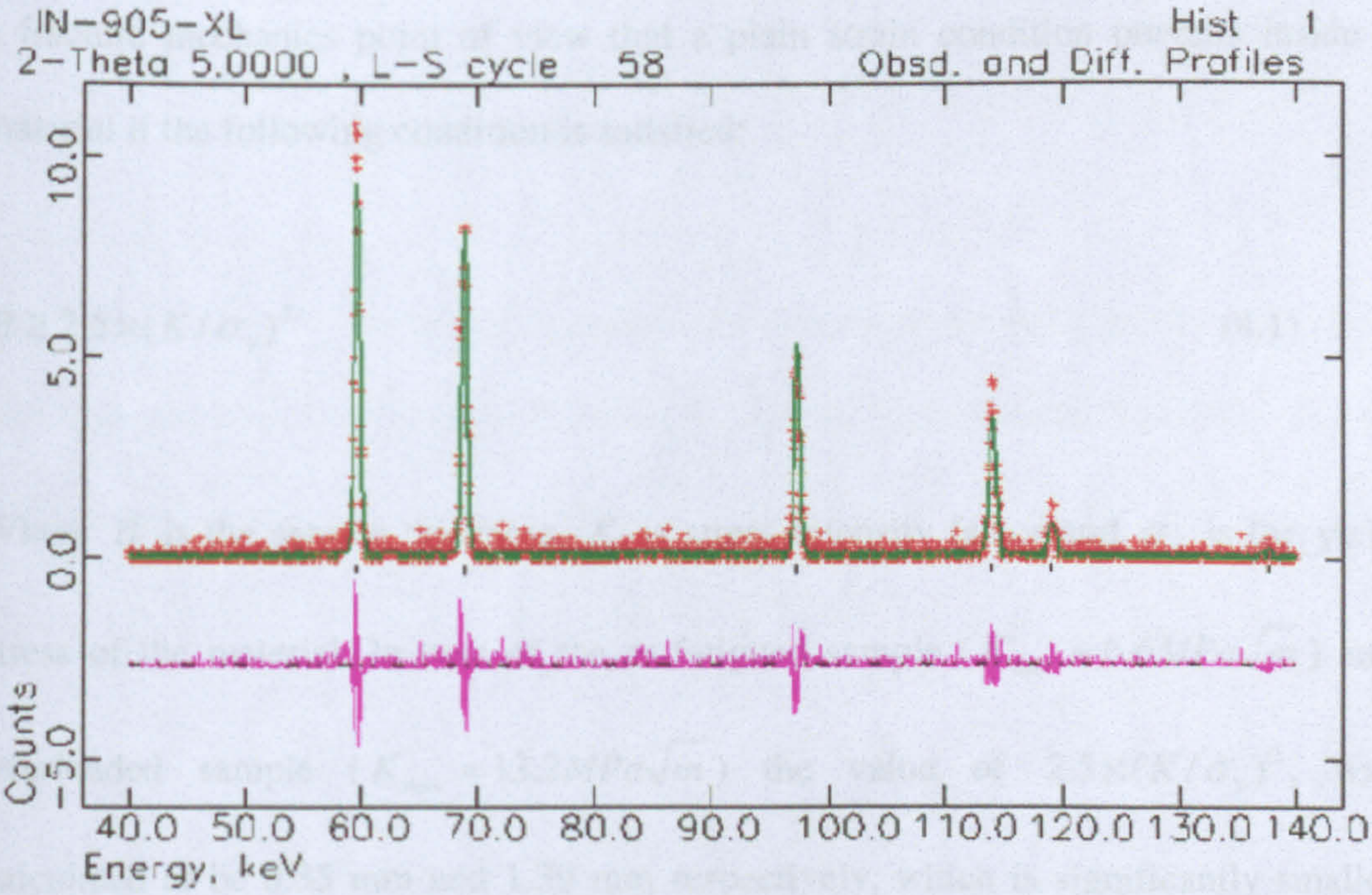

Figure 4.5: Typical diffraction spectrum of Al-5091 CT specimen obtained from ID15 (A) diffractometer in energy-dispersive mode. Only part of the spectrum seen in the figure has been used in the data analysis.

of reciprocal scale, and stored as a GSAS RALF format [4.4]. This spectrum was fitted using the time of flight peak profiling routine, Pawley refinement approach [4.7], using the software package GSAS [4.8]. The time of flight neutron peak profiling type routine was required because the peaks within the energy dispersive profile are typically asymmetric [4.9, 4.10]. The lattice parameter obtained from the GSAS analysis is used to calculate the strain using equation 2.8.

4.4.3 Plane strain approximation

The stresses were calculated (using equation 2.13) assuming a plane strain assumption, as the measurements were carried out in the middle of the relatively thick (12 mm) specimen. Furthermore, to justify this assumption the fracture mechanics approach is also applied to the specimen geometry. It is well known from a fracture mechanics point of view that a plain strain condition prevails inside a material if the following condition is satisfied:

$$B \geq 2.5 \times (K / \sigma_y)^2 \qquad (4.1)$$

Where B is the sample thickness, K is stress intensity factor and σ_y is the yield stress of the material. In case of the as-fatigued sample ($K_{max} = 6.6 MPa\sqrt{m}$) and overloaded sample ($K_{max} = 13.2 MPa\sqrt{m}$) the value of $2.5 \times (K / \sigma_y)^2$, was calculated to be 0.35 mm and 1.39 mm respectively, which is significantly smaller than the specimen thickness (B = 12 mm). Therefore, in both cases assumption of plain strain condition is clearly justified in terms of fracture mechanics approach.

4.4.4 Stress free lattice parameter measurement

Lattice parameter values measured far from the crack tip were used to determine the stress free reference value (a_0). For this purpose a set of measurements were carried out in the far field of both the specimens and an average value was used as a final unstressed lattice parameter value. All these measurements were carried out in the unloaded condition to ensure that no external stress was incorporated. The slits size ($25 \times 25\ \mu m^2$) was kept the same as for all the other measurement points.

4.5 Results and discussions

4.5.1 As-fatigued sample

Figure 4.6 (a and b) shows the longitudinal (direction perpendicular to the crack) direction and transverse (direction along the crack) direction strain profiles for the as-fatigued sample loaded to applied stress intensity of $K_{max} = 6.6 MPa\sqrt{m}$. The

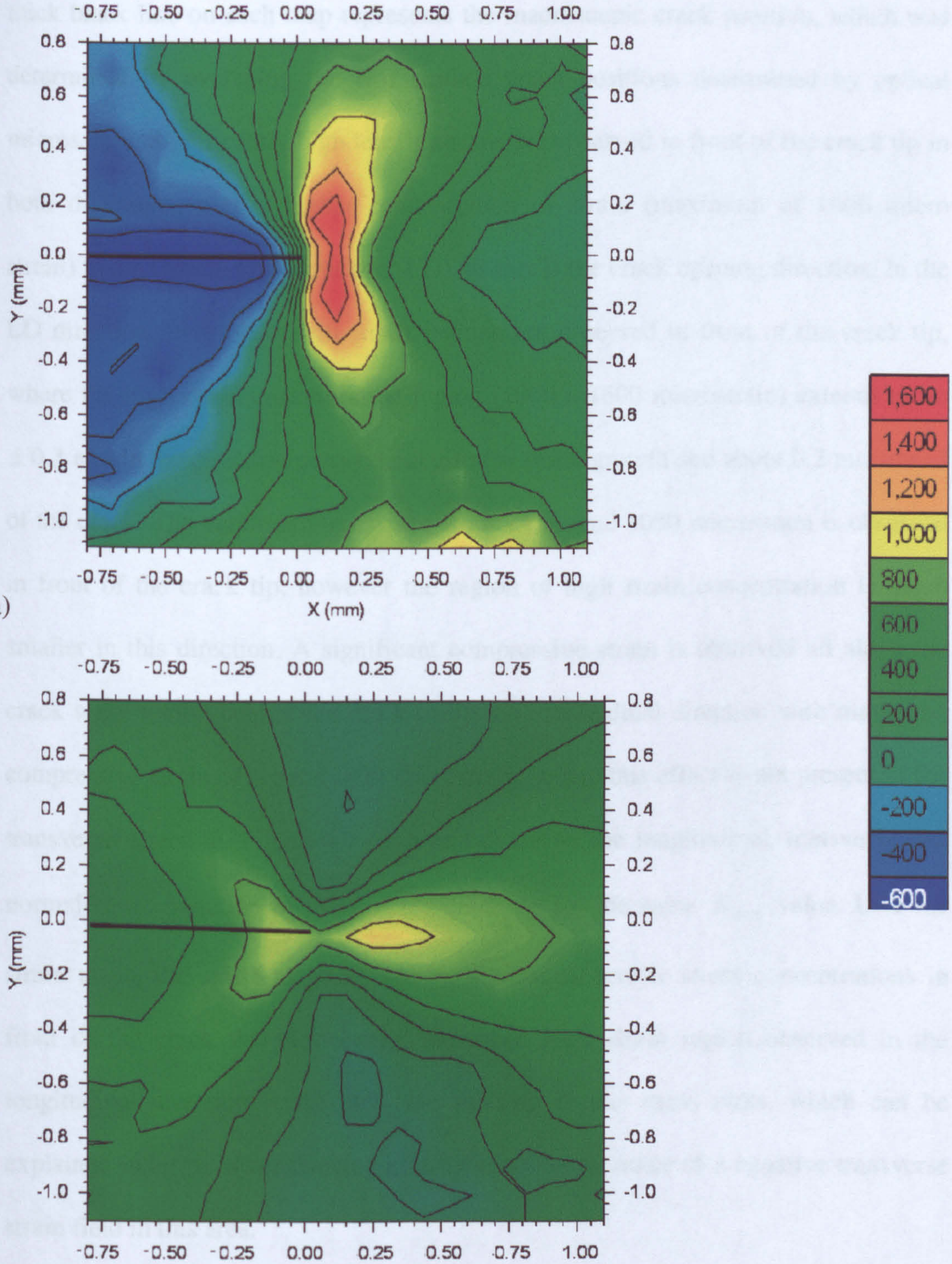

Figure 4.6: As-fatigued sample, $K_{max} = 6.6MPa\sqrt{m}$, (a) longitudinal and (b) transverse strain distribution.

thick black line on each map represents the macroscopic crack position, which was determined by averaging the two surface crack positions determined by optical microscopy. Significantly high tensile strains are observed in front of the crack tip in both directions, with a higher concentration of strain (maximum of 1600 micro strain) in the longitudinal direction (LD), as this is the crack opening direction. In the LD direction, two lobed high strain regions are observed in front of the crack tip, where the high strain concentration region (1000 to1600 microstrain) extends up to ± 0.3 mm in the direction perpendicular to the crack growth and about 0.2 mm ahead of the crack. The maximum transverse strain of around 1050 microstrain is observed in front of the crack tip, however the region of high strain concentration is much smaller in this direction. A significant compressive strain is observed all along the crack wake region behind the crack tip in the longitudinal direction with maximum compressive strain of around -800 microstrain, where this effect is not present in the transverse direction. Figure 4.7 (a, b and c) shows the longitudinal, transverse and normal stress variation in front of the crack tip for the same K_{max} value. Like the strain maps, the stress maps also show significant tensile stress concentrations in front of the crack tip. Noticeably, the lobed high strain region observed in the longitudinal direction strain plots are missing in the stress plots, which can be explained in terms of a balancing effect due to the presence of a negative transverse strain field in this area.

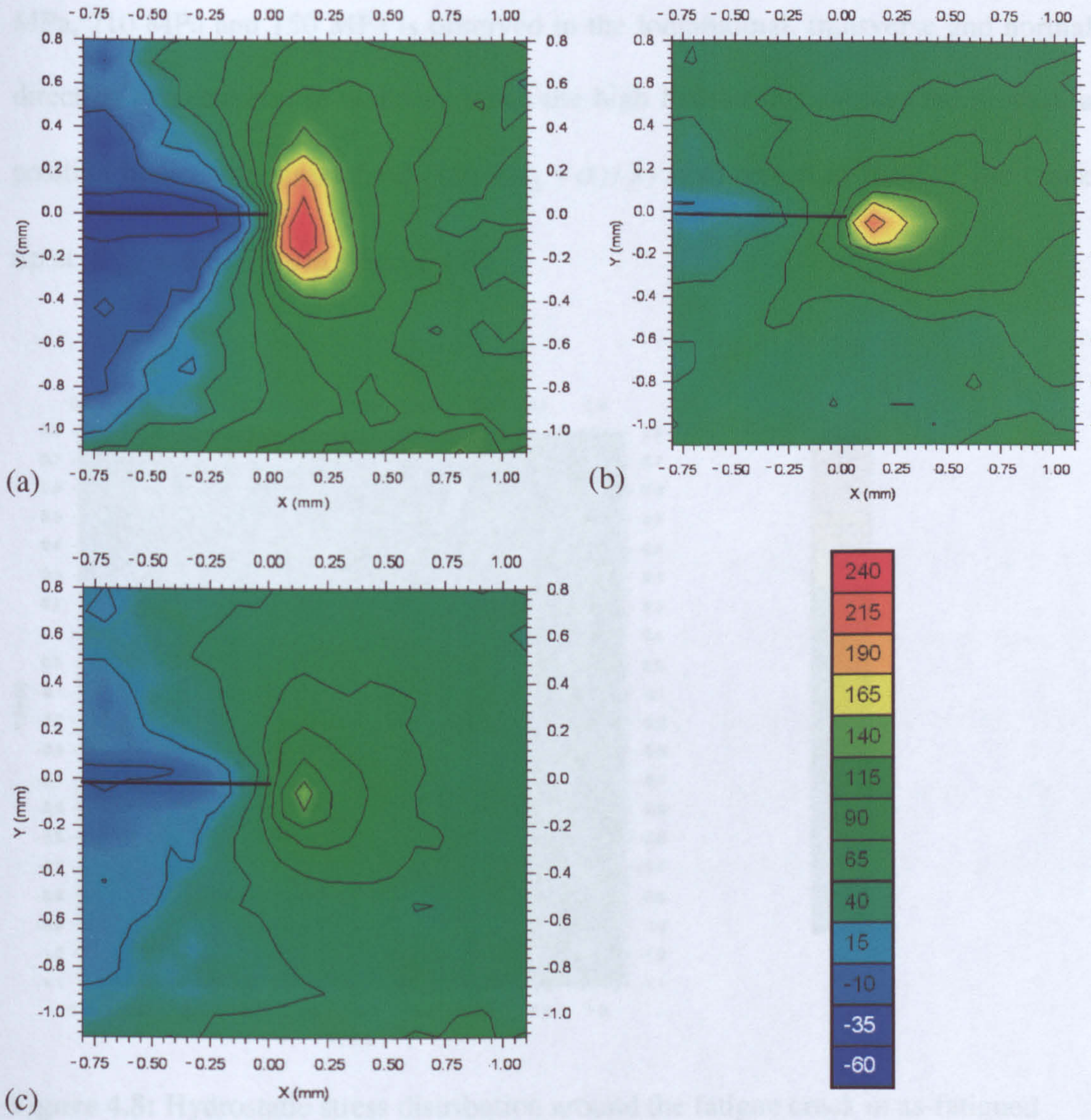

Figure 4.7: As-fatigued sample, $K_{max} = 6.6MPa\sqrt{m}$, (a) longitudinal, (b) transverse and (c) normal direction stress distribution.

The significantly high stress observed in the immediate vicinity of the crack tip in all three directions confirm the presence of a triaxial stress field, which is expected in front of crack tip in a plane strain condition. The maximum stress of around 240 MPa, 210 MPa and 150 MPa is observed in the longitudinal, transverse and normal direction respectively. In addition, when the high hydrostatic stresses are plotted, a positive hydrostatic stress field ($(\sigma_1+\sigma_2+\sigma)/3$) is observed in front of the crack tip at $K_{max}=6.6MPa\sqrt{m}$ (figure 4.8).

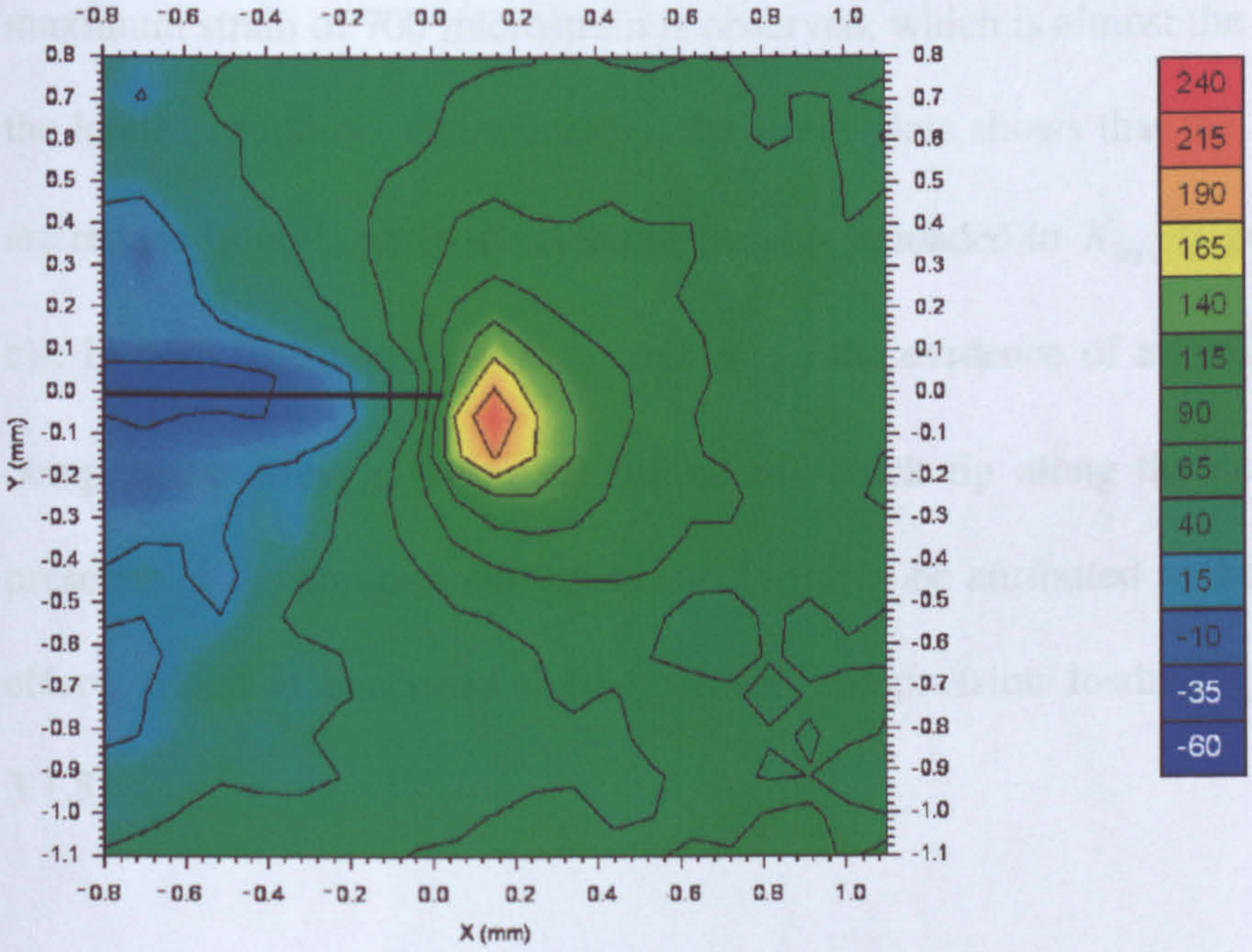

Figure 4.8: Hydrostatic stress distribution around the fatigue crack in as-fatigued sample at $K_{max}=6.6MPa\sqrt{m}$.

A constant compressive stress of around -50 MPa is observed all along the crack behind the crack tip in the longitudinal direction while these stresses are not pronounced in transverse and normal direction.

Figure 4.9 (a, b) and 4.10 (a, b and c) shows the crack tip strain and stress fields at $K_{min} = 0.6MPa\sqrt{m}$. The strain plots shows that the crack tip strain values reduces significantly in three directions when unloaded to K_{min}. However, the compressive strain values along the crack wake seems to be unaffected with maximum strain of 700 microstrain is observed, which is almost the same as found in the loaded condition. Consequently, the stress plots shows that the crack tip stresses are reduced significantly when the material is unloaded to K_{min} (figure 4.10 (a, b and c)). In both load cases, at K_{max} and K_{min}, the evidence of a similar magnitude of compressive stress is observed behind the crack tip along the crack surface. The presence of the compressive stress can certainly be attributed to the cyclic plasticity effect, which is generated during tension compression loading cycle (see section 3.1.5).

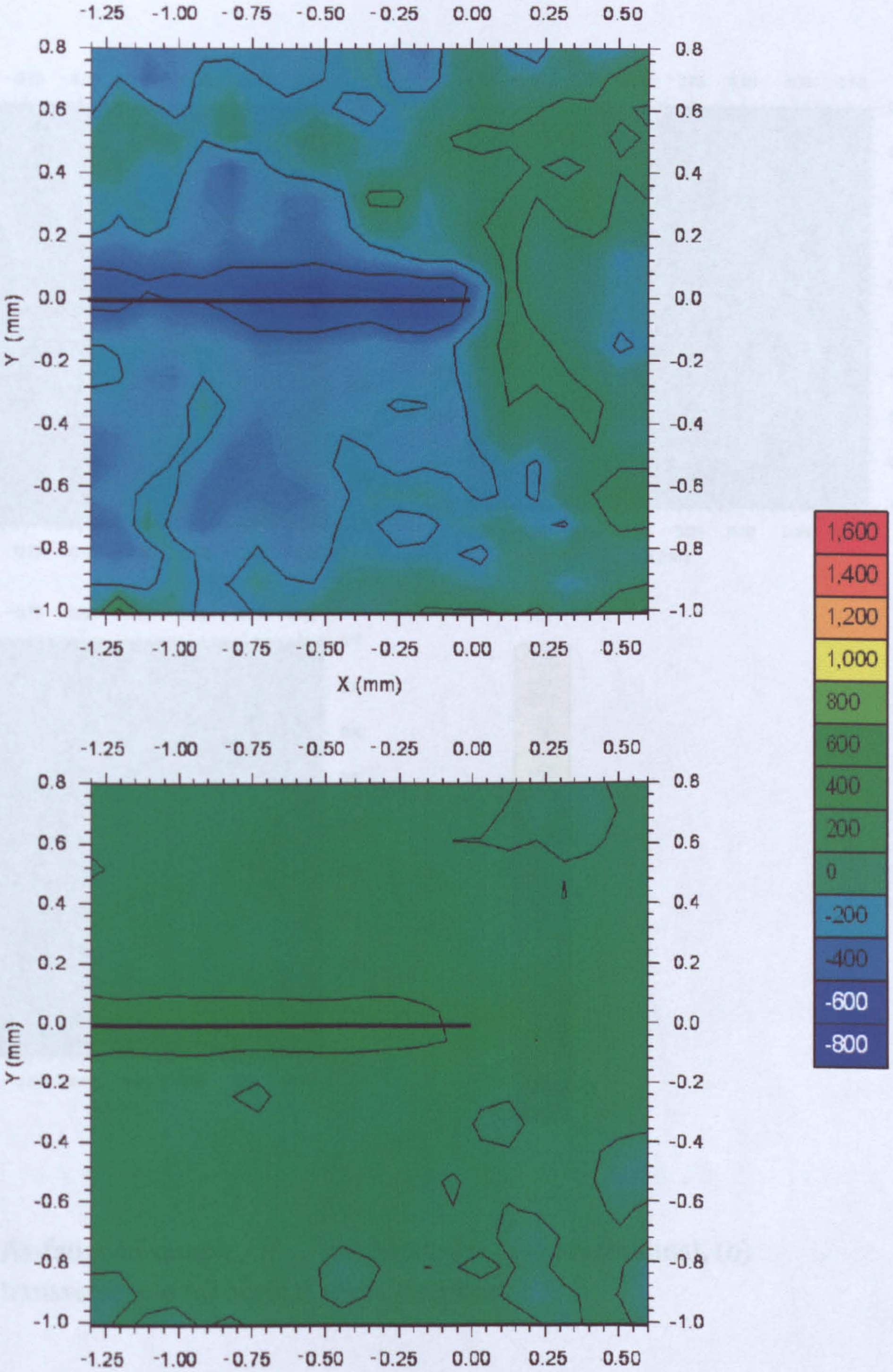

(a)

(b)

Figure 4.9: As-fatigued sample, $K_{\min} = 0.6MPa\sqrt{m}$, (a) longitudinal and (b) transverse strain distribution.

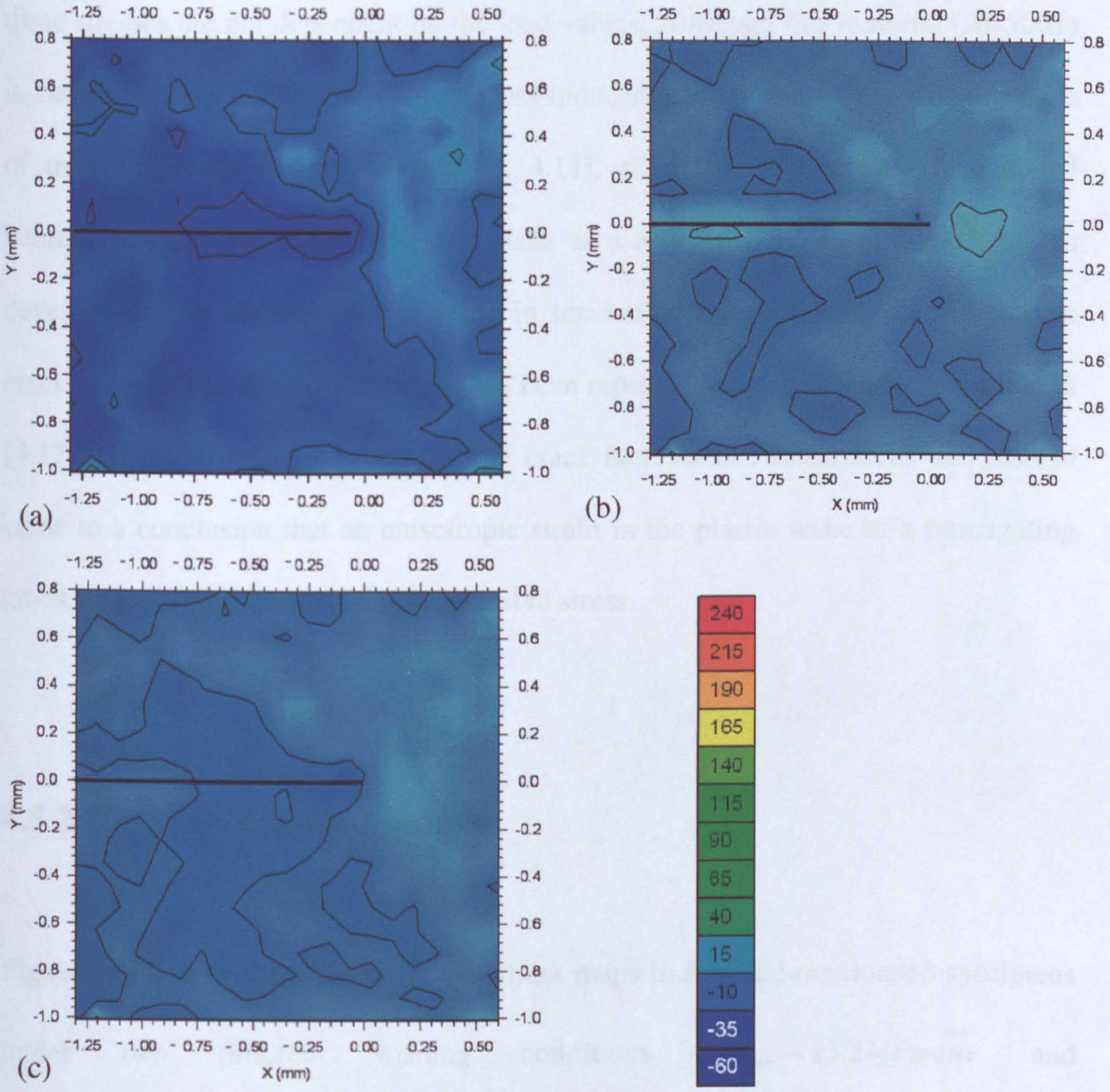

Figure 4.10: As-fatigued sample, $K_{\min} = 0.6MPa\sqrt{m}$, (a) longitudinal, (b) transverse and (c) normal stress distribution.

Furthermore, the similar compressive stress distribution along the crack surface behind the crack tip under two different load conditions clearly indicate that these stresses are not dependent on the load values. Although this material (Al-5091) is known to show a low level of roughness-induced crack closure due to the presence of microscopically–straight crack [4.3, 4.11], a compressive stress is developed behind the crack tip along the crack wake as a result of anisotropic strain, which develops during the repeated yielding in tension and compression during fatigue crack growth. The similar effect has also been reported in a recent study by croft et al [4.12], where he ruled out the effect of crack face contact interactions and instead came to a conclusion that an anisotropic strain in the plastic wake of a propagating crack tip is responsible for this compressive stress.

4.5.2 Overloaded sample

Figures 4.11- 4.14 show the strain and stress maps in fatigued-overloaded specimens under two different loading conditions ($K_{max} = 13.2MPa\sqrt{m}$ and $K_{min} = 0.6MPa\sqrt{m}$). Figure 4.11 (a and b) shows high strain concentration in front of crack tip in the longitudinal and transverse direction at K_{max}. The maximum strain

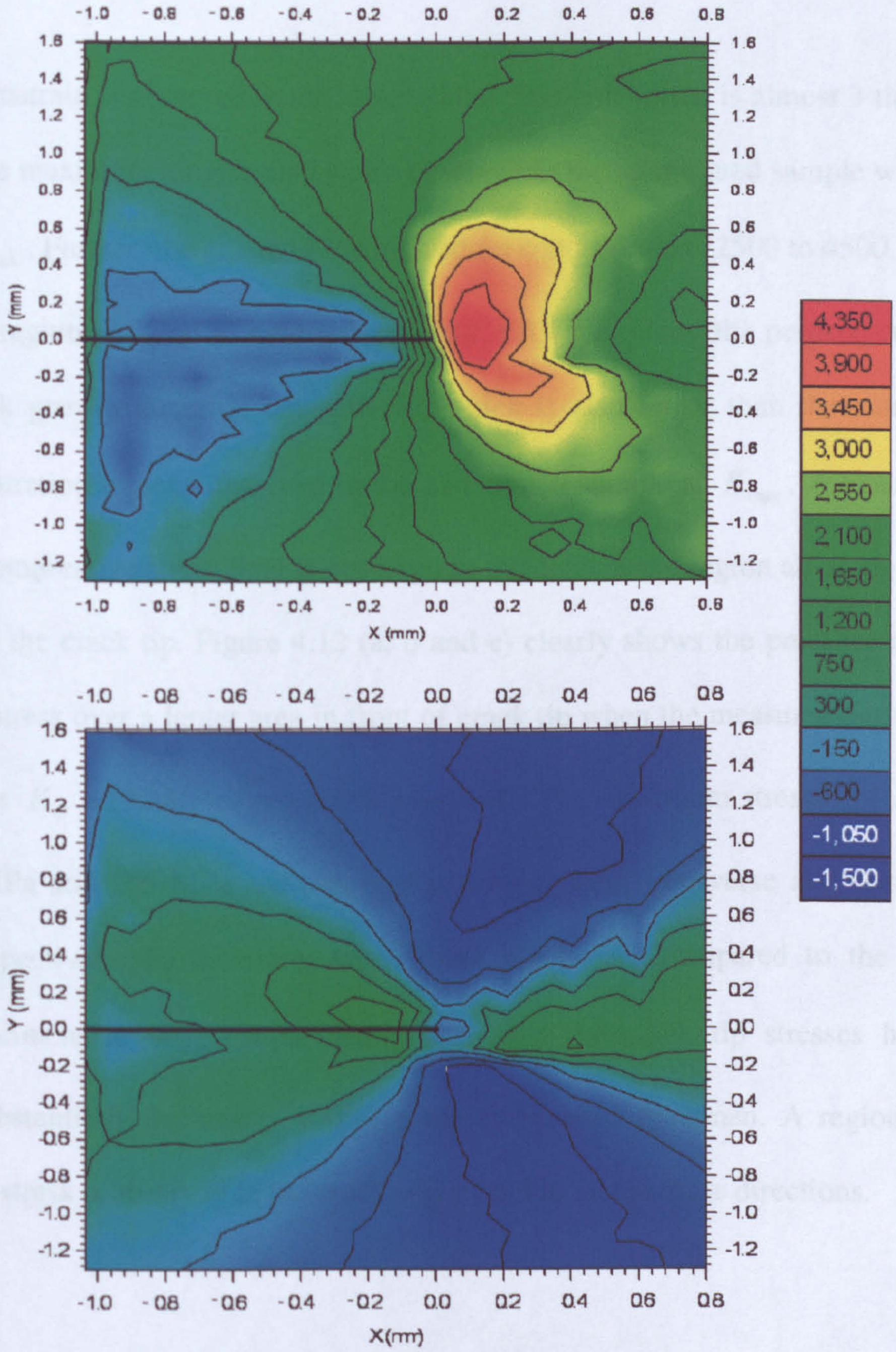

Figure 4.11: Overloaded sample, $K_{max} = 13.2MPa\sqrt{m}$, (a) longitudinal and (b) transverse strain distribution.

of 4450 microstrain is observed in the longitudinal direction which is almost 3 times more than the maximum longitudinal strain observed in the as-fatigued sample when loaded at K_{max}. Further, the extent of the high strain concentration (2500 to 4500 microstrain) region is found to be ± 0.6 mm and ± 0.4 mm along the perpendicular and the crack growth direction respectively, which is also larger than the similar strain concentration regions observed in the as-fatigued sample at K_{max}. A band of significant compressive strain field is observed in the crack wake region all along the crack behind the crack tip. Figure 4.12 (a, b and c) clearly shows the presence of a high tensile stress over a larger area in front of crack tip when the measurement was carried out at $K_{ol} = 13.2MPa\sqrt{m}$ (100% overload). The maximum stresses of 550 MPa, 325 MPa and 275 MPa are observed in longitudinal, transverse and normal direction respectively. Furthermore, when these results are compared to the as-fatigued specimens at K_{max}, it is clearly seen that the crack tip stresses have increased substantially, by nearly 100% in the overloaded specimen. A region of compressive stress is observed in the crack wake field in all the three directions.

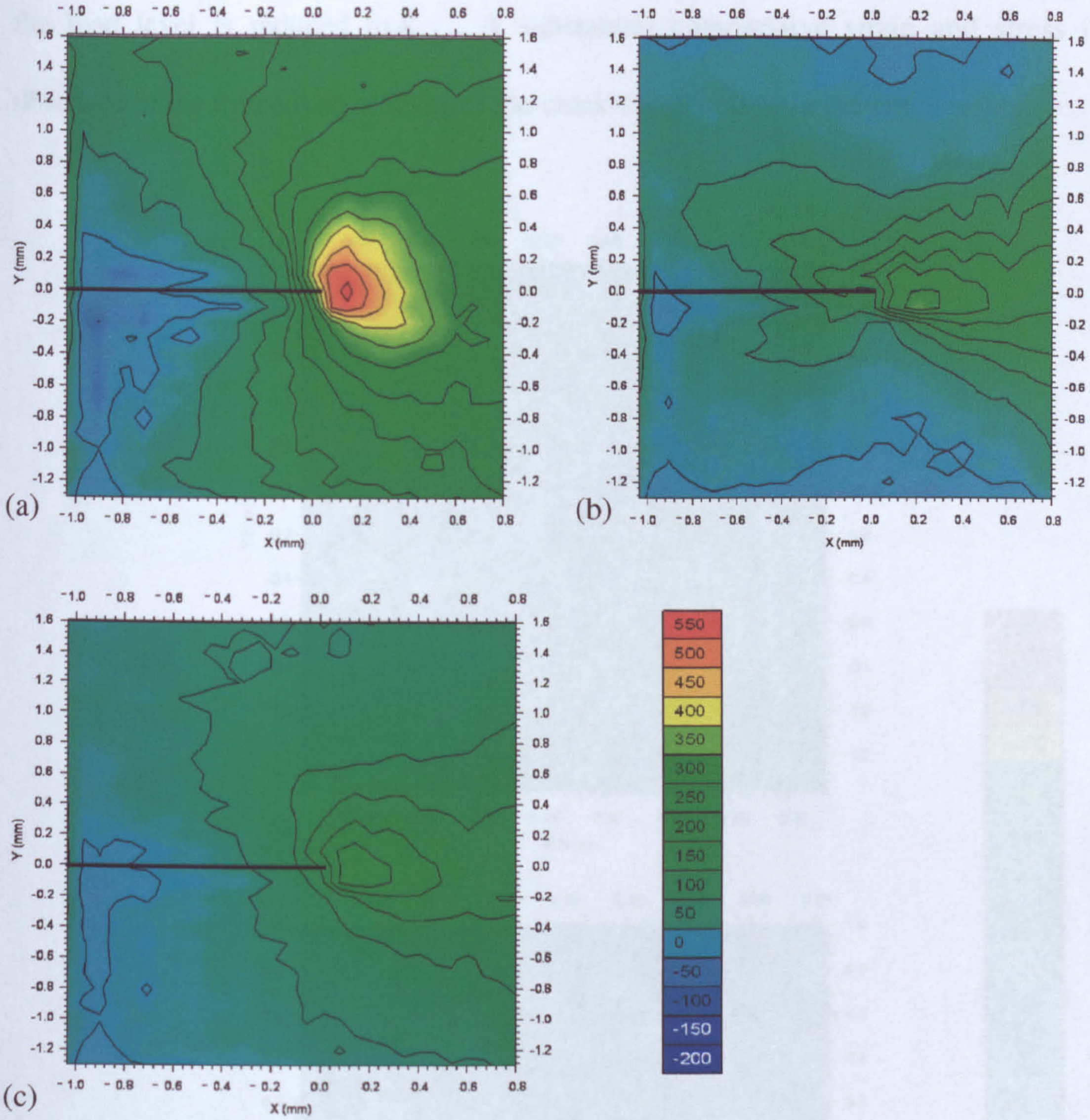

Figure 4.12: Overloaded sample, $K_{max} = 13.2MPa\sqrt{m}$, (a) longitudinal, (b) transverse and (c) normal direction stress distribution.

Figure 4.13 (a, b) and 4.14 (a, b and c) shows the strain and stress variations when the load level is reduced to K_{min}. A substantial compressive strain and stress is observed in the immediate vicinity of the crack tip as well as in the crack wake.

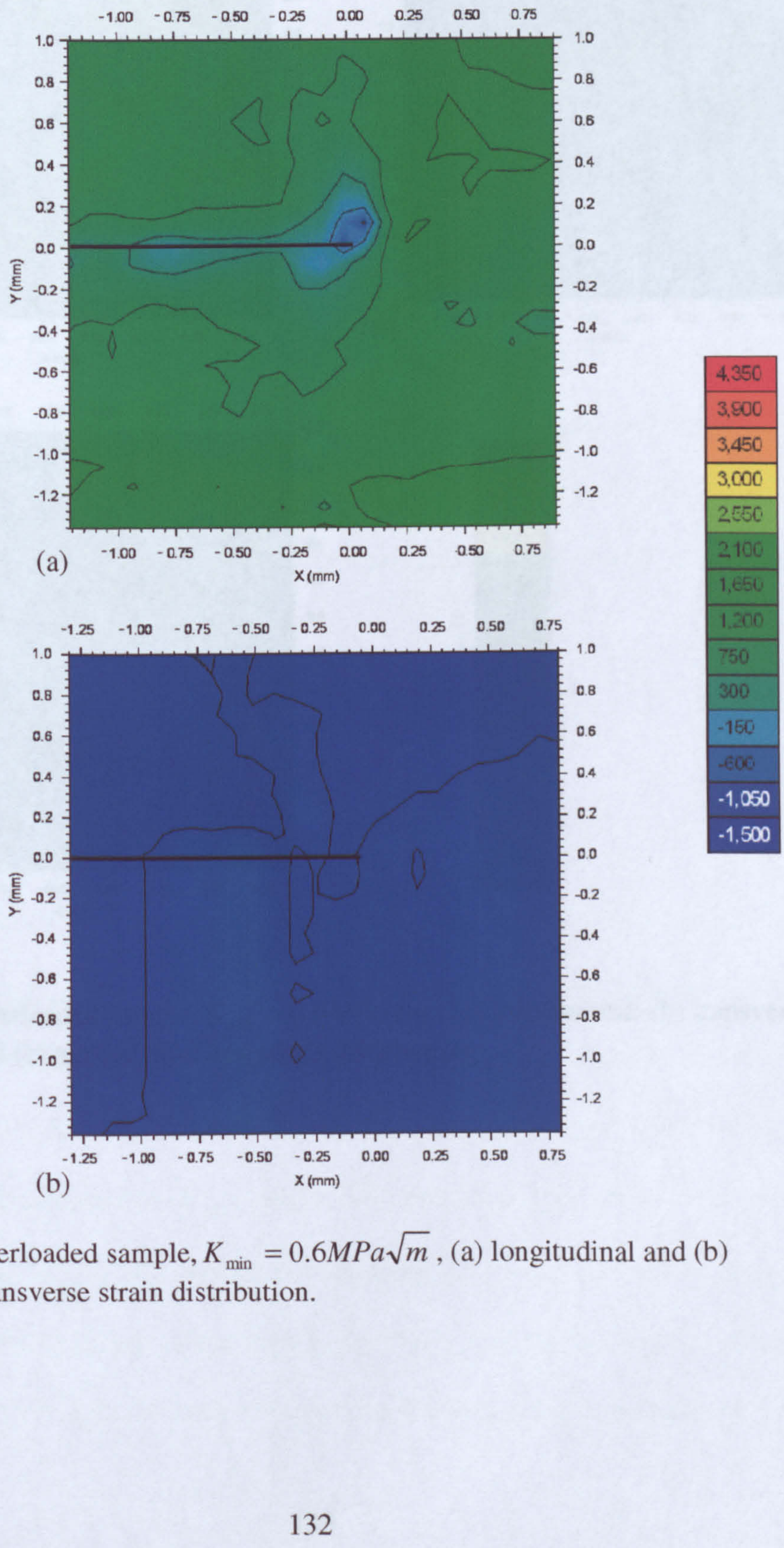

Figure 4.13: Overloaded sample, $K_{min} = 0.6MPa\sqrt{m}$, (a) longitudinal and (b) transverse strain distribution.

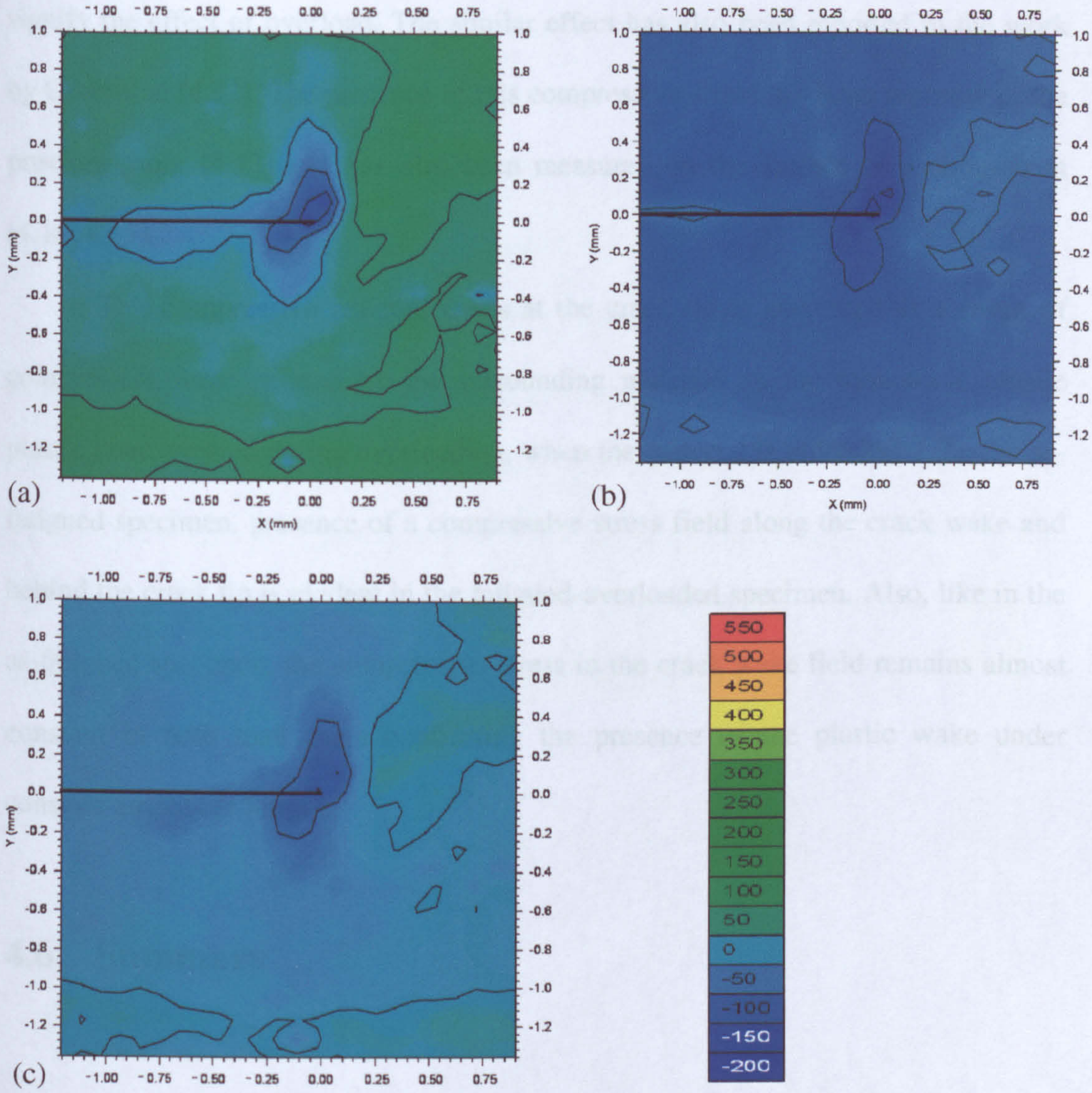

Figure 4.14: Overloaded sample, $K_{\min} = 0.6MPa\sqrt{m}$, (a) longitudinal (b) transverse and (c) normal direction stress distribution.

The maximum compressive stress of -150 MPa is observed near the crack tip in the longitudinal and transverse direction. These compressive stresses near the crack tip signify the effect of overload. The similar effect has also been reported in the work by Croft et al [4.12]. The presence of this compressive stress has been reported in the previous work [4.13] and has also been measured on the surface of a component [4.14, 4.15].

This compressive residual stress at the crack tip is generated as a result of compressive force exerted by the surrounding material on the monotonic tensile plastic zone, created during overloading, when the material is unloaded. Like the as-fatigued specimen, presence of a compressive stress field along the crack wake and behind the crack tip is evident in the fatigued-overloaded specimen. Also, like in the as-fatigued specimen, the compressive stress in the crack wake field remains almost constant in both load cases confirming the presence of the plastic wake under constant amplitude fatigue.

4.6 Summary

The crack tip strain and stress distribution has been successfully mapped non-destructively inside a bulk material in Al-5091 compact tension specimens using high-resolution synchrotron X-ray diffraction. A high triaxial stress is observed in the immediate vicinity of the crack tip in both the as-fatigued and overloaded specimens at their respective K_{max} values. The crack tip peak stress values were found almost double in the overloaded specimen compared to the as-fatigued specimen and also the extent of that high stress region was greater in the overloaded specimen. A considerable constant compressive stress is observed along the crack

wake just behind the crack tip in both the specimens irrespective of the loading history. This suggests that the plastic deformation, produced during fatigue loading, is the prime mechanism of the generation of compressive stress along the crack wake. The effect of the overload is also clearly evident in the fatigued-overloaded specimen, as a significant compressive stress is observed in the immediate vicinity of the crack tip when the material is unloaded to K_{min} .

This work provides a broad picture of the strain and stress distribution around a fatigue crack and their modification following an overload, inside a bulk metallic component. A detailed in depth analysis of the data will reveal more information regarding the crack tip stress distribution and the crack closure effect, which in turn will be very useful in developing accurate fatigue life prediction models. However, such an investigation is out of the scope of the present work.

4.7 Reference

4.1. E. Ferrie, J.-Y. Buffiere, W. Ludwig, A. Gravouil and L. Edwards, *Fatigue Crack Propagation: In situ Visualization Using X-ray Microtomography and 3D Simulation Using the Extended Finite Element Method.* Acta Mater, 2006. **54**: p. 1111-1122.

4.2. P. D. Pitcher, R. S. Bushby, W. Vine, A. F. Smith and A. D. Tarrant, *New Al-Li-Mg-C Dispersion Strengthened Alloy Part 2 - Optimisation of Material for Forging Applications.* Mat. Sci. Technol, 2001. **17**: p. 807-814.

4.3. G. H. Bray, A. P. Reynolds and E. A. Starke, *Mechanisms of Fatigue Crack Retardation Following Single Tensile Overloads in Powder Metallurgy Aluminum Alloys.* Met Trans A, 1992. **23**: p. 3055.

4.4. A. Steuwer, J. R. Santisteban, M. Turski, P. J. Withers and T. Buslaps, *High-Resolution Strain Mapping in Bulk Samples Using Full-Profile Analysis of Energy-dispersive Synchrotron X-ray Diffraction.* Journal of Applied Crystallography, 2004. **37**: p. 883-889.

4.5. T. Tschentscher and P. Suortti, *Experiments with Very High Energy Synchrotron Radiation.* J. Synchrotron Rad, 1998. **5**: p. 286-292.

4.6. P. J. Withers, *Use of Synchrotron X-ray Radiation for Stress Measurement*, in *Analysis of Residual Stress by Diffraction by Using Neutron and Synchrotron Radiation*, Fitzpatrick, M. E. and Lodini, A., Editors. 2003, Taylor and Francis: London. p. 170-188.

4.7. G. S. Pawley, *Unit-Cell Refinement From Powder Diffraction Scan.* J. Appl. Crystallography, 1981. **14**: p. 357-361.

4.8. A. C. Larson and R. B. V. Dreele, *"General Structure Analysis System (GSAS)"*, in *Los Alamos National Laboratory Report LAUR 86-748*. 2000.

4.9. A. J. C. Wilson, *Note on the Aberrations of a Fixed-Angle Energy-Dispersive Powder Diffractometer.* J. Appl.Cryst, 1973. **6**: p. 230-237.

4.10. J. W. Otto, *On the Peak Profiles in Energy-Dispersive Powder X-ray Diffraction with Synchrotron Radiation.* J. Appl.Cryst, 1997. **30**: p. 1008-1015.

4.11. K. T. V. Rao and R. O. Ritchie, Met Trans A, 1991. **22A**: p. 191.

4.12. M. Croft, Z. Zhong, N. Jisrawi, I. Zakharchenko, R. L. Holtz, J. Skarikta, T. Fast, K. Sadananda, M. Lakshmipathy and T. Tsakalakos, *Strain Profiling of Fatigue Crack Overload Effects Using Energy Dispersive X-ray Diffraction.* International Journal of Fatigue, 2005. **27**: p. 1408-1419.

4.13. J. R. Rice, *The Mechanism of Crack Tip Deformation and Extension by Fatigue.* Fatigue Crack Propagation, Special Technical Publication 415, ASTM, Philadelphia, 1967: p. 247-311.

4.14. J. E. Allison, *Fracture Mechanics, ASTM STP 677, (C.W. Smith, Ed).* American Society for Testing and Materials, 1979: p. 550-562.

4.15. M. S. Ramos, M. V. Pereira, F. A. Darwish, S. H. Motta and M. A. Carneiro, *Effect of Single and Multiple Overloading on the Residual Fatigue Life of a Structural Steel.* Fatigue Fract Engng Mater Struct, 2003. **26**: p. 115-121.

Chapter 5

Investigation of macro-residual stress distribution in welded components

In the previous chapter, high resolution strain and stress mapping using synchrotron X-ray diffraction around a fatigue crack has been described. Although this investigation allowed us to understand in detail about the local crack tip strain and stress variations, as well as the events taking place behind the crack tip, in practice such high resolution mapping is not possible in welded structures due to the presence of relatively larger grain sizes in the weld as well as in the bulk material. Industrial welds rarely use the fine–grained alloys used for the synchrotron X-ray experiments. Welding can generate significant macro residual stress within a component, which is of concern to engineers as fatigue life can be significantly affected by it. Due to the fact that most engineering structures have a larger grain size (typically 20-100 microns) than the fine grained Al-5091 alloy discussed in the previous chapter, a larger gauge volume (compared to the very small gauge used in the high resolution stress map described in previous section) needs to be used in order to obtain information from a sufficiently large population of grains to obtain macroscopic strain and stress. Thus, the neutron diffraction technique is the ideal tool in this sort of measurement, as it works with a large gauge volume, and where a diffraction angle close to 90^{o} enables investigation in three principal directions inside the bulk material.

This chapter describes the measurement of weld residual stress distributions and related issues in three parts. In the first part, a detailed description of macro-residual

stress measurement, using neutron diffraction, in a bead-on-plate 316L weld specimen is presented, along with a detailed study of the parent material. The neutron diffraction results are also compared with results obtained from the contour method. The second part discusses the significance of the use of sample-specific residual stress distribution results in fatigue life prediction models, particularly in the case of welded material. To illustrate this effect, a neutron diffraction experiment was carried out in two Metal Inert Gas (MIG) welded compact tension (CT) specimens of Al-alloy and the stress results were then compared to the residual stress measured in the original plate from where the CT specimens were extracted.

Finally, the third part describes the redistribution of residual stress in an MT (middle cracked tension) specimen due to fatigue crack growth. To study the redistribution phenomenon an experiment was conducted in fatigue-cracked VPPA welded MT specimens using neutron diffraction.

5.1 Residual stress in a bead-on-plate 316L welded specimen

5.1.1 Background

316L austenitic stainless steel is widely used in steam pipes in nuclear power plants. Different parts of these pipes are welded according to the precise design requirements. Residual stresses generated during the welding of these pipes are a cause of concern to engineers as crack generation could lead to a premature failure. Hence, it is very important to have a proper knowledge of the residual stress distribution around the weld region to be able to predict the service life. To address this problem an investigation was carried out by Task group 1 (TG1) of the European

NET project [5.1], as part of which nominally identical round robin 316L welding specimens have been prepared to study the weld residual stress distribution using several destructive and non-destructive techniques. The final objective was to validate the Finite Element weld simulation-modelling methods. In this current study, an attempt has been made to measure the variation in residual stress along the length of single weld bead-on-plate specimens using neutron diffraction and other techniques and thereby characterise stress gradients and the nature of welding torch start and stop end stress concentration effects. Finally, the neutron diffraction results are compared with the results obtained from other techniques i.e. the contour method.

5.1.2 Specimen description

Four nominally identical bead on plate AISI type 316L stainless steel specimens were manufactured by Mitsui Babcock. The chemical composition (wt%) of the 316L stainless steel plate was 0.02 C, 1.404 Mn, 0.027 P, 0.0011 S, 0.582 Si, 11.11 Ni, 17.834 Cr, 2.06 Mo, 0.0132 N, balance-Fe. All four specimens, labelled as A1.1, A1.2, A1.3, A1.4, were taken from a single piece of solution treated AISI type 316L stainless steel plate which had nominal dimensions of around 600 x 150 x 50 mm^3. A single weld bead was deposited along the centre line of all the specimens using automated Tungsten Inert Gas Welding (TIG) as shown in figure 5.1. The filler wire was 0.8 mm 316S96 Mini Mig with specification A5.9.93 (ASME) and ER316H. The weld torch traverse distance was 60 mm, labelled as AC in figure 5.1. The welding conditions were monitored and recorded to facilitate FE analysis. In this current work, the residual stress field of the A1.1 sample was measured using neutron diffraction at the ISIS facility of the Rutherford Appleton Laboratory, UK. A

schematic representation and a photograph of specimen A1.1 are given in figures 5.1 and 5.2 respectively. The thickness and width of specimen A1.1 were measured to be 17 mm and 120 mm respectively. The welding direction can be seen in figure 5.1, which will be referred to as the longitudinal direction (x). The direction across the

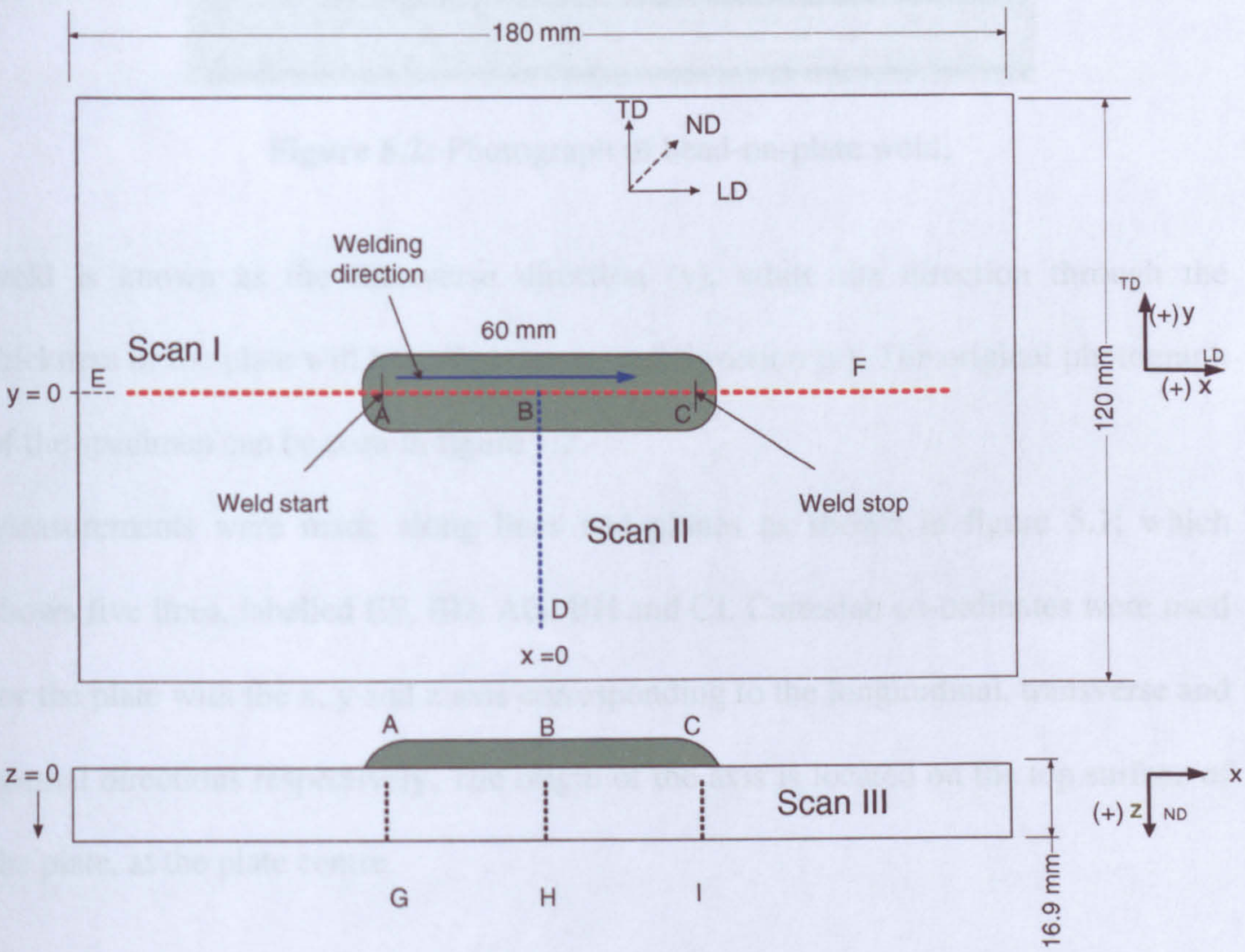

Figure 5.1: Schematic diagram of bead-on-plate weld.

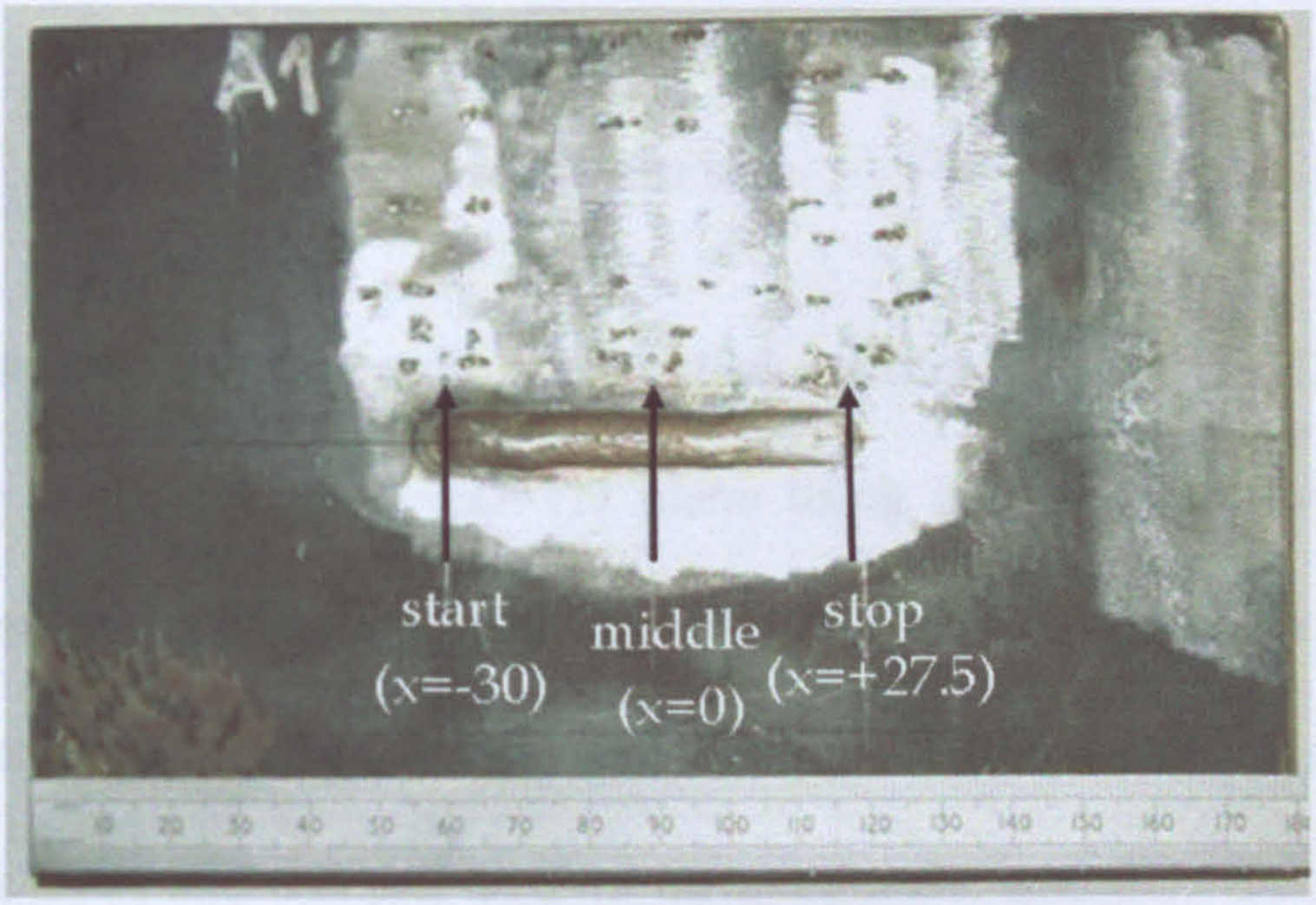

Figure 5.2: Photograph of bead-on-plate weld.

weld is known as the transverse direction (y), while the direction through the thickness of the plate will be called the normal direction (z). The original photograph of the specimen can be seen in figure 5.2.

Measurements were made along lines and planes as shown in figure 5.1; which shows five lines, labelled EF, BD, AG, BH and CI. Cartesian co-ordinates were used for the plate with the x, y and z axis corresponding to the longitudinal, transverse and normal directions respectively. The origin of the axis is located on the top surface of the plate, at the plate centre.

5.1.3 Specimen characterisation

It is a well known fact that material characteristics, such as microstructure, grain size and texture play an important role in determination of residual stress using the diffraction technique. In the next few sections the microstructure, grain size and texture studies on the investigated material will be presented.

5.1.3.1 Microstructure and grain size

The microstructures of the weld region, heat affected zone (HAZ) and parent material were observed in the LD–TD plane using optical microscopy. For that purpose the sample was first cut by electro discharge machining, which ensures very smooth cutting. After cutting, one of the cut sections was chosen for the microstructure study and was prepared for metallographic analysis. The macrograph

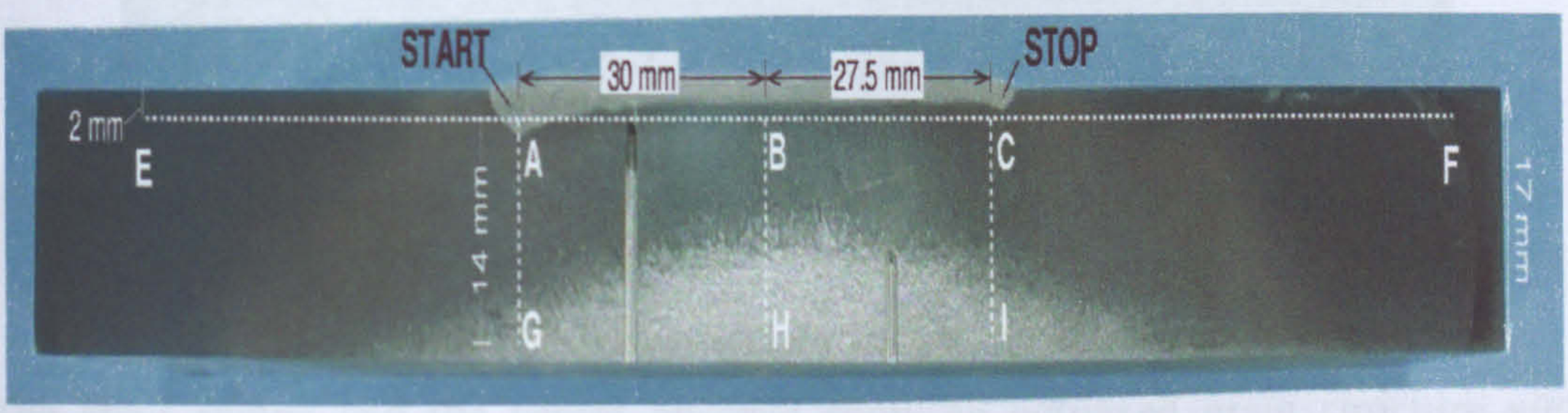

Figure 5.3: Cross- sectional macrograph of the LD-ND plane of the bead on plate weld.

of the investigated plane is shown in figure 5.3. The weld start and stop regions and its shape can be very clearly distinguished from the macrograph, although the heat affected zone is not visible. In the microstructural study, a columnar dendritic grain structure was observed in the weld region and the dendrites are elongated along the welding direction (figure 5.4).

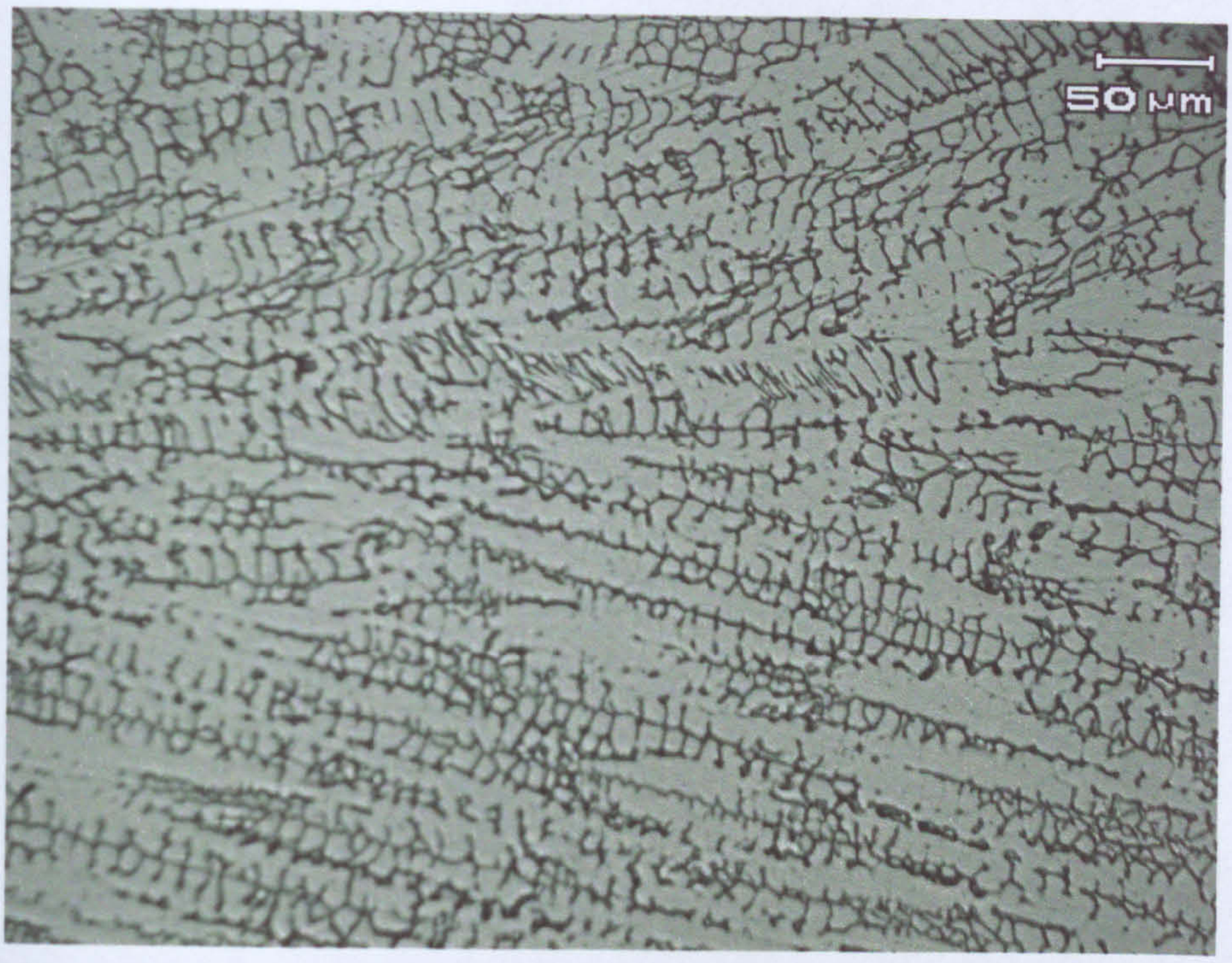

Figure 5.4: Columnar dendritic microstructure in the weld in the bead on plate specimen along the weld direction.

The HAZ region and the parent material show an equiaxed grain structure with carbide precipitation at the grain boundaries (figures 5.5 and 5.6). The grain size has also been measured using optical microscopy. The average grain size of the heat affected zone and the parent material does not seems to vary significantly. For the LD-ND plane, the grain size in the parent material varies between 50-70 microns in the longitudinal direction and around 30-40 microns in the through-thickness direction.

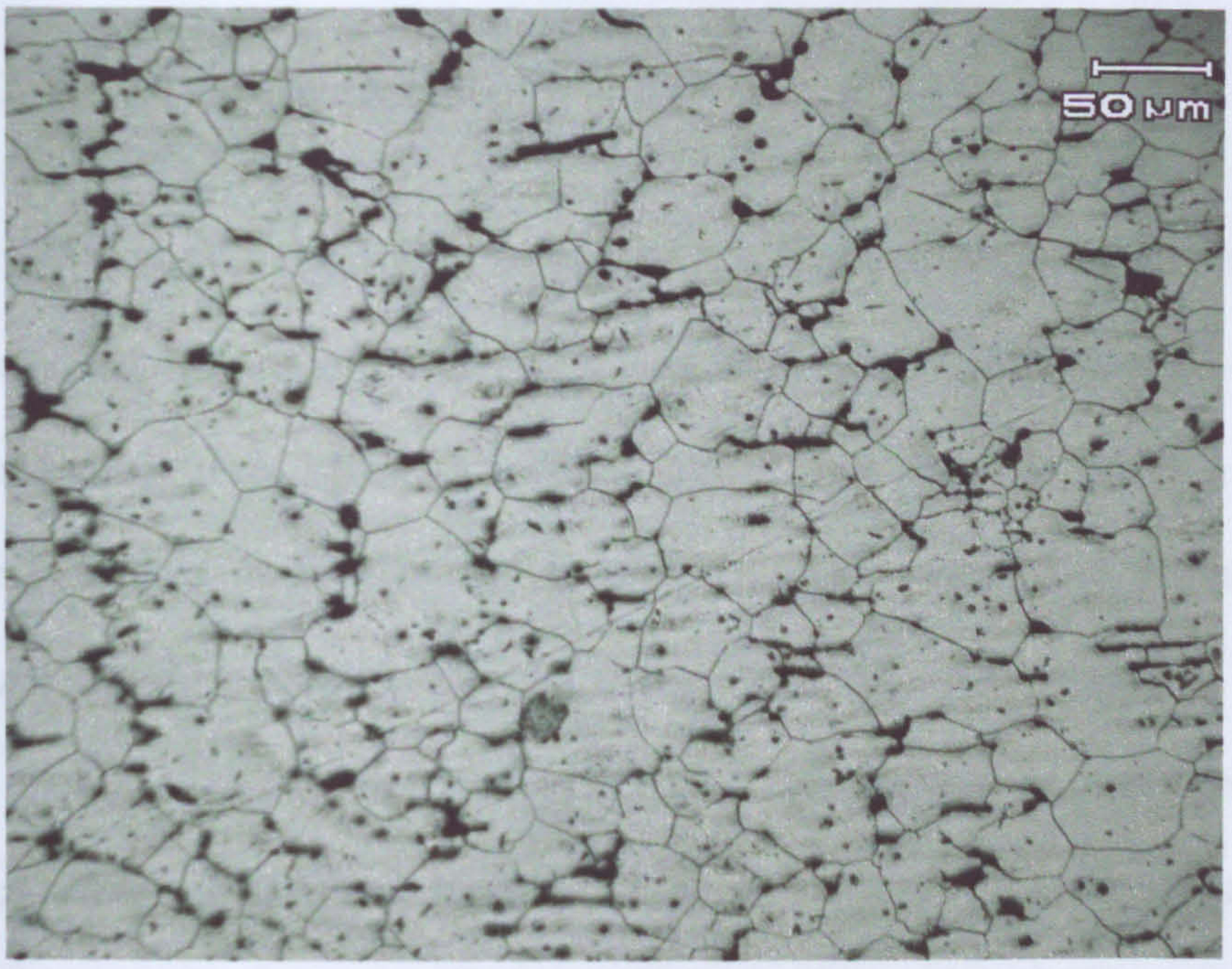

Figure 5.5: Equiaxed grain structure in the HAZ with carbide precipitates at the grain boundaries.

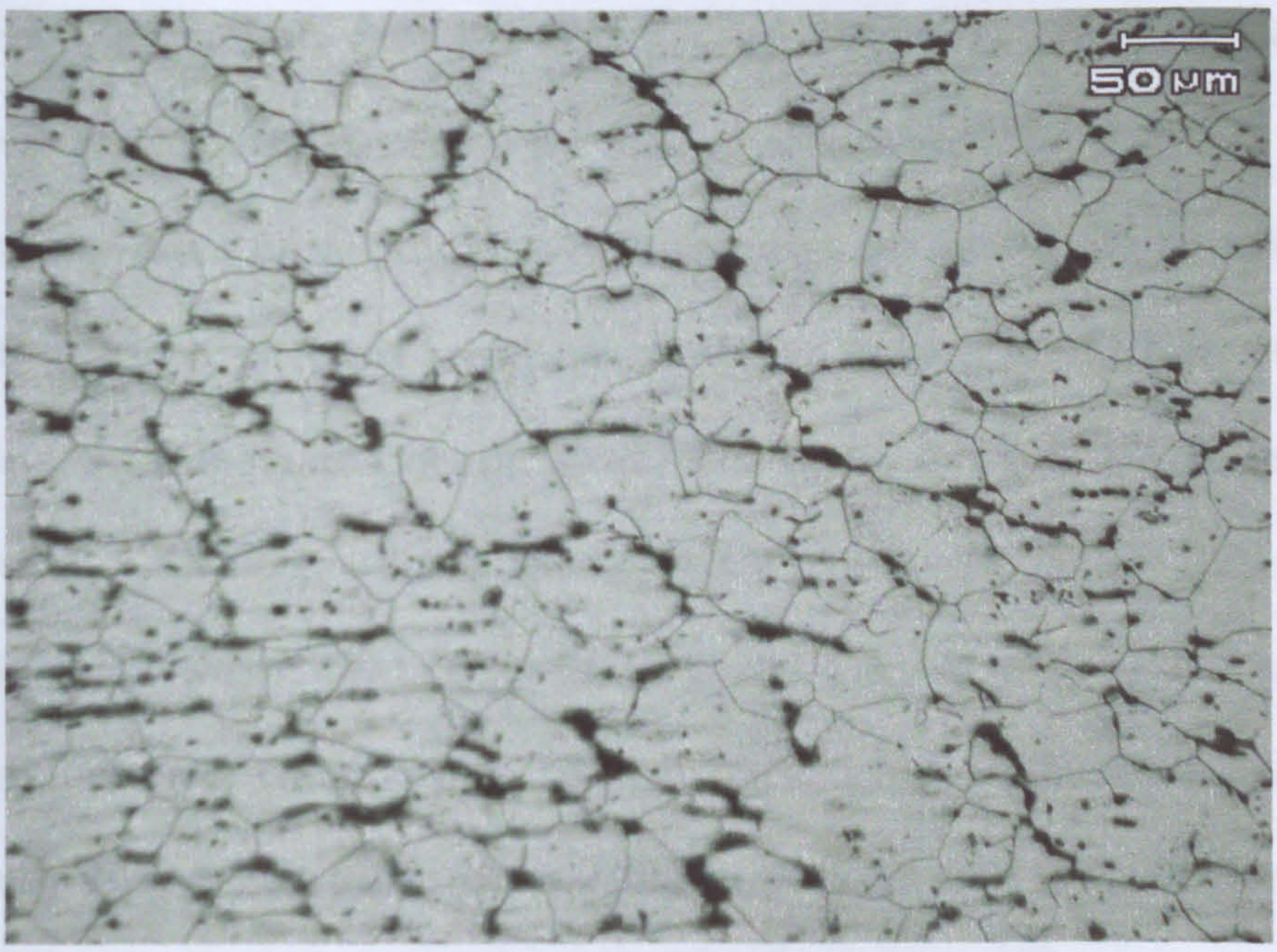

Figure 5.6: Equiaxed grain structure in the bulk material with carbide precipitate at the grain boundaries.

5.1.3.2 Texture analysis

The grain orientation relative to the sample axis has been determined by the electron back scattered diffraction (EBSD) technique. In the current investigation texture was measured using the Channel 5 software (from HKL technology) in a JEOL 820 scanning electron microscope (SEM) set up in EBSD mode [5.2]. For this purpose two small samples, each of 10 x 6 x 2 mm^3 were extracted, one from the welded region and the other one from the parent plate, from the bead on plate specimen. The samples were ground and then polished to a 1 micron finish and finally electropolished using a Struers electrolyte A2 solution. To ensure that a sufficient number of grains were being sampled, the EBSD scan was carried out using 20 x 20 microns step intervals over a total 1.5 x 1.5 mm^2 area. The results from these measurements are represented in the form of pole figures (figures 5.7 (a and b)). It can be seen from figure 5.7 (a), which represents the pole figure of bulk material, that there is no preferred orientation hence no texture in the bulk material. In contrast, the pole figure from the weld metal shown in figure 5.7 (b) shows some preferred orientation, with a strong <100> component in all three principal directions. Therefore, if the measured line contains any weld metal, the interpretation of the strain and corresponding stress of these particular points has to be done carefully which otherwise might incorporate significant error in the final results.

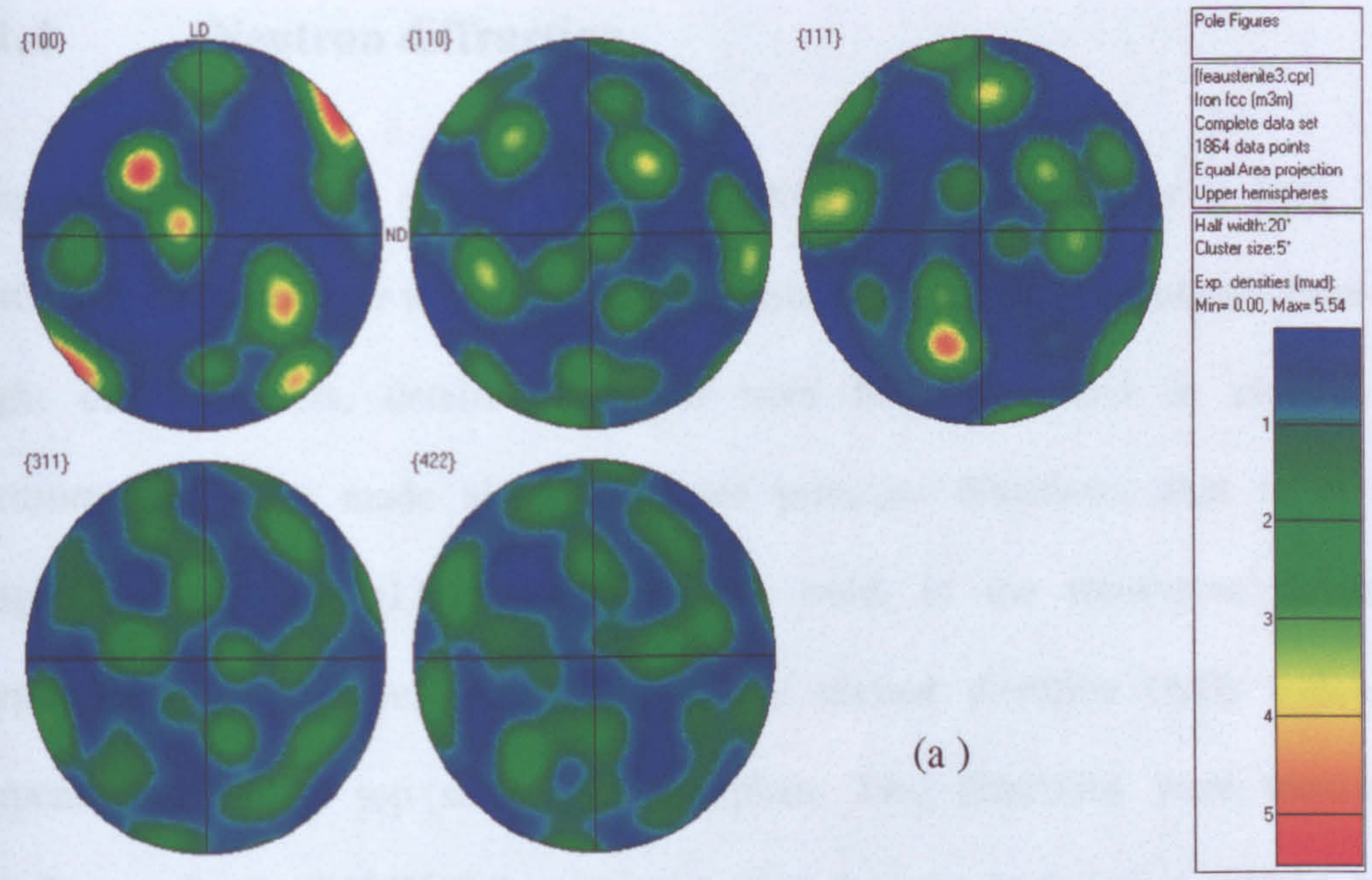

(a)

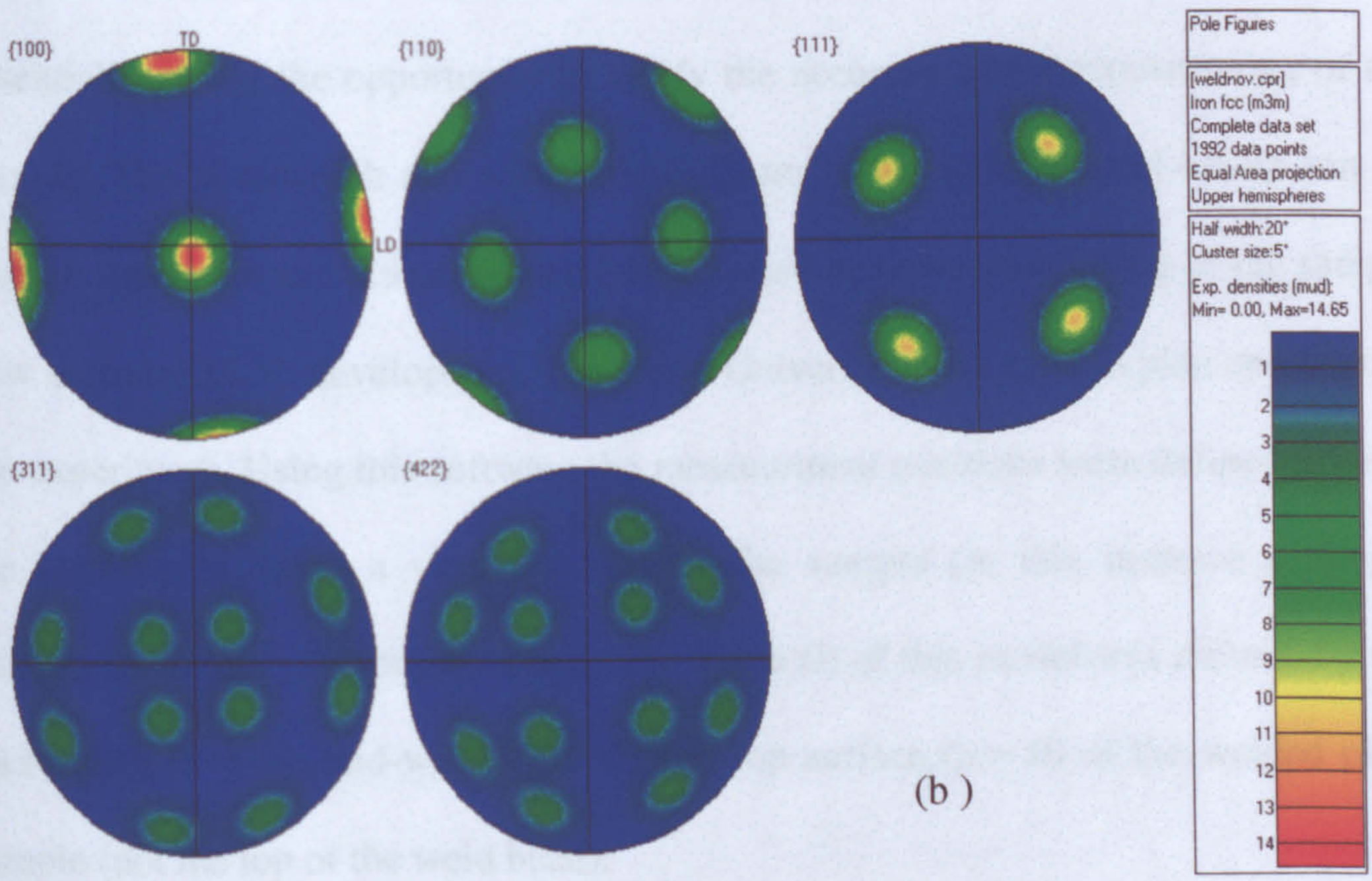

(b)

Figure 5.7: Pole figures of (a) bulk material and (b) weld material investigated by EBSD technique.

5.1.4 Neutron diffraction

Neutron diffraction was carried out in the ENGIN-X diffractometer at ISIS. The ENGIN-X diffractometer works on the same principle as other conventional time-of-flight diffractometers, details of which have been discussed in chapter 2. Measurements were made along the three principal directions: that is in the longitudinal direction (LD) parallel to the weld, in the transverse direction perpendicular to the weld (TD) and in the normal direction (ND) which is perpendicular to the top surface of the plate. Two directions were measured simultaneously, as ENGIN-X has two opposing detector banks each centred on a Bragg angle (2θ) of ± 90 degrees. The sample had to be repositioned once to measure the third direction; consequently, the normal direction was measured twice, essentially giving the opportunity to verify the accuracy of the repositioning of the sample. The photograph and schematic diagram of the experimental set-up can be seen in figure 5.8 and 5.9 (a) respectively. To aid accurate positioning of the sample new software [5.3], developed at The Open University, was used to plan and control the experiment. Using this software the measurement positions were defined prior to the experiment using a virtual model of the sample (in this instance a simple rectangular plate). The origin (x = 0, y = 0, z = 0) of this model was defined by the mid-length (x = 0), mid-width (y = 0) and top surface (z = 0) of the welded plate sample (not the top of the weld bead).

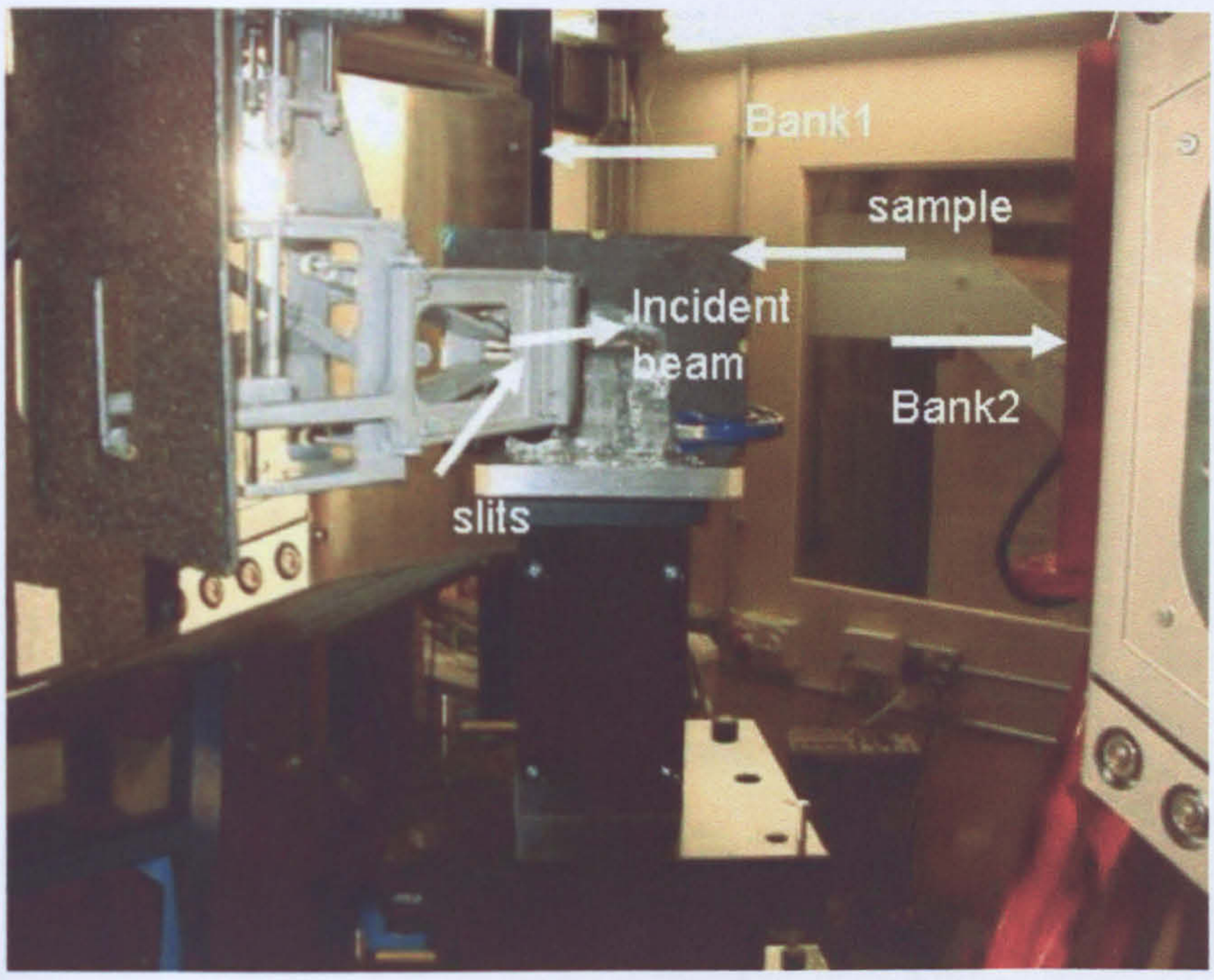

Figure 5.8: Experimental set-up of plate A1.1 on ENGIN-X at ISIS.

The position of the sample relative to the ENGIN-X instrument was determined using laboratory theodolites and input into the program. The exact weld bead start and stop positions were determined optically using the theodolites and were taken to be 30 mm (x = -30 mm) and 27.5 mm (x = +27.5 mm) respectively from the plate centre. Once this was done the location of each of the measurements was determined automatically by the software. The software was also used to calculate the neutron path length of each measuring point and this provided useful estimates of the

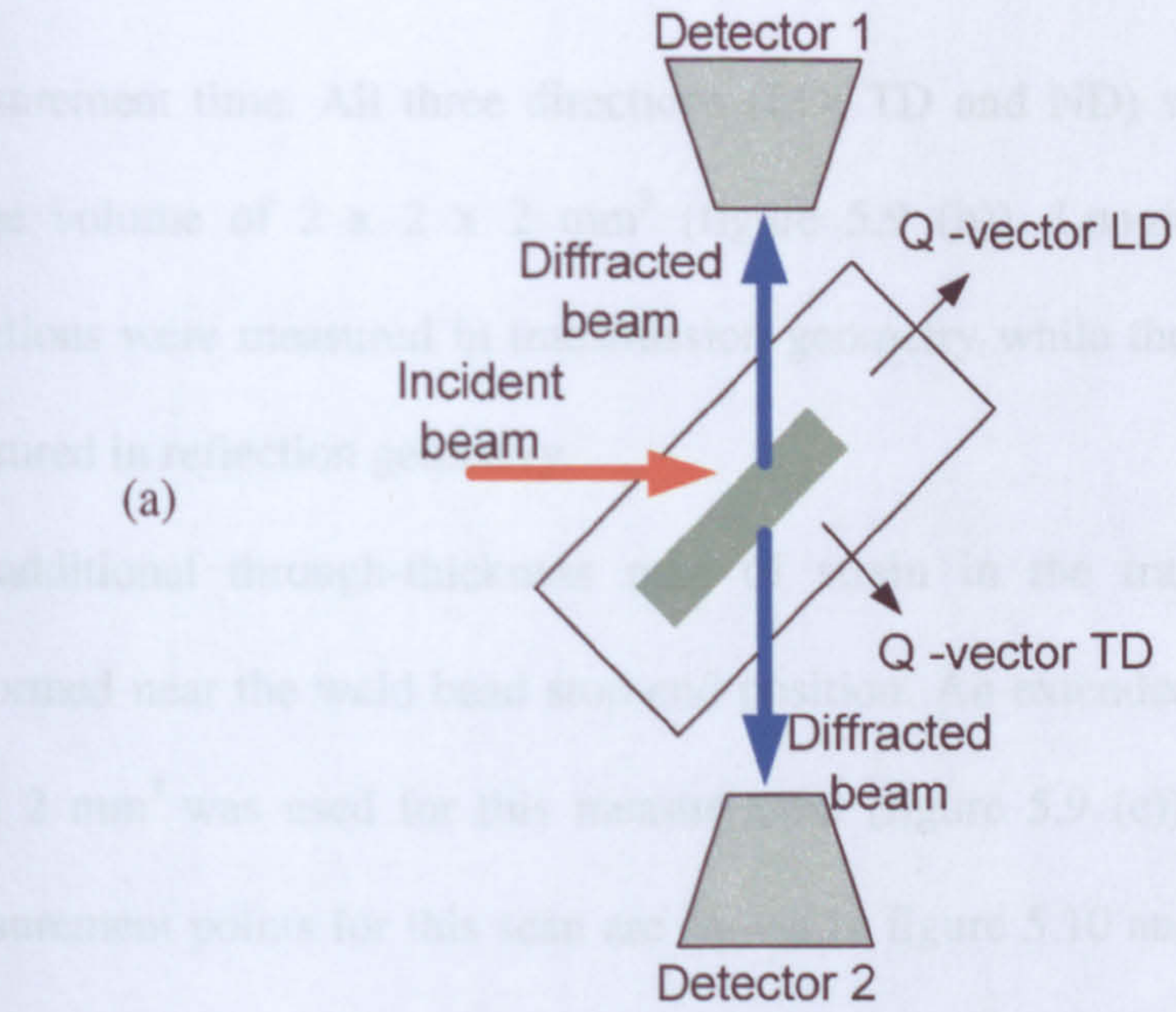

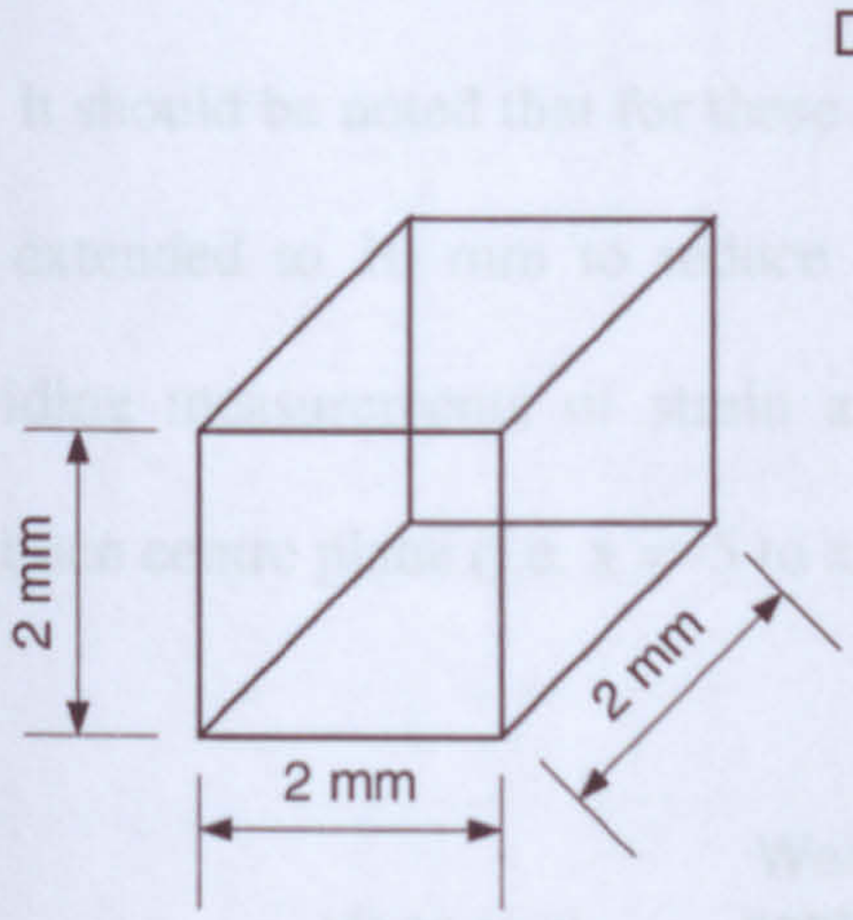

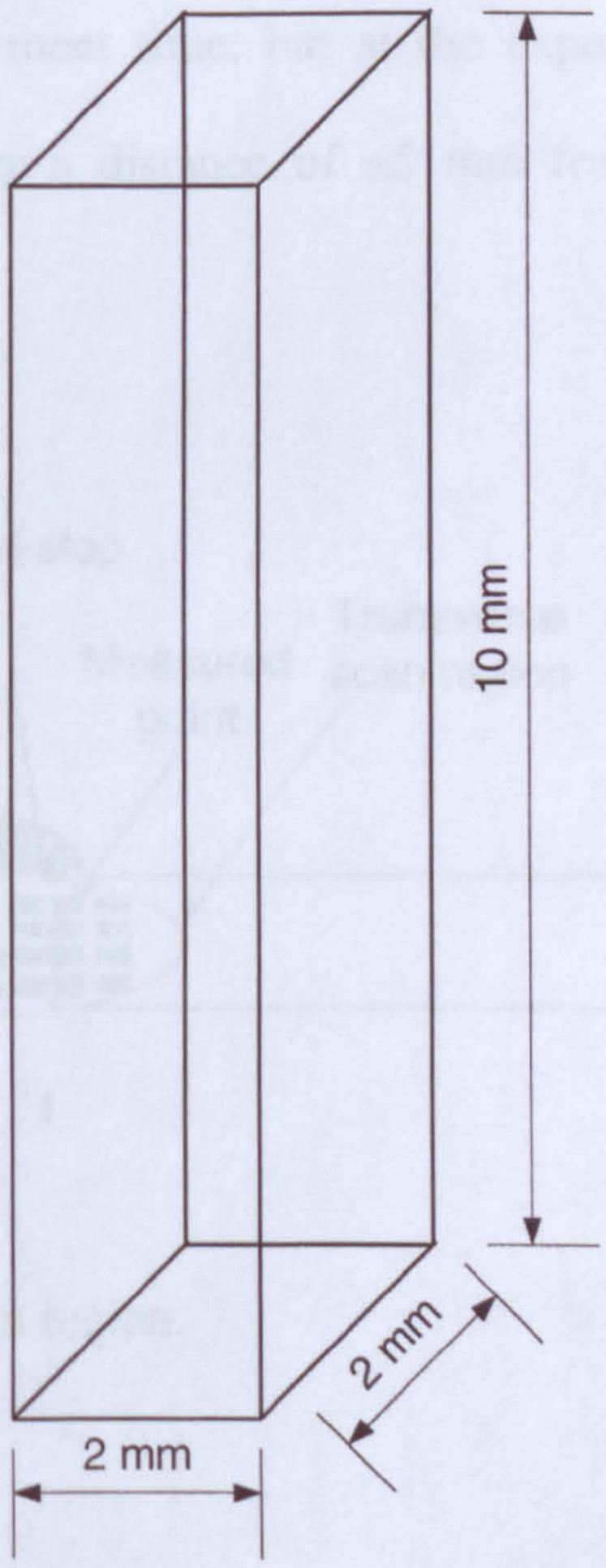

Figure 5.9: The schematic diagram of (a) diffraction geometry on ENGIN-X, (b) the cubic gauge volume using beam size of 2 x 2 x 2 mm^3 and (c) gauge shape used in the transverse scan using beam size 2 x 10 x 2 mm^3.

measurement time. All three directions (LD, TD and ND) were measured using a gauge volume of 2 x 2 x 2 mm^3 (figure 5.9 (b)). Longitudinal and transverse directions were measured in transmission geometry while the normal direction was measured in reflection geometry.

An additional through-thickness map of strain in the transverse direction was performed near the weld bead stop-end position. An extended gauge volume of 2 x 10 x 2 mm^3 was used for this measurement (figure 5.9 (c)). The locations of the measurement points for this scan are shown in figure 5.10 and are tabulated in table 5.1. It should be noted that for these measurements the height of the incoming beam was extended to 10 mm to reduce the measurement time, but at the expense of providing measurements of strain averaged over a distance of ±5 mm from the specimen centre plane (i.e. x = -5 to x = 5 mm).

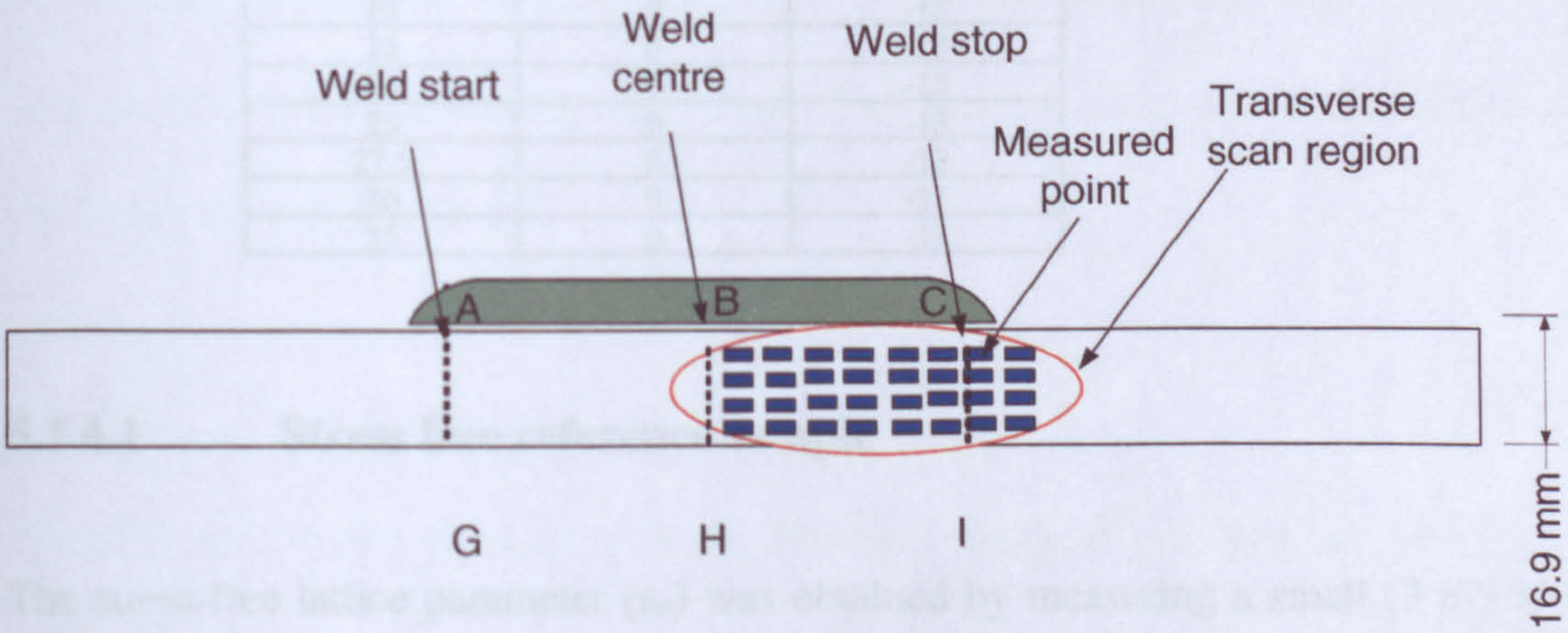

Figure 5.10: Schematic diagram of transverse scan region.

Table 5.1: Co-ordinates of transverse strain map measurements

X	Y	Z
0	0	-4
5	0	-4
10	0	-4
15	0	-4
20	0	-4
25	0	-4
27.5	0	-4
30	0	-4
35	0	-4
0	0	-7
5	0	-7
10	0	-7
15	0	-7
20	0	-7
25	0	-7
27.5	0	-7
30	0	-7
35	0	-7
0	0	-10
5	0	-10
10	0	-10
15	0	-10
20	0	-10
25	0	-10
27.5	0	-10
30	0	-10
35	0	-10
0	0	-13
5	0	-13
10	0	-13
15	0	-13
20	0	-13
25	0	-13
27.5	0	-13
30	0	-13
35	0	-13

5.1.4.1 Stress free reference sample

The stress-free lattice parameter (a_o) was obtained by measuring a small (3 x 3 x 3 mm^3) cube, which was cut from one corner of the sample by EDM. The small cube was carefully measured using a gauge volume of 2 x 2 x 2 mm^3, and the lattice parameter obtained was used to calculate the strain for all the points used in the measurement of the plate. In order to confirm whether the cube holds any substantial amount of stress, a conventional $\sin^2\psi$ measurement (discussed in chapter two)

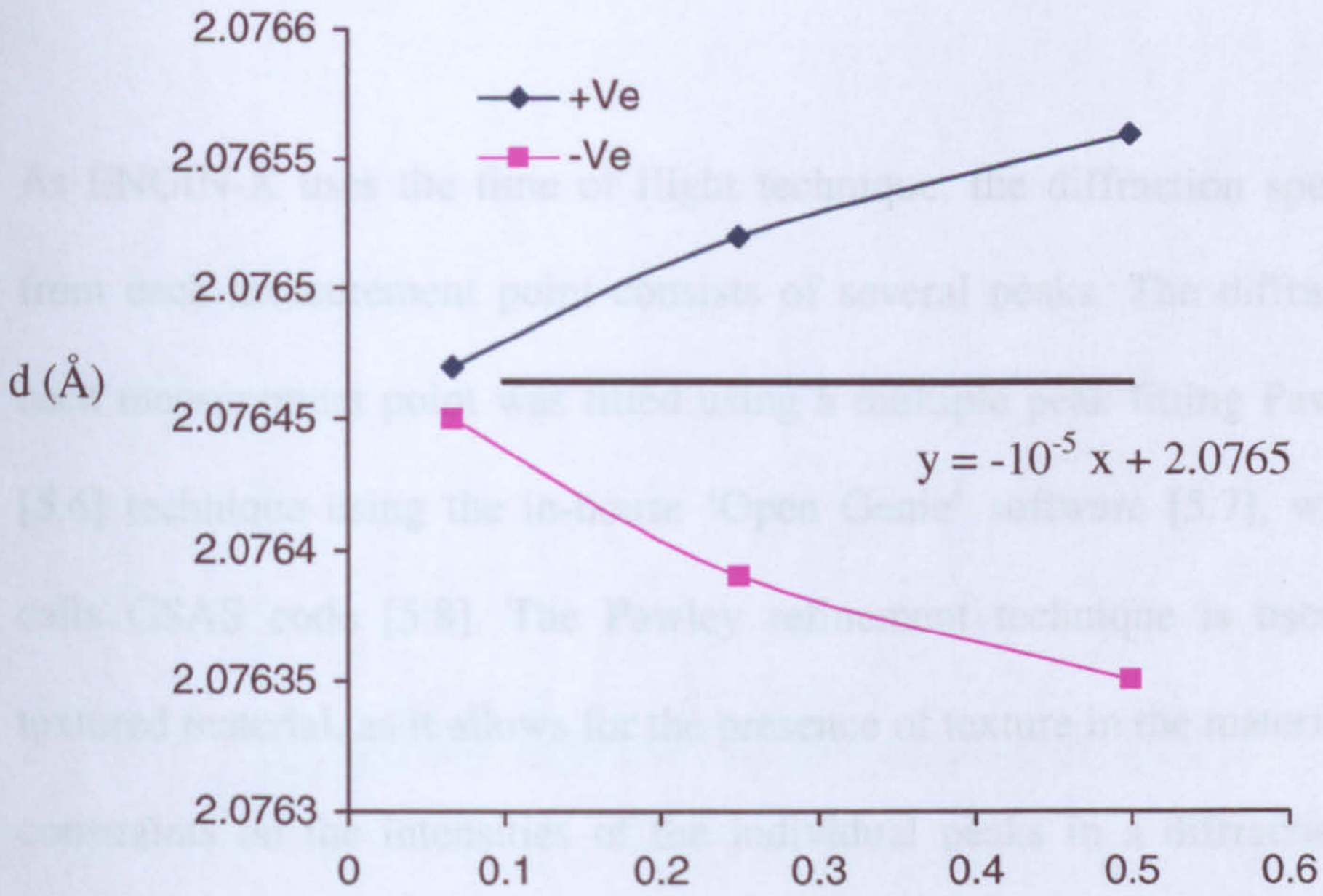

Figure 5.11: d versus $\sin^2\psi$ plots obtained from neutron diffraction experiment.

was carried out by measuring the cube sample at different ψ angles (+15,+30,+45,-15,-30,-45). The d vs $\sin^2\psi$ plot (figure 5.11) shows the ψ splitting of the curve which indicates the presence of shear stress. The principal stress was calculated using the following equation [5.4] :

$$\sigma_\phi = (\frac{E}{1+\upsilon})m \qquad (5.1)$$

Where E is the elastic modulus, ν is the Poisson's ratio and m is the slope of the d vs $\sin^2\psi$ plot. The value of m was calculated to be -10^{-5}. Finally, using equation 5.1 the stress was calculated to be -1.5 MPa which is significantly small and within the error range of stress calculation. The shear stress was also calculated using equations from Cohen et al [5.5] and calculated to be 5 MPa. This result confirms the fact that the cube does not hold any significant stress.

5.1.4.2 Data analysis

As ENGIN-X uses the time of flight technique, the diffraction spectrum obtained from each measurement point consists of several peaks. The diffraction profile of each measurement point was fitted using a multiple peak fitting Pawley refinement [5.6] technique using the in-house 'Open Genie' software [5.7], which eventually calls GSAS code [5.8]. The Pawley refinement technique is useful in studying textured material, as it allows for the presence of texture in the material by putting no constraints on the intensities of the individual peaks in a diffraction spectrum. A typical diffraction spectrum and its associated refinement are shown in figures 5.12 and 5.13. Although up to seven peaks could be distinguished in some diffraction spectra, the five strongest peaks (111), (200), (220), (311) and (222) were analysed using Pawley fitting routine to obtain a better statistic of uncertainty in the measured lattice parameter. From the measured lattice spacing of the welded specimen and stress-free reference cubes the strain was calculated from:

$$\varepsilon = \frac{a - a_0}{a} \tag{5.2}$$

Where a is the lattice parameter at each individual measurement point of the specimen and a_0 is the measured stress free lattice parameter in each detector bank.

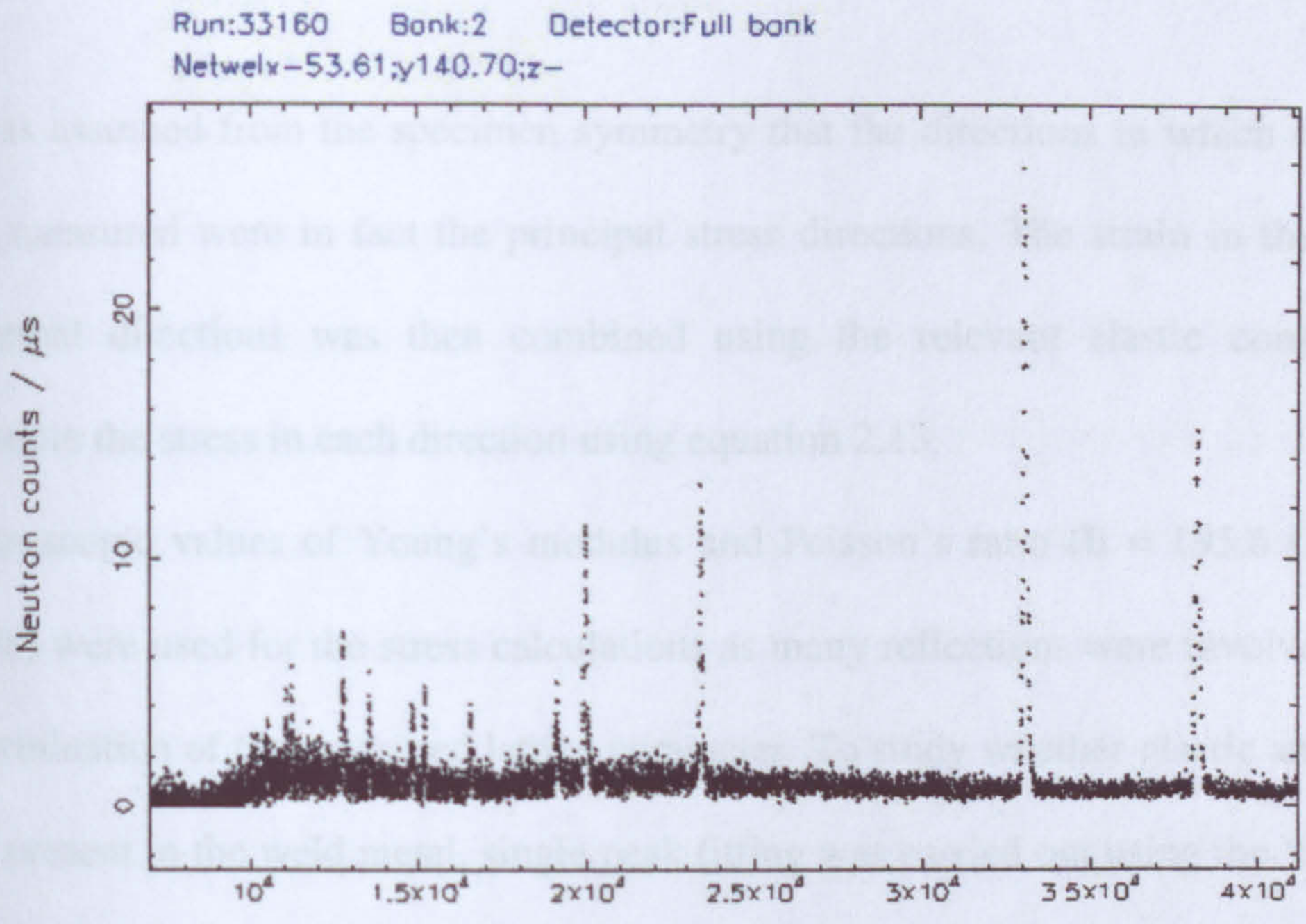

Figure 5.12: A typical diffraction spectrum from sample A1.1.

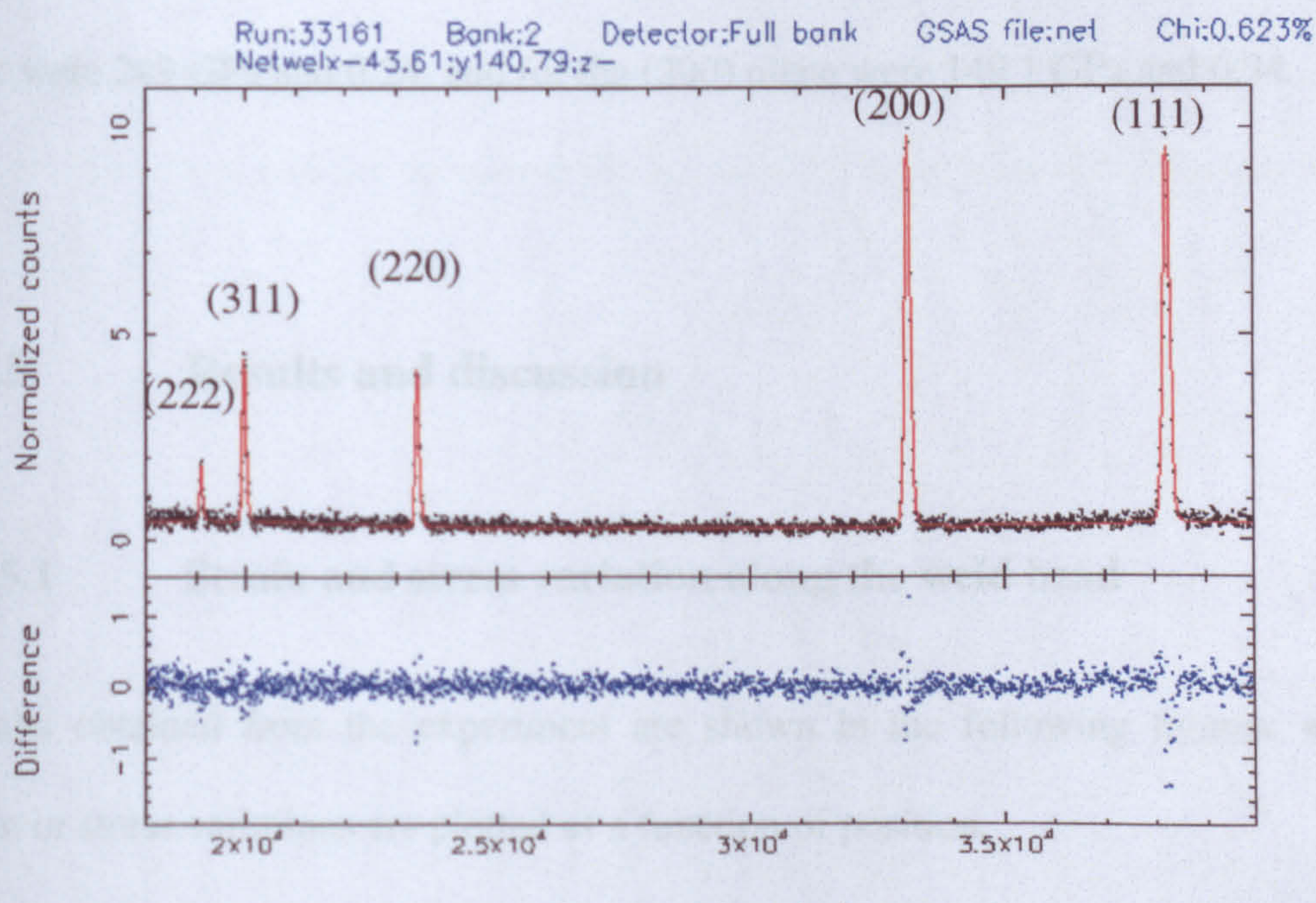

Figure 5.13: Pawley fitted diffraction spectrum from sample A1.1.

It was assumed from the specimen symmetry that the directions in which the strain was measured were in fact the principal stress directions. The strain in these three principal directions was then combined using the relevant elastic constants to calculate the stress in each direction using equation 2.13.

Macroscopic values of Young's modulus and Poisson's ratio (E = 195.6 GPa, v = 0.294) were used for the stress calculations as many reflections were involved in the determination of the measured lattice parameter. To study whether plastic anisotropy was present in the weld metal, single peak fitting was carried out using the 'fit_peak' routine, which is available within the Open Genie software package. Only (111) and (200) peaks were sufficiently intense to be fitted using the single peak fitting routine. To calculate the stress response using these individual peaks, different sets of Young's Moduli and Poisson's ratios were used which were calculated using the Kroner model [5.9]. The values of Young's moduli and Poisson's ratio for the (111) peak were 249 GPa and 0.24, and for the (200) plane were 149.1 GPa and 0.34.

5.1.5 Results and discussion

5.1.5.1 Strain and stress variation along the weld bead

Results obtained from the experiment are shown in the following figures, where strain or stress variations are plotted as a function of position.

Figures 5.14 and 5.15 show the longitudinal, transverse and normal direction residual strain and stress profiles measured along line EF (see figure 5.1), 2 mm below the top surface of the plate (y = 0, z = -2). It is evident from figure 5.14 that significant tensile strains have developed in both the longitudinal and transverse directions in the vicinity of the weld. The strain distribution patterns follow almost the similar trends in these two directions (LD and TD) with higher tensile strain near the welded region which reduces to almost zero in the bulk material, however the magnitude of the LD strain is higher than the TD strain. There appears to be a local increase in longitudinal strain associated with both the weld start and stop positions although the evidence for a weld stop effect is based mainly on a single measurement point. The maximum strain in the LD and TD direction is found to be 1590 microstrain and 940 microstrain respectively. The ND strain distribution shows a significant compressive strain near the weld region, with a maximum compressive strain of -1400 microstrain, which increases to zero in the bulk material. The transverse strain steadily increases and the normal strain decreases moving from the weld start to stop positions.

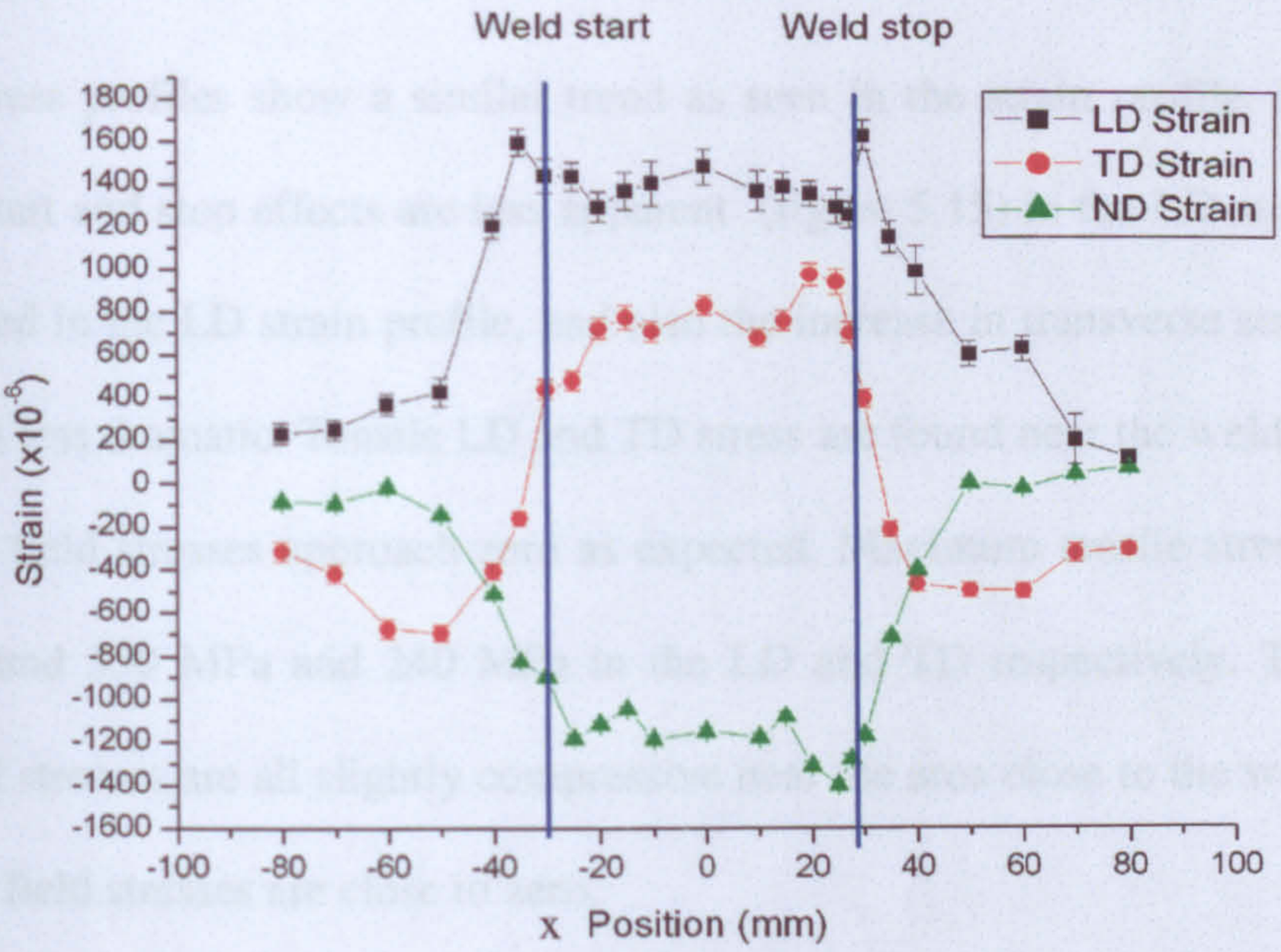

Figure 5.14: Residual strain variation along weld line EF, 2 mm under the top surface (y = 0, z = -2).

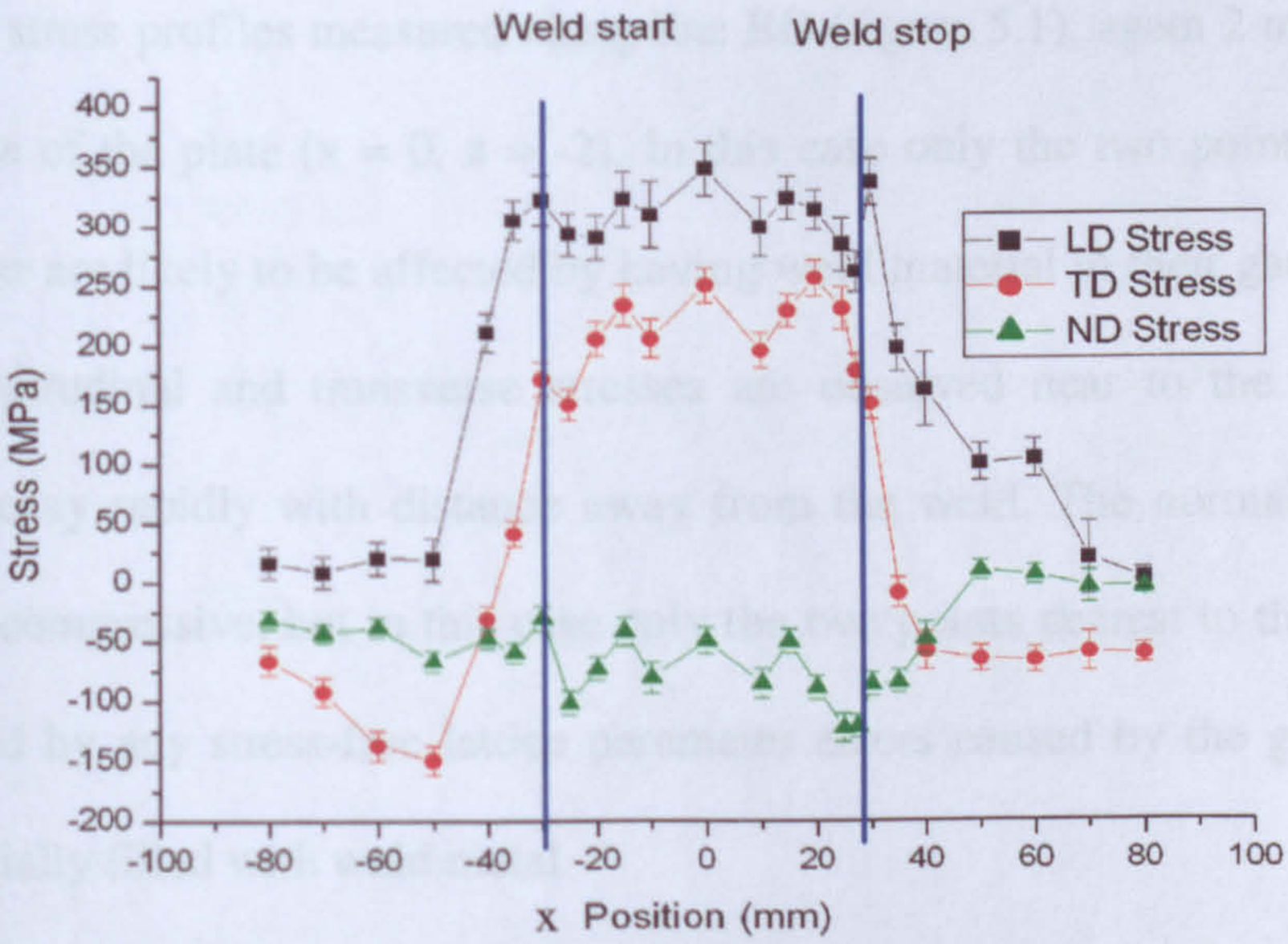

Figure 5.15: Residual stress variation along weld line EF, 2 mm under the top surface (y = 0, z = -2).

The stress profiles show a similar trend as seen in the strain profile. However, the weld start and stop effects are less apparent (figure 5.15) in the LD stress profile as observed in the LD strain profile, and also the increase in transverse stress along the weld is less dramatic. Tensile LD and TD stress are found near the weld region while the far field stresses approach zero as expected. Maximum tensile stress is found to be around 350 MPa and 240 MPa in the LD and TD respectively. The measured normal stresses are all slightly compressive near the area close to the weld metal and the far field stresses are close to zero.

5.1.5.2 Strain and stress variation across the weld bead

Figures 5.16 and 5.17 show the longitudinal, transverse and normal direction residual strain and stress profiles measured along line BD (figure 5.1), again 2 mm below the top surface of the plate (x = 0, z = -2). In this case only the two points nearest the weld centre are likely to be affected by having weld material in their gauge volumes. Large longitudinal and transverse stresses are observed near to the weld. These stresses decay rapidly with distance away from the weld. The normal stresses are again, all compressive, but in this case only the two points nearest to the weld could be affected by any stress-free lattice parameter errors caused by the gauge volume being partially filled with weld metal.

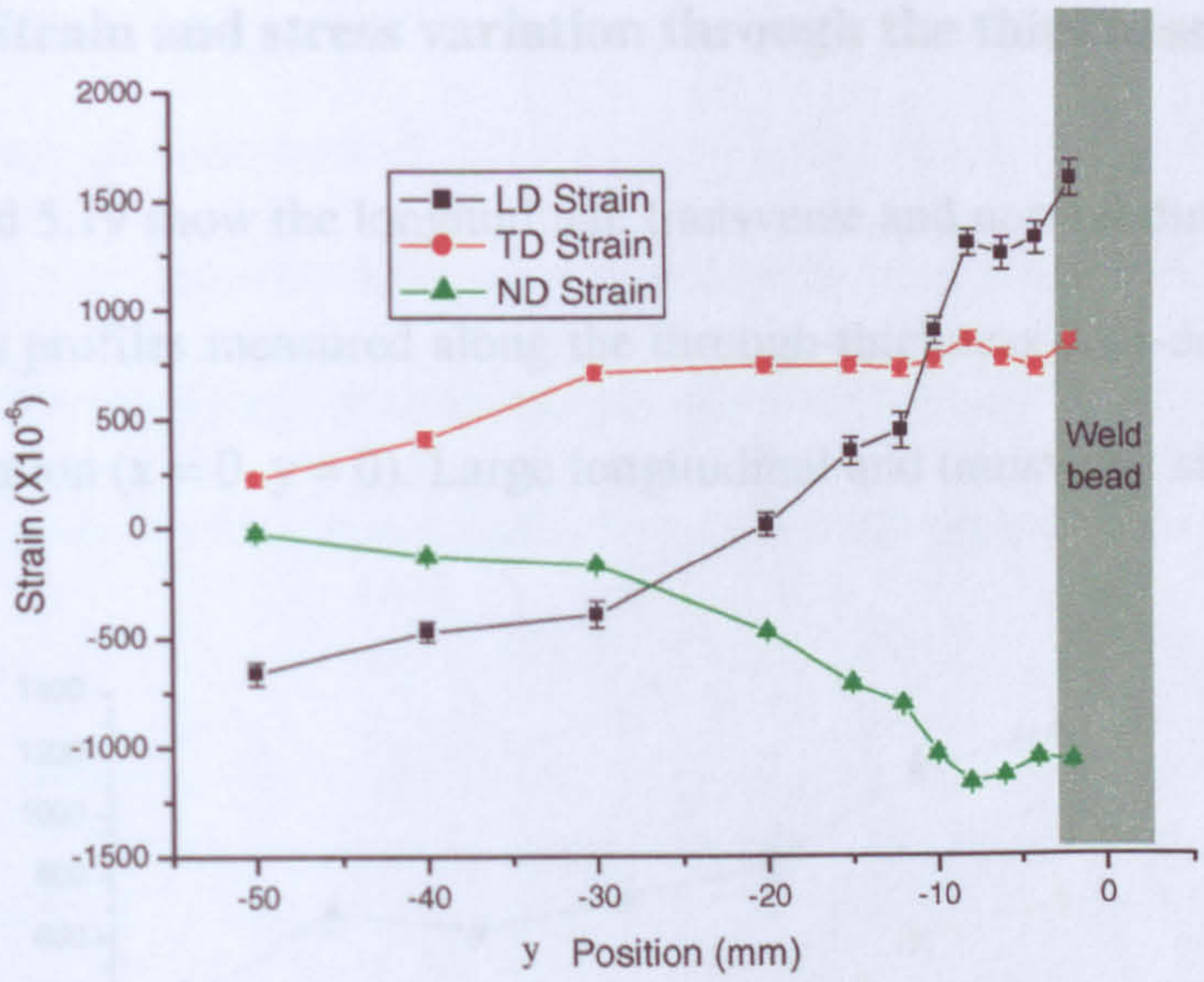

Figure 5.16: Residual strain variation along weld line BD, at 2 mm under the top surface (x = 0, z = -2).

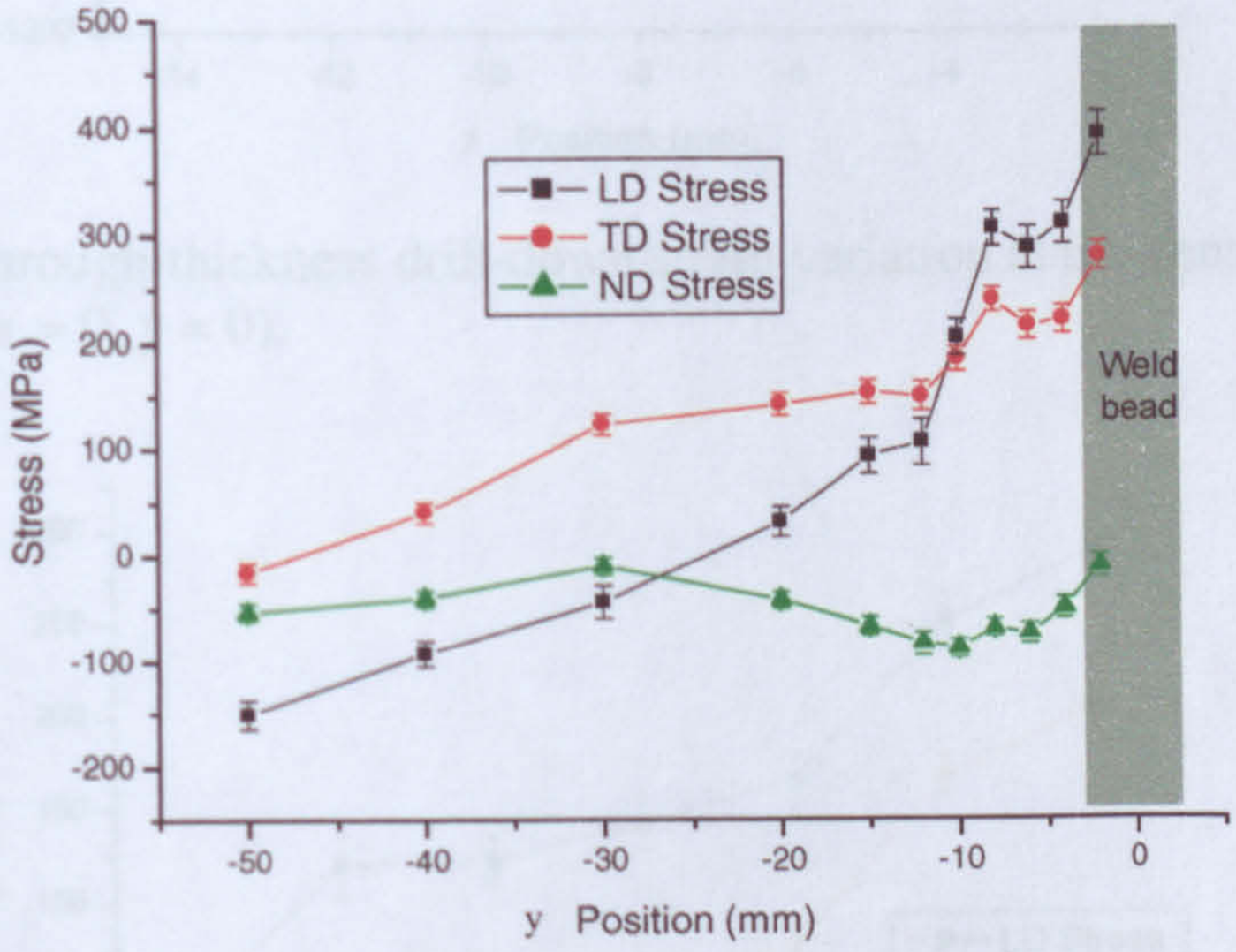

Figure 5.17: Residual stress variation along the weld line BD (figure 5.1) at 2 mm under the top surface (x = 0, z = -2).

5.1.5.3 Strain and stress variation through the thickness of the plate

Figures 5.18 and 5.19 show the longitudinal, transverse and normal direction residual strain and stress profiles measured along the through-thickness drill-down line at the weld centre location (x = 0, y = 0). Large longitudinal and transverse stresses occur

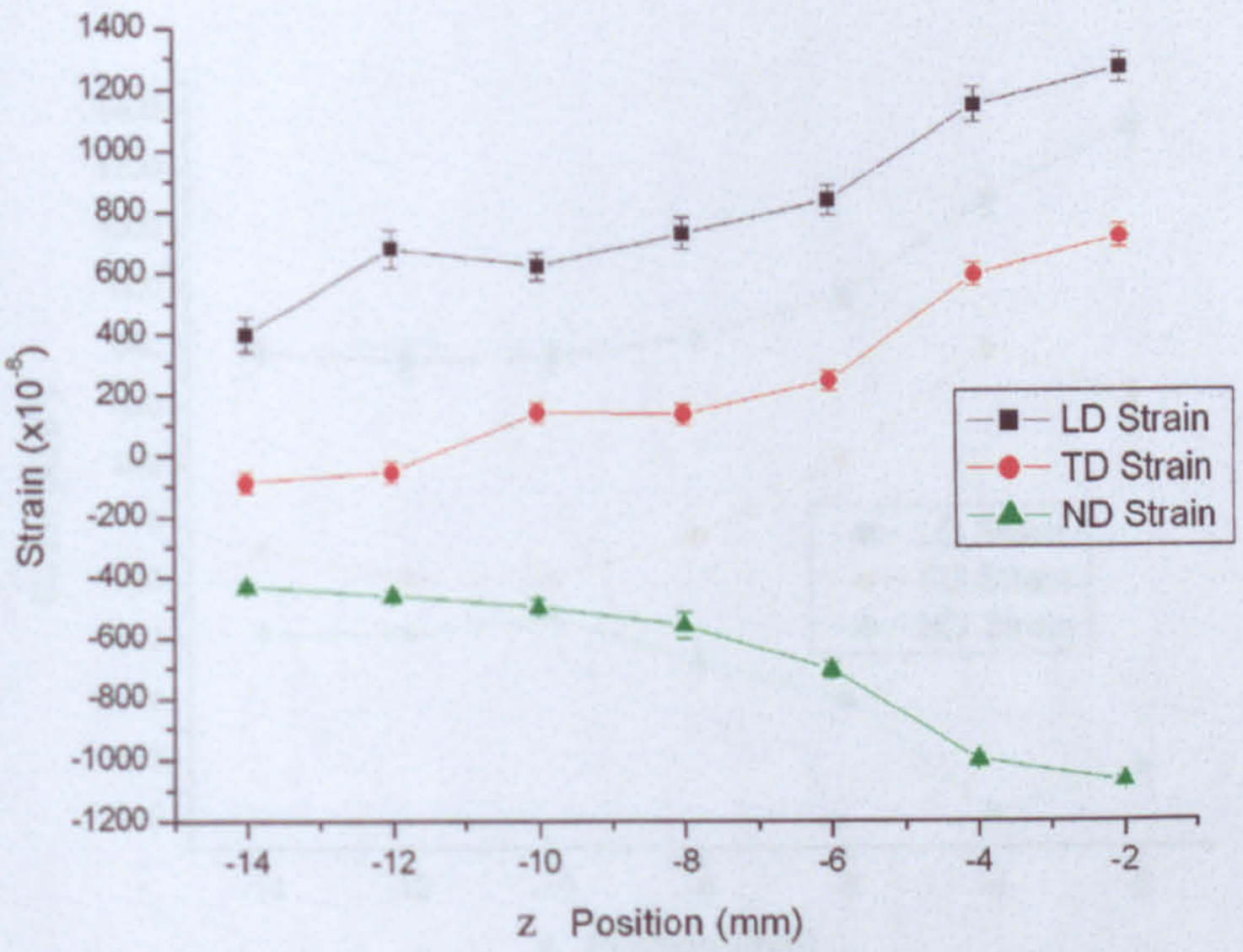

Figure 5.18: Through-thickness drill-down strain variation at the centre of the weld (x = 0, y = 0).

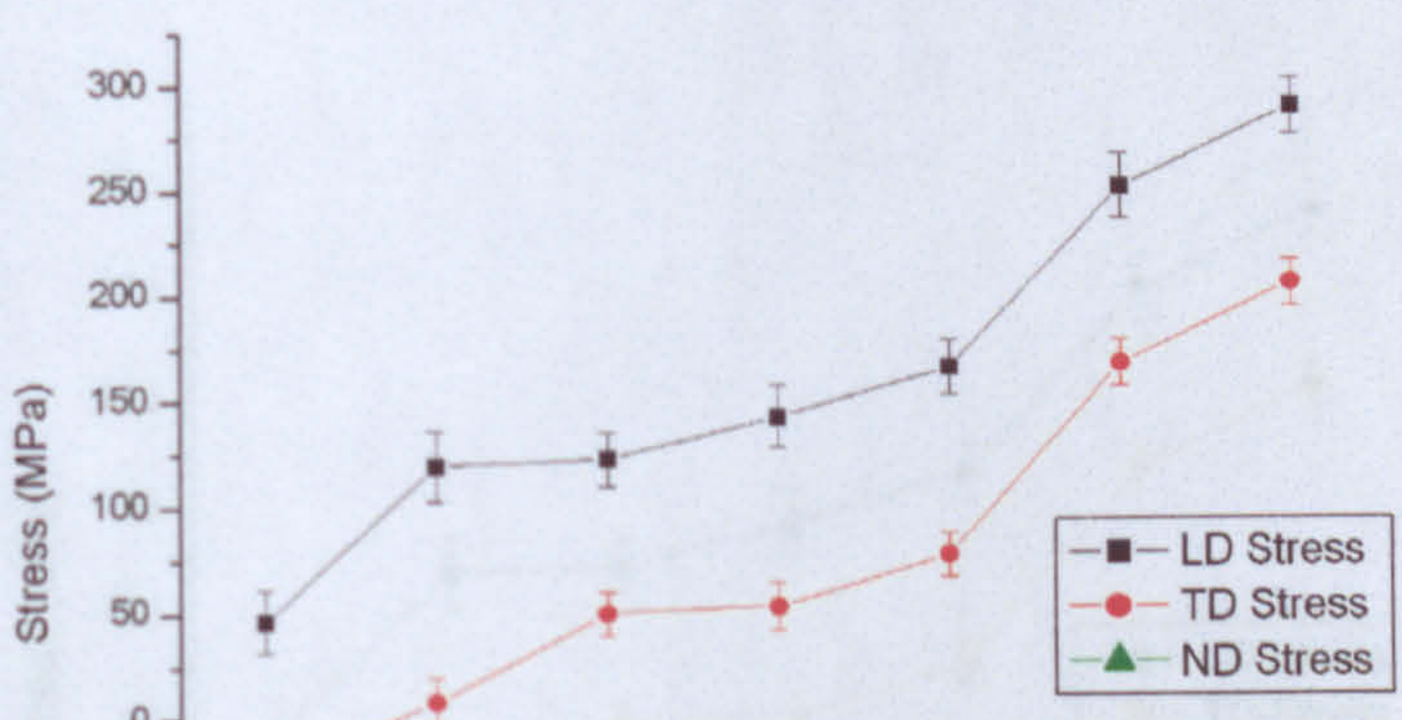

Figure 5.19: Through-thickness stress variation at the centre of the weld (x = 0, y = 0).

near to the weld and decay rapidly through the thickness away from the weld. The normal stresses are all compressive.

Figures 5.20 and 5.21 show the longitudinal, transverse and normal direction residual strain and stress profiles measured along the through-thickness drill-down line at the weld start location (x = -30, y = 0). Again, large longitudinal and transverse stresses

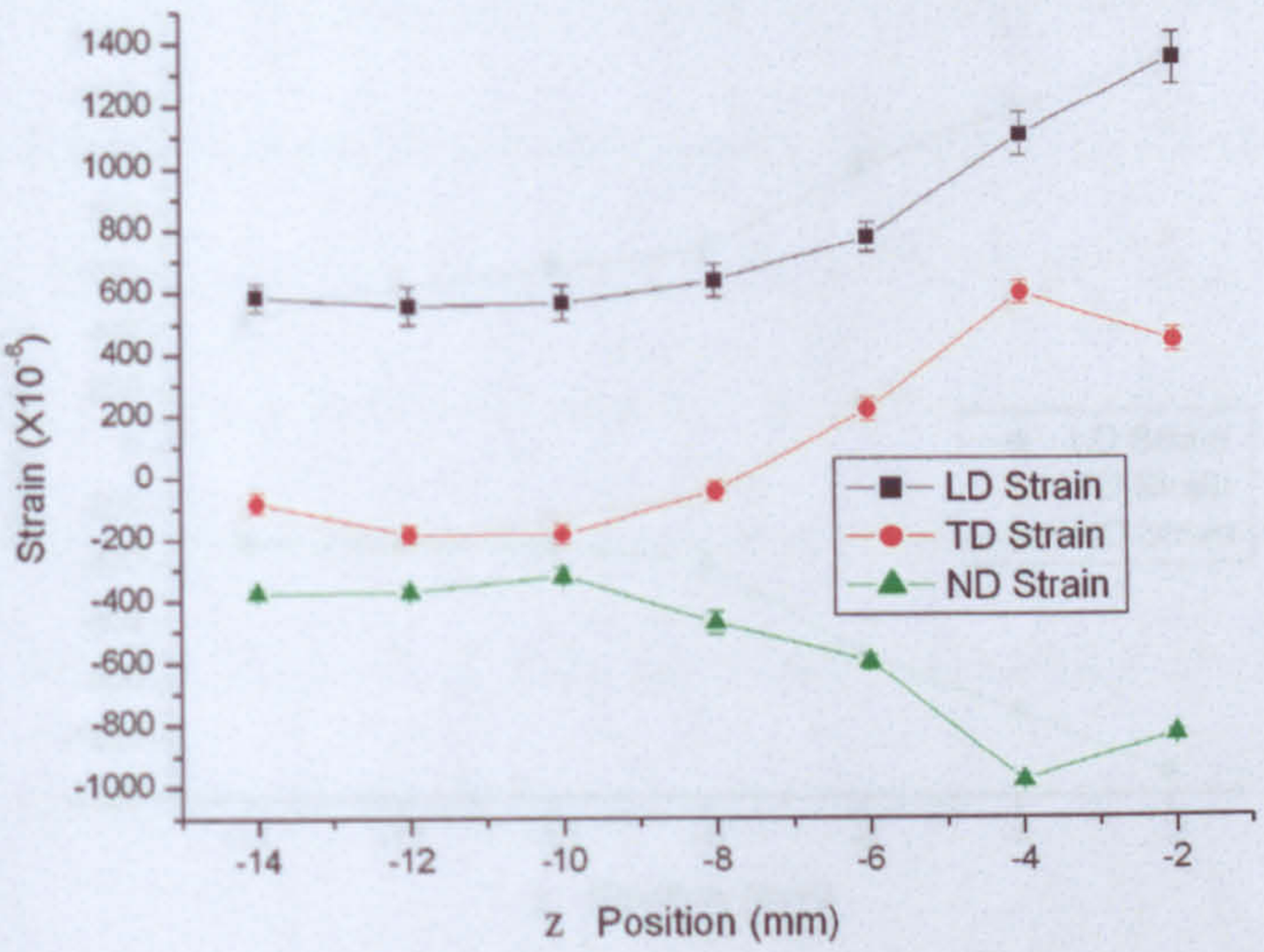

Figure 5.20: Through-thickness strain variation at the weld start position (x = -30, y = 0).

Figure 5.21: Through-thickness stress variation at the weld start position (x = -30, y = 0).

that decay rapidly away from the weld have been measured, and the normal stresses are compressive and remain almost constant through the thickness with the stress values varying from -70 to -80 MPa.

Figures 5.22 and 5.23 show the longitudinal, transverse and normal direction residual strain and stress profiles measured along the through-thickness drill-down line at the

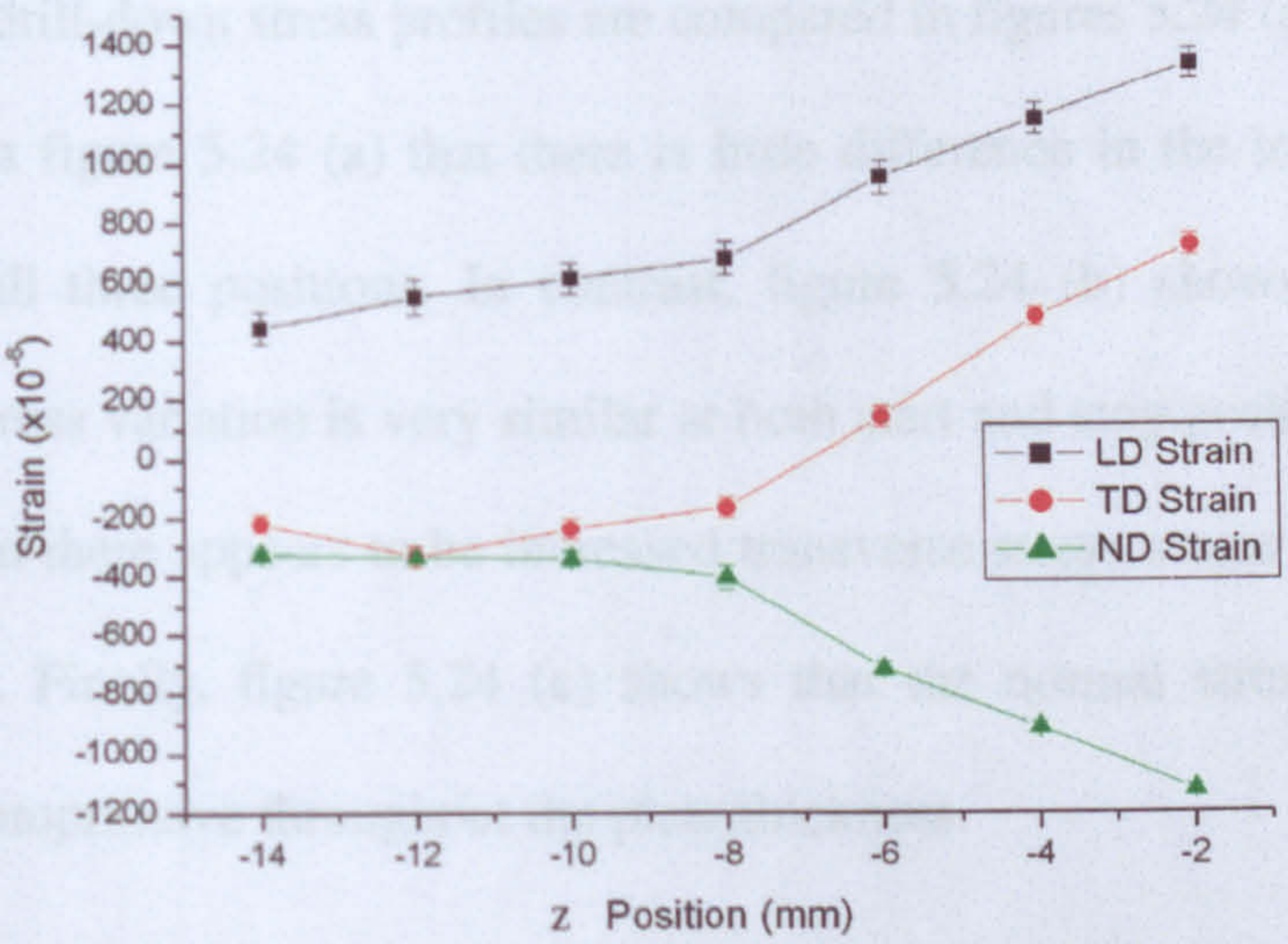

Figure 5.22: Through-thickness strain variation at the weld stop position (x = +27.5, y = 0).

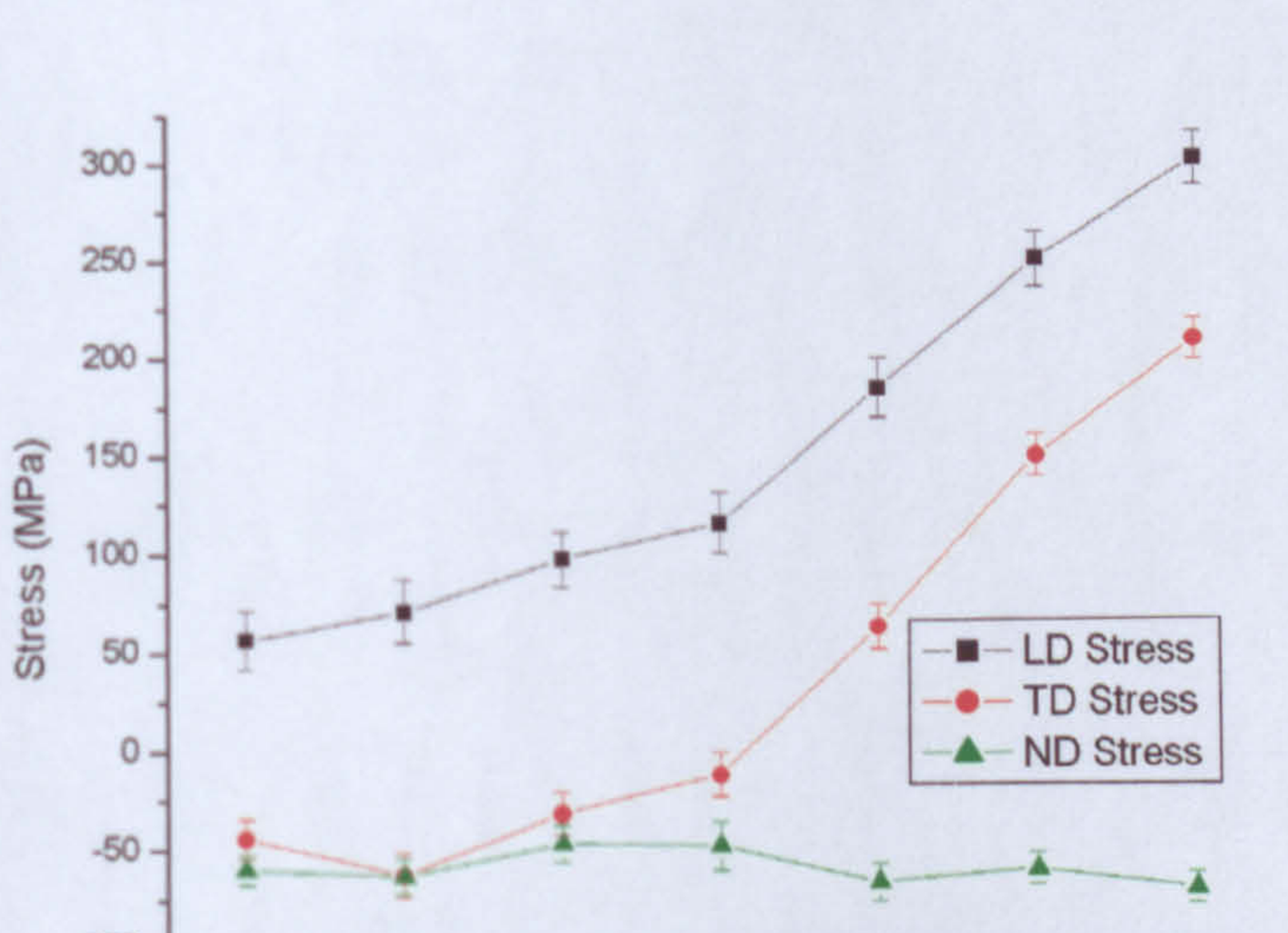

Figure 5.23: Through-thickness stress variation at the weld stop position (x = +27.5, y = 0).

weld stop location (x = + 27.5). As in the other drill-down lines significant longitudinal and transverse stresses have been measured near to the weld. These stresses decay rapidly away from the weld and the normal stresses are again, all compressive

These three drill-down stress profiles are compared in figures 5.24 (a, b and c). It can be seen from figure 5.24 (a) that there is little difference in the longitudinal stress profiles at all three positions. In contrast, figure 5.24 (b) shows that whilst the transverse stress variation is very similar at both start and stop positions, for the mid weld position there appears to be increased transverse stresses near at the mid-depth of the plate. Finally, figure 5.24 (c) shows that the normal stresses are low and uniformly compressive throughout the plate thickness.

(a)

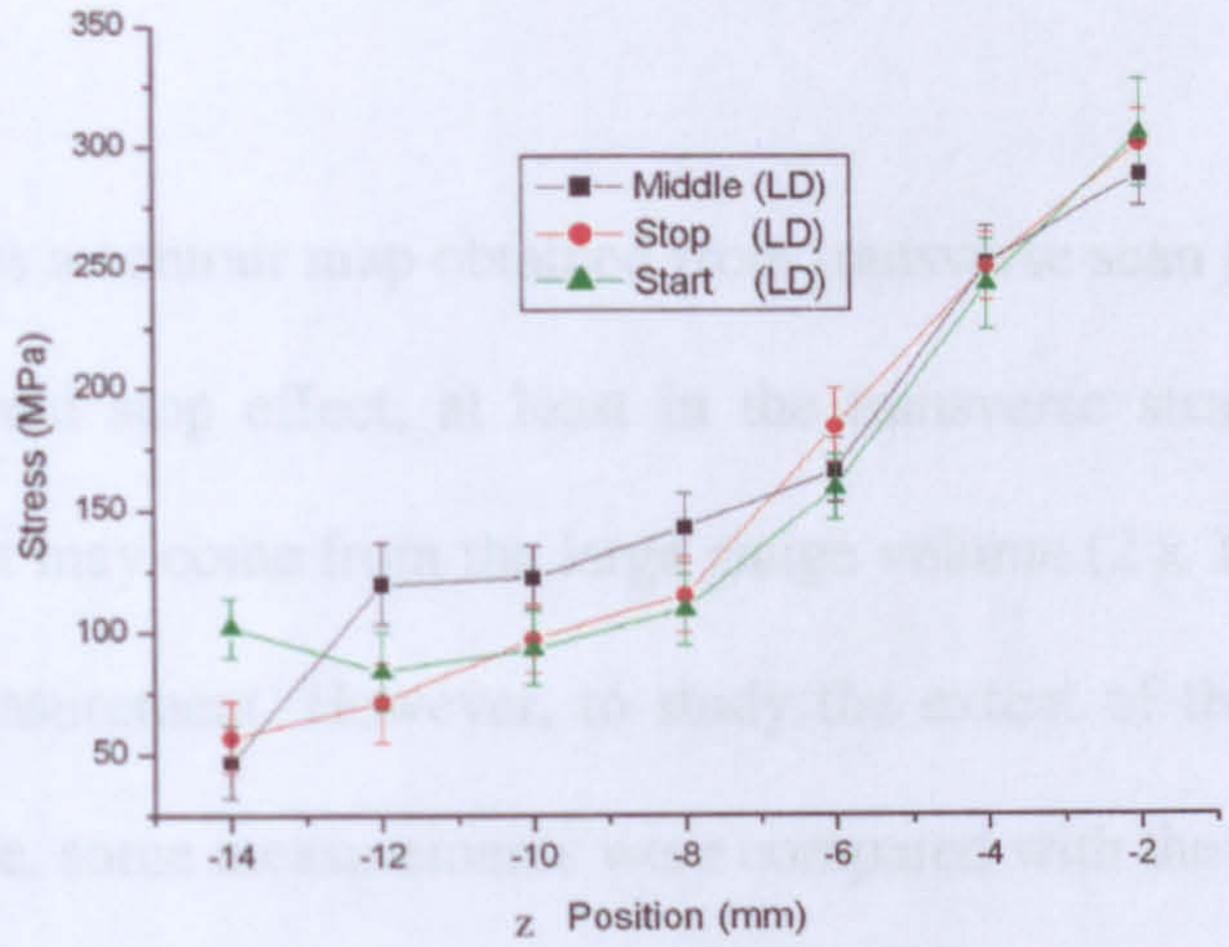

(b)

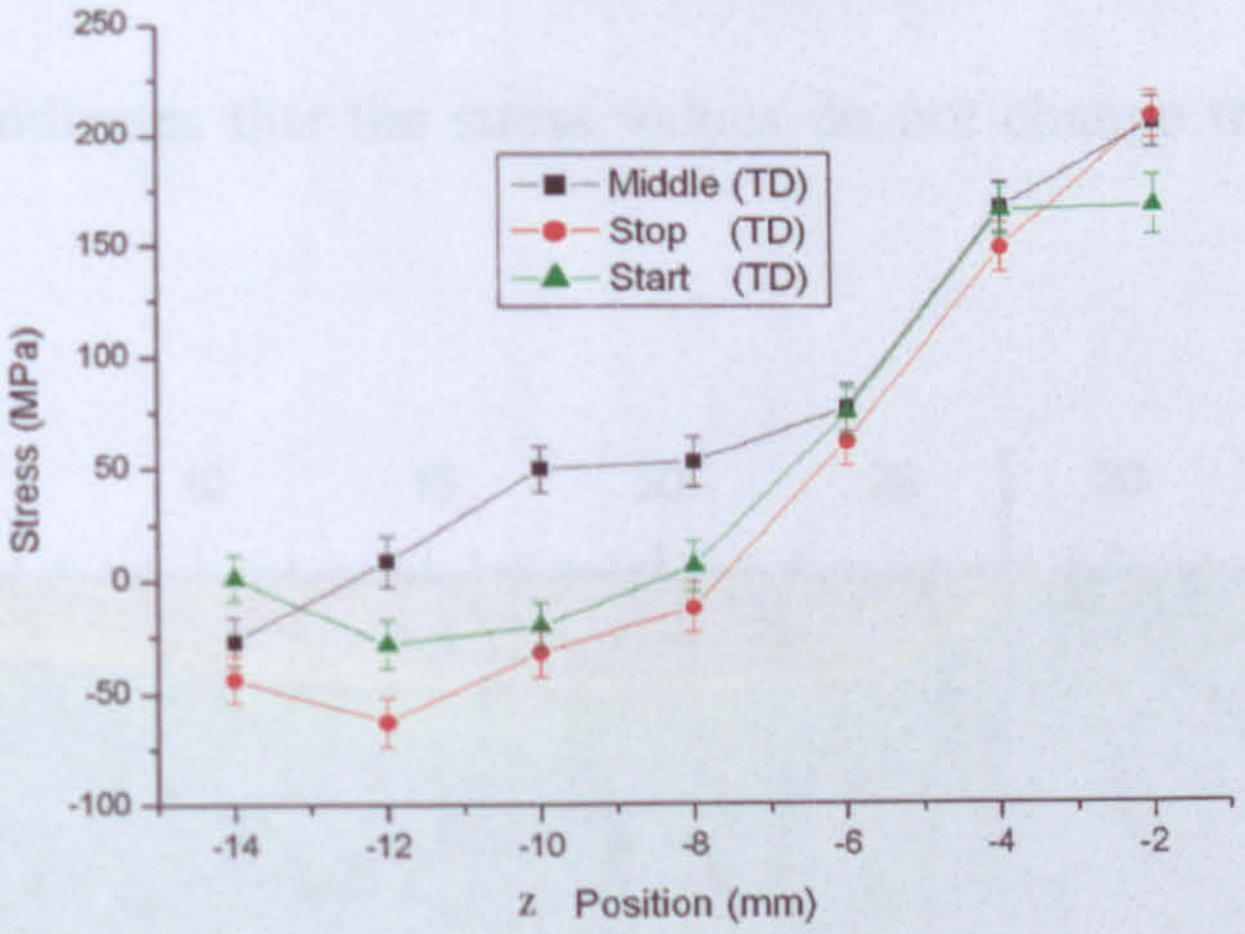

(c)

Figure 5.24: Comparison of through-thickness stresses in (a) longitudinal, (b) transverse and (c) normal direction at start, (x = -30, y = 0), mid (x = 0, y = 0) and stop (x = +27.5, y = 0) drill-down positions.

5.1.5.4 Through thickness strain map

Figure 5.25 shows a contour map obtained from transverse scan measurements. Clear evidence of a weld stop effect, at least in the transverse strain, can be seen. Of course, this effect may come from the large gauge volume (2 x 10 x 2 mm^3) that was used for this measurement. However, to study the extent of the effect of the large vertical beam size, some measurements were compared with the small gauge (2 x 2 x 2 mm^3) results. It can be seen from figures 5.26 and 5.27 that the strains compare very well with the drill-down measurements that used a smaller 2 x 2 x 2 mm^3 gauge volume, which indicates that the stress values do not change much along the weld bead.

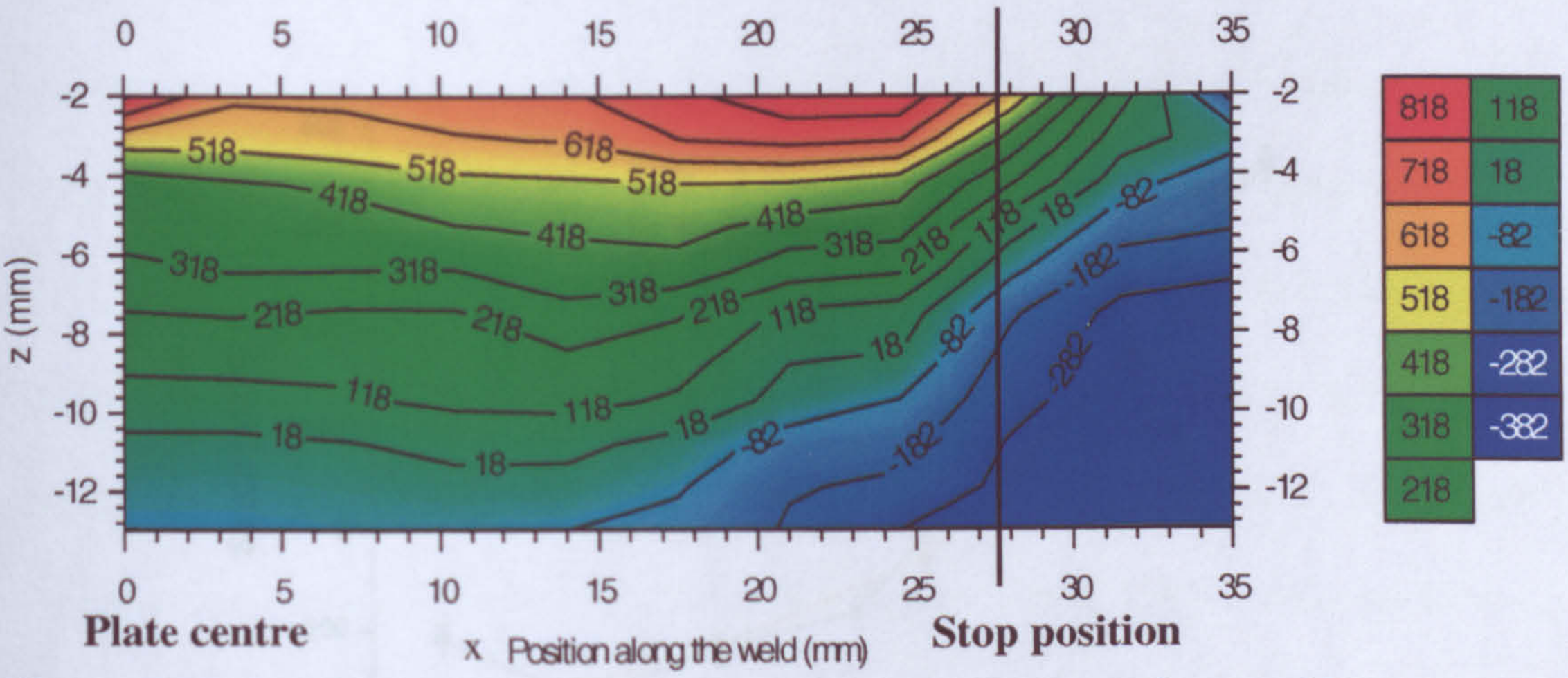

Figure 5.25: Through-thickness transverse strain variation map from weld centre (x = 0, y = 0) to beyond the weld stop position (x = + 27.5, y = 0); gauge volume = 2 x 10 x 2 mm^3.

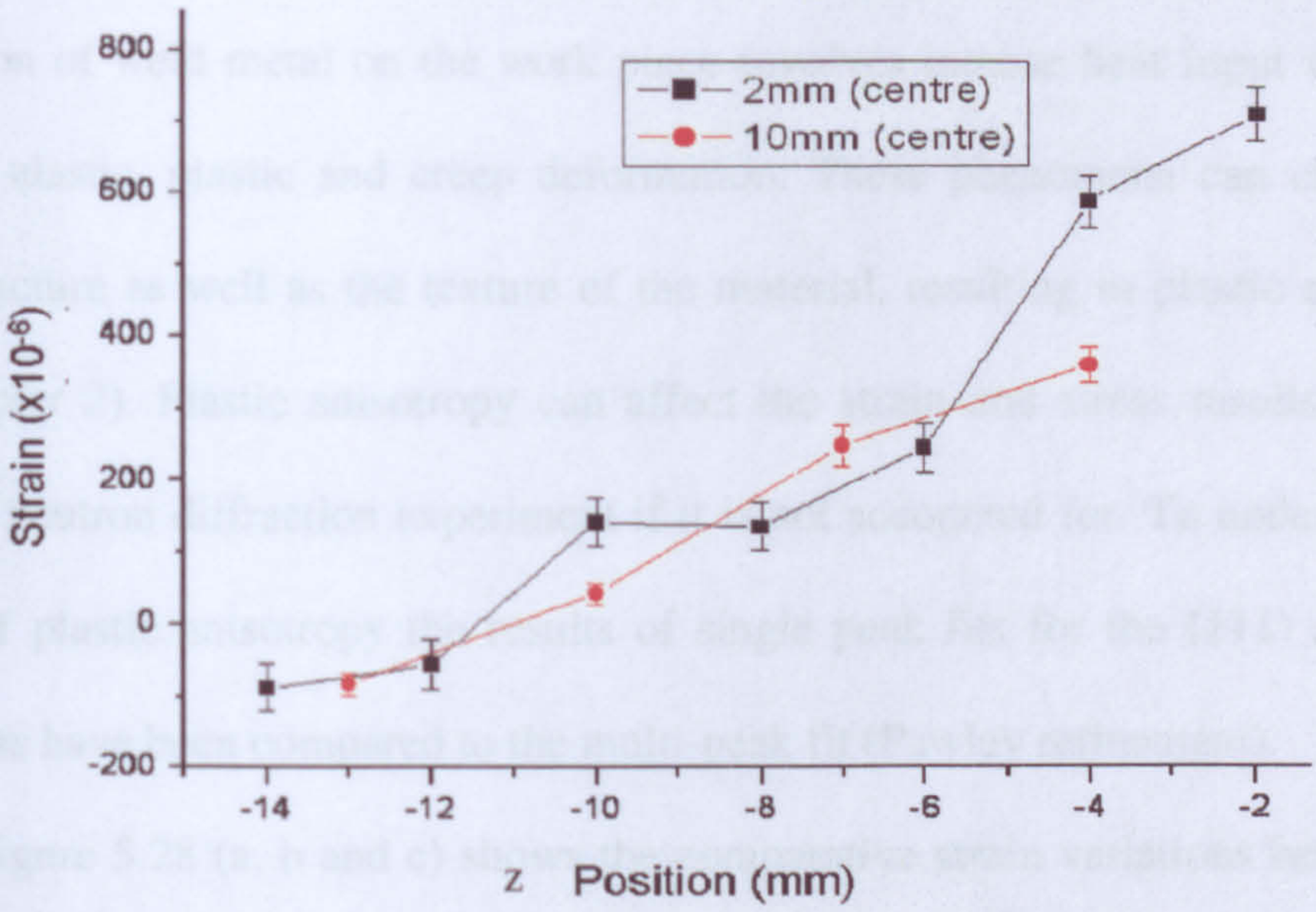

Figure 5.26: Through thickness drill-down transverse strains as measured using $2 \times 2 \times 2$ mm^3 and $2 \times 10 \times 2$ mm^3 gauge volumes at the weld centre ($x = 0$, $y = 0$).

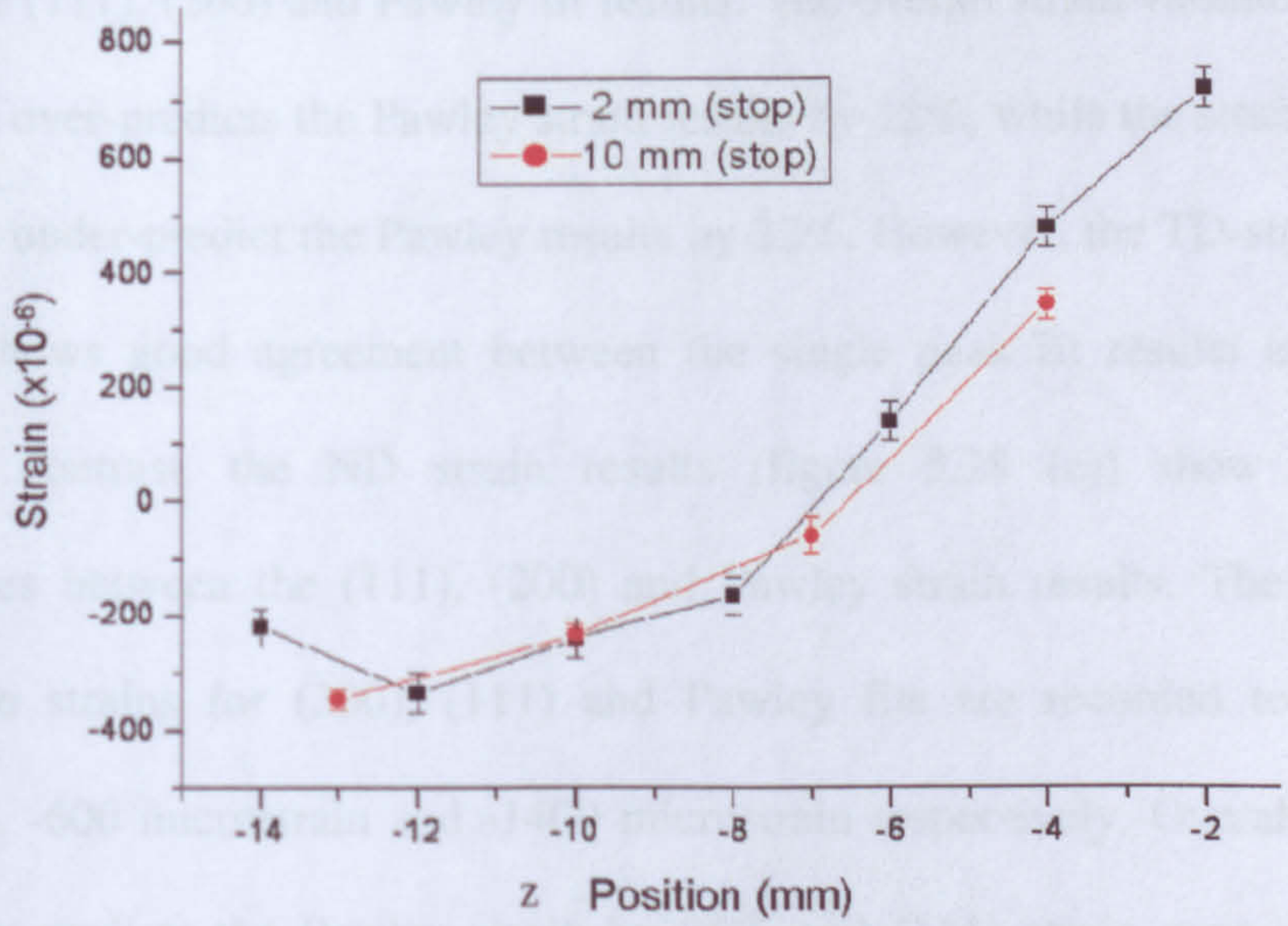

Figure 5.27: Through thickness drill-down transverse strains as measured using $2 \times 2 \times 2$ mm^3 and $2 \times 10 \times 2$ mm^3 gauge volumes at the weld stop end ($x = +27.5$, $y = 0$).

5.1.5.5 Plastic anisotropy in the weld material

Deposition of weld metal on the work piece involves intense heat input which can result in elastic, plastic and creep deformation. These phenomena can change the microstructure as well as the texture of the material, resulting in plastic anisotropy (see chapter 2). Plastic anisotropy can affect the strain and stress results obtained from the neutron diffraction experiment if it is not accounted for. To understand the effects of plastic anisotropy the results of single peak fits for the (111) and (200) reflections have been compared to the multi-peak fit (Pawley refinement).

Figure 5.28 (a, b and c) shows the comparative strain variations between the single peak and multi-peak fit results in LD, TD and ND directions measured along the weld bead (line EF in figure 5.1) line. It can be seen from figure 5.28 (a) that considerable differences in the magnitude of the LD strain variation are observed between the (111), (200) and Pawley fit results. The overall strain variation from the (200) plane over-predicts the Pawley strain results by 12%, while the strain results in (111) plane under-predict the Pawley results by 22%. However, the TD-strain (figure 5.28 (b)) shows good agreement between the single peak fit results and Pawley results. In contrast, the ND strain results (figure 5.28 (c)) show significant discrepancies between the (111), (200) and Pawley strain results. The maximum compressive strains for (200), (111) and Pawley fits are recorded to be -1800 microstrain, -600 microstrain and -1400 microstrain respectively. Overall the (200) strain under-predicts the Pawley strain by 35% and (111) strain over-predicts the Pawley results by 64%.

(a)

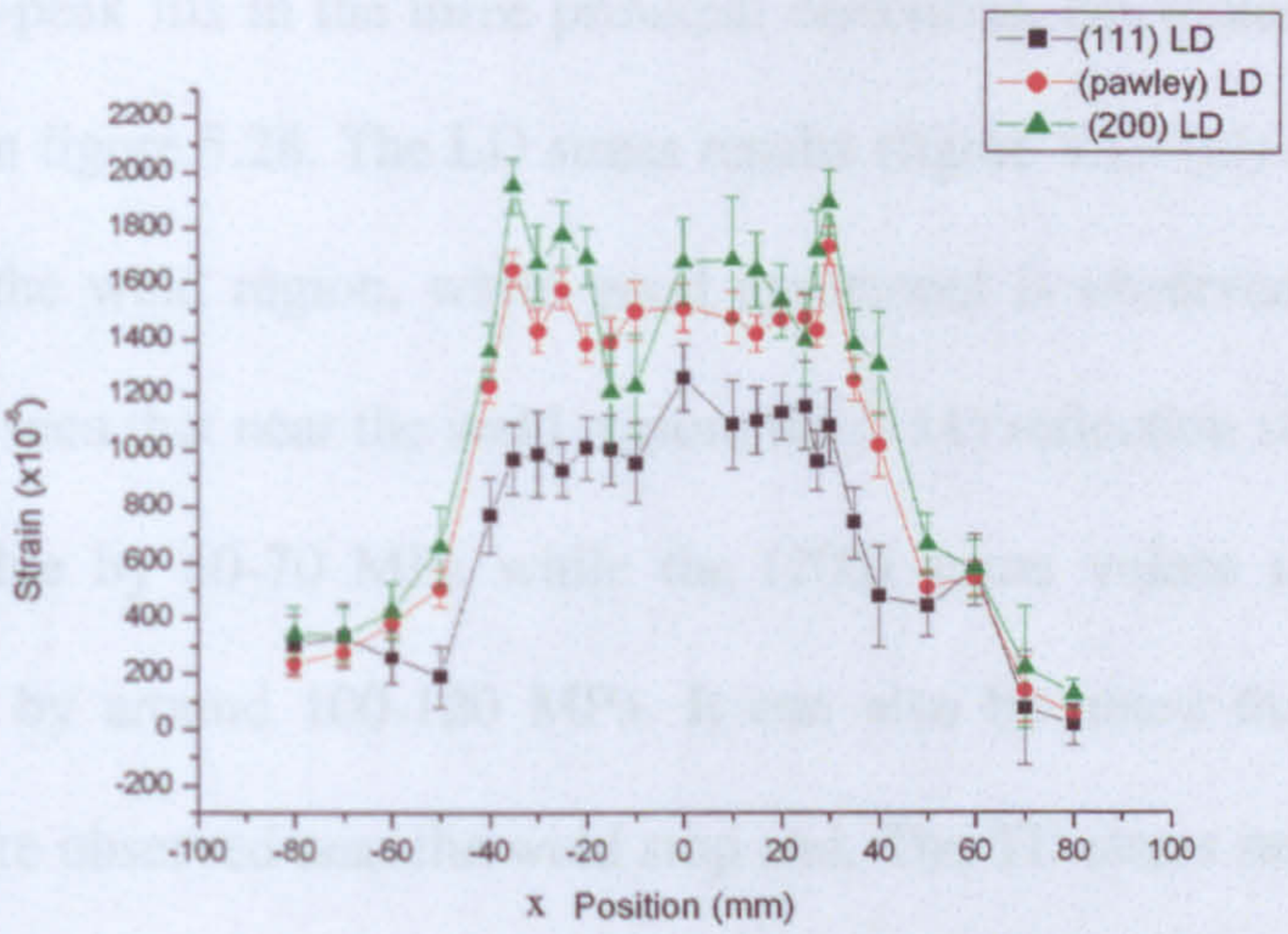

(b)

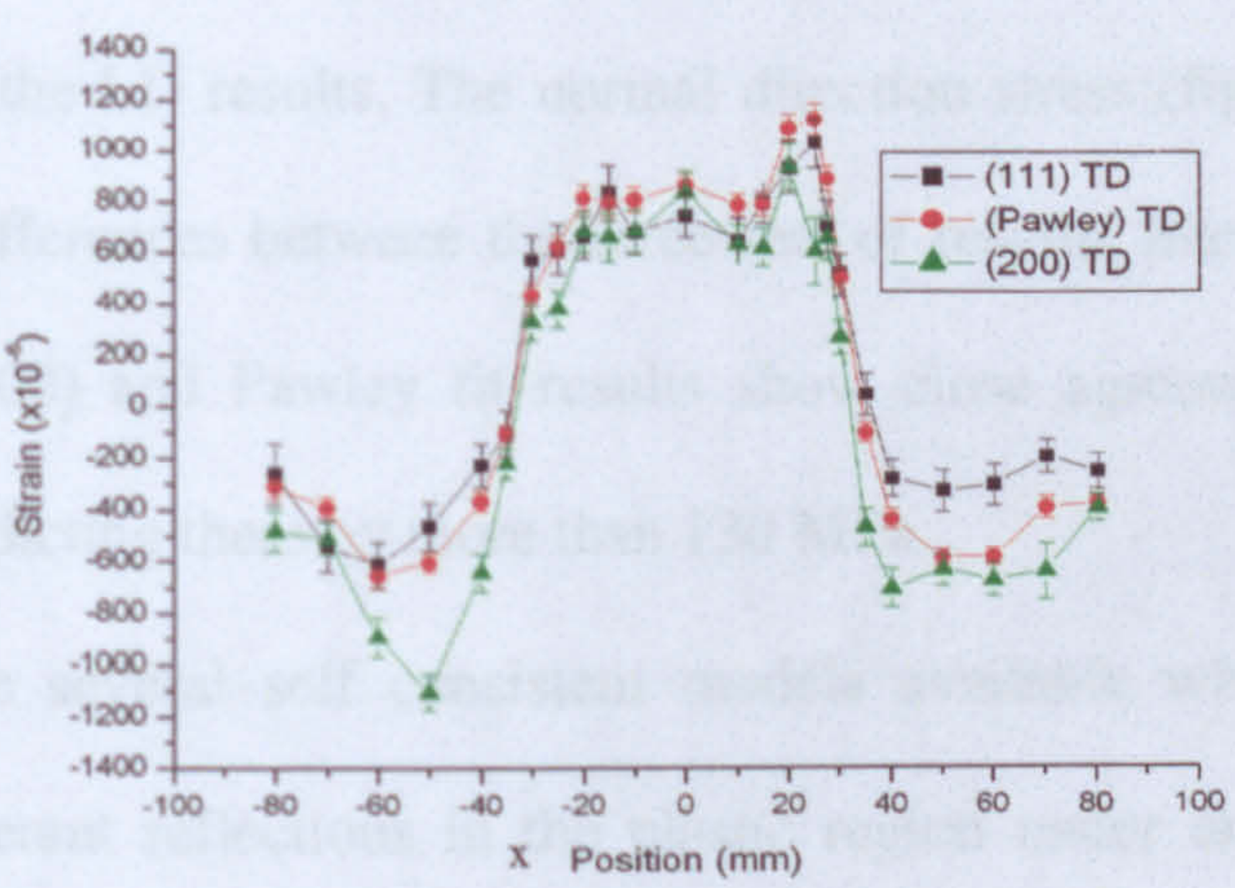

(c)

Figure 5.28: Comparative strain profiles of single peak ((111) and (200) peak) and multi-peak fit results along the EF line (figure 5.1) in (a) LD, (b) TD and (c) ND direction.

Figure 5.29 (a, b and c) shows the comparisons of residual stress results of single peak and multi-peak fits in the three principal directions, calculated from the strain results shown in figure 5.28. The LD stress results (figure 5.29 (a)) show differences in stress near the weld region, while good agreement is observed away from the weld. It can be seen that near the weld region, the (111) reflection stress differs from the Pawley value by 60-70 MPa while the (200) stress values under-predict the Pawley results by around 100-120 MPa. It can also be noted that the maximum discrepancies are observed near the weld stop end. The TD stress results (figure 5.29 (b)) show similar discrepancies among the single peak results and the Pawley fit results are as in the LD results. The normal direction stress (figure 5.29 (c)) shows the maximum differences between the three sets of results. Interestingly, in the ND direction, the (200) and Pawley fit results show close agreement, with the (111) stresses over predicting them by more than 130 MPa.

There are several self consistent models available which can predict the response of different reflections in the plastic region under uniaxial or multiaxial loading for the case of textured austenitic stainless steel [5.10, 5.11]. To understand the unusual behaviour in the ND strain and stresses in the current work, results from an elasto-plastic self-consistent (EPSC) study of austenitic stainless steel by Daymond [5.12] are considered. This model predicts the response of different planes of randomly textured austenitic stainless steel strained to 5% under the application of an external load.

(a)

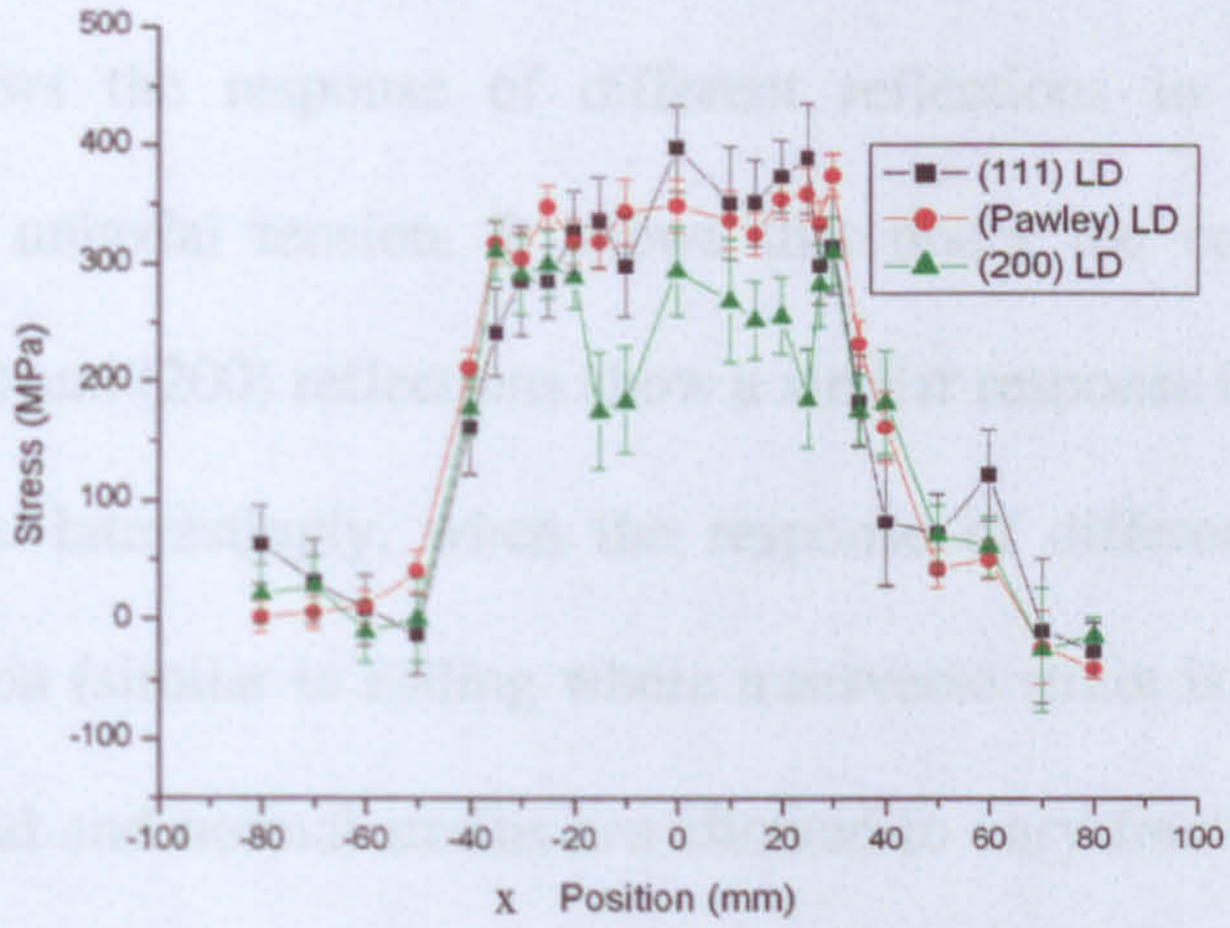

(b)

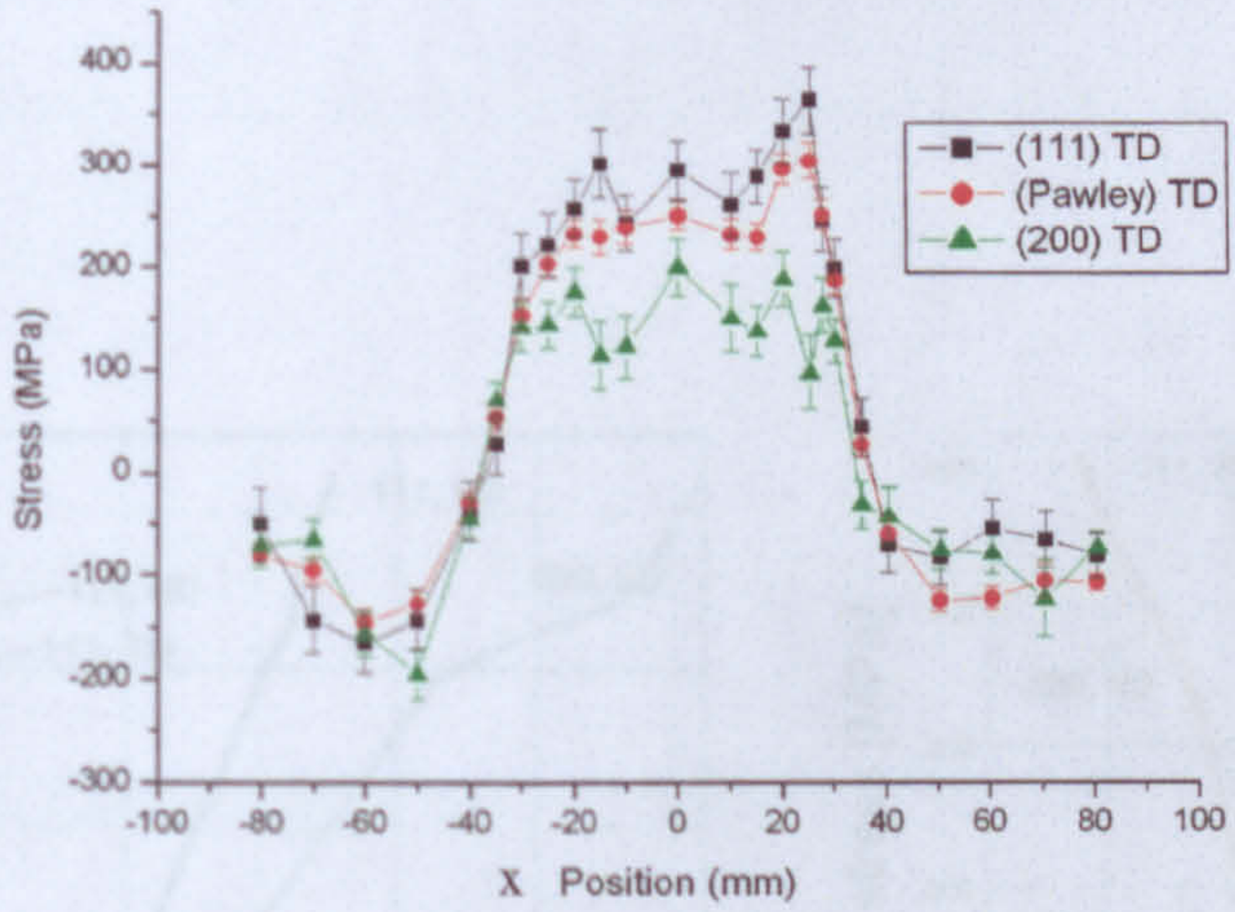

(c)

Figure 5.29: Comparative stress profiles of single peak ((111) and (200) peak) and multi-peak fit results along the EF line (figure 5.1) in (a) LD, (b) TD and (c) ND direction.

Figure 5.30 shows the response of different reflections in the three principal directions under uniaxial tension. It shows that under the condition of uniaxial loading, the (111) and (200) reflections show a similar response in the ND and TD in the plastic range. Interestingly, when the response of different reflections under constrained tension (similar to rolling where transverse strain is assumed to be zero where longitudinal and normal strains are allowed to vary freely) is studied (figure 5.31), which represents the current triaxial stress state in the weld, a significant difference in the plastic region is observed between the (111) and (200)

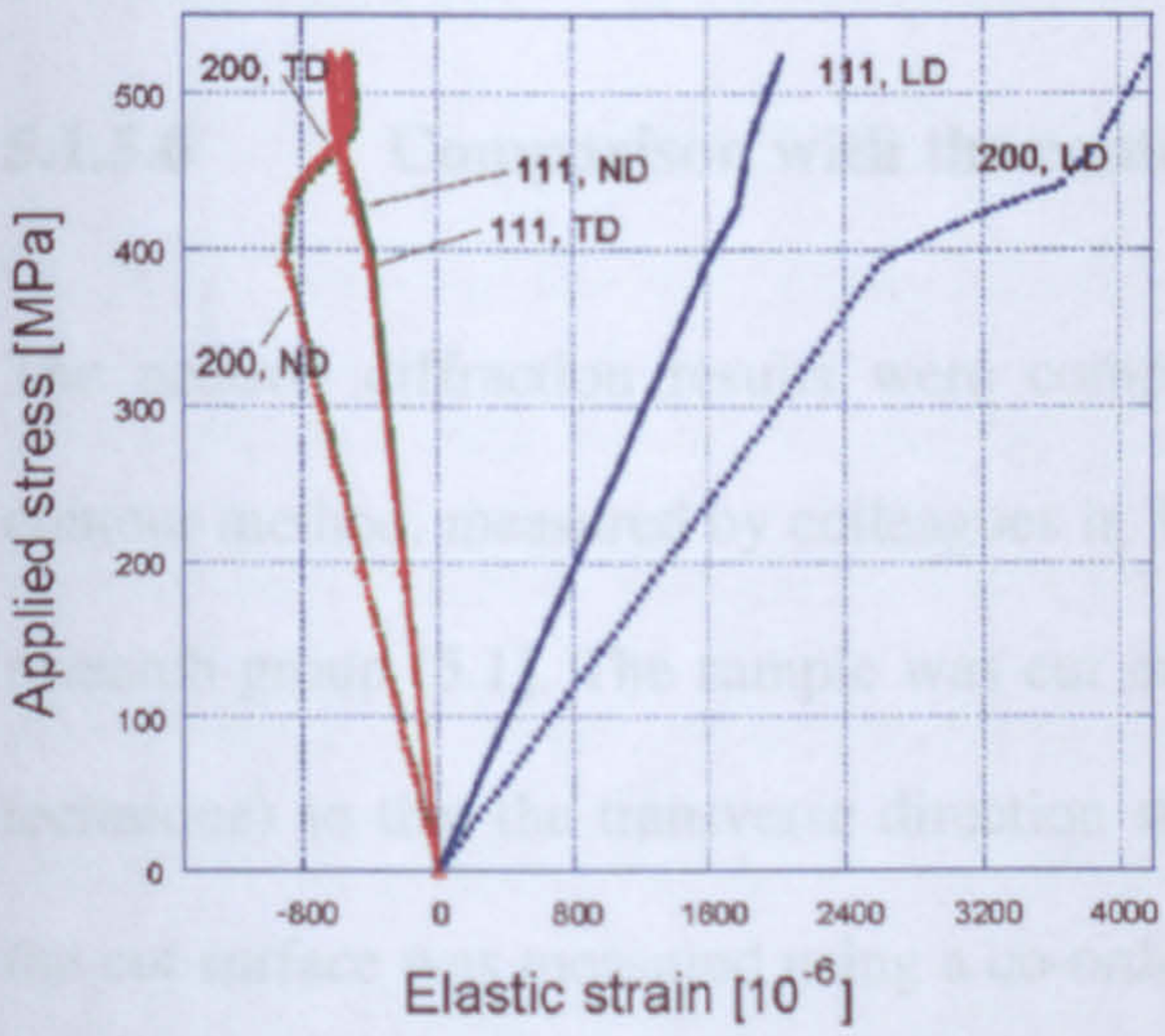

Figure 5.30: Elasto-plastic self-consistent model of austenitic stainless steel under uniaxial tension, random texture and 5% strain [5.12].

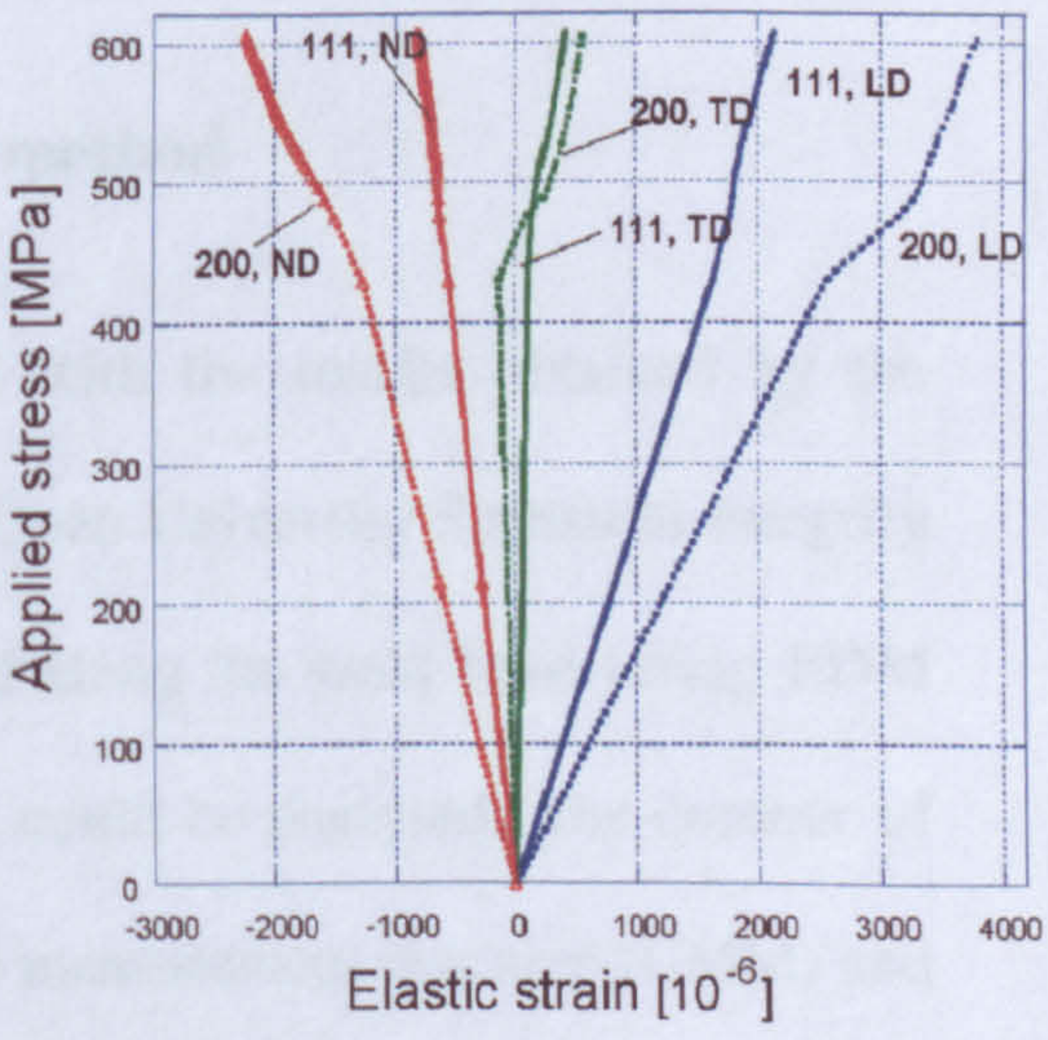

Figure 5.31: Elasto-plastic self-consistent model of austenitic stainless steel under constrained tension, random texture and 5% strain [5.12].

planes in the ND, while very similar response is observed in the TD. These results show that the single peak fit results of (111) and (200) show good agreement with the Pawley results in the LD and TD direction. However, significant discrepancies are observed in the ND direction. This suggests the presence of intergranular stress in the normal direction as a result of plastic anisotropy, which might have been generated due to the plastic deformation in the weld and adjacent material. This analysis shows the benefits of having diffraction spectra containing several peaks and the use of multi-peak fit routines, particularly, in those cases where the material is expected to have plastic anisotropy.

5.1.5.6 Comparison with the contour method

The neutron diffraction results were compared with the results obtained by the contour method, measured by colleagues in The Open University Structural Integrity research group [5.1]. The sample was cut in half along the weld bead (using EDM technique) so that the transverse direction stress could be analysed. The contour of the cut surface was measured using a co-ordinate measurement machine (CMM) and the surface profile was analysed using MATLAB software. This surface profile was finally applied as a boundary condition but with reversed sign, as a series of displacements to the cut face of a one-half plate FE model representation of the bead on plate specimen. The stresses were extracted from this FE analysis assuming elastic deformation. The detail of the contour analysis will not be discussed here as it is out of the scope of the present work. The transverse residual stress profile

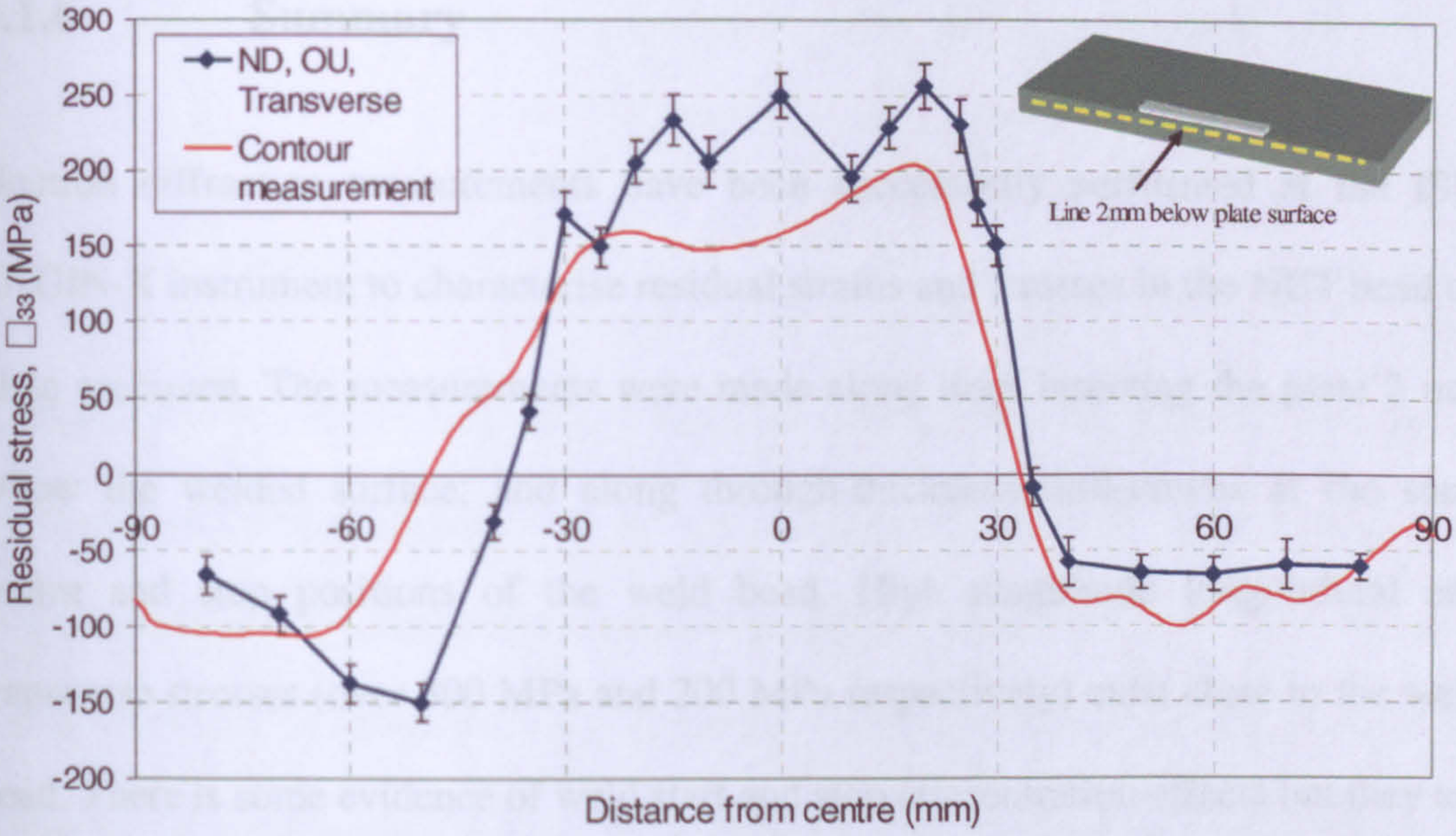

Figure 5.32: Comparison of transverse stress profile between the neutron diffraction and contour method at 2 mm below the weld surface.

measured along line EF shows good agreement between the techniques (figure 5.32). However, it is also evident from the results that there are some discrepancies (around 50 MPa) between the two measurements, mainly near the weld region. These discrepancies could be due to the fact that a single value of d_0 is used in the measurement analysis, whereas d_0 might vary point to point in the weld region. Also the presence of texture near the weld could have contributed to the variation. However, the contour method can introduce some error during EDM cutting of the sample, and also during the data smoothing operation necessary during processing of the measured contour [5.13]. Despite having these discrepancies, the techniques show results very close to each other in terms of trends as well as stress values.

5.1.6 Summary

Neutron diffraction measurements have been successfully performed at the ISIS ENGIN-X instrument to characterise residual strains and stresses in the NET bead on plate specimen. The measurements were made along lines bisecting the plate 2 mm below the welded surface; and along through-thickness drill-downs at the start, centre and stop positions of the weld bead. High magnitude longitudinal and transverse stresses (over 300 MPa and 200 MPa respectively) exist close to the weld bead. There is some evidence of weld start and stop concentration effects but they are more pronounced in the strain graphs than in the stress graphs. An apparent increase in transverse stress along the welding direction is also more evident in the strain data. The measured through-thickness stress profiles for the weld start, centre and stop positions are almost identical to each other implying that any weld start and stop stress concentration effects have little effect on the underlying through-wall stress distribution. However, the measured transverse strain map suggests that a short-range weld stop strain concentration effect is located before the actual weld stop position. Comparison of single peak fitting and multi-peak fitting results shows significant discrepancies in the ND strain and stress variation. These differences can be attributed to the plastic anisotropy effect in and near the weld region. However, the use of a multi-peak fitting routine (such as a Pawley fit) proved to be very useful to reduce the effect of anisotropy effect in the final results. The neutron diffraction results show very good agreement when the results were compared to the results of contour measurements.

5.2 Effect of specimen geometry on weld residual stress

5.2.1 Background

Traditionally, in fracture mechanics it has been assumed that the properties measured in laboratory-sized specimens will also be applicable to the real component as long as the conditions of similitude and small scale yielding hold true. However, although the introduction of a weld into a laboratory size specimen does not change the condition of small scale yielding, no assumption can be made on similitude as the residual stress condition in the component may be different once the sample is machined or any portion of it is cut, as this might cause stress relaxation.

The purpose of this current work is to investigate the extent of similitude through the measurement of residual stresses in compact tension specimens machined from MIG welded Al-2024 and Al-7150 plates. This work is part of a larger integrated program on the determination and consequences of residual stress on the fatigue performance of welded aircraft structures [5.14]. The measurements in this part of work were carried out using the newly-built POLDI instrument at PSI, Switzerland.

5.2.2 Specimen manufacture

Measurements were carried out in two compact tension specimens which had been machined from MIG welded Al-2024 alloy and Al-7150 alloy plates. Initially, two plates of dimension 500 x 186 x 12 mm^3 were joined using a double pass MIG welding technique at Cranfield University [5.15]. Finally each 12 mm thick specimen was reduced to a thickness of 6.9 mm (as seen in figure 5.33) and cut into compact tension specimen form. The thickness of the CT specimen was chosen to be around 7

mm as this is the typical thickness of the skin used in the wing skin stringer panel. The geometry and the size of the two specimens were identical, as shown in figure 5.33.

Al-2xxx series alloys are known for their poor weldability [5.16] due to their susceptibility to hot cracking as a result of the formation of a low melting point eutectic. The plates were welded using a new double pass MIG welding technique using AA-2319 filler wire, which has a composition of 6.2% Cu, 0.17% Fe and 0.32% Mn. The Al-2024 plate was heat treated to T351 conditions, namely: heat treatment and cold working followed by a natural aging treatment. The welded plate was not subjected to any post weld heat treatment except natural aging.

Al-7150 alloy plates were W51 treated. That is: solution treated, quenched and stress relieved by stretching in the rolling direction. These plates were double pass MIG welded using AA-5039 filler wire of composition (wt%) 3.3-4.3 % Mg; 2.4-3.4% Zn. Al-7150 was given a post weld heat treatment to the T651 condition, that is dual temperature precipitation heat treated [5.17]. The chemical composition of both alloys is presented in table 5.2.

A detailed study of microstructure and crystallographic texture analysis of MIG welded Al-2024 alloy and Al-7150 alloy has been performed by Ganguly [5.18, 5.19] and Stelmukh [5.20, 5.21]. It has been reported that MIG welded 2024 alloy does not show any significant texture, while Al-7150 alloy exhibits a strong texture variation of the (422) plane in the longitudinal direction (LD) and (222) planes in the transverse direction (TD).

Table 5.2: The typical chemical composition of the alloys (wt %) [5.17].

Alloy	Cu	Mg	Mn	Zn	Si	Fe	Al
Al-2024	4.00	1.20	0.5	<0.25	<0.15	<0.20	Bal
Al-7150	1.9-2.5	2.0-2.7	-	5.9-6.9	0.12	1.5	Bal

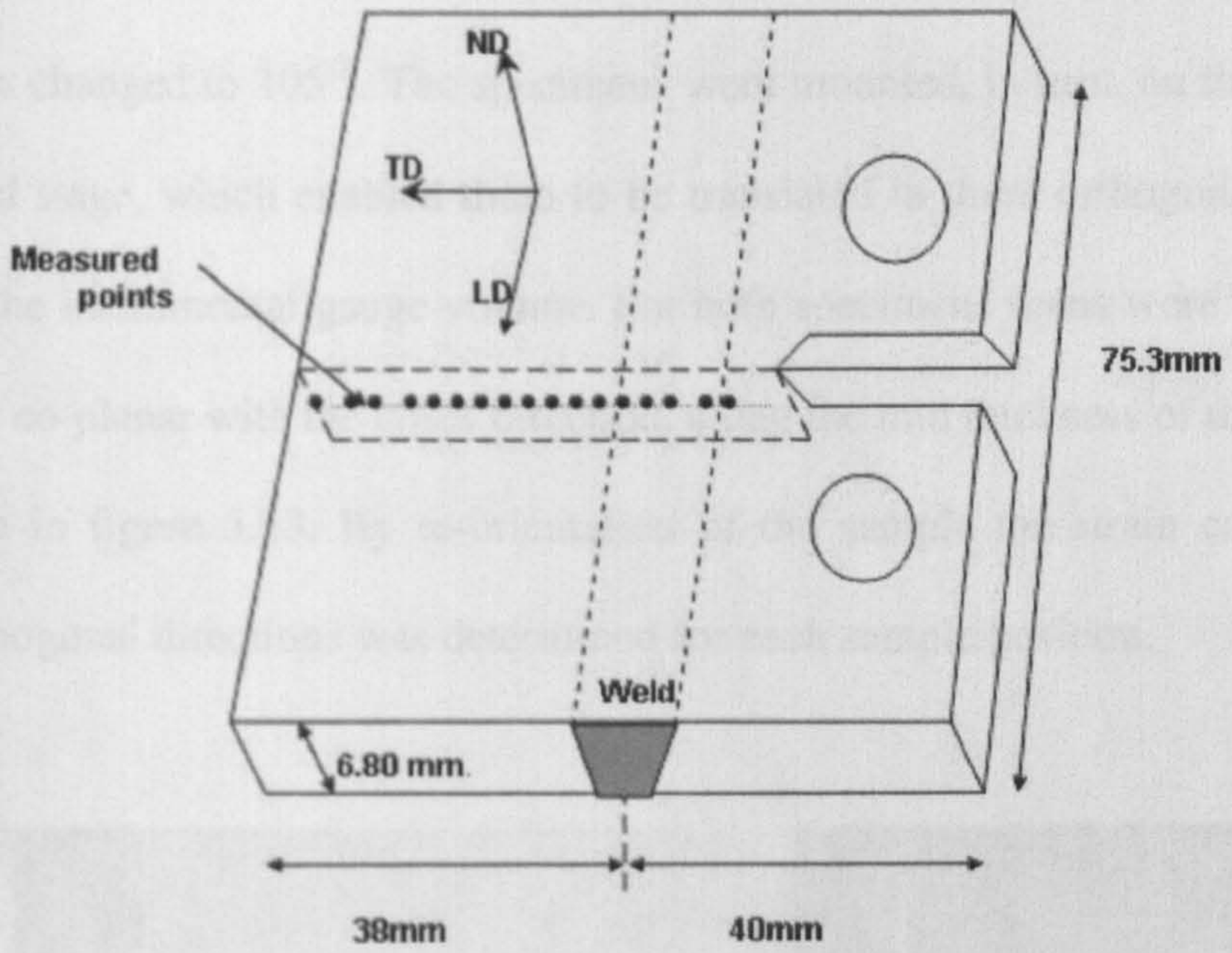

Figure 5.33: Schematic diagram of the geometry of the two samples, with the location of points at which the residual strain was measured.

5.2.3 Neutron diffraction measurement

Details of the Poldi instrument have already been presented in chapter 2. The (311) reflection was used for the measurement of the Al-2024 plate in all three directions, as no severe texture was reported [5.19], with a scattering angle of $2\theta = 90^{\circ}$. But in the case of the Al-7150 alloy, due to the presence of strong texture, different reflections were used for different strain directions. The longitudinal direction (LD) was measured using the (422) reflection, the transverse direction (TD) using the (222) reflection, and in the normal direction using the (220) reflection. In the case of

the Al-7150 alloy the LD direction had to be measured at a scattering angle of $2\theta = 105^{\circ}$. This is because, at a scattering angle of $2\theta = 90^{\circ}$, observation of (422) reflection requires a wavelength of λ=1.17Å, which is close to the POLDI cut off wavelength of 1.11Å [5.22]. The instrument was initially calibrated using standard silicon powder. Recalibration of the instrument was also carried after the scattering angle was changed to 105°. The specimens were mounted, in turn, on the computer-controlled stage, which enabled them to be translated in three orthogonal directions through the instrumental gauge volume. For both specimens scans were made across the weld, co-planar with the crack direction, along the mid thickness of the specimen, as shown in figure 5.33. By re-orientation of the sample the strain component in three orthogonal directions was determined for each sample position.

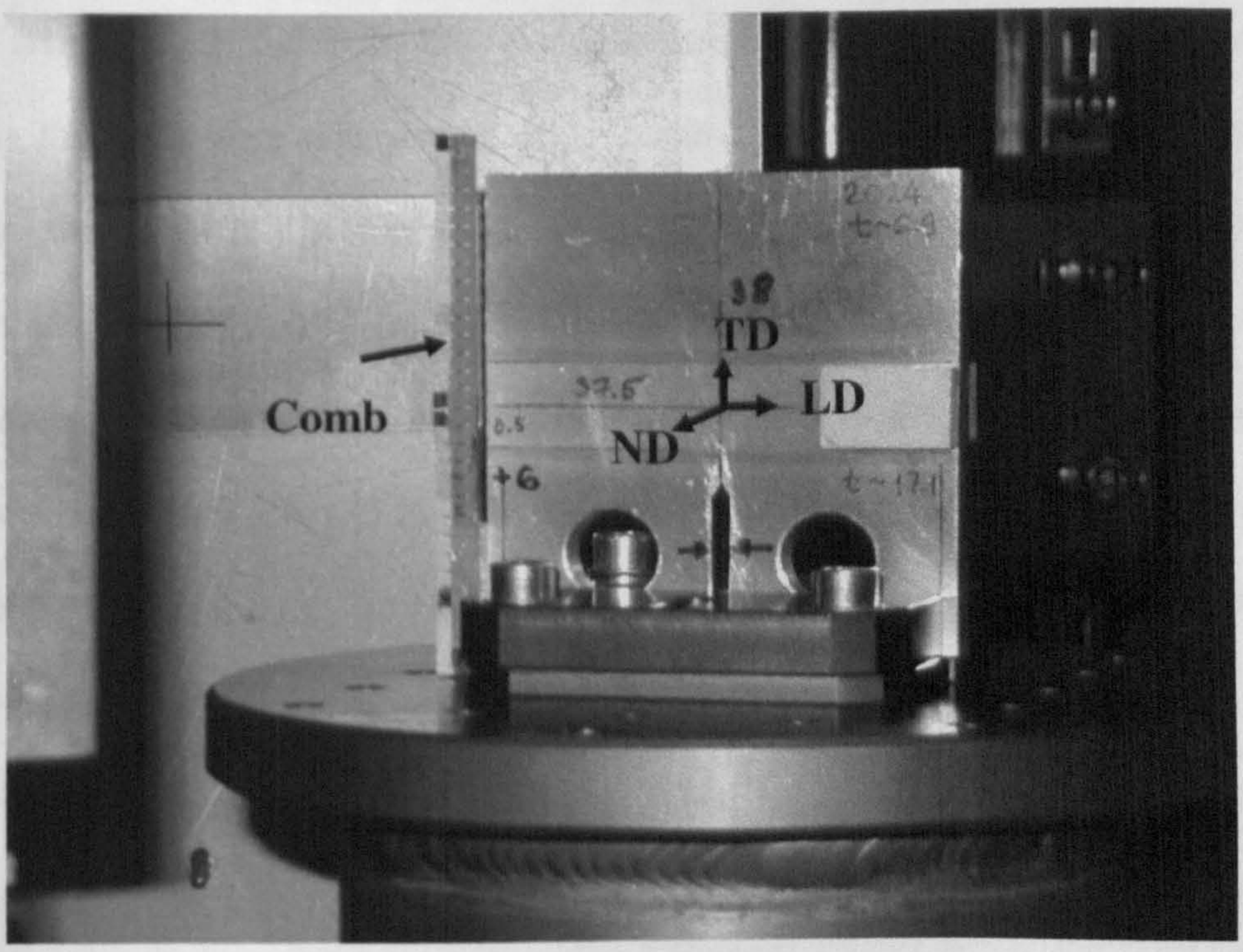

Figure 5.34: Experimental setup in POLDI.

The specimen, mounted on the sample table for measurement of strain in the *LD*, is shown in figure 5.34. For the measurement of the longitudinal strain component *a* gauge volume of $2 \times 2.5 \times 1.5$ mm^3 was used. In order to optimise the measurement time for the transverse and normal directions, a gauge volume of $2 \times 10 \times 1.5$ mm^3 was used, averaging the strain along the weld longitudinal direction where it was not expected to vary significantly with longitudinal position.

5.2.3.1 Stress-free lattice spacing

In a weld, it is important to measure the point to point variation of the stress-free reference lattice spacing, d_0, since this can vary significantly due to changes in chemical or structural composition, both in the weld itself and in the heat-affected zone (HAZ) [5.21, 5.23]. In this work the stress-free reference lattice parameters across the weld were determined using comb specimens, obtained from sections across the original 12 mm thick weld (figure 5.35) using Electro-Discharge Machining (EDM). The resulting comb contained teeth, centred at points corresponding to each position of strain measurement, which were small enough to be essentially stress-free [5.20]: the dimensions of each individual tooth were 2.4 mm × 2.7 mm in the LD-TD plane, and 9 mm along the ND. The strain components were measured along the three principal directions at the positions within each tooth corresponding to those in the original specimens, using a $2 \times 2.5 \times 1.5$ mm^3 gauge volume.

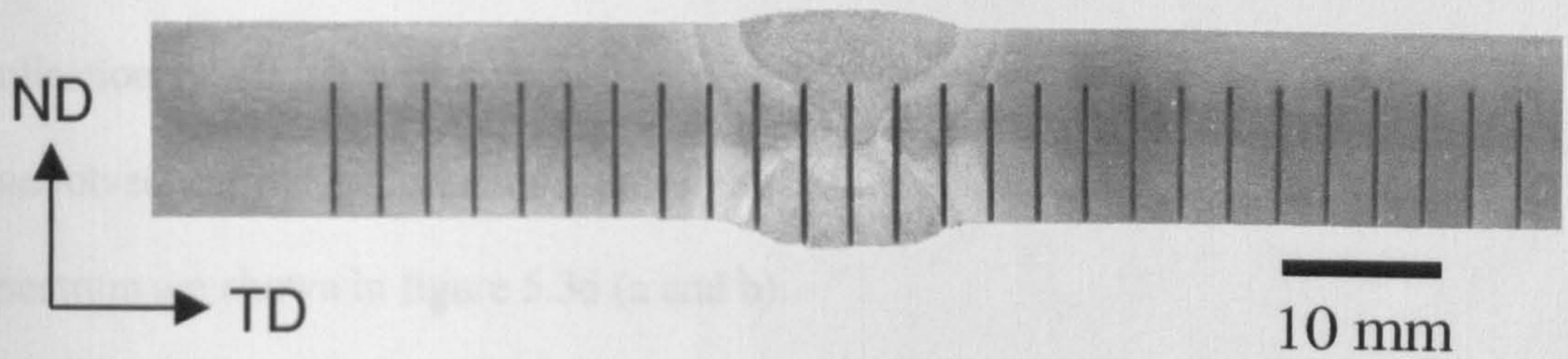

Figure 5.35: A comb specimen from which the stress-free lattice parameters were determined.

5.2.3.2 Data analysis

The overlapping diffraction patterns were deconvolved to give the variation of intensity vs. lattice spacing, d_{hkl}, in the range sampled by the instrument. The profile of each peak was fitted using a Levenberg-Marquardt routine [5.24] to give the lattice spacing of individual peaks. Although as many as 10 peaks were observed in the diffraction spectra of the Al powder, in the case of the Al-2024 specimen

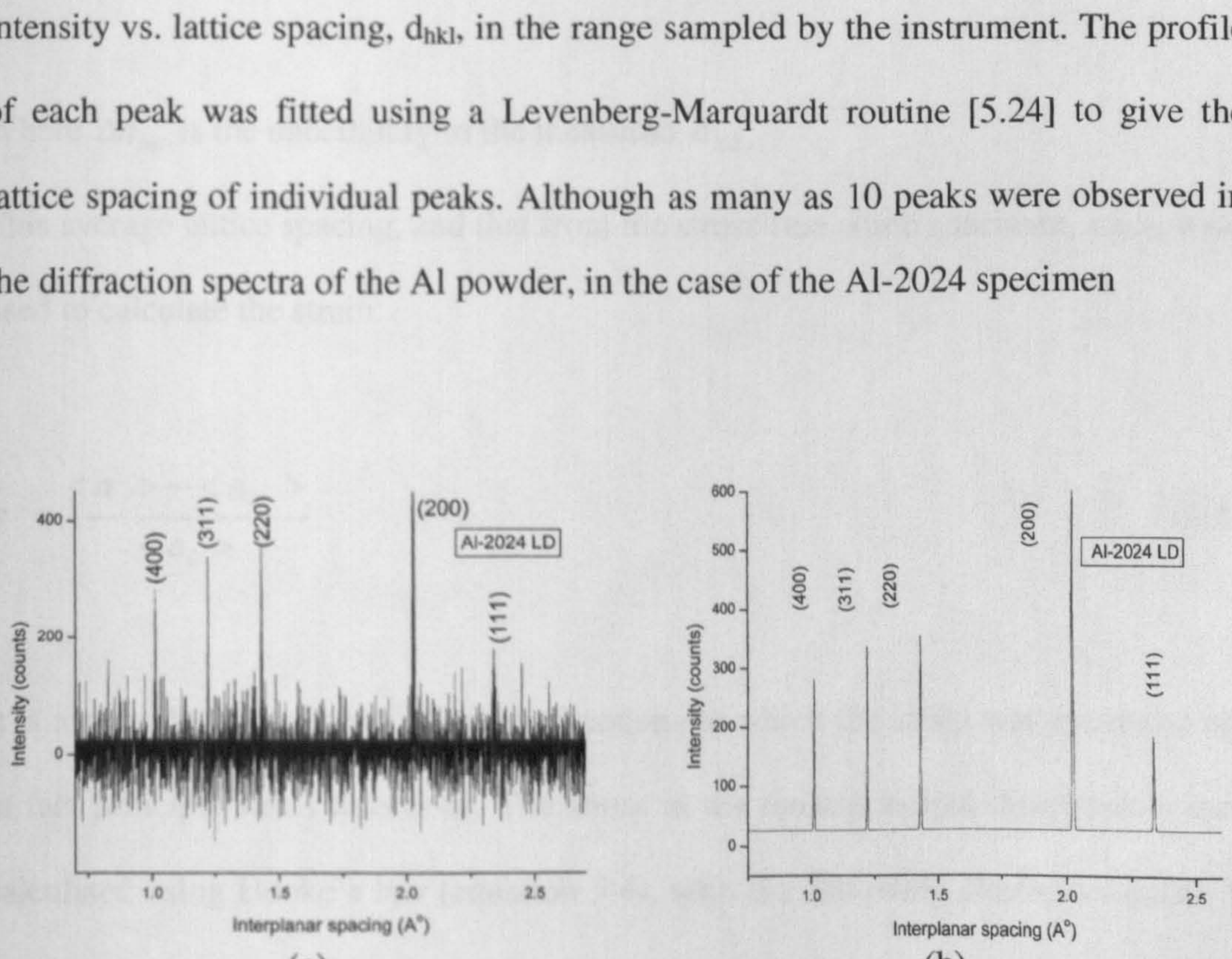

Figure 5.36: (a) De-convolved diffraction spectrum and (b) the fitted diffraction spectrum of Al-2024 specimen measured with scattering vector in the LD.

only the strongest (5) peaks, which can be seen in figure 5.36, were fitted as the collection of all 10 peaks would be prohibitively time consuming. A typical de-convolved diffraction spectrum from the Al-2024 specimen and the final fitted spectrum are shown in figure 5.36 (a and b).

The weighted average lattice parameter value <a> of the 5 individual peaks hkl used in the analysis is given by the following expressions:

$$< a >= \frac{\sum_{hkl} \frac{d_{hkl}\sqrt{h^2+k^2+l^2}}{|\Delta d_{hkl}|}}{\sum_{hkl} \frac{1}{|\Delta d_{hkl}|}} \qquad (5.3)$$

Where Δd_{hkl} is the uncertainty in the measured d_{hkl}.

This average lattice spacing, and that from the stress-free comb specimen, $<a_0>$, were used to calculate the strain:

$$\varepsilon = \frac{< a > - < a_0 >}{< a_0 >} \qquad (5.4)$$

It is assumed (by symmetry) that the directions in which the strain was measured are in fact principal stress directions. The stress in the three principal directions is then calculated using Hooke's law (equation 3.4), with the following elastic constants: E = 72 MPa and Poisson's ratio ν = 0.33. In the case of the strongly-textured MIG-welded Al-7150 specimen, different reflections were used to measure the strain components in the three principal directions. The (422), (222) and (220) peaks were used as described in the previous sections to determine the strain components.

The strain in each direction was calculated from the lattice spacing d_{hkl} of the individual reflections. The stress-free lattice parameter values obtained from the corresponding positions in the Al-7150 comb were used to calculate the strain, using the following expressions:

$$\varepsilon_{LD} = \varepsilon^{422} = \frac{d_{422} - d^0_{422}}{d^0_{422}} \qquad (5.5\text{ a})$$

$$\varepsilon_{TD} = \varepsilon^{222} = \frac{d_{222} - d^0_{222}}{d^0_{222}} \qquad (5.5\text{ b})$$

$$\varepsilon_{ND} = \varepsilon^{220} = \frac{d_{220} - d^0_{220}}{d^0_{220}} \qquad (5.5\text{ c})$$

The stress components were calculated from these strain values using equation 2.13. The same elastic constants were used for all three reflections since the degree of elastic anisotropy is small in the case of aluminium alloys, with the maximum deviation of any plane–specific elastic constants from the average value being ~ 3-4% [5.25]. Overall experimental uncertainties (considering only the uncertainty in peak position [5.26]) of approximately 20-30 MPa were determined near the weld and were around 10 MPa in the bulk material for both alloys.

5.2.4 Results and discussion

5.2.4.1 MIG welded Al-2024 specimen

The results obtained from the experiments are presented in the following figures where strain and stress variations are plotted as a function of distance from the weld

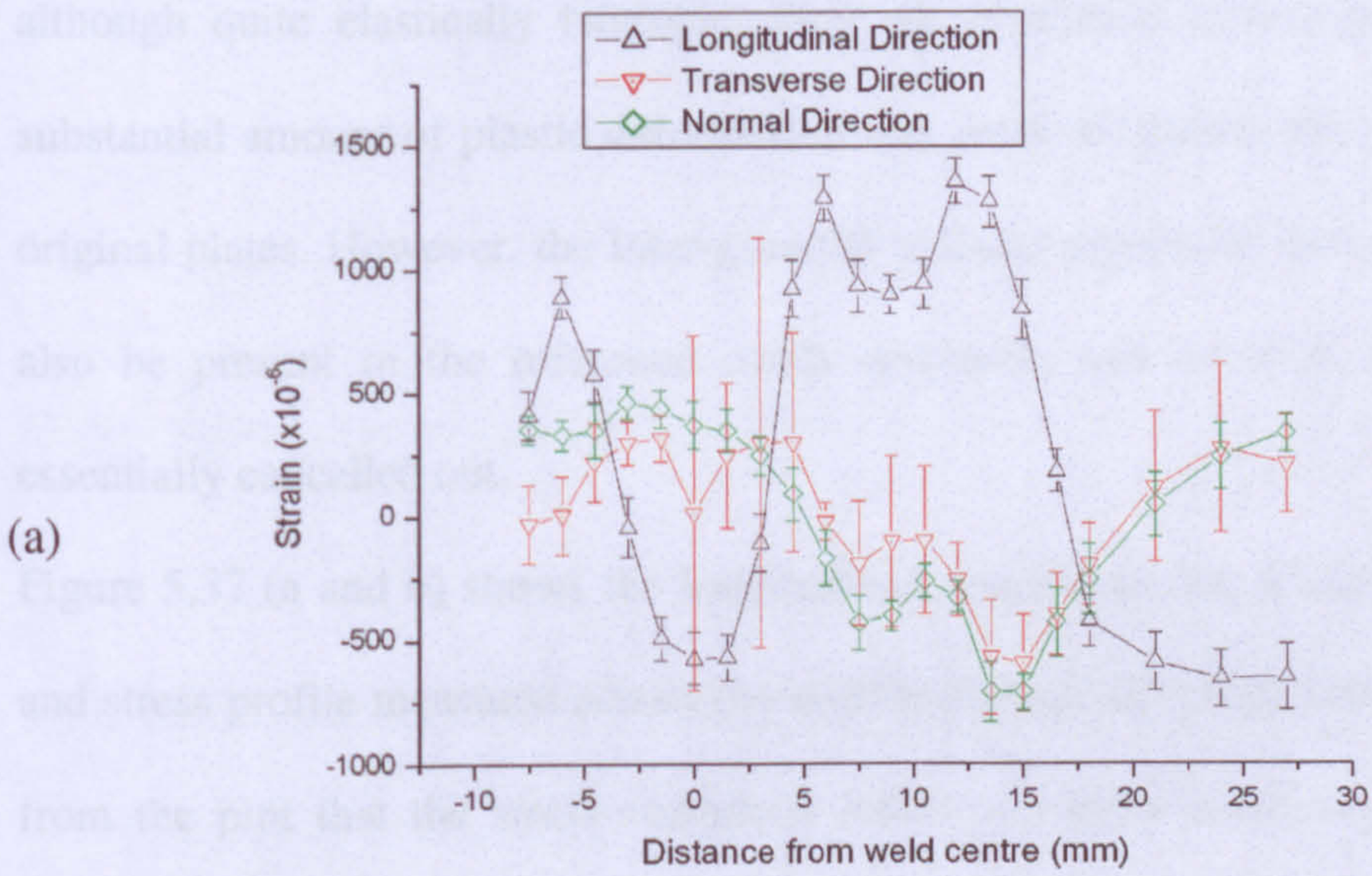

Figure 5.37: Variation in (a) strain and (b) stress measured along the principal directions in the MIG welded 2024 specimen.

centre. As noted previously, since the Al-2024 T351 alloy specimen did not exhibit any strong texture, weighted average values of lattice parameter from all the reflections were used to determine the strain. This average value gives elastic parameters close to the macroscopic values [5.27]. The resultant variation in the strain and the stress across the MIG welded Al-2024 sample is shown in figure 5.37 (a and b). The presence of inter-granular stresses cannot be ruled out in Al alloys as, although quite elastically isotropic, they are plastically anisotropic [5.28] and a substantial amount of plastic deformation was involved during the processing of the original plates. However, the inter-granular stresses present in the original plate will also be present in the reference comb specimen, and so their effect should be essentially cancelled out.

Figure 5.37 (a and b) shows the longitudinal, transverse and normal direction strain and stress profile measured across the weld in the middle of the sample. It is evident from the plot that the stress variations follow a similar trend in the longitudinal, transverse and normal directions with compressive stress near the weld centre and tensile stress near the HAZ region. A maximum tensile stress of around 140 MPa is observed in the longitudinal direction near the HAZ region at around 5 mm away from the weld centre while a maximum compressive stress of -40 MPa is found in the weld centre. The longitudinal stresses measured in the CT specimen are compared with those measured in the original welded plate [5.19, 5.29] in figure 5.38. It can be seen that there has been a substantial relaxation in longitudinal residual stress on machining the CT sample from the welded plate. In particular,

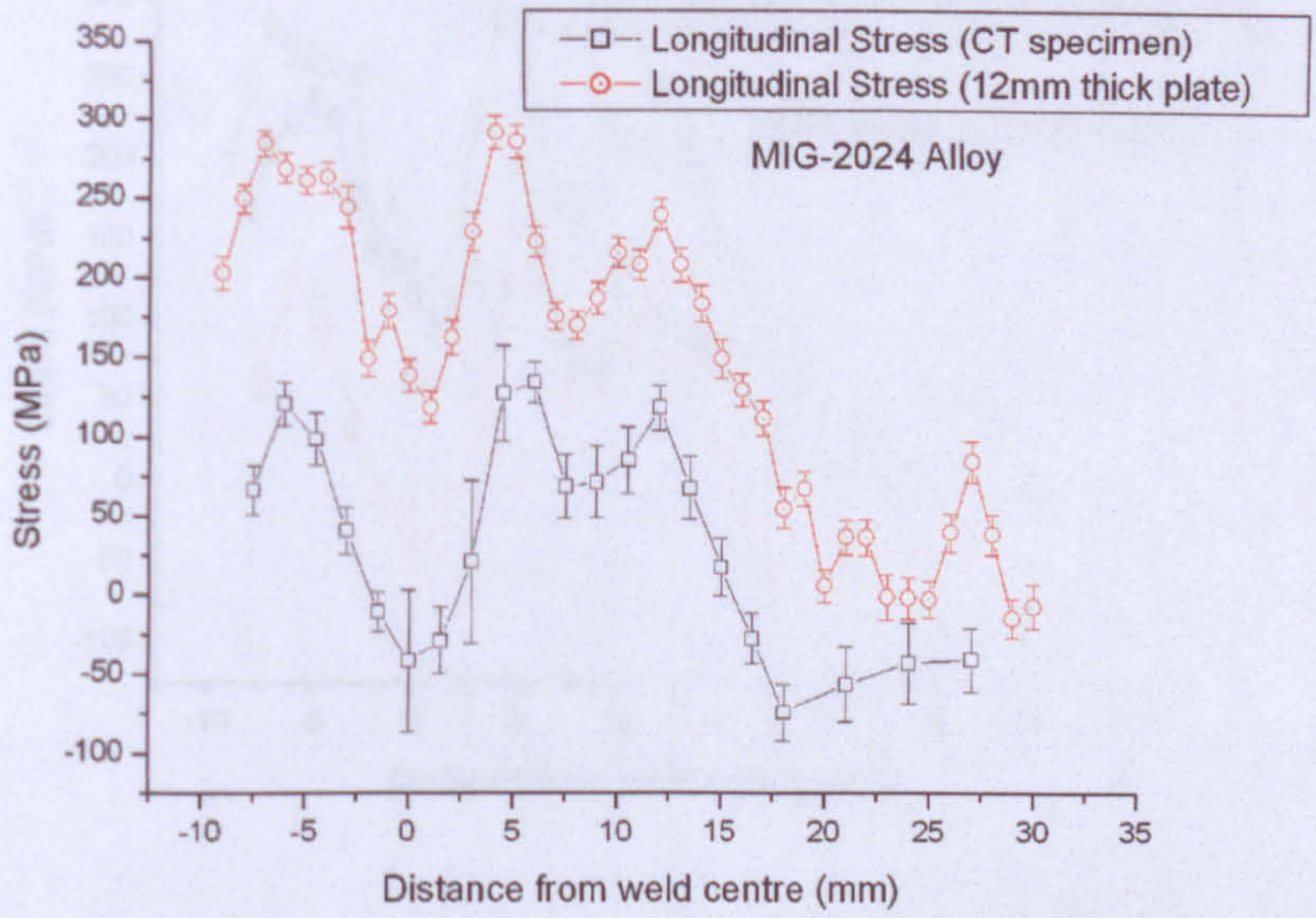

Figure 5.38: Comparison of the longitudinal stress distribution in the 2024 CT specimen and a plate representative of that from which it was machined

compressive stresses now exist at the weld centreline whereas the equivalent area in the original plate contained tensile stresses.

Further, the CT specimen results are compared (figure 5.39) with the results of 7 mm thick dog-bone shaped MT specimen [5.19, 5.29], which was also obtained from the original 12 mm thick as-welded plate. The result shows that both MT and CT, specimens show stress relaxation compared to the original welded plate, however the

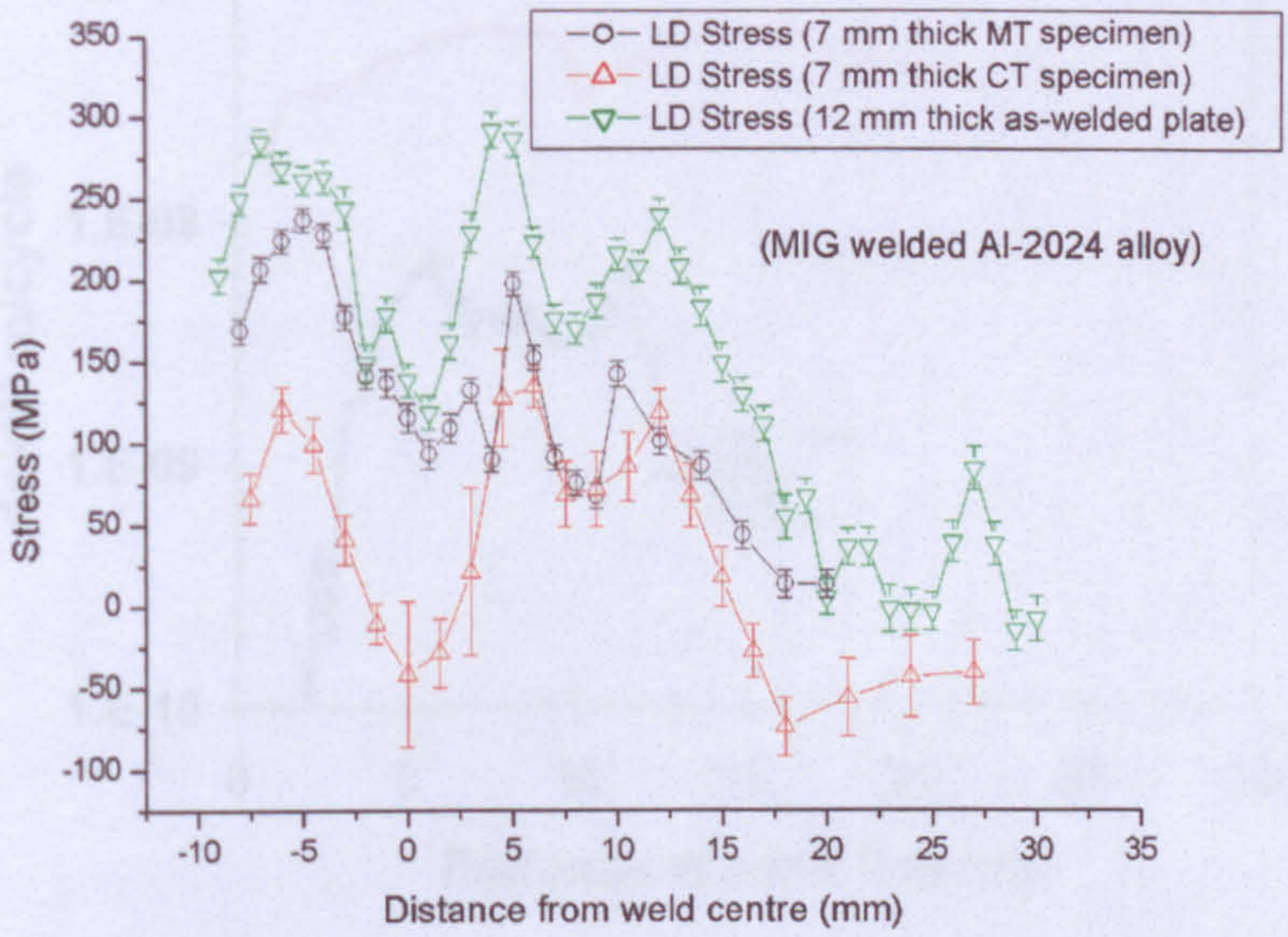

Figure 5.39: Comparison of the longitudinal stress distribution in the 2024 CT specimen, MT specimen and a plate representative of that from which these were machined.

MT specimen shows relatively less stress relaxation compared to the significant amount of stress relaxation observed in the CT specimen. It is evident from the plot that tensile stress of 100 MPa and 120 MPa is observed at the weld centre of the MT specimen and as-welded plate respectively whereas a compressive stress of -50 MPa can be found at the same location of the CT specimen. The larger amount of stress re-distribution in the CT specimen can be attributed to the introduction of a notch in this specimen

Consequently, the presence of this compressive and tensile residual stress at the weld

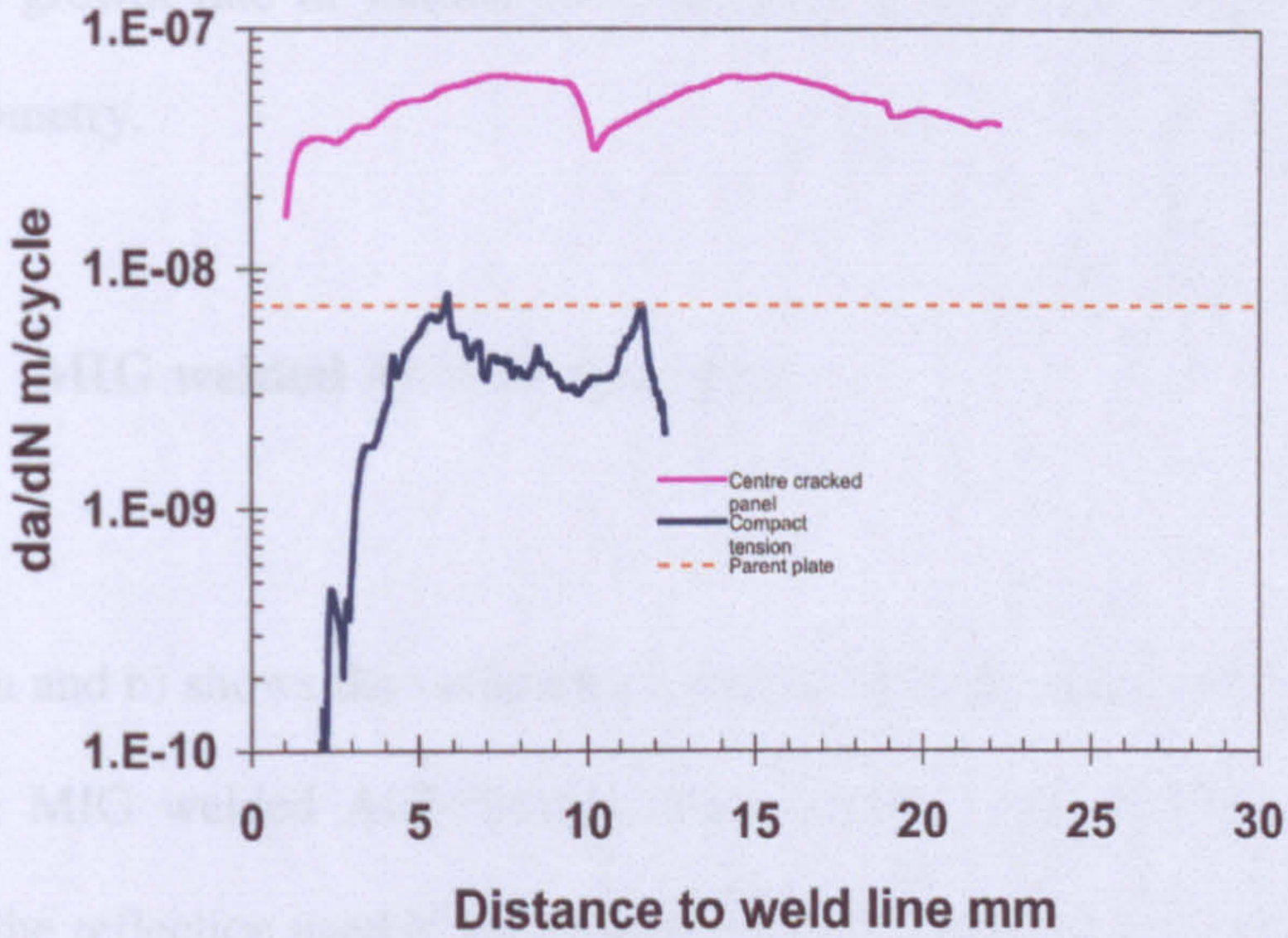

Figure 5.40: – da/dN Vs ΔK for VPPA welded Al-2024 T351, tested in centre cracked panels with 2 mm starting defect in centre of the weld line. with parent plate at R = 0.1 [5.14].

centre of CT and MT specimen respectively can affect the fatigue crack growth rate significantly and this can be better illustrated if the fatigue crack growth rate in these specimens are compared. Figure 5.40 compares the fatigue crack growth rate produced by constant ΔK test at $\Delta K = 6\ \text{MPa}\sqrt{m}$ in CT and MT samples [5.14]. It can be seen from the plot that the crack growth rate is significantly higher in the MT specimen compared to the CT specimen. In the MT specimen, the crack growth rate varies from 2.10^{-8} to 7.10^{-8} m/cycle, whereas in the CT specimen, the crack growth rate reduces to less than 10^{-10} m/cycle as the crack approaches the weld centre. As both the samples were obtained from the same parent plate and contain identical welds, the difference in the fatigue crack growth rate must be due to the residual stress difference, which arises due to the geometry change of different samples. These results clearly suggest that the residual stress distribution and consequently the

fatigue crack growth rate in welded components can be greatly influenced by the specimen geometry.

5.2.4.2 MIG welded Al-7150 specimen

Figure 5.41 (a and b) shows the variation of strain and stress with position across the weld for the MIG welded Al-7150 specimen. In this case individual d_o values obtained for the reflection used in each direction were used on a point by point basis to calculate the strain. This should remove any d_o and inter-granular variations present so that only the macroscopic strains are determined.

Like the Al-2024 alloy, figure 5.41 (b) shows similar variations in longitudinal residual stress for the Al-7150 alloy, tensile longitudinal stress being observed near the HAZ region with compressive stresses in the weld centre. The maximum tensile stress of 120 MPa was found at around 5mm away from the weld centre. However, the magnitude of compressive stress is around -150 MPa, which is significantly larger compared to the maximum compressive stress observed in the Al-2024 specimen.

(a)

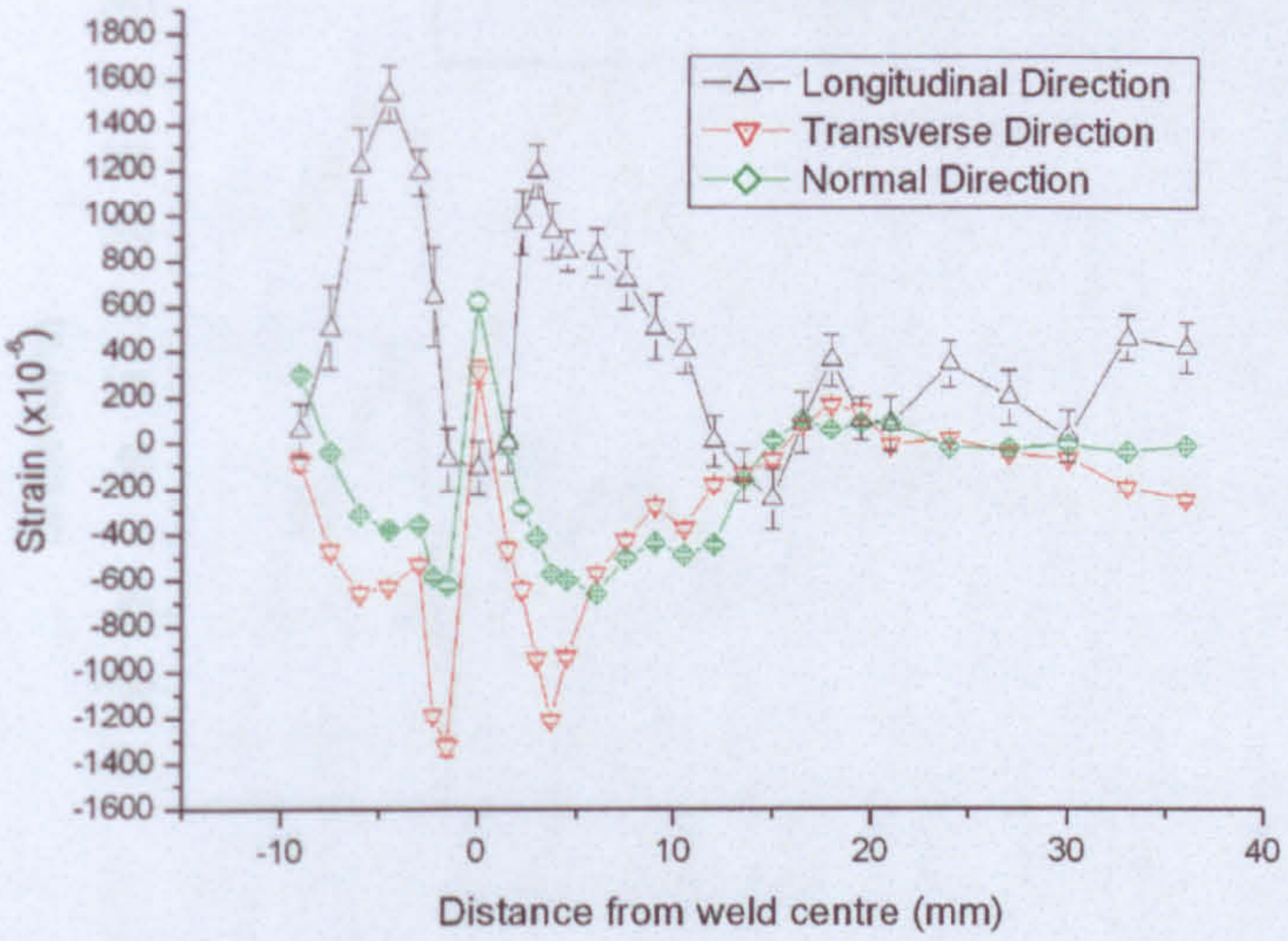

(b)

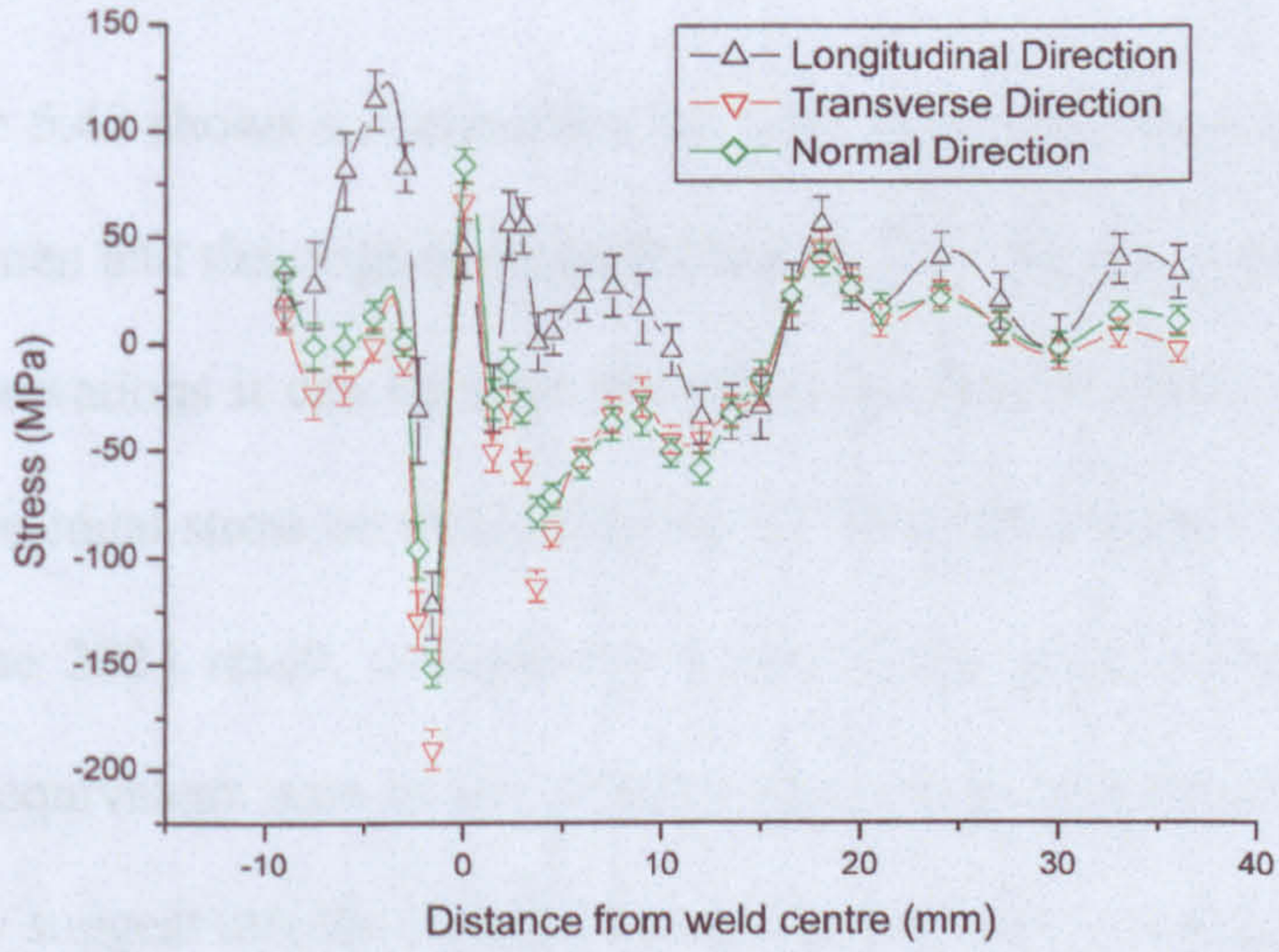

Figure 5.41: Variation in (a) strain and (b) stress measured along the principal directions in the MIG welded Al-7150 specimen.

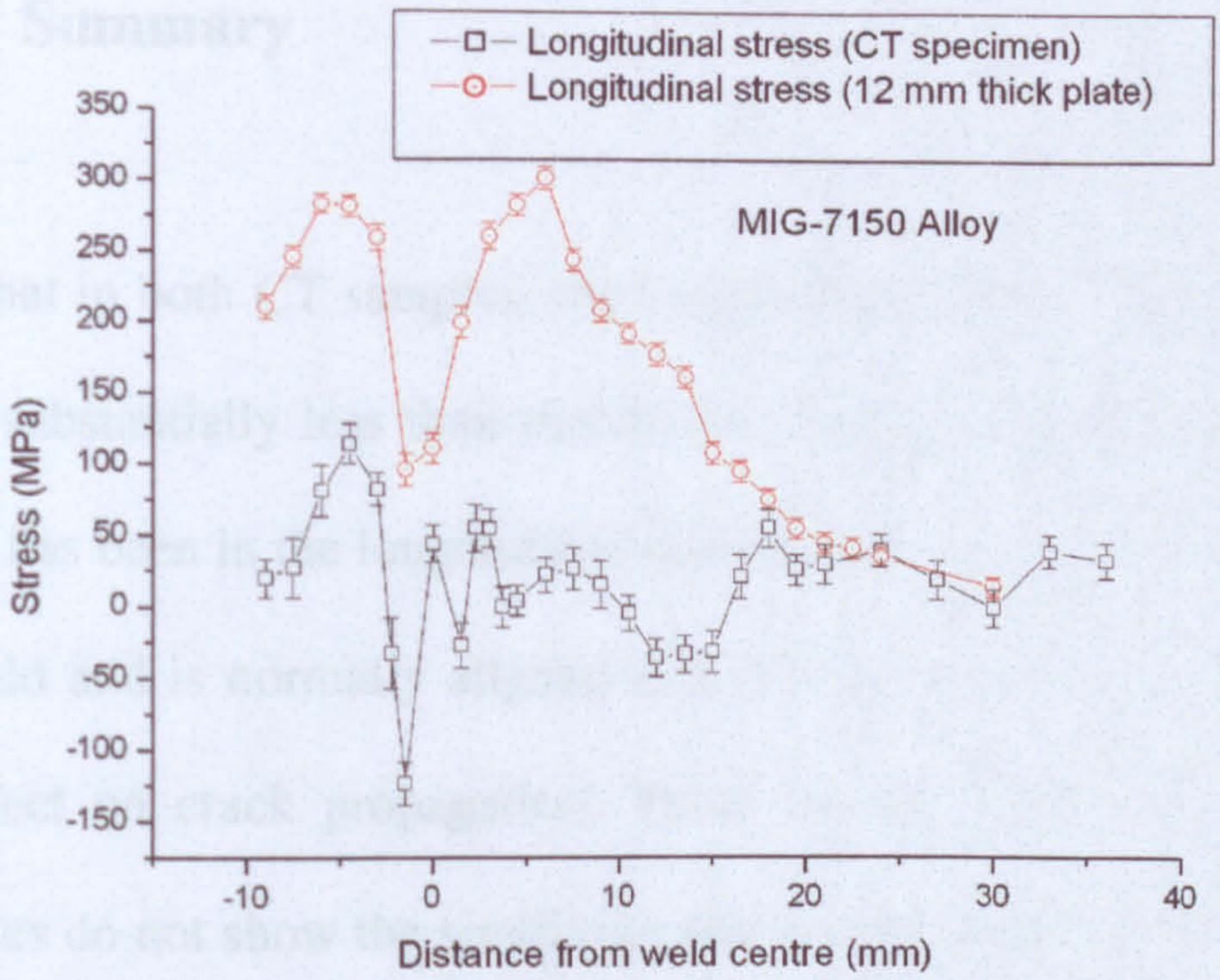

Figure 5.42: Comparison of the longitudinal stress distribution in the Al-7150 CT specimen and a plate representative of that from which it was machined.

Figure 5.42 shows a comparison between the longitudinal stress measured in the CT specimen and the original welded plate [5.21, 5.30]. In common with the Al-2024 CT observations it can be seen that there has been a substantial relaxation in longitudinal residual stress on machining the CT from the welded plate. Furthermore, confirming the 2024 result, compressive stresses now exist at the weld centreline whereas the equivalent area in the original plate contained tensile stresses. These results clearly suggest that the residual stress distribution in a welded component can be greatly influenced by the specimen geometry.

5.2.5 Summary

It is evident that in both CT samples, the longitudinal residual stress after specimen machining is substantially less than that in the original welded plate. Furthermore, this reduction has been in the longitudinal stress, which is usually the largest residual stress in a weld and is normally aligned in a CT specimen so that it will have the maximum effect on crack propagation. These results provide firm evidence that residual stresses do not show the similitude that is a fundamental pre-requisite of the application of data obtained from laboratory sized specimens to larger components and structures. The effect is particularly striking since the stress at the weld centre changes from tensile to compressive: from deleterious to fracture and fatigue properties in the welded plate to advantageous in the CT specimen. This work suggests that care must be taken in using the results obtained from laboratory sized fracture and fatigue specimens that have been machined from larger welded components or structures.

5.3 Example of residual stress redistribution due to the presence of a fatigue crack

5.3.1 Background

The effect of residual stress on fatigue crack growth has already been established and well understood qualitatively. Residual stress has been identified as a mechanism which affects the fatigue resistance of a material. From previous experience it is observed that a crack grown through compressive residual stress field shows retardation, but when it reaches a tensile zone it does not show the expected

accelerated crack growth. This phenomenon can only be explained in terms of redistribution and relaxation of the pre-existing residual stress due to the passage of the crack. Therefore, it is very important to know the distribution of residual stress after the crack is grown as the use of residual stress values prior to the crack growth might lead to a non-conservative fatigue life prediction.

In this current work, the neutron diffraction technique has been used to study the redistribution and relaxation of the original residual stress field in VPPA welded Al-2024 alloy due to the presence of fatigue cracks of different lengths. Further experiments were also carried out on these samples under in-situ loading condition to study the stress distribution due to the application of external loading.

5.3.2 Sample descriptions

Two VPPA-welded dog bone shaped MT (middle crack tension) Al-2024 samples with centre crack lengths of 13 mm and 25 mm were investigated. The joined plates

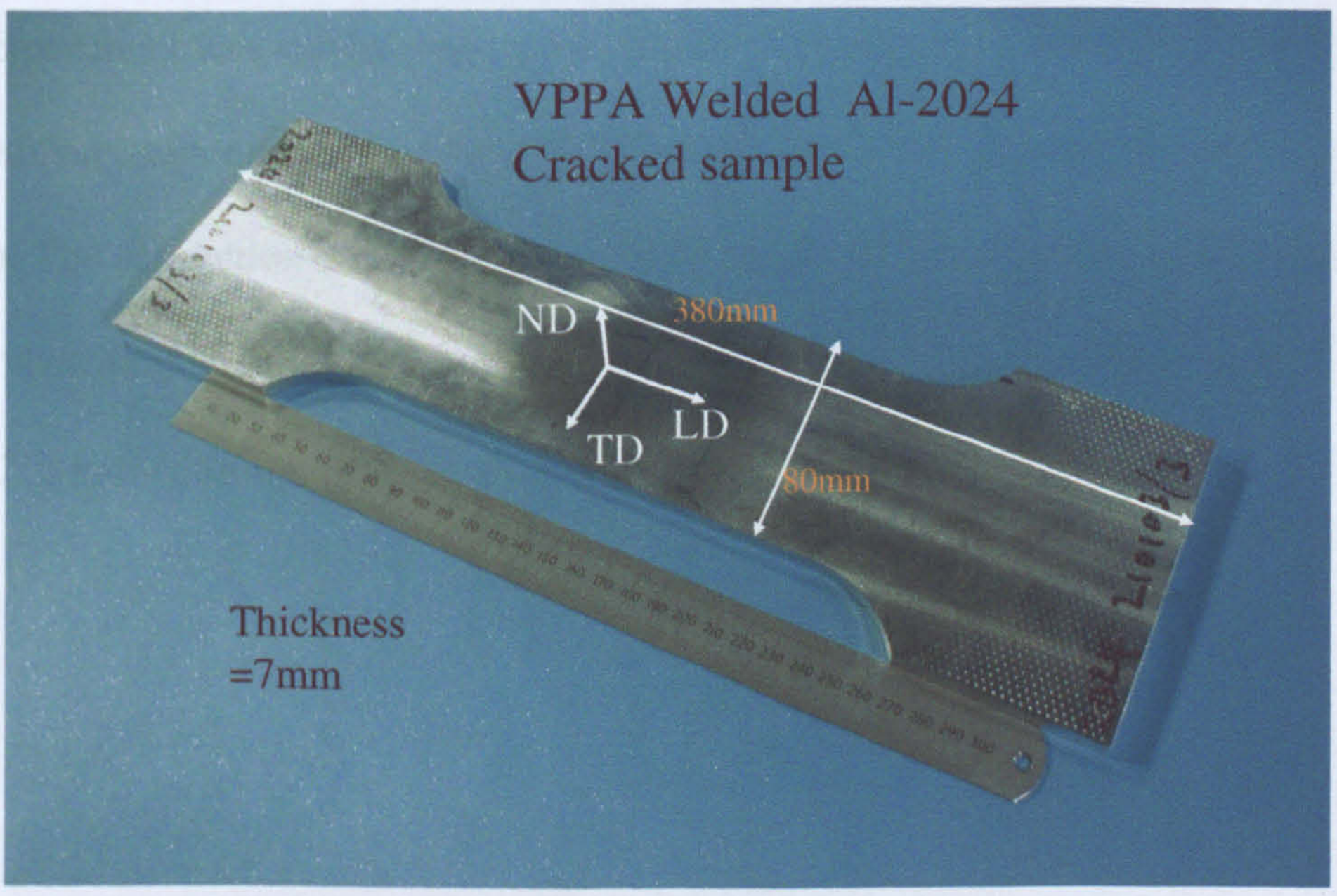

Figure 5.43: Photograph of the dog-bone sample.

were subsequently skimmed and fabricated to dog–bone specimens of dimensions 380 x 80 x 7 mm^3. A central notch of 1 mm nominal radius was placed using the Electro Discharge Machining (EDM) technique and then subsequently fatigue cracks (2a = 13 mm and 25 mm) were grown in both the specimens under the condition of constant $\Delta K = 8MPa\sqrt{m}$ and $6MPa\sqrt{m}$ respectively with a constant R value of 0.1. The photograph of the specimen can be seen in the figure 5.43. Three principal directions can be identified as the longitudinal direction (LD), which corresponds to the welding direction that is perpendicular to the crack growth direction, transverse direction (TD), which corresponds to transverse to the welding direction that is along the crack growth direction, and normal direction (ND), which corresponds to the through thickness direction.

5.3.3 Details of experiment in HMI Berlin

The experiment was carried out on the dedicated residual stress diffractometer, E3, at the neutron reactor source at the Berlin Neutron Scattering Centre (BENSC) at HMI, Berlin. The diffraction experiment was carried out using a monochromatic beam of fixed wavelength ($\lambda = 1.37$ Å), which was obtained from a vertically focused fixed Cu (220) monochromator orientated at a take off angle of $2\theta^{M} = 65^{0}$.

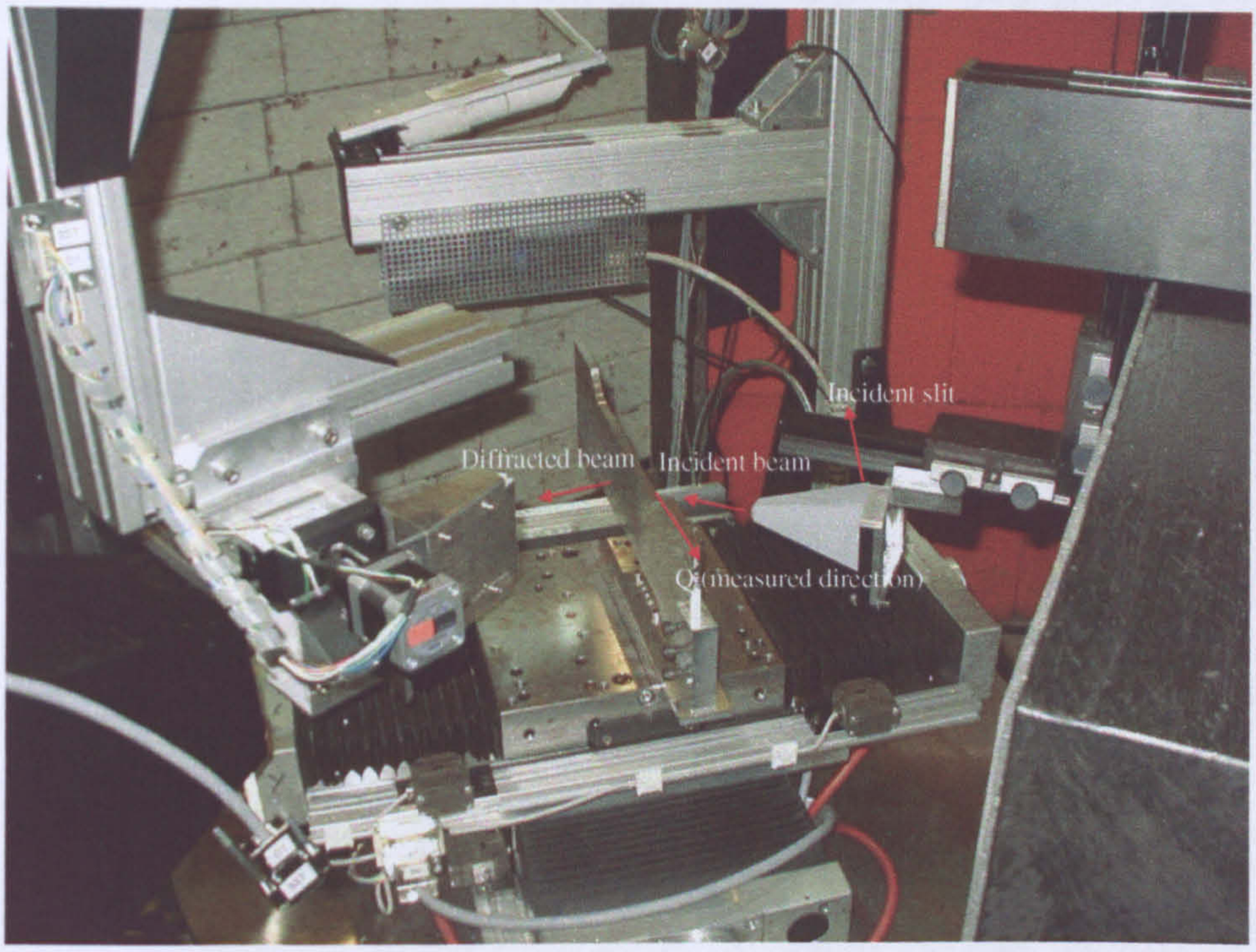

Figure 5.44: Experimental set-up on E3 instrument at HMI.

The instrument was calibrated by measuring a standard pure alpha-iron pin. All the measurements were carried out using the (311) reflection, which corresponds to a scattering angle of $2\theta = 69.93^0$. The gauge volume of 2 x 2 x 2 mm^3 was used to probe along the mid-thickness of the specimen starting from the centre notch, from where the crack was first initiated. Measurement locations can be seen in the figure 5.45. To capture the effect of only the fatigue cycle without the presence of a crack,

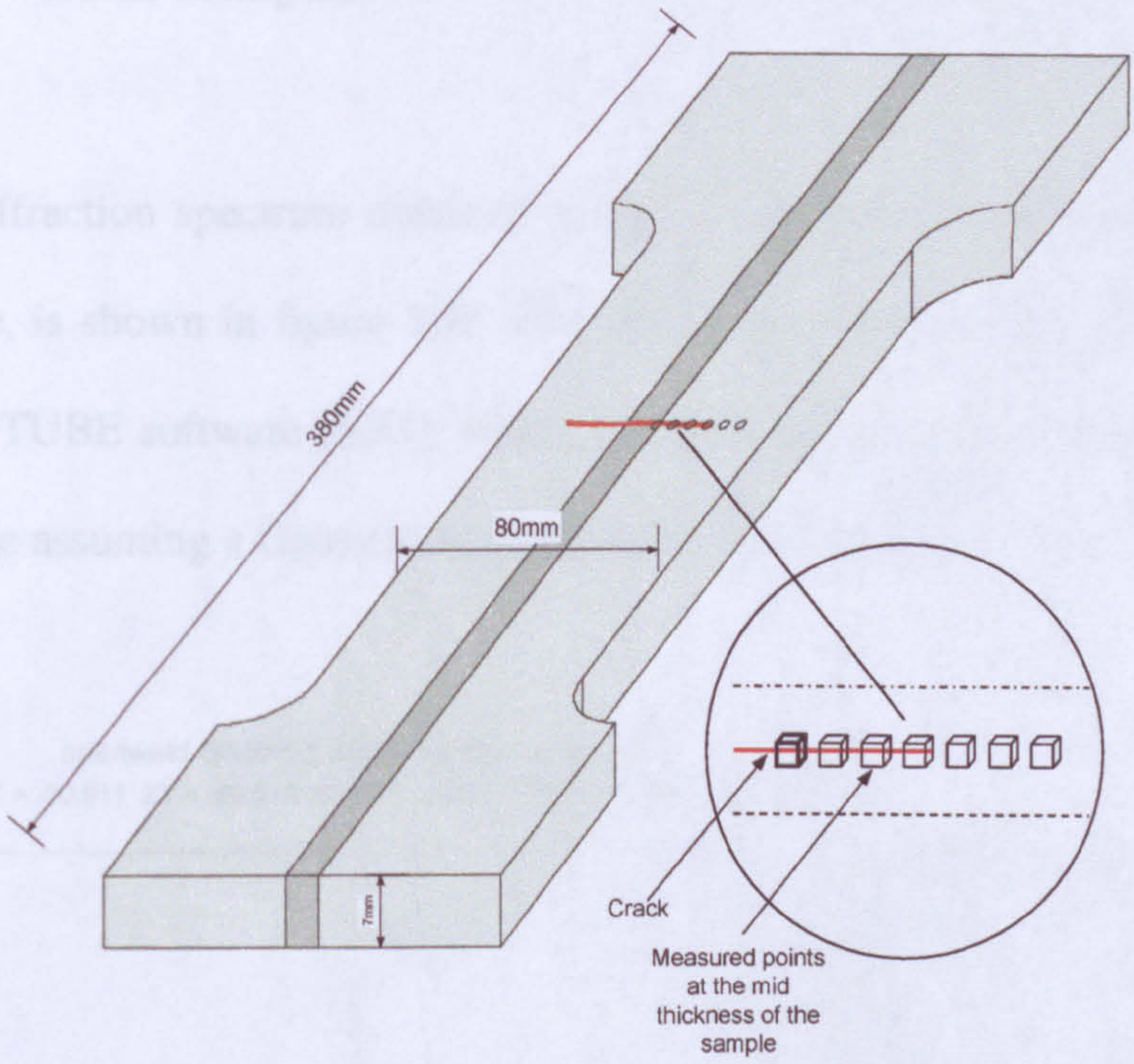

Figure 5.45: Schematic diagram of the dog-bone shaped MT specimen.

one extra set of measurements was carried out 20 mm away from the crack line. Three principal directions were measured and for that reason the sample had to be realigned three times as only one detector was used. The accurate positioning of the sample with respect to the beam was achieved by using a laser beam together with the use of conventional wall-scans of the sample across the beam.

Point to point stress free reference values were obtained by the measurement of the comb specimen, which was measured previously at the ENGIN facility, France [5.19]. Standard Al powder sample was used to normalize the data from the two sets of measurement points.

5.3.4 Data analysis

A typical diffraction spectrum obtained at the E3 instrument, measured on the Al-2024 sample, is shown in figure 5.46. The diffraction peak profile was fitted using in-house TVTUBE software [5.31], which fitted the diffraction profile using a peak fitting routine assuming a Gaussian-type intensity distribution profile.

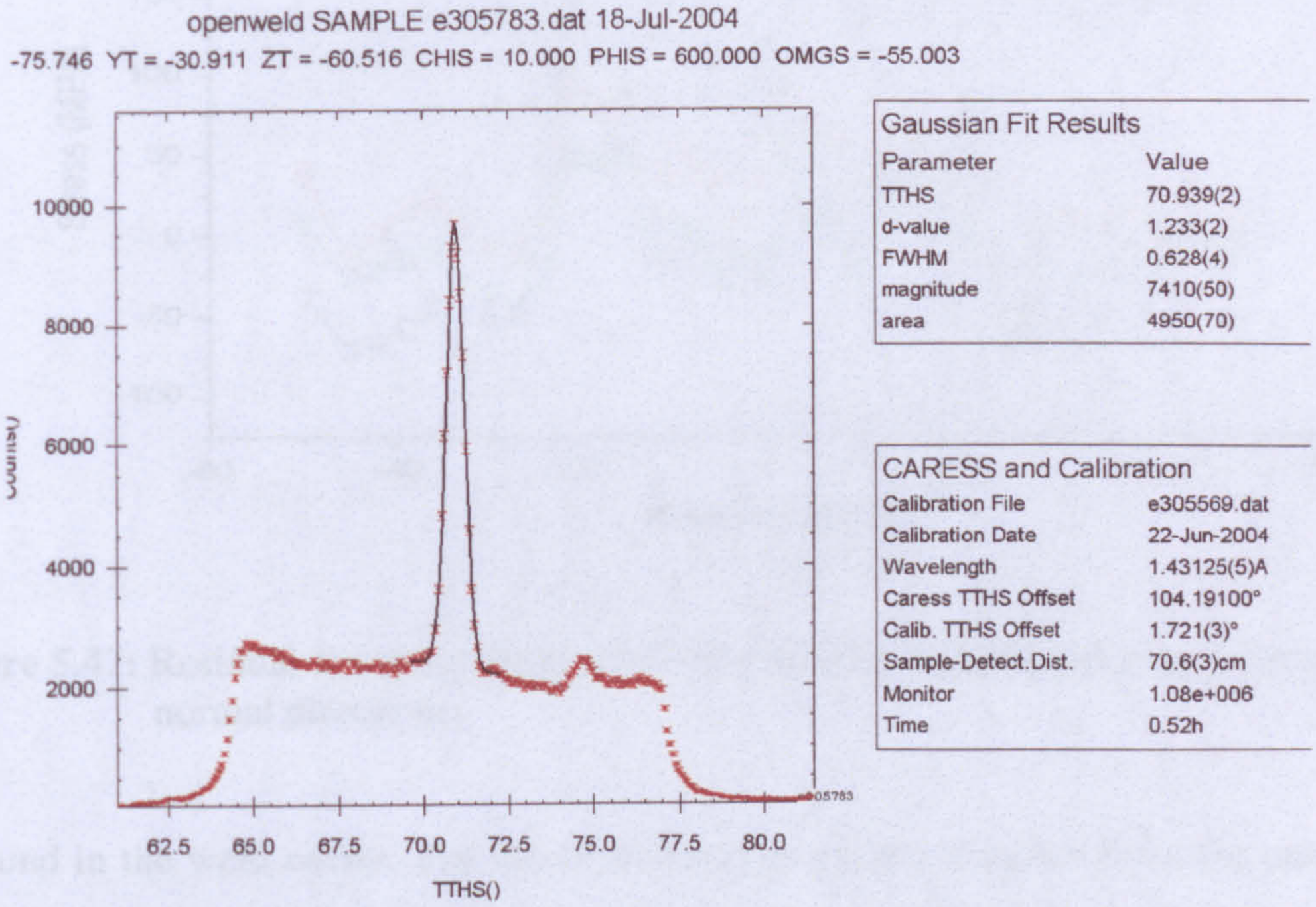

Figure 5.46: Diffraction spectrum obtained in the Al-2024 specimen on E3 instrument, Berlin.

5.3.5 Results and discussion

The 7 mm thick as-welded specimen (without the presence of any fatigue crack) was measured at ENGIN instrument, ISIS, by the Open University Structural Integrity Research Group [5.18, 5.19] and the stress distributions in the three principal directions are shown in figure 5.47. The results show that the stress distribution pattern is almost similar in three principal directions with a significant stress

variation in the longitudinal direction. A typical double peak stress is observed in the longitudinal direction with the maximum stress of around 240 MPa is observed at around 5 mm away from the weld centre (HAZ region) while around 50 MPa stress

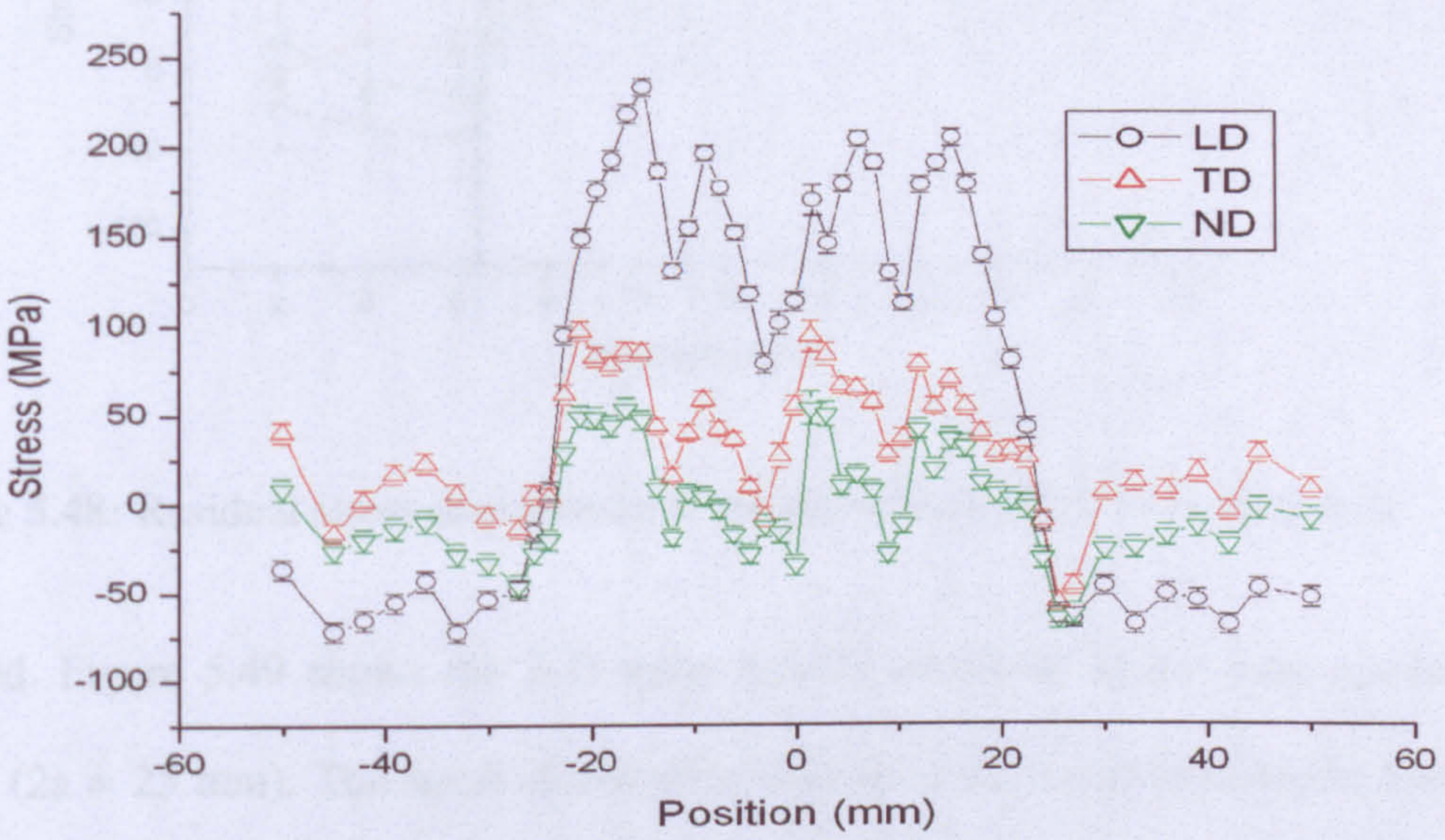

Figure 5.47: Residual stress variation across the weld in longitudinal, transverse and normal directions.

is found in the weld centre. The stress distribution profile obtained from the current experiments is shown in figures 5.48-5.50. Figure 5.48 shows the longitudinal, transverse and normal direction residual stress variation along the crack in the short cracked (2a = 13 mm) sample. The stress profile in these three directions shows similar trend, with the stresses in longitudinal direction showing the greatest variation. Interestingly, the stress variation along the crack behind the crack tip does not vary much and remains compressive while in front of crack tip the stresses, particularly the longitudinal stress, rises rapidly to a high tensile value, with a maximum stress of around 260 MPa. The far field stresses approach zero as

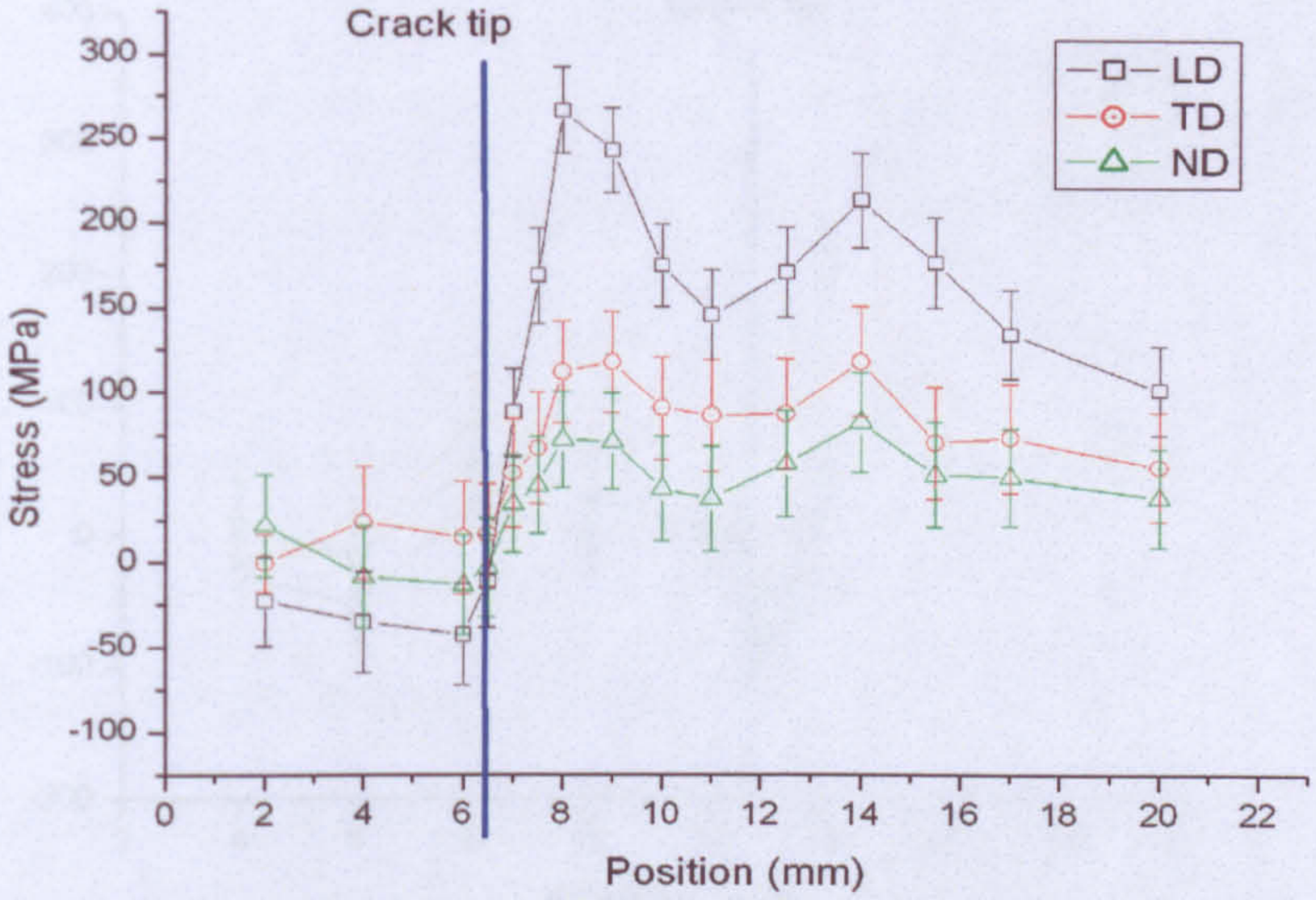

Figure 5.48: Residual stress distribution in the short crack (2a = 13 mm) sample.

expected. Figure 5.49 shows the 3-D stress profile measured in the long cracked sample (2a = 25 mm). The stress distribution follows a similar pattern to the short crack sample with compressive stress along the crack and a sharp rise of stresses in front of crack tip. The maximum tensile stress of around 310 MPa is observed in front of the crack tip which is at a distance of around 14 mm from the weld centre. A compressive stress of around -40 MPa is observed along the crack in the longitudinal direction and a maximum compressive stress of around -90 MPa is observed near the crack tip.

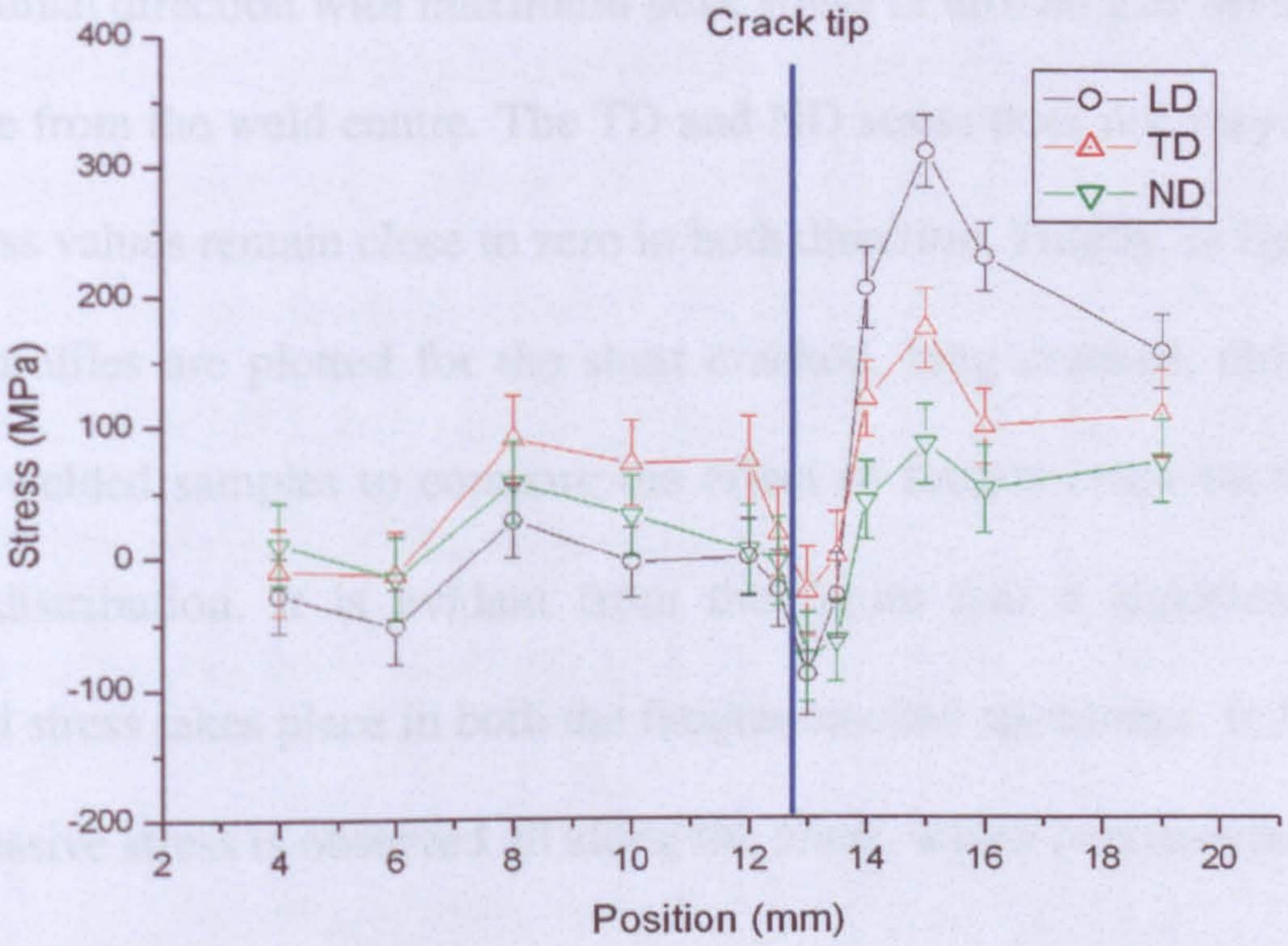

Figure 5.49: Residual stress distribution in the long crack (2a = 25 mm) sample.

To study whether the fatigue cycle applied to the sample to grow the crack has any effect on the previously present residual stress distribution, a line was measured 20 mm away from the crack line. The results from this measurement are plotted in figure 5.50, which shows that the typical double peak is observed in the

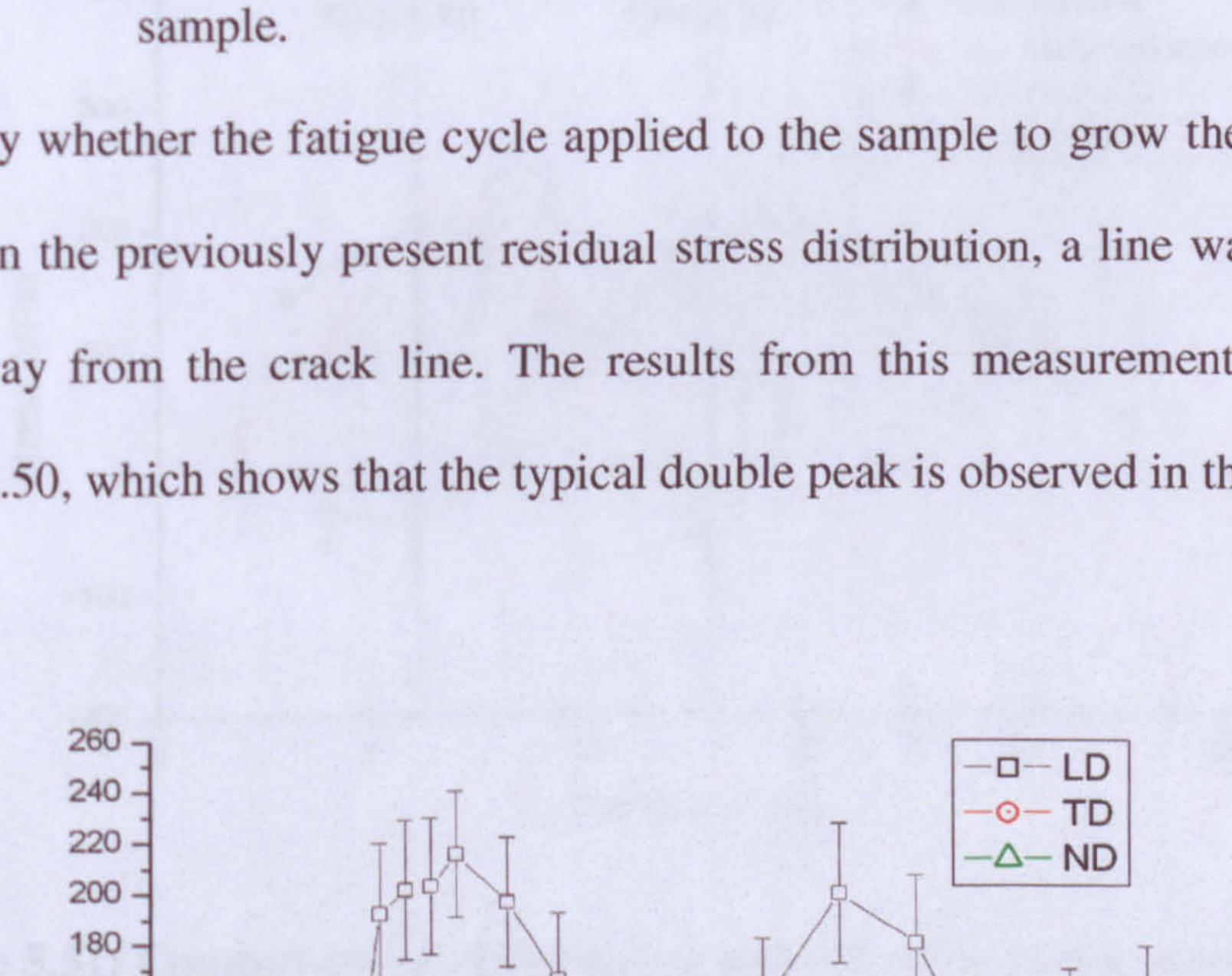

Figure 5.50: Residual stress distribution (across the weld) in the short crack specimen 20 mm away from the crack line.

longitudinal direction with maximum peak stress of around 220 MPa at around 8 mm distance from the weld centre. The TD and ND stress does not vary significantly and the stress values remain close to zero in both direction. Finally, in figure 5.51, the LD stress profiles are plotted for the short cracked, long cracked, fatigued un-cracked and as-welded samples to compare the effect of fatigue crack on the weld residual stress distribution. It is evident from the figure that a significant relaxation of residual stress takes place in both the fatigue-cracked specimens. In both specimens a compressive stress is observed all along the crack, which becomes tensile in front of

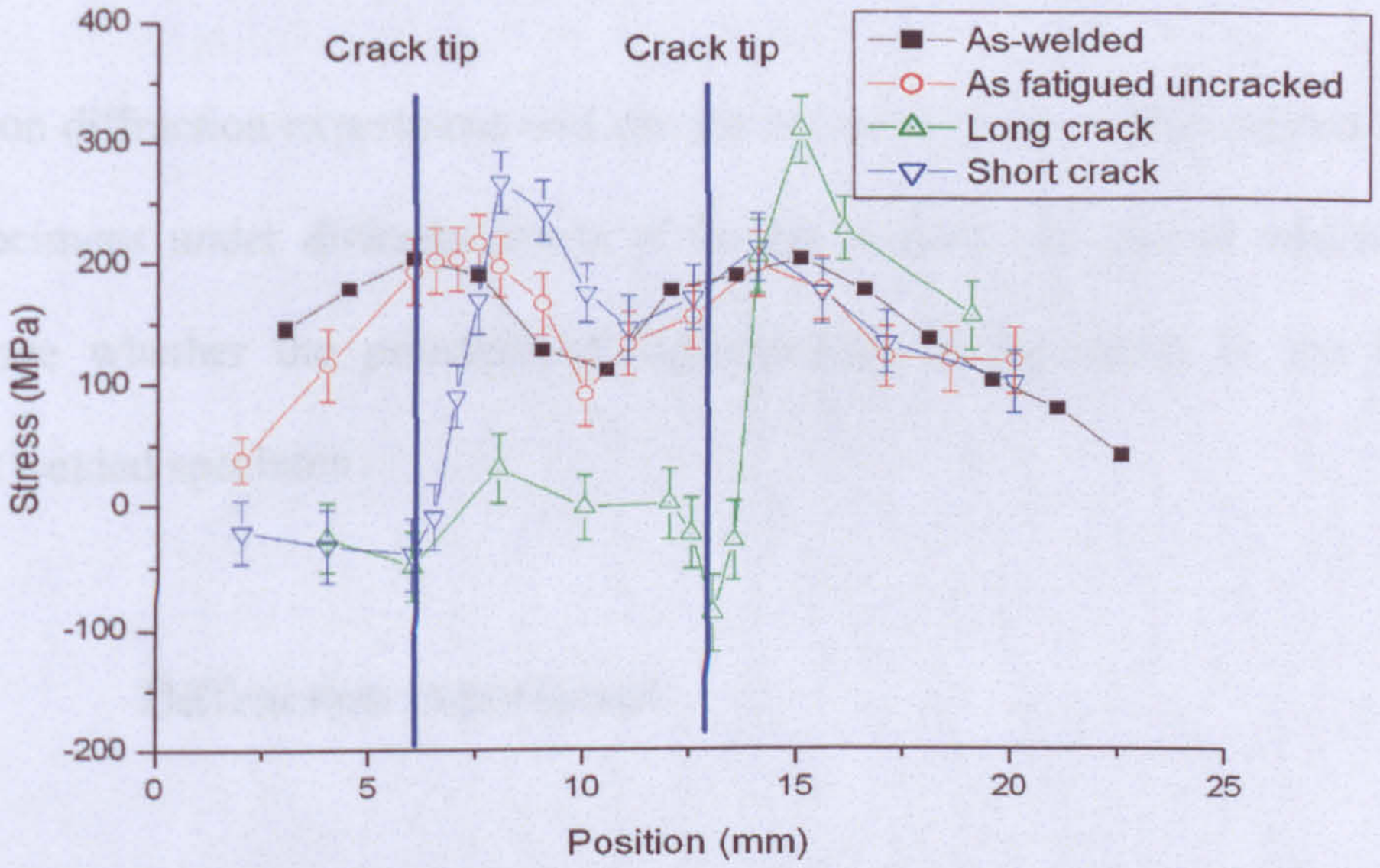

Figure 5.51: Comparisons of longitudinal residual stress profile among the as welded, short crack, long crack and fatigued specimen.

the crack tip. The presence of compressive stress along the crack and sharp rise of stresses in front of crack tip confirm the fact that residual stresses are redistributed due to the fatigue crack growth. However, the stress profile of the line measured away from the crack (without crack) line shows (figure 5.51) no significant difference in the stress distribution compared to the original welded specimen which suggests that the effect of redistribution is only limited in the region near the fatigue

crack. It is worth mentioning that the uncertainties of the measured stress values (around 40 MPa) obtained in E3 instrument (HMI) are relatively high than the typical stress uncertainties observed in ENGIN-X (around 10-20 MPa). This can be attributed to the presence of a higher background in the diffraction spectrum of the E3 instrument at HMI. Nevertheless, these results clearly demonstrate that significant redistribution of residual stress takes place due to the presence of fatigue crack and it might lead to non-conservative life approach if not accounted for.

5.3.6 Superposition of residual stress under external loading

A neutron diffraction experiment was carried out on both the VPPA welded Al-2024 MT specimens under different levels of in-situ loading, the aim of which was to investigate whether the principle of superposition is applicable in the fatigued cracked welded specimen.

5.3.6.1 Diffraction experiment

Both the VPPA welded dog-bone shaped MT specimen (short cracked and long cracked) of different crack lengths (2a = 13 mm and 2a = 25 mm) were measured using neutron diffraction technique under the application of different levels of in-situ loading by pulling the specimen using a stress rig at the ENGIN-X facility. The schematic diagram of the experimental set up at the ENGIN-X facility is shown in the figure 5.52. The in-situ load was varied between the K_{max} and K_{min}, for the fatigue cycle. The value of which was 8.90 and 0.90 for the short cracked specimen

and 6.67 and 0.67 for the long cracked specimen respectively. The K values were calculated using the following equation obtained from ASTM E 647:

$$\Delta K = \frac{\Delta P}{B}\sqrt{\frac{\pi\alpha}{2W}}\sec\left(\frac{\pi\alpha}{2}\right) \tag{5.6}$$

Where $\alpha = \frac{2a}{W}$, $\Delta P = P_{\max} - P_{\min}$ for $R > 0$ and $\Delta P = P_{\max}$ for $R \leq 0$.

Three principal directions were measured using a gauge volume of 2 x 2 x 2 mm^3. Two directions were measured simultaneously, as ENGIN-X has two detector banks, while the third direction was measured by unloading the sample and rotating it by

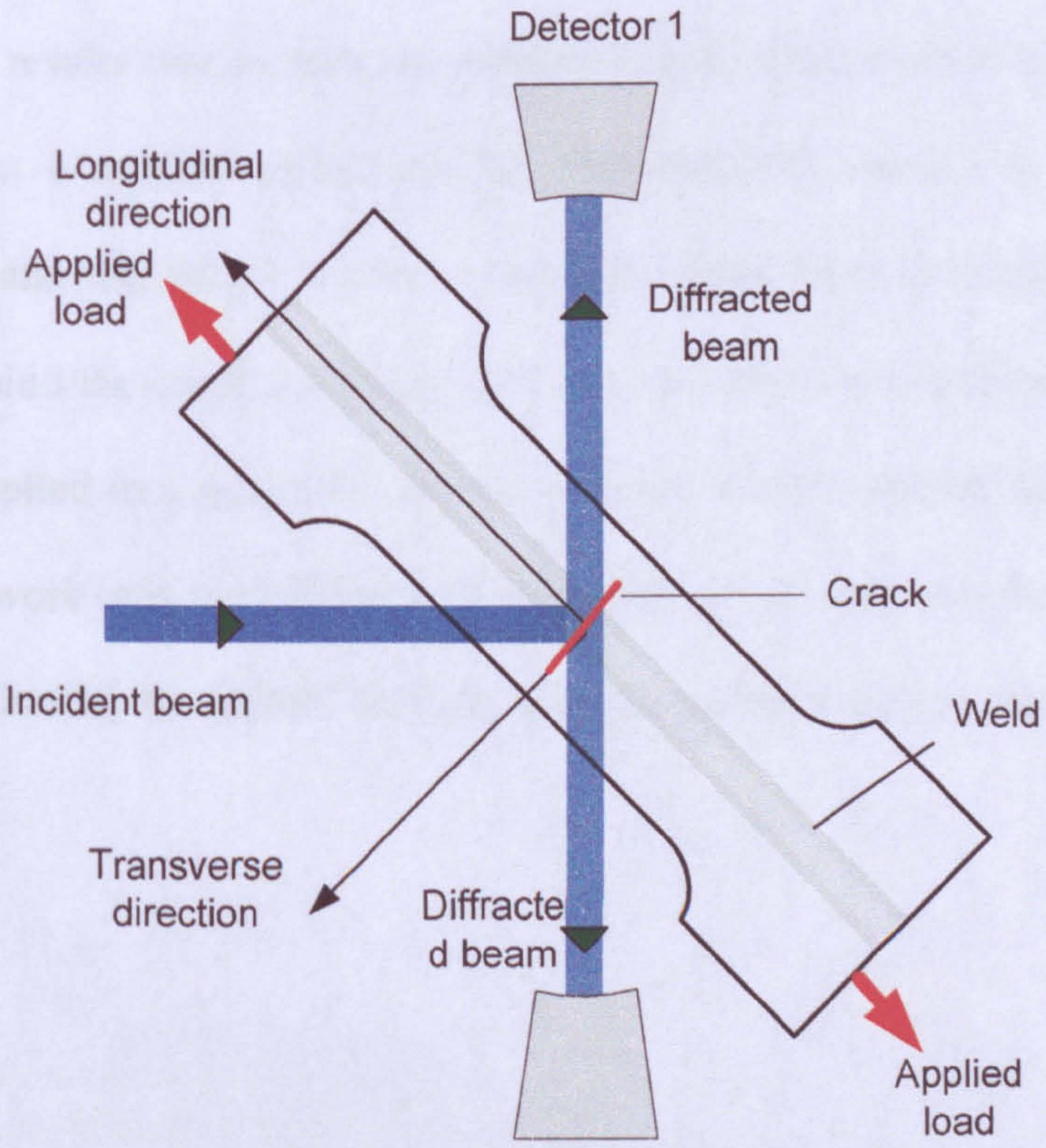

Figure 5.52: Schematic diagram of experimental set up at ENGIN-X instrument.

90^0 and reloading it again. Point to point stress free reference values were obtained by the measurement of the comb specimen, which was measured previously at the ENGIN [5.19] instrument at ISIS. A standard Al powder sample was used to normalize the data from two sets of measurement points.

5.3.6.2 Results and discussion

Figures 5.53 and 5.54 show the LD stress distribution in the short cracked and long cracked sample under the application of various level of in-situ loading. It can be seen from the results that in both the samples a systematic shift of combined stress (residual stress + applied stress) can be observed with respect to a increase of external load and this effect is more prominent away from the crack tip and less prominent behind the crack tip. This result suggests that the superposition principle can still be applied in a fatigued-cracked specimen where residual stress previously exists. In this work only the LD stress distributions are presented as the superposition principle can directly be applied in these direction stresses only as this is the loading direction.

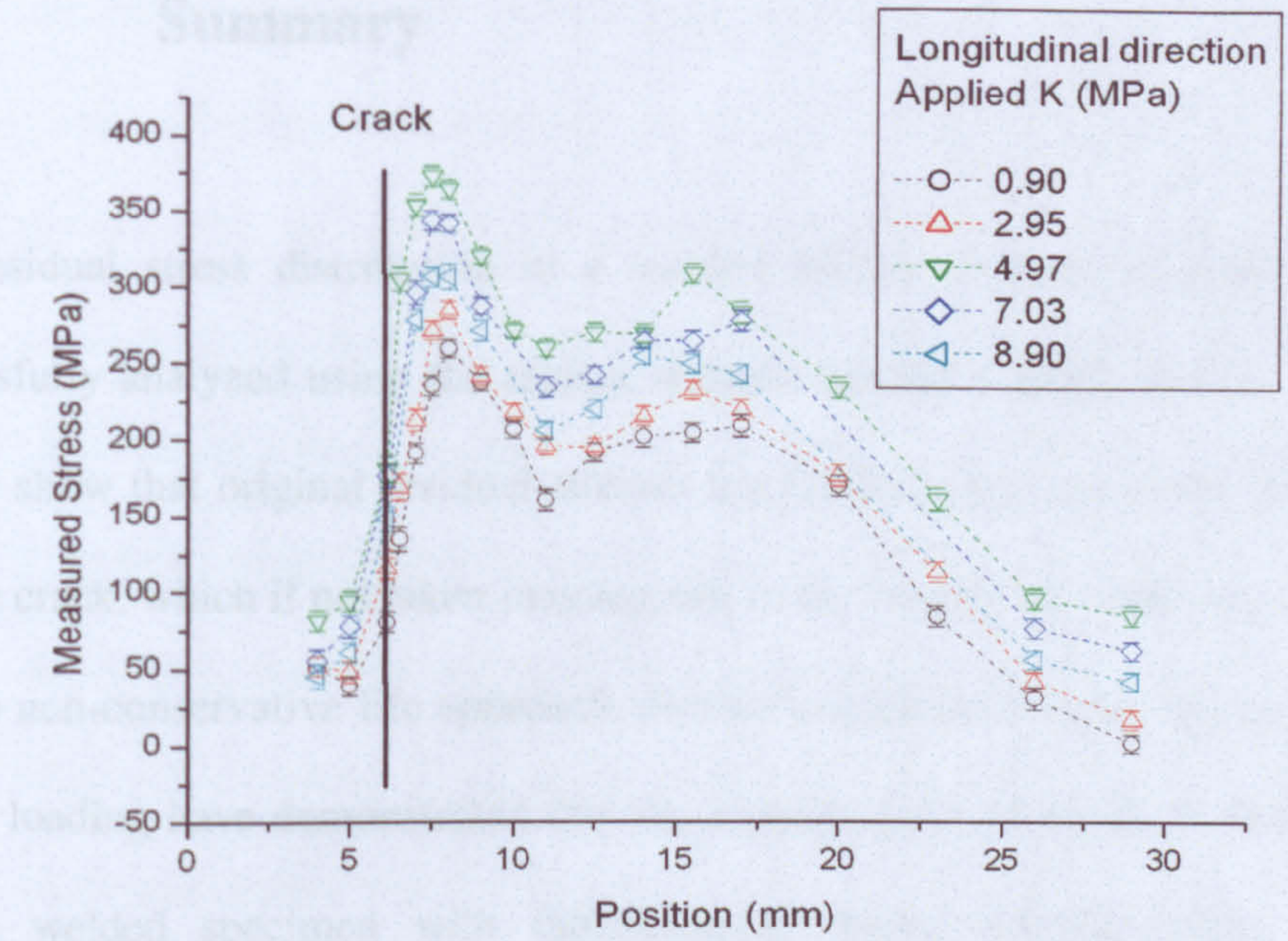

Figure 5.53: Stress distribution in the short-cracked (2a = 13 mm) under the application of external loading.

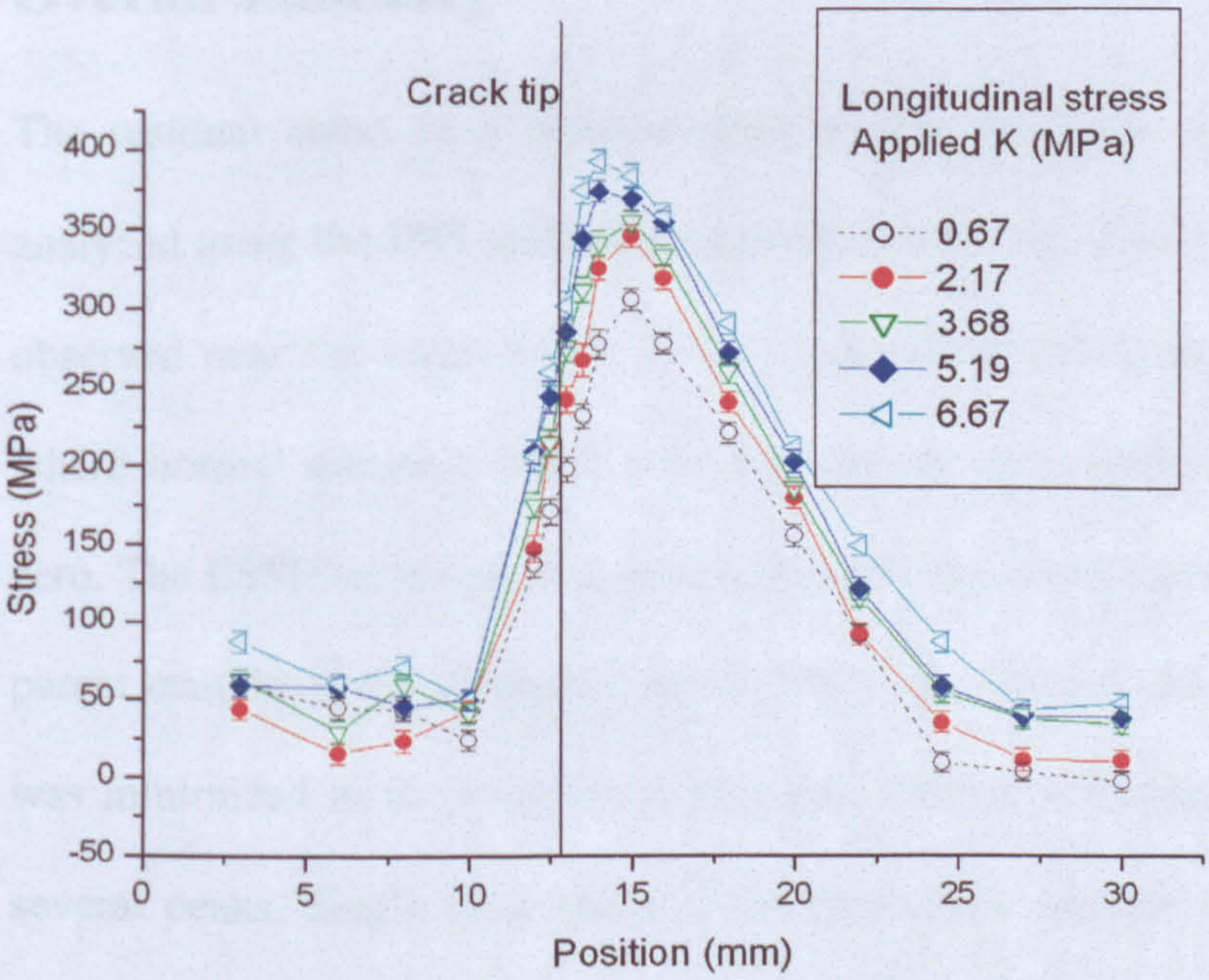

Figure 5.54: Stress distribution in the long-cracked (2a = 25 mm) sample under the application of different levels of external loading.

5.3.7 Summary

The residual stress distribution in a welded fatigue cracked specimen has been successfully analyzed using the reactor neutron facility at HMI, Berlin. The results clearly show that original residual stresses are redistributed due to the presence of a fatigue crack, which if not taken into account in the fatigue life prediction model may lead to non-conservative life approach. Further experiments under the application of in-situ loading have demonstrated that the superposition principle is also applicable in the welded specimen with fatigue-crack, where residual stress is present previously.

5.4 Overall summary

- The residual stress in a bead-on-plate welded specimen was successfully analyzed using the ISIS spallation neutron source. Significant tensile stress is observed near the weld region in the longitudinal and transverse directions where normal direction stress does not change much and remains close to zero. The ESSD technique was used to analyze the texture in the weld and the parent material and a strong texture of (100) was revealed, the effect of which was minimized in the final result by using Pawley refinement technique of several peaks. Single peak analysis and multi-peak analysis was carried out using Open Genie software, which revealed the effect of plastic anisotropy in the weld material.
- The 3-D residual stress distributions in MIG welded Al-2024 and Al-7150 alloy compact tension specimens have been determined using the newly developed POLDI instrument at the PSI, Switzerland. Near the weld centre,

the stresses are found to be compressive in both the specimens, but this compressive region is narrower in case of the Al-7150 specimen compared to the Al-2024 specimen. These results were compared to the stress results obtained from the original plate. In both cases, a substantial relaxation in the longitudinal stresses is observed when compared to the original welded plate. This work suggests that care must be taken in using the results obtained from laboratory sized fracture and fatigue specimens that have been machined from larger welded components or structures, which otherwise might lead to non-conservative life prediction.

- To study the effect of fatigue crack on the residual stress distribution, investigations were carried out on VPPA welded Al-2024 alloy specimens, with two different lengths of fatigue crack. Neutron diffraction results show significant redistribution of residual stress in both the specimens, with compressive stress all along the crack and a significant increase of stress to a tensile value is observed in front of the crack tip. Results obtained from the diffraction experiment under in-situ loading condition show a systematic increase of stress due to the application of external loading, indicating the fact that the superposition principle can be applied in the fatigue cracked specimen where residual stress exists previously.

5.5 References

5.1. P. J. Bouchard, J. R. Santisteban, L. Edwards, M. Turski, J. James, and S. Pratihar. *Residual stress Measurements Revealing Weld Bead Start and Stop Effects in Single and Multi-Pass Weld Runs*. in *ASME Pressure Vessels and Piping Division Conference*. 2005. Denver, Colorado.

5.2. *HKL Technology, Available at: www.hkltechnology.com, accessed on 31st July, 2006.*

5.3. J. James, J. R. Santisteban, L. Edwards and M. R. Daymond, *A Virtual Laboratory for Neutron and Synchrotron Strain Scanning*. Physica B : Condensed Matter 350, 2004. **350**(1-3): p. E743-E746.

5.4. M. E. Fitzpatrick, A. T. Fry, P. Holdway, F. A. Kandil, J. Shackleton and L. Souminen, *Determination of Residual Stresses by X-ray Diffraction*. Measurement Good Practice Guide. Vol. 52. 2002, NPL,London.

5.5. I. C. Noyan and J. B. Cohen, *Residual Stress-Measurement by Diffraction and Interpretation*, in *A very Complete Treatment of Stress and Stress Tensors and How Stresses are Measured in Polycrystalline Samples.*, IIschner, B. and Grant, N. J., Editors. 1987, Springer -Verlag: New York.

5.6. G. S. Pawley, *Unit-Cell Refinement From Powder Diffraction Scan*. J.Appl.Crystallography, 1981. **14**: p. 357-361.

5.7. *Available at : www.isis.rl.ac.uk/opengenie/, accessed on 31st July. 2006.*

5.8. R. B. V. Dreele, J. D. Jorgensen and C. G. Windsor, *Reitvelt Refinement with Spallation Neutron Powder Diffraction Data*. J.Appl.Crystallography, 1982. **15**: p. 581-589.

5.9. E. Kroner, *Zur Plastischen. Verformung des Vielkristalls*. Acta Materall, 1961. **9**: p. 155-161.

5.10. M. R. Daymond, C. N. Tome and M. A. M. Bourke, *Measured and Predicted Intergranular Strains in Textured Austenitic Stainless steel*. Acta Mater, 1999. **48**: p. 553-564.

5.11. B. Clausen, T. Leffers and T. Lorentzen, *On the Proper Selection of Reflections for the Measurement of Bulk Residual Stresses by Diffraction Method*. Acta Materrialia, 2003. **51**: p. 6181-6188.

5.12. M. R. Daymond, *Private Communication*. 2005.

5.13. M. B. Prime, R. J. Sebring, J. M. Edwards, D. J. Hughes and P. J. Webster, *Laser Surface- Contouring and Spline Data-Smoothing for Residual Stress Measurement*. Experimental Mechanics, April, 2004. **44**(2): p. 176-184.

5.14. L. Edwards, M. E. Fitzpatrick, P. E. Irving, I. Sinclair, X. Zhang and D. Yapp, *Submitted to ASTM Journal: Journal of Testing and Evaluation.*

5.15. A. W. Thomas, *Parameter Development for the MIG Welding of High Strength Aerospace Aluminium Alloys, Ph.D Thesis*, in *School of Industrial and Manufacturing Science*. 2000, Cranfield University.

5.16. R.V.Blewett. *Aluminium and its Alloys in Welded Constructions*. in *IIW Anual Assembly*. 1981. Porto,Portugal.

5.17. J. R. Davis, *Aluminium and Aluminium alloys*, in *ASM Handbook ASM International*. 1998. p. 20-21.

5.18. S. Ganguly, M. E. Fitzpatrick and L. Edwards, *Comparative Neutron and Synchrotron X-Ray Diffraction Studies to Determine Residual Stress on an As-Welded AA2024 Plate*. Material Science Forum, 2005. **490-491**: p. 223-228.

5.19. S. Ganguly, *Non-Destructive Measurement of Residual Stresses in Welded Aluminium 2024 Airframe Alloy, Ph.D Thesis*, in *Materials Engineering Dept*. 2004, The Open University: Milton Keynes. p. 255.

5.20. V. Stelmukh, L. Edwards and S. Ganguly, *Full Stress Tensor Determination in a Textured Aerospace Aluminium Alloy Plate Using Synchrotron X-Ray Diffraction*. Textures and Microstructures, 2003. **35**(3-4): p. 175.

5.21. V. Stelmukh, *Neutron and Synchrotron X-ray Residual Stress Mapping of 7XXX Aluminium, Ph.D Thesis*, in *Materials Engineering Deparetment*. 2003, The Open University: Milton Keynes.

5.22. U.Stuhr, *The New Time of Flight Diffactometer at PSI for Strain Field Measurement*. Journal of Neutron Rearch, 2001. **423**(9).

5.23. A. D. Krawitz and R. A. Winholtz, *Use of Position-dependent Stress-free Standards for Difraction Measurement*. Mat.Sci.Eng.A, 1994. **A 185**: p. 123-130.

5.24. U. Stuhr, *The New Time of Flight Diffractometer at PSI for Strain Field Measurement*. Journal of Neutron Research, 2001. **9**: p. 423.

5.25. V. Hauk, *Structural and Residual Stress Analysis by Nondestructive Methods*. 1977: Elsevier.

5.26. J. R. Taylor, *An Introduction to Error Analysis*. 1982, Oxford University Press, England.

5.27. J. D. Kaminga, T. H. D. Kejser, E. J. Mittemeijer and R. Delhez, J. Appl.Cryst, 2000. **33**: p. 1059.

5.28. J. W. L. Pang, T. M. Holden and T. E. Mason, *In situ Generation of Intergranular Strains in an AL-7050 Alloy*. Acta Mater, 1998. **46**: p. 1503-1518.

5.29. Y. Zhang, S. Ganguly, M. E. fitzpatrick and L. Edwards, Journal of Neutron Research, 2004. **11**: p. 181.

5.30. V. Stelmukh, L. Edwards, J. R. Santisteban, S. Ganguly and M. E. Fitzpatrick, Material Science Forum, 2002. **599**: p. 404-407.

5.31. R. Schneider and J.-U. Hoffman, *TV tueb. Version 1.88 (http://www.hmi.de/bereiche/N/NE/uni_tuebingen/TVtueb/tvtueb.htm). 2004.*

Chapter 6

Conclusions and suggestions of future work

This chapter concludes the work carried out in thesis by summarising the contribution of this thesis and finally suggesting some recommendations for future work.

6.1 Summary

The aim of this project was to study the residual stress distributions in engineering components, at the micro and macro-scales, using the synchrotron X-ray and neutron diffraction techniques as most appropriate for the problems being studied. In addition to the measurements themselves, specific features and challenges of the methods applied and their limitations have been highlighted. The work has been focussed on the interaction between fatigue cracks and residual stress fields in welded metallic alloys.

The first set of experiments investigated the strain and stress distribution around a fatigue crack. The small-scale (sub-millimetre) extent of the crack-tip stress field requires a probe with a very fine spatial resolution, and at present only synchrotron X-ray diffraction is capable of providing this. In turn, this needs a very small grain size, and so the crack tip strain field has been investigated in fine-grained Al-5091 CT specimens. Hence the aim of this part of the study was to show the feasibility of the high resolution (20 x 20 micron) strain and stress field mapping around a fatigue crack inside a bulk metallic component under the application of in-situ loading

condition using synchrotron X-ray diffraction technique. The strain maps were obtained successfully in two principal directions and from that stresses were calculated in three principal directions assuming plane strain condition.

Following determination of the crack tip stresses, three different problems related to weld residual stress have been investigated. The first part investigated the residual stress distribution in a 316L stainless steel bead-on-plate welded specimen using neutron diffraction, and compared the results with results obtained from one another technique. These results highlighted the need to account for plastic anisotropy when measuring stresses in something like a weld which has experienced considerable plastic deformation. It may be necessary to consider this in future studies of fatigue crack tip stress fields.

The objective of the second part was to study whether the condition of similitude can be applicable to the laboratory size welded specimens. To study this phenomenon neutron diffraction experiment was carried out in MIG welded Al-2024 and Al-7150 CT specimens.

The third set of experiments was to study the residual stress redistribution due the presence of fatigue crack with different crack length. Further experiment was carried out under in-situ loading condition to investigate the effect of applied loading on the stress distribution. The results obtained and the conclusions drawn from them are presented in the following sections.

6.2 High resolution strain and stress mapping around a fatigue crack

The following conclusions can be drawn from the high resolution synchrotron X-ray diffraction strain and stress mapping around a fatigue crack *under the application of* in-situ loading condition:

- A significant tri-axial stress is observed in front of the crack tip, both in the as-fatigued specimen and in the overloaded sample at their respective K_{max} values. The magnitude of maximum tensile stress in the overloaded specimen was found to be (at 550 MPa) almost double the maximum tensile stress (220 MPa) observed in front of the fatigued cracked specimen. A constant band of compressive stress is observed all along the crack wake in the as-fatigued and overloaded specimen irrespective of their loading condition. This result indicates that the plastic anisotropy effect is the prime source of the generation of compressive stress in the crack wake region. The effect of overloading was also evident from the result where a significant compressive stress is observed at the crack tip of the overloaded specimen in unloading condition.

6.3 Macro residual stress distribution in the welded specimens

6.3.1 Residual stress in the bead-on-plate welded specimen of 316L stainless steel

The following conclusions can be drawn from the neutron diffraction experiment on bead-on-plate welded specimen:

- Neutron diffraction technique was successfully used to determine 3-D macro residual stress distribution in a TIG welded 316L stainless steel plate. The results show high magnitude of longitudinal and transverse stresses (over 300 MPa and 200 MPa respectively) exist close to the weld bead. There is some evidence of weld start and stop concentration effects but they are more pronounced in the strain graphs than in the stress graphs. The normal stress does not vary much and remains close to zero.
- The measured through-thickness stress profiles for the weld start, centre and stop positions are almost identical to each other implying that any weld start and stop stress concentration effects have little effect on the underlying through-wall stress distribution.
- A clear evidence of transverse direction strain concentration is observed in the stop end with maximum strain concentration of 750 microstrain was found near the weld stop region.
- The comparative study of single peak analysis and multi peak analysis reveals the presence of plastic anisotropy in the region near the weld material.

Significant intergranular stress is observed particularly in the normal direction due to the plastic anisotropy. The effect of plastic anisotropy was reduced to minimum in the final results by the use of Pawley fitting routine while analysing the diffraction spectrum (section 5.1.5.5).

- The stress results obtained from the diffraction experiment shows good agreement when the results were compared with the finite element analysis results and the contour results.

6.3.2 Effect of weld residual stress in the similitude criteria in the laboratory size specimen

A number of conclusions can be drawn from the diffraction measurement of Al-7150 and Al-2024 CT specimen and are listed below:

- Near the weld centre, the stresses are found to be compressive in both the specimens, but this compressive region is narrower and the magnitude of compressive stress is higher in case of the Al-7150 specimen (around –150 *MPa*) compared to the Al-2024 specimen (around –50 MPa). The peak tensile longitudinal stresses of around 140 *MPa and 120 MPa were* observed near the HAZ region in Al-2024 and Al-7150 sample respectively.
- In both alloys, a substantial relaxation in the longitudinal stresses was observed when compared to the original welded plate. The stress distribution at weld centre changes from tensile (in the original specimen) to compressive in the CT specimen. These results provide firm evidence that residual stresses do not show the similitude that is a fundamental pre-requisite of the

application of data obtained laboratory sized specimens to larger components and structures.

6.3.3 Residual stress redistribution effect due to presence of fatigue crack

The effect of fatigue crack on the existing residual stress field in the welded specimen has been investigated using neutron diffraction technique and the results and conclusions are summarised below:

- In the short cracked (2a = 13 mm) sample, a significant compressive stress is observed all along the crack with the maximum compressive stress of –50 MPa is found near the crack tip. A sharp rise of stress is observed in front of a crack tip and the stress values increases to tensile from the compressive stress. The maximum tensile stress of 270 MPa is found at around 8 mm away from the weld centre.
- Like the short crack sample, the long cracked sample (2a = 25 mm) shows the similar stress distribution with a compressive stress field along the crack and a sudden increase of this compressive stress to the tensile region is observed in front of the crack tip. The maximum compressive stress of around -90 MPa was observed near the crack tip while the maximum tensile stress of around 300 MPa was found around 16 mm from the weld centre.
- A significant redistribution of the residual stress is observed in the fatigue-cracked specimens when the results were compared with the as-welded sample. Compared to the high tensile stress near the weld and HAZ region found in the as-welded specimen, a considerable amount of compressive

stress is observed in the fatigue-cracked specimen along the crack with maximum compressive stress in front of the crack tip.

- Diffraction experiment under the application of different level of in-situ loading reveals a systematic increase of measured stress which indicates that the superposition principle can be applicable in the fatigue cracked specimen where residual stress previously exists.

6.4 Suggestions of future work

This study has exploited the synchrotron X-ray and neutron diffraction techniques successfully aiming at determining residual stress distribution in micro and macro length scale.

Although synchrotron diffraction technique is successfully used to map the strain and stress field around the crack tip in as-fatigued sample and overloaded sample and results obtained from this gives a broad spectrum of the events happening in the crack tip strain and stress field under in-situ loading condition, a further in-depth analysis of the data can give us more detail information regarding the crack tip and crack wake strain and stress field behaviour. In addition, stress intensity factor can be calculated and compared with the applied values by fitting the experimental stress data to Westergaard equations. Further, an attempt can be made to model these results using FE simulations. In addition, further investigation can also be carried out for the specimens with different loading history for example, fatigued, fatigued–overloaded and fatigued-overloaded-fatigued samples for a range of load cases.

The macro residual stress distribution, obtained using neutron diffraction technique, in bead-on-plate welded 316L stainless steel specimen shows good

agreement with the contour and neutron diffraction results, however there is a scope for the texture corrections in terms of d_0 corrections if comb specimen can be extracted from the weld region and measured.

Regarding the residual stress redistribution study, there is a scope to continue the present work in studying the effect of this redistribution phenomenon on different crack length by growing fatigue crack of different length and measuring the residual stress. Furthermore, residual stress intensity factor can then be calculated directly by separating the measured and applied stress intensity factors. Finally the residual stress intensity factor obtained in this method can be compared with the model.